Implementation of an integred methodology for the evaluation of the phovotovoltaic potential at district scale : focus on the vertical facades

Benjamin Govehovitch

To cite this version:

Benjamin Govehovitch. Implementation of an integred methodology for the evaluation of the phovotovoltaic potential at district scale : focus on the vertical facades. Civil Engineering. Université de Lyon, 2021. English. NNT : 2021LYSE1032 . tel-03430281

HAL Id: tel-03430281
https://theses.hal.science/tel-03430281v1

Submitted on 16 Nov 2021

N°d'ordre NNT : 2021LYSE1032

THESE de DOCTORAT DE L'UNIVERSITE DE LYON
opérée au sein de
l'Université Claude Bernard Lyon 1

Ecole Doctorale 162
(MEGA – Mécanique, Energétique, Génie civil, Acoustique)

Spécialité de doctorat : Energétique, Génie civil

Soutenue publiquement le 08/02/2021, par :
Benjamin GOVEHOVITCH

Implémentation d'une méthodologie intégrée de l'évaluation du potentiel photovoltaïque à l'échelle de la ville – Cas des façades verticales

---

Devant le jury composé de :

Musy, Marjorie	Directrice de recherche, HDR, INSIS Nantes - IRSTV	Président
Bruse, Michael	Professor, Université Johannes Gutenberg, Mayence	Rapporteur
Migan-Dubois, Anne	Professeur, Université Paris-Saclay - GEEPS	Rapporteure
Ben Hadid, Hamda	Professeur, Université Claude Bernard Lyon 1, LMFA	Examinateur
Desthieux, Gilles	Professeur associé, HEPIA Genève - HESGE	Examinateur
Lobaccaro, Gabriele	Professeur associé, NTNU - DCEE	Examinateur
Musy, Marjorie	Directrice de recherche, HDR, INSIS Nantes - IRSTV	Examinatrice
Giroux-Julien, Stéphanie	Maître de conférences, HDR, Université Claude Bernard Lyon 1 – CETHIL	Directrice de thèse
Peyrol, Éric	Maître de conférences, Université Lyon 1 - BioDyMIA	Co-directeur de thèse
Ménézo, Christophe	Professeur, Université Savoie Mont-blanc - LOCIE	Invité
Rusaouen, Gilles	Maître de conférences, Université Lyon 1- CETHIL	Invité

Doctoral school MEGA (ED 162) – Mechanical Engineering, Energetics, Civil Engineering and Acoustics

DOCTORAL THESIS

A thesis submitted in fulfillment of the requirements for the degree of Doctor of Philosophy

of the University Claude Bernard Lyon 1

Doctoral Speciality "Energetics and Civil Engineering"

presented and publicly defended by

Benjamin Govehovitch

on February 8, 2021

Implementation of an Integrated Methodology for the Evaluation of the Photovoltaic Potential at District Scale – Focus on the Vertical Facades

Thesis supervisor: **Stéphanie Giroux–Julien**
Thesis co-supervisor: **Éric Peyrol**

Approved by:

Michael Bruse	Professor, Johannes Gutenberg University Mainz	Rapporteur
Anne Migan-Dubois	Professor, Univ. Paris-Saclay – GEEPS	Rapporteur
Hamda Ben Hadid	Professor, Univ. Lyon 1 – LMFA	Examiner
Gilles Desthieux	Associate professor, HEPIA Genève – HESGE	Examiner
Gabriele Lobaccaro	Associate professor, NTNU – DCEE	Examiner
Marjorie Musy	Director of research, HDR, INSIS Nantes – IRSTV	Examiner
Stéphanie Giroux–Julien	Associate professor, HDR, Univ. Lyon 1 – CETHIL	Thesis supervisor
Éric Peyrol	Associate professor, Univ. Lyon 1 – BioDyMIA	Thesis co-supervisor
Christophe Ménézo	Professor, Univ. Savoie Mont-blanc – LOCIE	Invited
Gilles Rusaouen	Associate professor, Univ. Lyon 1 – CETHIL	Invited

“Ce que l’on conçoit bien s’énonce clairement,
Et les mots pour le dire arrivent aisément.”

Nicolas Boileau

ACKNOWLEDGMENTS

I would not have successfully executed this project without the support and guidance of various people at the University Claude Bernard Lyon 1 and the Center for Energy and Thermal Sciences of Lyon (CETHIL).

I wish to express my dearest gratitude to each and every member of the different projects in which I was involved during my three years of thesis and with whom I had the chance to collaborate. Your skills and expertise have been a great source of inspiration for me. I was able to hone my skills through various national and international projects, which also provided invaluable support to my work: the ORCHIDEE project, the G2 Solaire project and the task 63 of the International Energy Agency. For all that this has brought me professionally and personally, I will be forever indebted to you.

I would like to thank all the members of my thesis jury: my rapporteurs Anne Migan-Dubois and Michael Bruse, professors Hamda Ben Hadid, associate professors Gilles Desthieux and Gabriele Lobaccaro, and research director Marjorie Musy who accepted to be examiners. I am honoured by the interest that you have shown for my work.

I grant my special thanks to Dr Stéphanie Giroux–Julien and Dr Éric Peyrol, my thesis supervisor and co-supervisor. Their support and advice greatly contributed to the quality of my work. I also wish to show my gratitude to Christophe Ménézo, who has been a precious support.

This thesis, although carried by a student and his directors, is also the fruit of many interactions and discussions. Thus, I would like to thank all my colleagues, with whom I have discussed or exchanged at one time or another: Mathieu and Maxime for their skills in radiative transfers, Hervé for his in fluid mechanics, Loïc for his IT

support so essential for these digital works. I would like to pay my special regards to Lucie who has given me support when I needed it. I also thank Edwige, Maryline Mériem and Nazaré for their unwavering administrative support.

I extend my sincere gratitude to all my galley companions, who carried out their work at the same time as me and who represent so many beautiful encounters: Bao, Baptiste, Julie, Martin. Special thanks to Khriscia who shared my office for 3 years.

On the other hand, and since I would not have considered doing a thesis without my past experiences and the chances of life, I wanted to thank all those who have led me to be here today. First of all Cindy, who gave me my first research experience, as well as all the people I worked with at the Lawrence Berkeley National Laboratory: Ari, Baptiste, Christian, Darryl, Joshua, Paul.

A thesis is a three-year course full of pitfalls, at the end of which it is almost impossible to arrive alone. The support of his friends is essential. So I especially want to thank Julien who did not hesitate to take his time to help me when I needed it, even going so far as to make his apartment my second office.

Finally, although a thesis is a professional experience, it is impossible to complete it without personal support. This is why I would like to acknowledge the irreplaceable support of Iris, who had the patience to read this work many times, who cheered me up when I needed it, who brings me so much on a daily basis and who will continue to do so after my thesis. And since writing a thesis is not an easy task, a pleasant environment is more than welcome. This is why I would like to thank Iris' parents, Murielle and Pierre, who welcomed me this summer and allowed me to write this document in very pleasant conditions.

Last but not least, I reserve my most sincere thanks to my parents, Danielle and Jean, who have always supported me in each of my projects. I wouldn't be who I am or where I am today without them. Thank you also to my sisters, Adeline, Clémence, Dora and Églantine who have always believed in me, have given me so much and will continue to do so.

ABSTRACT

The main objective of this thesis is to evaluate the potential of photovoltaic (PV) energy production of the buildings' facades in urban areas. The existing production models usually consider the buildings in isolation and take into consideration the close environment as masks. However, several specific physical phenomena occur in urban areas. Some are due to natural weather conditions, such as the days/seasons cycle (time variability of the solar resource) or the cloud movement (intermittency of the solar radiation). Others are due to the built environment, such as the spatial heterogeneity due to the surrounding buildings, the inter-building reflections or the wind channeling due to the narrow space between buildings in urban areas.

Among the aforementioned phenomena, some may have a positive impact on the solar potential of buildings' facades whereas others may have a negative one. Considering an integrated methodology taking into consideration a multi-physics (including solar radiation and airflow modeling) and multi-scale (evaluation of the spatial heterogeneity) appears then as a crucial issue for the evaluation of the solar potential of buildings.

The chosen tool is the software ENVI-met. As an urban microclimate (UMC) simulation software, it aims to take into consideration all the phenomena that occur in urban context. Thus, it includes, among other, an airflow model as well as a radiative model able to account for the inter-building reflections.

The first step is to evaluate and position the two above-mentioned models through case studies dealing with theoretical or actual cases. Thus, the airflow model is confronted with measurements carried out in a wind tunnel while the radiative model is applied to an actual district. Regarding the performances of the considered PV power generation models, the predicted values are compared with measurements obtained under standard test conditions.

Once the ability of the ENVI-met software to take into consideration and accurately simulate the urban-specific phenomena demonstrated, the simulation output data are used as inputs for the PV generation models. Two studies are carried out:

1. The influence of the series connections on the buildings' facades PV potential is evaluated;
2. The seasonal behavior of the production model is assessed.

The first case of study, dealing with the series connection of the PV modules, aims to predict the direction of the connections (vertical or horizontal) to optimize the PV potential of facades while meeting the photovoltaic technology requirements.

The second study, aims to show the evolution of the accuracy in terms of PV power generation prediction over the year. Thus, the influence of several weather parameters' ranges are assessed: the shortwave radiation, the surface temperature of the PV modules and the wind velocity near the buildings' facades.

RÉSUMÉ

Le principal objectif de cette thèse est de mettre en place une méthodologie intégrée d'évaluation du potentiel photovoltaïque des façades de bâtiments en milieu urbain. Les modèles de production existants considèrent généralement les bâtiments de manière isolée et prennent en compte l'environnement proche uniquement comme des masques. Cependant, plusieurs phénomènes physiques spécifiques se produisent dans les zones urbaines. Certains sont dus aux conditions météorologiques naturelles, comme le cycle journalier / saisonnier (variabilité temporelle de la ressource solaire) ou le mouvement des nuages (intermittence du rayonnement solaire). D'autres sont dus à l'environnement bâti, comme l'hétérogénéité spatiale due aux bâtiments environnants, les réflexions inter-bâtiments ou la canalisation du vent due à l'espace étroit entre les bâtiments dans les zones urbaines.

Parmi les phénomènes mentionnés ci-dessus, certains peuvent avoir un impact positif sur le potentiel solaire des façades des bâtiments tandis que d'autres peuvent avoir un impact négatif. La mise en place d'une méthodologie intégrée prenant en compte une multi-physique (comprenant la modélisation du rayonnement solaire et de l'écoulement d'air) et multi-échelle (évaluation de l'hétérogénéité spatiale) apparaît alors comme un enjeu crucial pour l'évaluation du potentiel solaire des bâtiments.

L'outil choisi pour cette étude est le logiciel ENVI-met. En tant que logiciel de simulation de microclimat urbain, il vise à prendre en compte tous les phénomènes qui se produisent en contexte urbain. Ainsi, il comprend, entre autres, un modèle aéraulique ainsi qu'un modèle radiatif capable de rendre compte des réflexions inter-bâtiments.

La première étape consiste à évaluer et à positionner les deux modèles susmentionnés à travers des études de cas traitant de cas théoriques ou réels. Ainsi, le modèle aéraulique est confronté à des mesures effectuées en soufflerie tandis que le modèle

radiatif est appliqué à un quartier réel. En ce qui concerne les performances des modèles de production d'énergie photovoltaïque considérés, les valeurs prédites sont comparées aux mesures obtenues dans des conditions de test standard.

Une fois la capacité du logiciel ENVI-met à prendre en compte et à simuler avec précision les phénomènes urbains démontrée, les données de sortie des simulations sont utilisées comme entrées pour les modèles de production photovoltaïque. Deux études sont menées:

1. Dans un premier temps, l'influence des connexions série sur le potentiel photovoltaïque des façades des bâtiments est évaluée;

2. D'autre part, le comportement saisonnier du modèle de production est caractérisé au travers d'une confrontation entre les résultats numériques obtenus et des mesures réalisées in-situ.

Le premier cas d'étude, traitant de la connexion en série des modules photovoltaïque, vise à prédire la direction des connexions (verticale ou horizontale) à choisir afin d'optimiser le potentiel photovoltaïque des façades tout en respectant les exigences techniques de la technologie photovoltaïque.

La seconde étude vise à montrer l'évolution de la précision en termes de prévision de la production d'énergie photovoltaïque au cours de l'année. Ainsi, l'influence de plusieurs paramètres météorologiques est évaluée: le rayonnement solaire, la température de surface des modules photovoltaïques et la vitesse du vent à proximité des façades des bâtiments.

CONTENTS

LIST OF FIGURES

LIST OF TABLES

LIST OF SYMBOLS

The next list describes the symbols that will be later used within the body of the document. The equation of the first occurence of each symbol is provided as well as the page where it occurs.

Symbol	Quantity	Unit	Reference
Latin Letters			
A	Area	$[\mathrm{m}^2]$	eq. (5.3), page 87
a	Albedo	[-]	eq. (3.30), page 49
a_w	Albedo of the cloud layers	[-]	eq. (3.30), page 49
a_{so}	Albedo of the soil	[-]	eq. (3.30), page 49
APE	Absolute Percentage Error	[%]	eq. (5.4), page 94
B	Black-body radiance	$[\mathrm{W} \cdot \mathrm{m}^{-2} \cdot \mathrm{sr}^{-1} \cdot \mathrm{nm}^{-1}]$	eq. (3.19), page 44
BR	Blockage ratio	[%]	eq. (5.3), page 87
c	Speed of light $c = 299\,792\,548\,\mathrm{m} \cdot \mathrm{s}^{-1}$	$[\mathrm{m} \cdot \mathrm{s}^{-1}]$	eq. (3.19), page 44

c ; d	Constants of Oke's empirical model for long-wave radiation	[-]	eq. (3.38), page 51
c_1 ; c_2 ; c_3	Coefficients of the closure model of Mellor and Yamada	[-]	eq. (3.16), page 43
c_μ	Constant of the turbulence model	[-]	eq. (3.5), page 41
c_p	Specific heat of air	$[\mathrm{J} \cdot \mathrm{K}^{-1} \cdot \mathrm{kg}^{-1}]$	eq. (3.14), page 42
E	Turbulent kinetic energy	$[\mathrm{m}^2 \cdot \mathrm{s}^{-2}]$	eq. (3.16), page 43
E_g	Bandgap energy	[eV]	eq. (C.15), page XI
e_{2m}	Vapor pressure at a height of two meters	[hPa]	eq. (3.26), page 49
F	External constraints	$[\mathrm{m} \cdot \mathrm{s}^{-2}]$	eq. (3.5), page 41
f	Coriolis parameter	$[\mathrm{s}^{-1}]$	eq. (3.11), page 42
G	Solar irradiance	$[\mathrm{W} \cdot \mathrm{m}^{-2}]$	eq. (3.49), page 62
g	Gravitational acceleration	$[\mathrm{m} \cdot \mathrm{s}^{-2}]$	eq. (3.8), page 41
H	Height	[m]	eq. (5.3), page 87
h	Planck's constant $h = 6.626\,070\,15 \cdot 10^{-34}\,\mathrm{J} \cdot \mathrm{s}$	$[\mathrm{J} \cdot \mathrm{s}]$	eq. (3.19), page 44
h	Sun height	[°]	eq. (3.22), page 48
I	Current	[A]	eq. (3.44), page 58

i	i-th spatial dimension		eq. (3.5), page 41
I_0	Radiation intensity of the Sun	$[\mathrm{W} \cdot \mathrm{m}^{-2} \cdot \mathrm{nm}^{-1}]$	eq. (3.21), page 47
j	j-th spatial dimension		eq. (3.18), page 43
k	Boltzmann's constant $k = 1.381 \cdot 10^{-23}\,\mathrm{J} \cdot \mathrm{K}^{-1}$	$[\mathrm{J} \cdot \mathrm{K}^{-1}]$	eq. (3.44), page 58
K_ε	Turbulent exchange coefficient for the turbulence dissipation rate	$[\mathrm{m}^2 \cdot \mathrm{s}^{-1}]$	eq. (3.16), page 43
K_h	Turbulent coefficient for heat	$[\mathrm{m}^2 \cdot \mathrm{s}^{-1}]$	eq. (3.14), page 42
K_m	Local exchange coefficient	$[\mathrm{m}^2 \cdot \mathrm{s}^{-1}]$	eq. (3.5), page 41
K_w	Turbulent exchange coefficient for humidity	$[\mathrm{m}^2 \cdot \mathrm{s}^{-1}]$	eq. (3.14), page 42
L	Length	[m]	eq. (5.3), page 87
m	Optical air mass	[-]	eq. (3.21), page 47
m_{vap}	Amount of absorbing water vapor	[kg]	eq. (3.33), page 50
N	Number of photovoltaic cells	[-]	eq. (C.8), page IX
n	Ideality factor	[-]	eq. (3.44), page 58
N_l, N_m, N_h	Cloud level of low, medium and high clouds	[octa]	eq. (3.31), page 49
N_{at}	Total number atmospheric layers	[-]	eq. (3.33), page 50

n_{at}	n-th layer of the atmosphere		eq. (3.33), page 50
N_{clo}	Total degree of cloudiness	[octa]	eq. (3.29), page 49
p	Pressure	[Pa]	eq. (3.5), page 41
p'	Local pressure perturbation	[Pa]	eq. (3.5), page 41
P_{MAX}	Maximal output power generated by the PV panel	[W]	eq. (3.49), page 62
P_{out}	Output power generated by the PV panel	[W]	eq. (3.49), page 62
Pr	Mechanical shearing	$[\mathrm{m}^2 \cdot \mathrm{s}^{-3}]$	eq. (3.16), page 43
Q	Radiation flux	$[\mathrm{W} \cdot \mathrm{m}^{-2}]$	eq. (3.21), page 47
q	Elementary electrical charge $q = 1.602 \cdot 10^{-19}\,\mathrm{C}$	[C]	eq. (3.44), page 58
Q_T	Heat exchange between air and vegetation	$[\mathrm{K} \cdot \mathrm{s}^{-1}]$	eq. (3.14), page 42
Q_w	Exchange of humidity between air and vegetation	$[\mathrm{kg} \cdot \mathrm{kg}^{-1} \cdot \mathrm{s}^{-1}]$	eq. (3.14), page 42
R	Resistance	$[\Omega]$	eq. (3.44), page 58
S	Local source / sink terms of wind drag	$[\mathrm{m} \cdot \mathrm{m}^{-2}]$	eq. (3.5), page 41
T	Temperature	[K]	eq. (3.49), page 62
t	Time	[s]	eq. (3.5), page 41

Th	Thermal forces	$[\mathrm{m}^2 \cdot \mathrm{s}^{-3}]$	eq. (3.16), page 43
u	Wind velocity	$[\mathrm{m} \cdot \mathrm{s}^{-1}]$	eq. (3.5), page 41
V	Voltage	[V]	eq. (3.44), page 58
x	Spatial dimension	[m]	eq. (3.5), page 41
y	Measurement value	[-]	eq. (5.8), page 141
z	Height	[m]	eq. (3.8), page 41
z_v	Height of the edge of the water vapor atmosphere	[m]	eq. (3.32), page 50
Greek Letters			
α_M	Mie scattering	[-]	eq. (3.21), page 47
α_R	Rayleigh scattering	[-]	eq. (3.21), page 47
α_T	Temperature coefficient of the short-circuit current	$[\% \cdot {}^{\circ}\mathrm{C}^{-1}]$	eq. (C.14), page XI
β_T	Temperature coefficient of open-circuit voltage	$[\% \cdot {}^{\circ}\mathrm{C}^{-1}]$	eq. (C.7), page IX
β_{tr}	Turbidity coefficient	[-]	eq. (3.24), page 48
γ	Temperature-power coefficient of the PV panel	$[\% \cdot {}^{\circ}\mathrm{C}^{-1}]$	eq. (3.49), page 62
Δ	Difference between two discrete elements		eq. (3.33), page 50

ε	Turbulence dissipation rate	$[\mathrm{m}^2 \cdot \mathrm{s}^{-3}]$	eq. (3.16), page 43
λ	Wavelength	[m]	eq. (3.19), page 44
ν	Kinematic viscosity	$[\mathrm{m} \cdot \mathrm{s}^{-2}]$	eq. (3.5), page 41
ρ	Fluid density	$[\mathrm{kg} \cdot \mathrm{m}^{-3}]$	eq. (3.14), page 42
σ_ε	Coefficient of the turbulence model	[-]	eq. (3.16), page 43
σ_E	Coefficient of the turbulence model	[-]	eq. (3.16), page 43
φ	Latitude of the model's location	[°]	eq. (3.11), page 42
Ω	Pulsatance of the earth's rotation	$[\mathrm{s}^{-1}]$	eq. (3.11), page 42

Superscripts

$*$	At the model upper edge		eq. (3.21), page 47
0	Absolute		eq. (3.25), page 48
$\downarrow$	Downward		eq. (3.32), page 50

Subscripts

1, 2, 3	Spatial dimensions		eq. (3.5), page 41
abs	Absorbed		eq. (3.25), page 48
at	Atmosphere		eq. (3.33), page 50

$diff$	Diffuse	eq. (3.27), page 49
dir	Direct	eq. (3.25), page 48
exp	Experimental	eq. (5.4), page 94
g	Geostrophic	eq. (3.11), page 42
irr	Irradiation	eq. (C.8), page IX
lw	Longwave	eq. (3.32), page 50
M	Module	eq. (C.1), page VII
mp	Maximum power	eq. (C.8), page IX
MPP	Maximum power point	eq. (C.5), page VIII
N_{day}	Number of days in the month	eq. (5.7), page 119
OC	Open-circuit	eq. (C.8), page IX
p	Parallel	eq. (3.44), page 58
$peak$	Wavelength where the black-body spectra radiance peaks	eq. (3.20), page 44
RAD	Representative Average Day	eq. (5.7), page 119
ref	Reference condition	eq. (3.8), page 41

s	Series	eq. (3.44), page 58
SC	Short-circuit	eq. (C.8), page IX
sh	Shunt	eq. (3.44), page 58
sim	Simulated	eq. (5.4), page 94
STC	Standard test conditions	eq. (3.50), page 62
sw	Shortwave	eq. (3.21), page 47

LIST OF ABBREVIATIONS

A

APE absolute percentage error. 94
AVF averaged view factor. 108–110

B

BHI beam horizontal irradiance. 12, 73, 74, 185
BIM building information model. 19
BIPV building integrated photovoltaic. 19, 20, 108, 131
BL boundary layer. 88
BNI beam normal irradiance. 12, 73, 185
BR blockage ratio. 86, 87, 90

C

CAD computer-aided design. 19
CFD computational fluid dynamics. 22, 24, 39
CSV coma-separated values. 73

D

DBMS database management system. 77
DTS dynamic thermal simulation. 22

F

FF fill factor. 54, 56

G

GIS geographic information system. 17–19

I

IV current-voltage. 52, 54, 56, 58, 59, 61, 62
IVS indexed view sphere. 108–110, 116

L

LBC lateral boundary conditions. 10, 11
LES large eddy scale. 39, 193
LIDAR light detection and ranging. 18
LW longwave. 42, 44, 73, 74, 138, 140, 167

M

MAPE mean absolute percentage error. 94, 95, 97, 98, 141–146, 177, 182, XLIV, XLIX
MPP maximum power point. VIII

N

NOCT nominal operating cell temperature. 62, 63, 118

P

PV photovoltaic. 4, 6–8, 12, 13, 16, 19, 20, 22, 37, 38, 43, 58, 71, 72, 75–78, 80, 83, 85, 108, 109, 115, 116, 118, 120, 123, 126, 127, 129, 131, 132, 137, 141, 145, 147, 148, 151, 153, 157, 158, 161, 166, 171, 173–177, 182, 183, 185, 190–197, XLI, XLIV, XLIX

R

RAD representative average day. 128
RANS Reynolds-averaged Navier-Stokes. 37, 39, 40, 85
RMSE root mean squared error. 141–146, 177, 182, XLIV, XLIX

S

STC standard test conditions. 62, 63, X
SW shortwave. 44, 47, 73, 74, 76, 108, 109, 116, 118, 120, 123–125, 129, 131, 133, 134, 138, 140, 145, 167, 173, 175, 182, 183, 185, 194, 195

U

UAS unmanned aerial systems. 18
UBEM urban building energy model. 23
UHI urban heat island. 5, 20, 137
UMC urban microclimate. 5, 8, 21–25, 71, 80, 105, 148, 190, 191, 194, 195, 197
UMI urban modeling interface. 25

1

INTRODUCTION

They did not know it was impossible so they did it.

Mark Twain

Facing the ever-increasing demand for energy, while fighting against climate change, is one of the major challenges of the coming century. This will necessarily go through rational energy consumption and the development of the use of renewable energies.

Among the renewable energy sources, the one with the highest potential available is solar energy. This can be used in different forms, including: photovoltaic, thermal, or concentrating solar power.

The work presented in this document is carried out through various projects aimed at better characterizing the solar resource, as well as its exploitation, and the related issues in urban areas.

The evaluation of the photovoltaic potential of buildings' facades at city scale is undertaken with the urban microclimate simulation software ENVI-met. Therefore, this tool is introduced in the last part of this introduction, with the main assumptions and models that it takes into account, including: airflow and radiative fluxes. Finally the chaining to evaluate the photovoltaic power generation is described.

1.1 GENERAL INTRODUCTION AND CONTEXTUALIZATION OF THE WORK

1.1.1 *Energy and Environment Context*

Since the various industrial revolutions, world energy consumption has not ceased to grow, as shown in figure 1.1 on the facing page (Ritchie, 2014). This increase has, of course, allowed the technological development that we know but has also contributed to profoundly modify our environment.

At the same time, the world's population is increasingly found in cities. Nowadays, more than half of the population is concentrated in the cities. By 2030, this amount will rise to 60 % and exceed 68 % by 2050, as shown in figure 1.2 on the next page ("The World's Cities in 2018", n.d.).

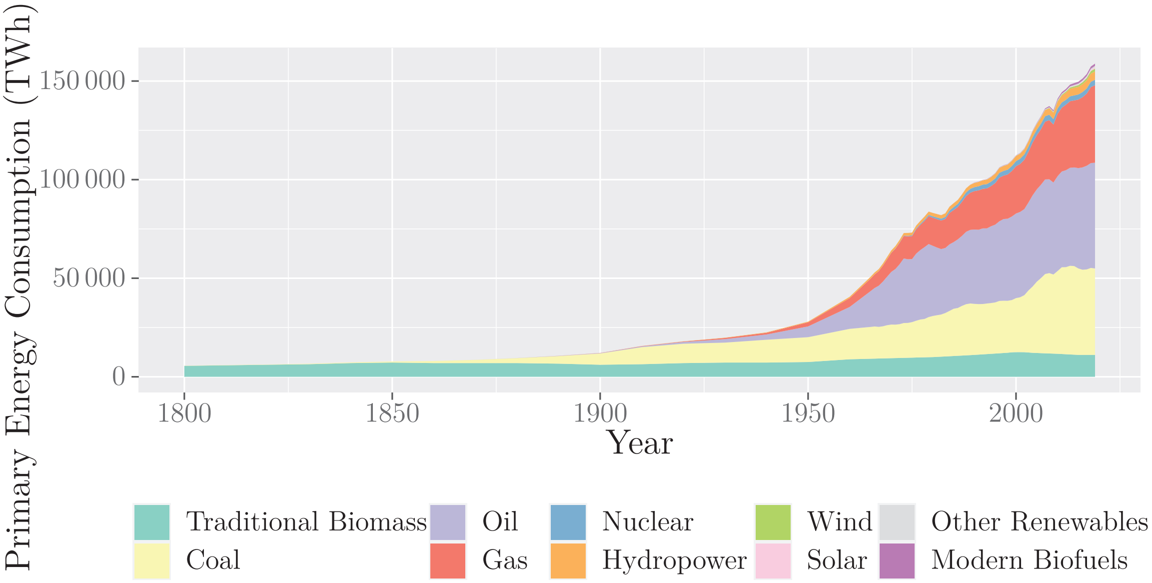

Figure 1.1.: Global Primary Energy Consumption

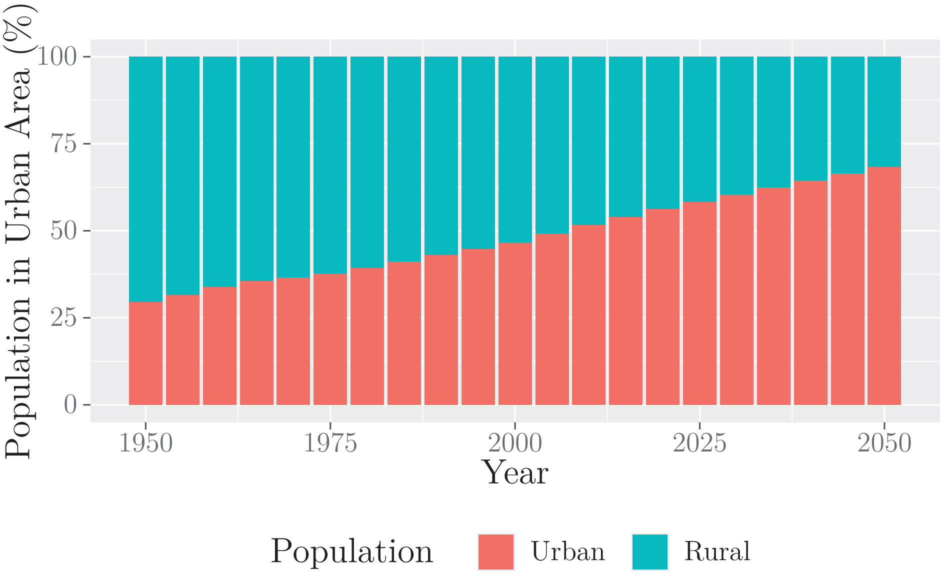

Figure 1.2.: Percentage of the World's Population at Mid-Year Residing in Urban Areas – 1950 - 2050

One of the major issues of the coming century is therefore to meet the ever-increasing demand for energy, while fighting against climate change. Reconciling these two issues involves the exploitation of renewable energy sources.

Among those, the one offering the greatest potential is solar energy (Moriarty and Honnery, 2012), and more particularly photovoltaic (PV) technology. However, this resource is still poorly understood in an urban context. The work presented in this paper is therefore part of the solution to this problem: better characterize the solar potential (PV) of buildings in order to be able to exploit it to the maximum, while taking into account the specific features of the urban context. These features include the morphology of the considered neighborhood, as well as the local weather conditions.

Usually, the assessment of the PV potential of buildings is carried out with isolated buildings, potentially surrounded by other buildings, which are only considered as masks. In addition, the modelization of the solar radiation is simplified and the aeraulic phenomena are disregarded. Moreover, the weather conditions are from typical weather data, which usually correspond to measurements results averaged over several years or decades. The measurements being usually udertaken at airport weather stations, they can not reflect the local weather observed in cities.

To better characterize the solar potential (PV) of buildings, the work presented here is part of various projects, aimed at exploiting solar resources or evaluating the thermal comfort of cities.

1.1.2 *Projects in which this Work is Conducted*

Interest in the solar potential of cities has grown steadily over the past decades. Numerous studies have been carried out, with a common goal: make the cities greener. Depending on the considered country, it passes through different laws and regulations. In France, the evaluation of the thermal regulation highlights the goal to reduce the carbon footprint of the buildings. Thus, the thermal regulations 2012 (French RT 2012) impose an energy consumption ratio that must not be exceeded (inspired from the low-energy building label), depending on the geographical location, while the future 2020 environmental regulations tend to both reduce the environmental impact of buildings while making them energy producers (positive energy buildings). The energy can be produced by the buildings with photovoltaic systems, delivering a low voltage electricity, not in relation with the centralized energy production system. The producted energy can then be consumed by the building itself (self-consumption) or close buildings via smart-grids or low-voltage power network (with buildings at a maximum distance of about a hundred meters).

The projects, in which the work presented here take part, follow the dynamic of aiming at making the cities greener. Three main projects contributed to the development of this work: ORCHIDEE, RESSOURCES and G2 Solaire. They are described below. The work presented here has been an active part of the projects ORCHIDEE and G2 Solaire, while the RESSOURCES project was already closed but made it possible to provide measurement results.

1.1.2.1 *ORCHIDEE*

The ORCHIDEE[1] project is funded by the French Agency for the Environment and the Energy Management (ADEME). This project is a cooperation between different scientific partners, both academic and industrial, including: University of the Reunion Island, iRSTV[2], FédEsol[3], Solener, Imageen. It intends to deal with the problem of design tools for neighborhoods in tropical environment by addressing the effects of the neighborhood on the urban heat island (UHI) effect and on the aeraulic conditions around and through buildings. The methods and tools developed can be applied as much to rehabilitated neighborhoods and buildings as for new projects.

The work presented here is part of the task of this project aimed at modeling the studied neighborhood and optimizing the urban morphology. In this task, the district Vauban, located in Saint-Denis (Reunion Island), is studied. The associated work is discussed in 5.1.2 on page 103.

The other parts of this project are related to interior comfort, in an island context and in a tropical environment. Thus, better comfort is targeted, by exploiting natural ventilation and optimizing it by taking into account the morphology of the neighborhoods. The various studies can be carried out thanks to measurements (wind tunnel tests) and simulations (modeling of the urban microclimate (UMC) with Solene-microclimate or of the solar production potential with different tools such as ENVI-met or EnergyPlus / Radiance). The assessment of comfort is carried out using questionnaires.

---

[1] ORCHIDEE stands for Renovation and design tools for smart housing and eco-neighborhoods in tropical environments, in French.

[2] Institut de Recherche en Sciences et Techniques de la Ville

[3] Solar Energy Research Federation

1.1.2.2 *RESSOURCES*

The RESSOURCES project[4] aims to redefine the building's envelope (roof and facade) classically defined (including insulation and waterproofing) by adding functions combining technological and aesthetic innovations making it active. This project is a cooperation between different scientific partners, both academic and industrial, including: CNRS[5] / CETHIL[6], EDF[7], HBS – Technal, Tenesol and Jacques-Ferrier Architecte. Maintaining electrical performance under warm weather conditions, by enhancing the thermal draw (chimney effect) between the building wall and the PV wall, has been a key issue in those developments.

Two prototypes have been designed, developed and instrumented. They are made up of PV double-skins. The two prototypes are described below:

ETNA The ETNA building is located in the south east of the Paris region. It is composed of two almost twins test cells, as shown in figure 1.3.

Figure 1.3.: ETNA Building – EDF R&D – Moret-sur-Loing

The two green and pink facades are covered with PV cells, as well as the slanted walls. The green test cell has an additional twelve-squared-meter-area, which can be valued from a thermal point of view during the winter period with a preheating of the air of the greenhouse by the incident solar radiation.

---

[4] RESSOURCES stands for Redefinition of building envelopes, optimization and rational use of solar power generation components, in French.

[5] Centre National de la Recherche Scientifique - French National Center for Scientific Research

[6] Centre d'Energétique et de Sciences Thermiques de Lyon - Centre for Energy and Thermal Sciences of Lyon

[7] EDF is the main electricity producer in France

The vertical facades are 5.6 m high and 3 m wide, the slanted walls are 6.77 m and 8.69 m long for the pink and green test cells, respectively. The whole building's facade (vertical and slanted facade) has a total power of 3.5 kWp.

The measurements on this prototype, in terms of temperature, solar irradiation and wind velocity, are used to evaluate different PV power generation models in section 5.2 on page 136.

HBS-TECHNAL The HBS prototype is located in Toulouse, on a tertiary building, in service all year round (see figure 1.4). This allows to evaluate the actual behavior of the active facade under operating conditions.

This building is composed of open space offices, spread over three floors. The total height of the building is 11.9 m. Regarding the active facade, it is 7.4 m high. The facades are fully glazed, which is a challenge in terms of thermal comfort. The active facade has a total power of 1.2 kWp.

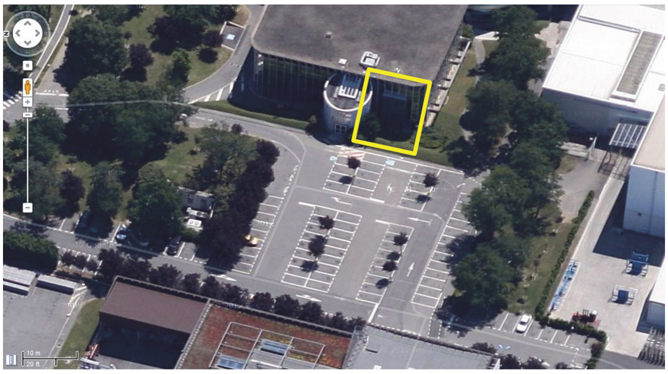

Figure 1.4.: HBS-Technal Headquarters – Toulouse (Google Maps)

Although this project was already completed before the start of this work, it provides a database of measurements carried out in-situ on buildings. These serve as a basis for validation or positioning for the developments presented here. The measurements of this prototype are used in section 6.2 on page 173 to characterize the seasonal behavior of the PV power generation model.

1.1.2.3 *G2 Solaire*

The G2 Solaire is a Swiss-French Interreg project. The main objective of this project is to intensify the use of solar energy, developing economic activities related to the solar sector and finally to achieve the energy transition in a context of urban densification.

The project is divided into two components:

1. a technical approach, aiming to develop a map of solar potential at the scale of the Greater Geneva;
2. a second approach, insitutional and political, aiming to ease the use of the solar cadastre for the concerned actors, including: elected officials, public administrations, professional in the sector of solar energy, or individuals.

The developments carried out under this project are also part of the task 63 of the International Energy Agency: Solar Neighborhood Planning. This aims to carry out a benchmark of tools for simulating radiative phenomena on a city scale. At the time of writing it includes: ENVI-met, Rhino/Radiance, EnergyPlus and the solar cadastre developped for this project. More tools are to come, such as: Indalux, CitySIM or Ladybug + Honeybee & Climate studio. The goal of this benchmark is to identify the strengths and weaknesses of the different tools.

In this project, ENVI-met brings more information about the UMC. Indeed, other considered tools are specialized in the simulation of radiative phenomena or are a combination of different tools. Thus, no aeraulic phenomenon is taken into account, which results in not taking into account the influence of the wind on the PV potential and does not provide precise knowledge of the surface temperatures of buildings.

The theoretical studied neighborhood is used in the presented work to evaluate the influence of the wind velocity on the PV potential of buildings' facades (5.1.3 on page 118), as well as the influence of the horizontal/vertical series connections on this potential (section 6.1 on page 153).

1.2 PRESENTATION OF THE ENVI-MET TOOL

ENVI-met is a prognostic three-dimensional climate model (Bruse and the ENVI-met Team, 2020). It aims to take into consideration all the phenomena that occur in urban area to simulate realistic districts. This tool has different goals, including: sun analysis, air pollutant dispersion, outdoor thermal comfort or influence of vegetation or water on weather conditions in urban areas. Thus, ENVI-met is aimed at various professions, such as researchers, architects or uban planners.

ENVI-met appears as the most evaluated urban microclimate model tool, with more than 3 000 independent studies. This model has been validated and applied though different topics of study.

1.2.1 *ENVI-met 3D Model*

Due to its holistic approach, ENVI-met includes several models addressing the different physical phenomena occuring in urban areas. This includes three sub-models:

1. a 1D boundary model. It is mainly used for the initialization of the model and the boundary conditions of the 3D atmospheric model;
2. a 3D atmospheric model. This model contains buildings, vegetation and air flow;
3. a 3D/1D soil model. It is used to calculate the temperature and moisture fluxes within the soil. At the time of writing, it is composed of 14 layers, with a telescoping vertical spacing, reaching 1.75 m below ground level. The computation of the fluxes is worked out only along the vertical axis, hence the 3D/1D name, although the fluxes are in three dimensions.

A basic layout of these models is given in figure 1.5. Since the main goal of the presented work is to evaluate the solar potential of buildings' facades in an urban context, only the atmospheric model is detailed.

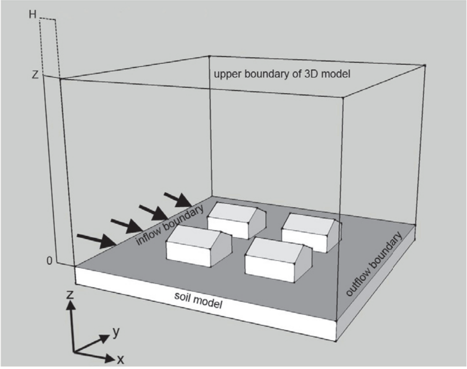

Figure 1.5.: ENVI-met 3D Basic Layout (Huttner, 2012)

The upper boundary of the 3D model is at a fixed height of 2 500 m. Between the soil and this bound, the modeled domain is divided into cubicoidal cells in all space directions. The horizontal spacings are constant for all grid cells. The vertical ones may vary, according to the height.

An overview of the ENVI-met sub-models is given in figure 1.6. This allows to evaluate the main variables calculated by ENVI-met:

- air and soil temperature and humidity;
- radiative fluxes;
- wind speed and direction;
- turbulence;
- gas and particle dispersion.

All of these physical values are inter-related. This inter-relation justifies the need of a tool that includes all the phenomena that occur in an urban area.

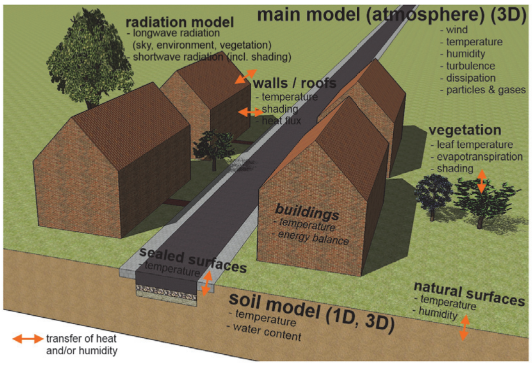

Figure 1.6.: Schematic of the Sub Models of ENVI-met (Huttner, 2012)

As aforementionned, the modeled domain in ENVI-met is composed of cubicoidal cells. Thus, the sketch presented in figure 1.6 is modeled as follows (figure 1.7 on the facing page).

This method of spatial modelization leads to approximations for the buildings' shapes. This implies a limitation, especially regarding the lack of details for the facades and the slanted walls but the latter does not have very much impact on the vertical facades. The work presented here is then barely impacted by this modelization. However, another parameter may have a large impact on the simulation results: the lateral boundary conditions (LBC) and the associated weather conditions values.

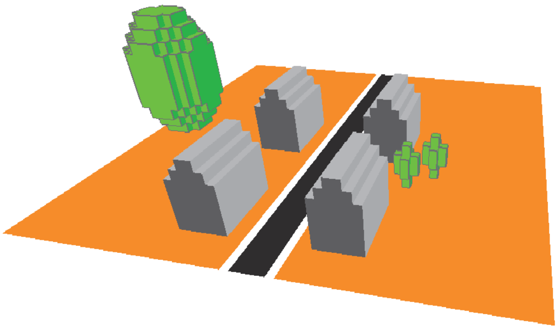

Figure 1.7.: Sketch of a Domain Modeled with ENVI-met

1.2.2 *Importance of the Simulation Input Data*

As a modeling tool including airflow calculation and radiative fluxes evaluation, ENVI-met requires the definition of LBC. This requires to provide the modeled domain with physical values and numerical conditions.

The numerical LBC have three different options in ENVI-met (Huttner, 2012):

1. open: the values of the next grid point close to the border are copied to the border for each time step;
2. forced (closed): the values of the 1D model are copied to the border;
3. cyclic: the values of the downstream model border are copied to the upstream model border.

Regarding the weather conditions provided by the user to the model, they have to follow a formalism. It can be issued either from typical values or from on-site measurements. At the time of writing, the input data can be in an EnergyPlus weather file (`.epw` or `.try`). The measurements must follow the same temporal structure, namely to provide values by steps of 30 minutes, and in a `.csv` file with ten columns. This file allows to provide the model with physical values, including:

- shortwave radiation (direct and diffuse) in $\mathrm{W \cdot m^{-2}}$;
- longwave radiation in $\mathrm{W \cdot m^{-2}}$;
- cloud cover (low, medium and high clouds) in octas;
- absolute temperature in K;

- relative humidity in %;
- wind speed in $m \cdot s^{-1}$;
- wind direction in °;
- precipitation in mm.

The provided direct solar radiation can either be the beam horizontal irradiance (BHI) or the beam normal irradiance (BNI).

This formalism allows to evaluate the urban microclimate in accordance with the evolution of the actual local climate conditions. Nonetheless, 30 minutes is a quite large time step. Thus, intermittency is hardly reproducible. To bridge this gap, ENVI-met uses linear interpolation for the evaluation of the evolution of the weather conditions between two time steps of 30 minutes. This makes the evolution of the physical values smoother.

1.2.3 *Workflow Process for the Evaluation of the Photovoltaic Potential of Buildings' Surfaces*

The use of input data as accurate as possible is a crucial issue in the evaluation of the PV potential of buildings' facades in a urban context. Thus, the higher the accuracy of the input data, the lower the bias in the simulations results.

The conditions passed to the ENVI-met simulation input can come from different sources. Apart from the generic data necessary for the creation of the profiles presented in section 1.2.1 on page 9, the meteorological conditions can be forced. The data required for forcing can come from two sources: typical representative year conditions or on-site weather measurements. The latter has the advantage of providing greater precision making it possible to reproduce more faithfully the conditions of the district considered. The needed work to match the required format is detailed in section 4.1.2 on page 74.

The accuracy of the simulation output is even more important, since they are used as the input for the PV power generation models. Thus, the chaining between ENVI-met and these models is as follows.

The developments implemented to use the output data as input for the PV power generation models is detailed in chapter 4 on page 71.

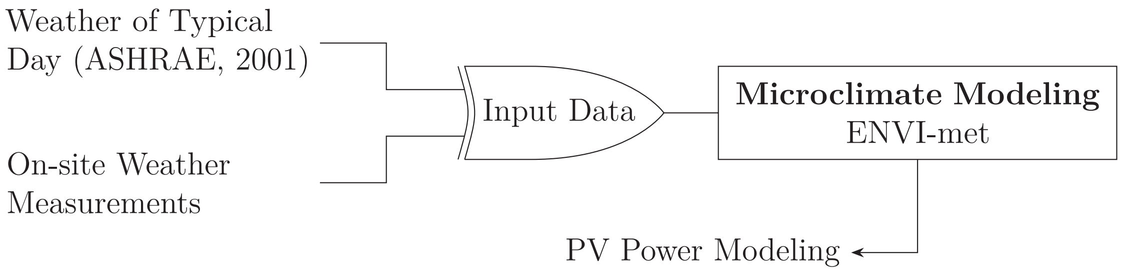

Figure 1.8.: Chaining Between ENVI-met and the Photovoltaic Power Generation Models

By taking into account all the phenomena that occur in an urban environment, ENVI-met aims to accurately simulate the urban microclimate, through different coupled models.

As an urban mciroclimat simulation software, ENVI-met makes it possible to study various issues, such as pedestrian thermal comfort or outdoor air quality.

The evaluation of the PV potential on a city scale brings a novelty to this tool by no longer considering buildings only as consumers but also as energy producers. This evaluation is carried out through different projects, including comparisons between numerical results and experimental data.

REFERENCES

Bruse, M., & the ENVI-met Team. (2020). *Envi-met: Decoding urban nature*. https://www.envi-met.com/. (Cited on page 8)

Huttner, S. (2012). *Further development and application of the 3D microclimate simulation ENVI-met* (Doctoral dissertation). Mainz. (Cited on pages 9–11).

Moriarty, P., & Honnery, D. (2012). What is the global potential for renewable energy? *Renewable and Sustainable Energy Reviews*, *16*(1), 244–252. https://doi.org/https://doi.org/10.1016/j.rser.2011.07.151 (Cited on page 4)

Ritchie, H. (2014). Energy [https://ourworldindata.org/energy]. *Our World in Data* (Cited on page 2).

The world's cities in 2018 (Cited on page 2).

2

STATE OF THE ART

> *There is a crack in everything; that's how the light gets in.*
>
> Leonard Cohen

The evaluation of the solar potential in urban context, in order to assess the photovoltaic potential of buildings at district scale, is a complex process, which involves different tools. The main goal is to make the cities greener by turning the buildings from energy consumers to energy producers.

The considered solution of this study is the photovoltaic power generation on buildings' facades. Therefore, a focus is put on the building integrated photovoltaic systems and the methods to evaluate the photovoltaic potential at district scale. This assessment requires the modeling of two types of phenomena in urban context:

1. The radiative phenomena;
2. The aeraulic phenomena.

The radiative phenomena are heavily impacted by the urban morphology, with shading or inter-building reflections. Wind channeling due to close buildings may have impact on both buildings' and air temperatures. This has an impact on the efficiency of the photovoltaic modules. Thus, a comprehensive modeling of the urban context, coupling both radiative and aeraulic phenomena appears necessary to obtain accurate results in assessing the photovoltaic potential of buildings at urban scale.

Interest in the design of energy-efficient and comfortable buildings, as much as from thermal and aeraulic point of view has not ceased to grow in the last decades. Making the cities greener requires comprehensive consideration of the urban environment and the associated phenomena, which include mainly airflow and solar radiation.

Urban areas are complex contexts with various morphologies and various phenomena to take into consideration in order to evaluate correctly the solar potential of buildings. First, a focus is put on the different methodologies developed for this purpose. Emphasis is then placed on the way in which the different existing tools consider the phenomena that occur in urban context.

2.1 ENERGY PRODUCER BUILDINGS

The solar access of a building is heavily impacted by its surrounding environment. Then, so is its solar potential. The following focuses on the different existing tools aiming at evaluating the solar potential at different scales.

The buildings can use solar energy with different technologies (photovoltaic (PV) or solar thermal systems). The accurate evaluation of the buildings' solar potential appears then as a key issue to turn them from energy consumers to energy producers. This is a requirement to achieve the energy transition. This evaluation can be carried out according to different spatial resolutions and scales. The different methods of measurement and evaluation are described, according to their scale, in the following.

2.1.1 *Territory Scale*

The interest for the evaluation of the solar potential at large scale has increased in the last decades. These evaluations are based on different methodologies (Ronzino et al., 2015), among which geographic information system (GIS) is an important part. Indeed, this technology is usable for the estimation of the renewable energy potential at region scales (Arnette and Zobel, 2011; Freitas et al., 2015; Sarralde et al., 2015; Van Hoesen and Letendre, 2010), as well as for decisions in energy planning (Domínguez and Amador, 2007; Voivontas et al., 1998; Wiginton et al., 2010) at urban scale. GIS can be the base of development for new models of renewable energies use (Díaz-Cuevas and Domínguez-Bravo, 2015).

Initially designed to provided with information at a large scale and relatively high spatial resolution, GIS tools are increasingly used to provide with local information, and more particularly information about buildings. Freitas et al., 2015 classified the urban-oriented methods for solar potential estimation. It appears that the GIS-based tools are usable for the evaluation of rooftops' solar potential. Nonetheless, the 2D models are still hardly usable for 3D models. This requires to develop new features, such as 2.5D[1] and 3D approaches to take into consideration the buildings' vertical facades (Machete et al., 2018). These models make it possible to evaluate the solar potential of buildings, while taking into consideration the surrounding environment. The implementation of 3D models, unlike the 2D models, is even able to evaluate the solar potential of slanted facades (Erdélyi et al., 2014).

Among the existing GIS-based software, three of them are widely used: ArcGIS Solar Analyst, GRASS GIS r.sun and PVGIS (Photovoltaic Geographical Information System). They have been used for many studies aiming at evaluating the solar potential at urban scale (Ancuta et al., 2013; Fu and Rich, 1999; Hofierka and Zlocha, 2012; Sun et al., 2013; Šúri and Hofierka, 2004). Nevertheless, these software were originally made for 2D analysis. As described by (Hofierka and Zlocha, 2012), this may lead to imprecise results. In addition, the compromise induced by the large scale calculation leads to simplification in the models. Thus, PVGIS does not take into

---

[1] A 2.5D model consists of actual data on 2D layers and an estimation of data on the third dimension, based on a projection of the known data.

consideration the presence of other buildings in the overshadowing effects, as well as the inter-building reflections (Freitas et al., 2015).

The information contained in GIS can be obtained by measurements, either with unmanned aerial systems (UAS) (Kylili et al., 2014; Rakha and Gorodetsky, 2018), or light detection and ranging (LIDAR) systems (Lukač and Žalik, 2013; Redweik et al., 2013). Nelson and Grubesic, 2020 carried out a confrontation between the results obtained with LIDAR or UAS. The results of these measurements can be used to build a 3D GIS city model (Gil et al., 2011).

2.1.2 *District Scale*

The evaluation of the solar potential with GIS-based tool has the advantage of providing information for large areas. This allows to deliver suitable information for a large number of buildings and then to increase the potential of renewable energy production of a large area. Nonetheless, these tools also have a drawback: they are initially based on layers of information. Thus, they can be used to evaluate the solar potential of roofs but not the one of vertical facades. The interest for this type of walls has particularly increased within the last years, and led to developing new tools or improving existing ones.

Many case studies have been carried out to evaluate the solar potential of rooftops (Cellura et al., 2012; Hachem et al., 2012; Orioli and Di Gangi, 2013; Wiginton et al., 2010) at urban scales. Focus has been put on this type of walls because their solar potential is the most important and they are less subject to shading, which has a negative impact on the solar potential. However, the solar potential of all facades can be evaluated, whilst remaining a relatively low computational time, for a limit amount of considered buildings.

The evaluation of the solar potential can be carried out as much on theoretical districts as on actual ones. In the first case, the domain of application is the research (Lobaccaro, Fiorito, et al., 2012), while in the second is to bring solution to building professionals, such as urban planners or architects (Lobaccaro, Frontini, et al., 2012).

As aforementioned, the tools dedicated to the evaluation of the solar potential has to be available for designers and urban planners. Thus, methods are needed to bridge the gap between the need of accurate assessments and usability for users. New methods are then developed to provide users with relevant data embedded in off-the-shell software. Catita et al., 2014 has developed a GIS-based method to evaluate the solar potential of vertical facades. Esclapés et al., 2014 have focused on the evaluation of the PV potential of buildings' facades, taking into consideration the technical feasibility of the installation of building integrated photovoltaic (BIPV) systems. Saretta et al., 2020 have applied the same type of tools to estimate the potential of installation of BIPV systems in the case of buildings' facades retrofits.

GIS-based tools does not define precisely the geometry of the buildings, which are needed by building professionals. Architects extensively use computer-aided design (CAD) software for building design. A consideration of solar potential in the early design phase helps its optimization (Lobaccaro, Frontini, et al., 2012). Thus, tools are needed to help design cities and buildings, whilst optimizing the solar potential of the buildings. This issue is addressed by recent tools, such as PVcad (Rogers and Russell, 2019) or building information model (BIM) software.
BIM aims at offering a solution to design, build and operate buildings, within a share interface for both architects and engineers. Regarding, the PV power generation, such tools have proved their efficiency, as much on theoretical application (Rahmani Asl et al., 2015) as on actual ones (Ning et al., 2017). BIM can help optimizing the energy production (increase of 36.1 %) while decreasing the cost (decrease of 4.5 % of the capital investment).

2.1.3 *Vertical Facades*

Long neglected, because of a lower intrinsic potential, vertical facades have been subject to an increasing interest in recent years (Redweik et al., 2013). This interest is mainly due to the evolution of the urban context. Thus, even if a given amount of vertical surface can produce less energy than a horizontal one, the multiplication of this kind of verticalities in a context of urban densification can make their potential predominant compared to the one of roofs (Díez-Mediavilla et al., 2019; Hachem et al., 2014; Hsieh et al., 2013; Vulkan et al., 2018). Indeed, with buildings surfaces made up with 60 % to 80 % (Esclapés et al., 2014) of facades, even if their irradiation per square meter is lower than that of roofs, their total solar potential can exceed the one of roofs. In addition, the flat roofs are monodirectional, whereas the facades mainly have four orientations. Thus the peaks of power generation of facade occur at several times a the day. The magnitude of each of them is, of course, less important than that of the roofs, but it has the advantage to distribute the energy production over the day, thus contributing to a better match between the PV power generation and the energy demand (Hummon et al., 2013).

Without regard to any technical consideration, the use of BIPV on facade may contribute to achieve the energy transition by contributing to the acceptation of the general public (Montoro et al., 2011) and an increased use by the architects (Brito et al., 2017). In addition, BIPV can be an effective way to tackle the urban heat island (UHI) effect (Wang et al., 2005), as well as other solutions such as using highly reflective surfaces (Akbari and Matthews, 2012; Santamouris, 2013; Santamouris et al., 2011) or increase the use of vegetation in the cities (Lobaccaro and Acero, 2015; Matthews et al., 2015; Tan et al., 2016; Tzoulas et al., 2007).

As temperature-dependent systems, BIPV systems have their performance impacted by the urban environment and the UHI effect. Tian et al., 2007 reported a decrease of almost 20 % due to the urban environment. In addition, the UHI can also be responsible for weak decrease (−0.33 %) in terms of PV productivity on facades, say (Boccalatte et al., 2020). Conversely, the massive use of BIPV systems can contribute to a decrease of inter-building reflections because of usually dark shades of PV modules. This can be tackled by the use of BIPV systems with highly reflective surfaces (Wang et al., 2005).

2.2 SIMULATION OF URBAN PHENOMENA

Multiple phenomena occur in urban areas. Regarding the evaluation of the solar potential at city scale, two of them appear as crucial issues: the solar and the aeraulic phenomena. They impact all types of buildings' facades, and more particularly vertical ones. Thus, particular attention is devoted to the tools able to simulate both radiative and aeraulic phenomena in the next section. First, they are discussed independently, prior to being considered as inter-related phenomena.

2.2.1 *Solar Phenomena*

The urban fabric forms a complex environment where solar radiation is unevenly distributed, especially when dealing with dense urban areas. It is essential to quantify the dynamic effects of drop shadow and multi-reflection occurring between built surfaces, in order to accurately predict the level of solar radiation that can significantly affect solar gains. The latter determine the energy consumption of buildings and their potential of solar energy production. Design constraints and the complexity of three-dimensional dynamic interactions between solar radiation and urban form represent a real challenge for designers and urban planners who need flexible and efficient tools for the study of these phenomena. For the study of radiative exchanges, a compromise between power and calculation precision is therefore necessary (Allegrini and Carmeliet, 2017).

Regarding the accuracy of the modeling of solar potential in urban areas, (Freitas et al., 2015) identified Radiance, Daysim and Solene as the software allowing to simulate the most accurately the anisotropy and specularity of the solar radiation, as well as inter and multi-reflection phenomena within an urban 3D model.

Radiance is a comprehensive solar radiation simulation tool. Initially developed for interior lighting calculations, it is increasingly used for urban analysis, especially since its integration into the DIVA tool connecting it to Rhinoceros (Rhino) and Grasshopper (two software widely used by architects and urban planners). This way, 3D geometry and materials can be easily set up before performing any simulation. DIVA is used in several studies of solar potential or outdoor daylight (Kanters et al., 2014; Lobaccaro and Masera, 2014; Nault et al., 2015) and the availability of solar energy for photovoltaic and solar thermal systems integrated in facades (Kanters, 2015). Also developed on the basis of the Radiance calculation code, the Urban Daylight simulation tool (Dogan et al., 2012), integrated into Rhino, brings some simplifications to Radiance in order to reduce calculation times.

The Solene (Miguet and Groleau, 2002) and CitySim (Robinson et al., 2009) software use models for calculating solar irradiation that are more simplified than that of Radiance, while maintaining an acceptable level of precision for the study of the urban microclimate (UMC).

In most cases, the calculation of radiative exchanges is confined to short wavelengths. Long-wavelength radiative exchanges between built surfaces require knowledge of surface temperatures, which involves the calculation of the thermal balance of the surface in relation to the whole transfer phenomena.

The results of radiative simulations can be used to take into account the impacts of exchanges in the urban environment on the energy balance of a building. Thus (Evins et al., 2014) have made various modifications to the EnergyPlus program which allow the temperature differences of the facades and floors considered to be represented in much more detail, unlike the standard calculation assumptions of EnergyPlus where all the surrounding masks have the same temperature as the outside air. Similarly, (Yang et al., 2012) improved the taking into account of the surrounding context of the dynamic thermal model of the building produced with EnergyPlus by coupling it to the UMC simulation software ENVI-met. To do this, the data simulated by the latter are transferred as boundary conditions for EnergyPlus, improving its internal assumptions concerning long-wavelength radiation, as well as convective exchanges linked to urban air conditioning.

2.2.2 *Aeraulic Phenomena*

To take into account the impact of urban thermo-aeraulic phenomena on building thermal conditions, numerous couplings between computational fluid dynamics (CFD) tools and building energy simulation tools are developed. This coupling makes it possible to estimate more precisely wind speed and temperatures around buildings. The contribution of such a coupling has been further studied by (Malys et al., 2015) which show that taking into account the precise distribution of air speeds around the building is not necessary for the energy calculations at the district scale, but can be replaced by an adapted wind profile or an average speed that takes into account the effects of the district.

Evins et al., 2014 demonstrated that the use of local wind velocity values in building energy simulations can have a significant impact on the energy demand of buildings included in an urban environment. They demonstrate the value of using CFD simulation data to generate a statistical emulator, thus making it possible to obtain reasonably precise data that can be transmitted to an energy simulation model and this with reduced calculation times. Merlier, 2015 was also interested in the more precise calculation of the external convective transfer coefficients. For the calculation of these coefficients, it shows the need to use very sophisticated CFD tools that are poorly suited to the extent of the areas to be modeled and the need to simulate several variants of a project.

Finally, while most studies attempt to use corrected pressure coefficients for isolated buildings or a single building that fits into a regular urban fabric (and not a regular arrangement of buildings), the use of coefficients of pressure and convective transfer coefficients from aeraulic studies of neighborhoods in dynamic thermal simulation (DTS) models still represent a key challenge in taking into account natural ventilation at the scale of a neighborhood.

Regarding thermal impacts, most studies have focused on energy consumption and a global vision of the building. An objective of an estimation of thermal comfort (Malys, 2012) as well as the PV power generation potential at district scale creates a new problem because average values are not sufficient (especially in taking into consideration the spatial heterogeneity) and the distribution of wind speeds and temperature must then be taken into account.

2.2.3 *Coupling of Phenomena for a Better Evaluation of Urban Context*

Urban energy modeling is a recent field of research whose goal is to model a group of buildings and possibly the UMC surrounding it according to different levels of representativeness of the phenomena involved. In practice, these exchanges are often limited to radiative exchanges (Robinson et al., 2009). An urban building energy model (UBEM) is based on the use of physical calculation models of heat and mass exchange in and around buildings. This makes it possible to assess the energy required to maintain indoor comfort, as well as to assess the different phenomena that occur in an urban environment.

Energy models of urban buildings mainly use the calculation possibilities offered by dynamic thermal building simulation tools such as EnergyPlus. Nevertheless, these models remain limited in their representation of micro-climatic phenomena. Indeed, compared to an isolated building, a building in a dense urban environment is subject to so-called modified thermofluid properties, namely:

- Surface and soil temperatures varying with the solar accessibility of surfaces and their neighbors, their albedo and the phenomena of convection, conduction and evapotranspiration;
- Local wind velocity and pressure fields influencing the coefficient of performance of air conditioning systems, convection heat exchanges and air infiltration rates;
- Heat exchanges and specific thermo-fluid properties at the interior-exterior interfaces.

Single-phenomenon approaches tend towards coupling approaches and the tools, initially dedicated to a phenomenon, have gradually broadened their field of competence to all or part of the thermal phenomena involved in the urban heat balance. In fact, only a multi-phenomena approach provides access to the micro-climatic results represented by air and surface temperatures.

One of the major difficulties in fully integrating climatic phenomena into the energy models of urban buildings remains in the diversity of approaches between building energy models and aeraulic models, particularly in spatial and temporal terms. This

difference in response time is found, for example, in the time to reach stable temperature conditions of a wall compared to that of air: in the order of the hour to the day for a wall and in order of the minute for the air around it. This difference in response time suggests exchanging data between aeraulic simulation in steady state at certain times of the dynamic energy simulation (Srebric et al., 2015).
Furthermore, from the spatial point of view, the discretization of the building is finer than that of the urban space, resulting in a significant increase in calculation times.

Many urban simulation tools exist, all developed for specific purposes and objectives, but very few of them fully integrate all of the criteria necessary for the urban microclimatic study. Bozonnet et al., 2013 classify these models according to the phenomena taken into account at the origin of their development (initially radiative, aeraulic or energetic models) because the initial approach strongly conditions the consideration of additional phenomena. For example, the grid-mesh discretization used in Envi-met, resulting from aeraulic modeling, induces the impossibility, in the radiative model then added, of properly processing inter-reflections.

Thus, the selection of a modeling and simulation tool depends on parameters such as the precision, stability and time of the calculations, as well as the spatial and temporal scales studied. Bozonnet et al., 2013 identified a large panel of existing tools classified according to the level of representativeness of the phenomena and systems necessary for a complete representation of an urban scene. Lauzet et al., 2019 classified the existing chaining or coupling between the urban climate modeling and the building energy models, with regards of the typical studied period.

Very few of the available tools are able to simulate all the important physical phenomena of the UMC. ENVI-met (Bruse, 1999; Huttner, 2012) includes models of irradiation, CFD, heat and moisture transfer, plants or building energy. But its spatial resolution, its very long computation times and its model construction method limit its use to the study of very limited periods. Solene-microclimate, CitySim and EnergyPlus are also among the most comprehensive tools for taking into account the context and the UMC in their respective building energy model. However, regarding these latter, they all remain limited in the representation of certain phenomena and require coupling or exchanging data with complementary tools.

Internal coupling (use or modification of internal software modules) or external (exchange of data between independent software) makes it possible to go beyond the limitations of existing tools. Allegrini and Carmeliet, 2017 used an aeraulic simulation tool and a building energy model to improve the exchange coefficients of the surfaces of the latter. Yang et al., 2012 used ENVI-met to generate an environment-aware weather file then used by EnergyPlus. Surface temperature and air data from EnergyPlus were also used to determine the heat exchange coefficient corrected by ENVI-met and fed back at certain time steps into the building energy model. Yaghoobian and Kleissl, 2012 have developed complete coupled models. Merlier, 2015; Srebric et al., 2015 also identify a large number of studies integrating this coupling approach for the study of the building and the UMC.

The strict coupling of physical models represents a real challenge in terms of dynamic data exchanges (at each time step), of the format of these data and of the necessary computing power (in particular for radiative exchanges and aeraulics) making their use mainly limited to research. Design-oriented tools have recently been developed. These tools use the capacities of free and validated calculation codes such as EnergyPlus, Radiance or OpenFoam allowing to represent in a decoupled manner the main phenomena taking place at the urban scale.

The urban modeling interface (UMI) (Reinhart et al., 2013) is a plugin for Rhino designed for the assessment of gray energy consumption using EnergyPlus. The solar potential is evaluated thanks to Daysim. Finally, thanks to Grasshopper's programmatic capabilities, UMI integrates Python scripts to study the pedestrian accessibility of an urban network.

Ladybug and Honeybee (Sadeghipour Roudsari and Pak, 2013) are two free and open-source plugins for Grasshopper, developed to provide a comprehensive range of performance evaluation tools. Ladybug and Honeybee make it possible to carry out a large number of studies based on typical climatic data (UTCI mapping, sky view factor, wind rose, psychometric diagram, indoor and outdoor comfort, etc.), while easily exchanging data generated between the different calculation modules.

All of these initiatives offer possibilities, which are more suited to the design process. However, they are still to be evaluated, because the consideration of coupled phenomena is much less extensive.

The phenomena related to urban areas have been studied for many years. The subject of study first focused on the impact of the urban environment on the energy consumption of buildings. Subsequently, the growing interest in renewable energies led to the assessment of solar potential, taking into account the specific features of the urban context. These studies have long been limited to roofs.

In recent years, the evaluation of solar potential has been extended to facades of buildings; thus opening up new prospects for the production of renewable energy and research topics. Nevertheless, these studies need to be completed because of their limits, in particular: the evaluation of the solar potential in terms of annual average or by taking into account only the radiative phenomena (thus not taking into account the aeraulic phenomena).

REFERENCES RELATED TO THE RELATED WORKS

Akbari, H., & Matthews, H. D. (2012). Global cooling updates: Reflective roofs and pavements. *Energy and Buildings*, *55*, 2–6. https://doi.org/https://doi.org/10.1016/j.enbuild.2012.02.055 (Cited on page 20)

Allegrini, J., & Carmeliet, J. (2017). Coupled CFD and building energy simulations for studying the impacts of building height topology and buoyancy on local urban microclimates. *Urban Climate*, *21*, 278–305. https://doi.org/https://doi.org/10.1016/j.uclim.2017.07.005 (Cited on pages 21, 24)

Ancuta, R., CIOBAN, A., CRIVEANU, H., Matei, F., & Ioana, P. (2013). Aspects of Solar Radiation Analysis using ArcGis. *Buletinul Universităţii de Ştiinţe Agricole şi Medicină Veterinară Cluj-Napoca* (Cited on page 17).

Arnette, A. N., & Zobel, C. W. (2011). Spatial analysis of renewable energy potential in the greater southern Appalachian mountains. *Renewable Energy*, *36*(11), 2785–2798. https://doi.org/https://doi.org/10.1016/j.renene.2011.04.024 (Cited on page 17)

Boccalatte, A., Fossa, M., & Ménézo, C. (2020). Best arrangement of BIPV surfaces for future NZEB districts while considering urban heat island effects and the reduction of reflected radiation from solar façades. *Renewable Energy*, *160*, 686–697. https://doi.org/https://doi.org/10.1016/j.renene.2020.07.057 (Cited on page 20)

Bozonnet, E., Musy, M., Calmet, I., & Rodriguez, F. (2013). Modeling methods to assess urban fluxes and heat island mitigation measures from street to city scale. *International Journal of Low-Carbon Technologies*, *10*, 62–77. https://doi.org/10.1093/ijlct/ctt049 (Cited on page 24)

Brito, M. C., Freitas, S., Guimarães, S., Catita, C., & Redweik, P. (2017). The importance of facades for the solar PV potential of a Mediterranean city using LiDAR data. *Renewable Energy*, *111*, 85–94. https://doi.org/https://doi.org/10.1016/j.renene.2017.03.085 (Cited on page 20)

Bruse, M. (1999). *Die Auswirkungen kleinskaliger Umweltgestaltung auf das Mikroklima*. Univeristy of Bochum. (Cited on page 24).

Catita, C., Redweik, P., Pereira, J., & Brito, M. C. (2014). Extending solar potential analysis in buildings to vertical facades. *Computers & Geosciences*, *66*, 1–12.

https://doi.org/https://doi.org/10.1016/j.cageo.2014.01.002 (Cited on page 18)

Cellura, M., Di Gangi, A., Longo, S., & Orioli, A. (2012). Photovoltaic electricity scenario analysis in urban contests: An Italian case study. *Renewable and Sustainable Energy Reviews*, *16*(4), 2041–2052. https://doi.org/https://doi.org/10.1016/j.rser.2012.01.032 (Cited on page 18)

Díaz-Cuevas, P., & Domínguez-Bravo, J. (2015). GIS, Territory, and Landscape in Renewable Energy Management in Spain BT - Renewable Energies and European Landscapes: Lessons from Southern European Cases. In M. Frolova, M.-J. Prados, & A. Nadaï (Eds.). Springer Netherlands. https://doi.org/10.1007/978-94-017-9843-3_15. (Cited on page 17)

Díez-Mediavilla, M., Rodríguez-Amigo, M. C., Dieste-Velasco, M. I., García-Calderón, T., & Alonso-Tristán, C. (2019). The PV potential of vertical façades: A classic approach using experimental data from Burgos, Spain. *Solar Energy*, *177*, 192–199. https://doi.org/https://doi.org/10.1016/j.solener.2018.11.021 (Cited on page 19)

Dogan, T., Reinhart, C., & Michalatos, P. (2012). Urban Daylight Simulation Calculating the Daylit Are of Urban Designs (Cited on page 21).

Domínguez, J., & Amador, J. (2007). Geographical information systems applied in the field of renewable energy sources. *Computers & Industrial Engineering*, *52*(3), 322–326. https://doi.org/https://doi.org/10.1016/j.cie.2006.12.008 (Cited on page 17)

Erdélyi, R., Wang, Y., Guo, W., Hanna, E., & Colantuono, G. (2014). Three-dimensional SOlar RAdiation Model (SORAM) and its application to 3-D urban planning. *Solar Energy*, *101*, 63–73. https://doi.org/https://doi.org/10.1016/j.solener.2013.12.023 (Cited on page 17)

Esclapés, J., Ferreiro, I., Piera, J., & Teller, J. (2014). A method to evaluate the adaptability of photovoltaic energy on urban façades. *Solar Energy*, *105*, 414–427. https://doi.org/https://doi.org/10.1016/j.solener.2014.03.012 (Cited on page 19)

Evins, R., Allegrini, J., & Moonen, P. (2014). Emulating Site-Specific Wind Flow Information for Use in Building Energy Simulations. *Building Simulation and Optimization* (Cited on pages 21, 22).

Freitas, S., Catita, C., Redweik, P., & Brito, M. C. (2015). Modelling solar potential in the urban environment: State-of-the-art review. *Renewable and Sustainable Energy Reviews*, *41*, 915–931. https://doi.org/https://doi.org/10.1016/j.rser.2014.08.060 (Cited on pages 17, 18, 21)

Fu, P., & Rich, P. (1999). Design and implementation of the Solar Analyst: an ArcView extension for modeling solar radiation at landscape scales. *Proceedings of the 19th Annual ESRI User Conference* (Cited on page 17).

Gil, J., Almeida, J., & Duarte, P. (2011). The backbone of a City Information Model (CIM): Implementing a spatial data model for urban design Duarte, Jose. *Respecting Fragile Places: 29th eCAADe Conference Proceeedings*, 143–151. http://papers.cumincad.org/data/works/att/ecaade2011%7B%5C_%7D104.content.pdf (Cited on page 18)

Hachem, C., Athienitis, A., & Fazio, P. (2012). Design of roofs for increased solar potential BIPV/T systems and their applications to housing units. *ASHRAE Transactions*, *118*, 660–676 (Cited on page 18).

Hachem, C., Athienitis, A., & Fazio, P. (2014). Energy performance enhancement in multistory residential buildings. *Applied Energy*, *116*, 9–19. https://doi.org/https://doi.org/10.1016/j.apenergy.2013.11.018 (Cited on page 19)

Hofierka, J., & Zlocha, M. (2012). A New 3-D Solar Radiation Model for 3-D City Models. *Transactions in GIS*, *16*(5), 681–690. https://doi.org/10.1111/j.1467-9671.2012.01337.x (Cited on page 17)
doi: 10.1111/j.1467-9671.2012.01337.x

Hsieh, C.-M., Chen, Y.-A., Tan, H., & Lo, P.-F. (2013). Potential for installing photovoltaic systems on vertical and horizontal building surfaces in urban areas. *Solar Energy*, *93*, 312–321. https://doi.org/https://doi.org/10.1016/j.solener.2013.04.021 (Cited on page 19)

Hummon, M., Denholm, P., & Margolis, R. (2013). Impact of photovoltaic orientation on its relative economic value in wholesale energy markets. *Progress in Photovoltaics: Research and Applications*, *21*(7), 1531–1540. https://doi.org/10.1002/pip.2198 (Cited on page 19)
doi: 10.1002/pip.2198

Huttner, S. (2012). *Further development and application of the 3D microclimate simulation ENVI-met* (Doctoral dissertation). Mainz. (Cited on page 24).

Kanters, J. (2015). *Planning for Solar Buildings in Urban Environments* (Doctoral dissertation). (Cited on page 21).

Kanters, J., Wall, M., & Dubois, M.-C. (2014). Development of a Façade assessment and design tool for solar energy (FASSADES). *Buildings*, *4*, 43–59. https://doi.org/10.3390/buildings4010043 (Cited on page 21)

Kylili, A., Fokaides, P. A., Christou, P., & Kalogirou, S. A. (2014). Infrared thermography (IRT) applications for building diagnostics: A review. *Applied Energy*, *134*, 531–549. https://doi.org/https://doi.org/10.1016/j.apenergy.2014.08.005 (Cited on page 18)

Lauzet, N., Rodler, A., Musy, M., Azam, M.-H., Guernouti, S., Mauree, D., & Colinart, T. (2019). How building energy models take the local climate into account in an urban context – A review. *Renewable and Sustainable Energy Reviews*, *116*, 109390. https://doi.org/https://doi.org/10.1016/j.rser.2019.109390 (Cited on page 24)

Lobaccaro, G., & Acero, J. A. (2015). Comparative analysis of green actions to improve outdoor thermal comfort inside typical urban street canyons. *Urban Climate*, *14*, 251–267. https://doi.org/https://doi.org/10.1016/j.uclim.2015.10.002 (Cited on page 20)

Lobaccaro, G., Fiorito, F., Masera, G., & Poli, T. (2012). District Geometry Simulation: A Study for the Optimization of Solar Façades in Urban Canopy Layers. *Energy Procedia*, *30*, 1163–1172. https://doi.org/https://doi.org/10.1016/j.egypro.2012.11.129 (Cited on page 18)

Lobaccaro, G., Frontini, F., Masera, G., & Poli, T. (2012). SolarPW: A New Solar Design Tool to Exploit Solar Potential in Existing Urban Areas. *Energy Procedia*, *30*, 1173–1183. https://doi.org/https://doi.org/10.1016/j.egypro.2012.11.130 (Cited on pages 18, 19)

Lobaccaro, G., & Masera, G. (2014). A digital language for a new Sustainable Urban Planning: design and simulation tools for Solar Architecture. *Building Simulation and Optimization* (Cited on page 21).

Lukač, N., & Žalik, B. (2013). GPU-based roofs' solar potential estimation using LiDAR data. *Computers & Geosciences*, *52*, 34–41. https://doi.org/https://doi.org/10.1016/j.cageo.2012.10.010 (Cited on page 18)

Machete, R., Falcão, A. P., Gomes, M. G., & Moret Rodrigues, A. (2018). The use of 3D GIS to analyse the influence of urban context on buildings' solar energy potential. *Energy and Buildings*, *177*, 290–302. https://doi.org/https://doi.org/10.1016/j.enbuild.2018.07.064 (Cited on page 17)

Malys, L. (2012). *Evaluation des impacts directs et indirects des façades et des toitures végétales sur le comportement thermique des bâtiments* (Doctoral dissertation). (Cited on page 22)
Thèse de doctorat Génie civil Ecole Centrale de Nantes 2012 2012ECDN0052.

Malys, L., Musy, M., & Inard, C. (2015). Microclimate and building energy consumption: study of different coupling methods. *Advances in Building Energy Research*, *9*(2), 151–174. https://doi.org/10.1080/17512549.2015.1043643 (Cited on page 22)
doi: 10.1080/17512549.2015.1043643

Matthews, T., Lo, A. Y., & Byrne, J. A. (2015). Reconceptualizing green infrastructure for climate change adaptation: Barriers to adoption and drivers for uptake by spatial planners. *Landscape and Urban Planning*, *138*, 155–163. https://doi.org/https://doi.org/10.1016/j.landurbplan.2015.02.010 (Cited on page 20)

Merlier, L. (2015). *On the Interactions Between Urban Structures and Air Flows: A Numerical Study of the Effects of Urban Morphology on the Building Wind Environment and the Related Building Energy Loads* (Doctoral dissertation). INSA Lyon (National Institute for Applied Sciences, Lyon). http://theses.insa-lyon.fr/publication/2015ISAL0070/these.pdf. (Cited on pages 22, 25)

Miguet, F., & Groleau, D. (2002). A daylight simulation tool for urban and architectural spaces—application to transmitted direct and diffuse light through glazing. *Building and Environment*, *37*(8), 833–843. https://doi.org/https://doi.org/10.1016/S0360-1323(02)00049-5 (Cited on page 21)

Montoro, D. F., Vanbuggenhout, P., & Ciesielska, J. (2011). Building Integrated Photovoltaics: An overview of the existing products and their fields of application. *Report Prepared in the Framework of the European Funded Project* (Cited on page 20).

Nault, E., Peronato, G., & Andersen, M. (2015). Forme urbaine et potentiel solaire. (Cited on page 21).

Nelson, J. R., & Grubesic, T. H. (2020). The use of LiDAR versus unmanned aerial systems (UAS) to assess rooftop solar energy potential. *Sustainable Cities and Society*, *61*, 102353. https://doi.org/https://doi.org/10.1016/j.scs.2020.102353 (Cited on page 18)

Ning, G., Junnan, L., Yansong, D., Zhifeng, Q., Qingshan, J., Weihua, G., & Geert, D. (2017). BIM-based PV system optimization and deployment. *Energy and Buildings*, *150*, 13–22. https://doi.org/https://doi.org/10.1016/j.enbuild.2017.05.082 (Cited on page 19)

Orioli, A., & Di Gangi, A. (2013). Load mismatch of grid-connected photovoltaic systems: Review of the effects and analysis in an urban context. *Renewable and Sustainable Energy Reviews*, *21*, 13–28. https://doi.org/https://doi.org/10.1016/j.rser.2012.12.035 (Cited on page 18)

Rahmani Asl, M., Zarrinmehr, S., Bergin, M., & Yan, W. (2015). BPOpt: A framework for BIM-based performance optimization. *Energy and Buildings*, *108*, 401–412. https://doi.org/https://doi.org/10.1016/j.enbuild.2015.09.011 (Cited on page 19)

Rakha, T., & Gorodetsky, A. (2018). Review of Unmanned Aerial System (UAS) applications in the built environment: Towards automated building inspection procedures using drones. *Automation in Construction*, *93*, 252–264. https://doi.org/https://doi.org/10.1016/j.autcon.2018.05.002 (Cited on page 18)

Redweik, P., Catita, C., & Brito, M. (2013). Solar energy potential on roofs and facades in an urban landscape. *Solar Energy*, *97*, 332–341. https://doi.org/https://doi.org/10.1016/j.solener.2013.08.036 (Cited on pages 18, 19)

Reinhart, C., Dogan, T., Jakubiec, J., Rakha, T., & Sang, A. (2013). *UMI - An urban simulation environment for building energy use, daylighting and walkability*. (Cited on page 25).

Robinson, D., Haldi, F., Leroux, P., Perez, D., Rasheed, A., & Wilke, U. (2009). *CITYSIM: Comprehensive Micro-Simulation of Resource Flows for Sustainable Urban Planning*. (Cited on pages 21, 23).

Rogers, D., & Russell, J. (2019). Solar Energy Site Selection and Design in Madison, WI (Cited on page 19).

Ronzino, A., Osello, A., Patti, E., Bottaccioli, L., Danna, C., Lingua, A., Acquaviva, A., Macii, E., Grosso, M., Messina, G., & Rasconà, G. (2015). The Energy

Efficiency Management at Urban Scale by Means of Integrated Modelling. *Energy Procedia*, *83*, 258–268. https://doi.org/https://doi.org/10.1016/j.egypro.2015.12.180 (Cited on page 17)

Sadeghipour Roudsari, M., & Pak, M. (2013). Ladybug: A parametric environmental plugin for grasshopper to help designers create an environmentally-conscious design. *Proceedings of BS 2013: 13th Conference of the International Building Performance Simulation Association*, 3128–3135 (Cited on page 25).

Santamouris, M. (2013). Using cool pavements as a mitigation strategy to fight urban heat island—A review of the actual developments. *Renewable and Sustainable Energy Reviews*, *26*, 224–240. https://doi.org/https://doi.org/10.1016/j.rser.2013.05.047 (Cited on page 20)

Santamouris, M., Synnefa, A., & Karlessi, T. (2011). Using advanced cool materials in the urban built environment to mitigate heat islands and improve thermal comfort conditions. *Solar Energy*, *85*(12), 3085–3102. https://doi.org/https://doi.org/10.1016/j.solener.2010.12.023 (Cited on page 20)

Saretta, E., Caputo, P., & Frontini, F. (2020). An integrated 3D GIS-based method for estimating the urban potential of BIPV retrofit of façades. *Sustainable Cities and Society*, *62*, 102410. https://doi.org/https://doi.org/10.1016/j.scs.2020.102410 (Cited on page 19)

Sarralde, J. J., Quinn, D. J., Wiesmann, D., & Steemers, K. (2015). Solar energy and urban morphology: Scenarios for increasing the renewable energy potential of neighbourhoods in London. *Renewable Energy*, *73*, 10–17. https://doi.org/https://doi.org/10.1016/j.renene.2014.06.028 (Cited on page 17)

Srebric, J., Heidarinejad, M., & Liu, J. (2015). Building neighborhood emerging properties and their impacts on multi-scale modeling of building energy and airflows. *Building and Environment*, *91*, 246–262. https://doi.org/https://doi.org/10.1016/j.buildenv.2015.02.031 (Cited on pages 24, 25)

Sun, Y.-w., Hof, A., Wang, R., Liu, J., Lin, Y.-j., & Yang, D.-w. (2013). GIS-based approach for potential analysis of solar PV generation at the regional scale: A case study of Fujian Province. *Energy Policy*, *58*, 248–259. https://doi.org/https://doi.org/10.1016/j.enpol.2013.03.002 (Cited on page 17)

Šúri, M., & Hofierka, J. (2004). A New GIS-based Solar Radiation Model and Its Application to Photovoltaic Assessments. *Transactions in GIS*, *8*(2), 175–190.

https://doi.org/10.1111/j.1467-9671.2004.00174.x (Cited on page 17) doi: 10.1111/j.1467-9671.2004.00174.x

Tan, Z., Lau, K. K.-L., & Ng, E. (2016). Urban tree design approaches for mitigating daytime urban heat island effects in a high-density urban environment. *Energy and Buildings*, *114*, 265–274. https://doi.org/https://doi.org/10.1016/j.enbuild.2015.06.031 (Cited on page 20)

Tian, W., Wang, Y., Ren, J., & Zhu, L. (2007). Effect of urban climate on building integrated photovoltaics performance. *Energy Conversion and Management*, *48*(1), 1–8. https://doi.org/https://doi.org/10.1016/j.enconman.2006.05.015 (Cited on page 20)

Tzoulas, K., Korpela, K., Venn, S., Yli-Pelkonen, V., Kaźmierczak, A., Niemela, J., & James, P. (2007). Promoting ecosystem and human health in urban areas using Green Infrastructure: A literature review. *Landscape and Urban Planning*, *81*(3), 167–178. https://doi.org/https://doi.org/10.1016/j.landurbplan.2007.02.001 (Cited on page 20)

Van Hoesen, J., & Letendre, S. (2010). Evaluating potential renewable energy resources in Poultney, Vermont: A GIS-based approach to supporting rural community energy planning. *Renewable Energy*, *35*(9), 2114–2122. https://doi.org/https://doi.org/10.1016/j.renene.2010.01.018 (Cited on page 17)

Voivontas, D., Assimacopoulos, D., Mourelatos, A., & Corominas, J. (1998). Evaluation of Renewable Energy potential using a GIS decision support system. *Renewable Energy*, *13*(3), 333–344. https://doi.org/https://doi.org/10.1016/S0960-1481(98)00006-8 (Cited on page 17)

Vulkan, A., Kloog, I., Dorman, M., & Erell, E. (2018). Modeling the potential for PV installation in residential buildings in dense urban areas. *Energy and Buildings*, *169*, 97–109. https://doi.org/https://doi.org/10.1016/j.enbuild.2018.03.052 (Cited on page 19)

Wang, Y., Tian, W., Zhu, L., Ren, J., Liu, Y., Zhang, J., & Yuan, B. (2005). Interactions between Building Integrated Photovoltaics and Microclimate in Urban Environments. *Journal of Solar Energy Engineering*, *128*(2), 168–172. https://doi.org/10.1115/1.2188533 (Cited on page 20)

Wiginton, L. K., Nguyen, H. T., & Pearce, J. M. (2010). Quantifying rooftop solar photovoltaic potential for regional renewable energy policy. *Computers,* *Environment and Urban Systems*, *34*(4), 345–357. https://doi.org/https://doi.org/10.1016/j.compenvurbsys.2010.01.001 (Cited on pages 17, 18)

Yaghoobian, N., & Kleissl, J. (2012). An indoor–outdoor building energy simulator to study urban modification effects on building energy use – Model description and validation. *Energy and Buildings*, *54*, 407–417. https://doi.org/https://doi.org/10.1016/j.enbuild.2012.07.019 (Cited on page 25)

Yang, X., Zhao, L., Bruse, M., & Meng, Q. (2012). An integrated simulation method for building energy performance assessment in urban environments. *Energy and Buildings*, *54*, 243–251. https://doi.org/https://doi.org/10.1016/j.enbuild.2012.07.042 (Cited on pages 21, 24)

3

MODELS NEEDED FOR THE EVALUATION OF THE PHOTOVOLTAIC POTENTIAL IN AN URBAN CONTEXT

> *If you knew how much I love you, how much you are essential to my life, you would not dare to be away for a single moment, you would always stay with me, your heart against my heart, your soul against my soul.*
>
> Victor Hugo

The evaluation of the photovoltaic (PV) potential at urban scale requires the implementation of several models. Indeed, the weather conditions have to be assessed prior to using them as input data for PV power generation models.

This chapter details the different models considered by ENVI-met, which are useful to get input data for the PV generation models. Thus, the models and the method of resolution are described first.

ENVI-met uses Reynolds-averaged Navier-Stokes (RANS) method for the aeraulic phenomena. Therefore, instead of calculating low-scale phenomena, it models them. This is a requirement to reduce the computational cost but, as a counterpart, it requires the use of additional equations. The closure models used by ENVI-met are then detailed.

Regarding the radiative phenomena, ENVI-met uses models in regard with two wavebands: the short and the long wavelengths. The first ones are related to solar radiation, while the latter are related to bodies with a temperature close to the ambient temperature (i.e: the built or the natural surfaces).

Finally, the PV power generation models use input data issued from ENVI-met simulation: the buildings' surface temperature and the shortwave solar irradiance received at their surface. Several types of PV power generation models exist. They are detailed and discussed, in accordance with their basic hypothesis as well as their strengths drawbacks.

3.1 AIRFLOW MODEL

The simulation of the atmosphere is a crucial issue in the urban micro-climate modeling. Among the available numerical tools some are specialized in modeling only airflow phenomena while some are able to couple airflow and radiative phenomena.

3.1.1 *Computational Fluid Dynamics Tools*

Lots of computational fluid dynamics (CFD) software exist. Two of them are particularly popular: ANSYS Fluent and StarCCM+. They are extensively used by the scientific community for wide applications, including combustion gases circulation (Đugum and Hanjalić, 2019; Rago et al., 2018; Silva et al., 2017), airflow distribution in systems (Liang et al., 2018; Liu et al., 2019), interfaces between fluids (Vassilev et al., 2007) and particles concentration and dissipation in atmosphere (Sun and Zhang, 2018; Zhang et al., 2017; Zhao et al., 2018).

These tools bring more precision in terms of CFD results thanks to large eddy scale (LES) models, but faster methods of resolution as well, such as Reynolds-averaged Navier-Stokes (RANS). Nevertheless, due to their time of calculation and time resolution, these software are not usable for high spatial scales. Indeed, taking into consideration both high- and low-scale phenomena is resource-intensive. Thus, some models are needed to speed up the calculation, while keeping accuracy in the results.

3.1.2 *Model Used by ENVI-met*

Unlike other urban climate modeling tools, ENVI-met tends to integrate all the physical phenomena that occur in urban area. This includes aerodynamics, heat and mass transfer between the built or the natural environment or solar radiation. Thus, ENVI-met has a holistic approach in urban area modeling and does not require coupling between different specialized tools. This method of resolution ensures that the inter-related phenomena are considered consistently.

The choice to include all the phenomena within the same computing core makes ENVI-met a highly consuming tool in terms of computing resources. Thus for computational cost reasons, ENVI-met uses RANS solving method. This method reduces the computational cost by solving only the mean flow and modeling all turbulence scales, which are the most resource-intensive phenomena. It represents a workable compromise between performances and accuracy at the district to city scale.

Instead of solving the turbulence equations, RANS method models all turbulence scales. Thus, it requires two steps for the computation :

1. Averaging of Navier-Stokes within the meaning of Reynolds;
2. Use of closure model for turbulence.

As RANS suggests, the Navier-Stokes equations are averaged following the Reynolds decomposition. It means that every quantity of interest is decomposed as the sum of a mean value and the deviations from the expectation value.

3.1.2.1 *Reynolds Decomposition*

Reynolds decomposition is commonly used in fluids dynamics and turbulence theory. It is a mathematical technic involving the decomposition of the variables of interest X into two variables: the expectation value $\overline{X}$ and its fluctuations X'. Thus, in the case of urban climatology, the variables of interest are the fluid velocity u and the pressure p:

$$\begin{cases} u = \overline{u} + u' & (3.1) \\ p = \overline{p} + p' & (3.2) \end{cases}$$

3.1.2.2 *Atmospheric Model*

Navier-Stokes equations are commonly used. Using the Reynolds decomposition, they can be written as:

$$\frac{\partial u_1}{\partial t} + u_i \frac{\partial u_1}{\partial x_i} = -\frac{\partial p'}{\partial x_1} + K_m \left(\frac{\partial^2 u_1}{\partial x_i^2} \right) + f \left(u_2 - u_{2_g} \right) - S_{u_1} \left(x_1, x_2, x_3 \right) \tag{3.3}$$

$$\frac{\partial u_2}{\partial t} + u_i \frac{\partial u_2}{\partial x_i} = -\frac{\partial p'}{\partial x_2} + K_m \left(\frac{\partial^2 u_2}{\partial x_i^2} \right) - f \left(u_1 - u_{1_g} \right) - S_{u_2} \left(x_1, x_2, x_3 \right) \tag{3.4}$$

$$\frac{\partial u_3}{\partial t} + u_i \frac{\partial u_3}{\partial x_i} = -\frac{\partial p'}{\partial x_3} + K_m \left(\frac{\partial^2 u_3}{\partial x_i^2} \right) + g \frac{\theta (z)}{\theta_{ref} (z)} - S_{u_3} \left(x_1, x_2, x_3 \right) \tag{3.5}$$

with:

$$K_m = c_\mu \frac{E^2}{\epsilon}$$
$$c_\mu = 0.09$$

where u is the fluid velocity $[\mathrm{m} \cdot \mathrm{s}^{-1}]$, p' [Pa] is the local pressure perturbation with respect to the reference pressure and K_m $[\mathrm{m} \cdot \mathrm{s}^{-2}]$ is the fluid viscosity. The subscripts refer to the three spatial dimensions. The external constraints include the gravitational acceleration g, the Coriolis parameter f which describes the rotation of the wind near the ground compared to the geostrophic wind and the local source / sink terms S that model the wind drag of semi-permeable obstacles such as vegetation.

In ENVI-met, only the vertical component of the gravitational acceleration is taken into consideration. Thus:

$$g_1 = 0 \tag{3.6}$$

$$g_2 = 0 \tag{3.7}$$

$$g_3 = g \frac{T (z)}{T_{ref} (z)} \tag{3.8}$$

with g the gravitational acceleration $[\mathrm{m} \cdot \mathrm{s}^{-2}]$ and θ the temperature [°C] at the height z [m].

On the contrary, for the Coriolis parameter, only horizontal components are non-null:

$$f_1 = f\left(u_2 - u_{2_g}\right) \tag{3.9}$$

$$f_2 = -f\left(u_1 - u_{1_g}\right) \tag{3.10}$$

$$f_3 = 0 \tag{3.11}$$

with $f = 2\Omega \sin\varphi$, where $\Omega = 7 \cdot 10^{-5}\,\mathrm{s}^{-1}$ is the pulsatance of the earth's rotation and φ is the latitude of the model's location. Note that the Coriolis parameter is implemented in ENVI-met but is switched off by default.

Finally, using the Boussinesq approximation, the air density can be assumed constant (except for the gravity term) and be eliminated from the Navier-Stokes equations. In addition, since is treated as incompressible fluid (Boussinesq approximation), the conversation mass (equation (3.12)) has to be ensured (Bruse, 1999; Bruse and Fleer, 1998; Huttner, 2012):

$$\frac{\partial u_1}{\partial x_1} + \frac{\partial u_2}{\partial x_2} + \frac{\partial u_3}{\partial x_3} = 0 \tag{3.12}$$

The combination of the advection-diffusion equation gives the potential temperature and the humidity of the air:

$$\frac{\partial T}{\partial t} + u_i \frac{\partial T}{\partial x_i^2} = K_h \frac{\partial^2 T}{\partial x_i^2} + \frac{1}{c_p \rho} \frac{R_{lw}}{\partial x_3} + Q_T \tag{3.13}$$

$$\frac{\partial w}{\partial t} + u_i \frac{\partial w}{\partial x_i^2} = K_w \frac{\partial^2 w}{\partial x_i^2} + Q_w \tag{3.14}$$

with K_h and K_w the turbulent coefficients for heat and humidity, respectively $[\mathrm{m}^2 \cdot \mathrm{s}^{-1}]$, Q_T the heat exchange between air and vegetation $[\mathrm{kg} \cdot \mathrm{m}^{-3}]$, Q_w the exchange of humidity between air and vegetation $[\mathrm{kg} \cdot \mathrm{kg}^{-1} \cdot \mathrm{s}^{-1}]$. The term $\frac{1}{c_p \rho} \frac{R_{lw}}{x_3}$ represents the change in air temperature due to the divergence of the longwave (LW) radiation. This latter term highlights the necessity of taking into consideration the radiative phenomena in the evaluation of aeraulic phenomena. It pinpoints the strength of the ENVI-met model, which considers the phenomena that occur in urban environment altogether instead of independently.

3.1.2.3 *Closure Models*

At the time of writing, four closure models are proposed in ENVI-met. Three of them are widely used and developed by the scientific community. The last and most recent one is developed and implemented by Michael Bruse and the ENVI-met team.

MELLOR AND YAMADA MODEL

The first proposed model is a 1.5 order closure model (E–ε Model) based on the work of (Yamada and Mellor, 1975). It adds two more equations for local turbulence (E) and its dissipation rate (ε).

$$\frac{\partial E}{\partial t} + u_i \frac{\partial E}{\partial x_i} = K_E \left(\frac{\partial^2 E}{\partial x_i^2} \right) + Pr - Th + Q_E - \epsilon \tag{3.15}$$

$$\frac{\partial \varepsilon}{\partial t} + u_i \frac{\partial \varepsilon}{\partial x_i} = K_\varepsilon \left(\frac{\partial^2 \varepsilon}{\partial x_i^2} \right) + c_1 \frac{\varepsilon}{E} Pr - c_3 \frac{\varepsilon}{E} Th - c_2 \frac{\varepsilon^2}{E} + Q_\varepsilon \tag{3.16}$$

with: $c_1 = 1.44$; $c_2 = 1.92$; $c_3 = 1.44$ (based on (Launder and Spalding, 1974))

$$\text{and } K_E = \frac{K_m}{\sigma_E} \; ; \; K_\varepsilon = \frac{K_m}{\sigma_\varepsilon} \; ; \; \sigma_E = 1 \; ; \; \sigma_\varepsilon = 1.3$$

The influence of mechanical shearing (Pr) and the thermal forces (Th) is given by:

$$Pr = K_m \left(\frac{\partial u_i}{\partial x_j} + \frac{\partial u_j}{\partial x_i} \right) \frac{\partial u_i}{\partial x_j} \tag{3.17}$$

$$Th = K_h \frac{g}{T_{ref}(z)} \frac{\partial \theta}{\partial z} \tag{3.18}$$

with: $K_h = K_m$

OTHER MODELS

ENVI-met includes other models such vegetation, soil and water flow. However, these models are not essential in a first approach of the evaluation of the photovoltaic (PV) potential of buildings. Thus, they are not described in this paper.

3.2 RADIATION MODEL

In the ENVI-met model, the radiative phenomena are broken into two wavelengths' bands: the shortwave (SW) and the LW radiation. This separation is used to model differently the solar-related phenomena to the one that are due to the terrestrial environment (built or natural).

The two following sections describe the wavelength's separation theory. First this separation is justified with the study of the black bodies. Then, the differences between the SW and LW are described.

3.2.1 *Black Body Radiation*

A black body is an object that is perfectly absorbing and is in thermodynamic equilibrium (which means it has a uniform and constant temperature). The spectral radiation of such a body has been theorized by the physicist Max Planck in 1900. Planck's law (see equation (3.19)) gives the spectral radiation of a black body, according to its temperature:

$$B\left(\lambda, T\right) = \frac{2hc^2}{\lambda^5} \cdot \frac{1}{\exp\left(\dfrac{hc}{\lambda k T}\right) - 1} \tag{3.19}$$

Wien's displacement law gives the wavelength at which the black-body radiation will peak, according to its temperature:

$$\lambda_{peak} \cdot T = 2\,898\,\mu\mathrm{m} \cdot \mathrm{K} \tag{3.20}$$

Plots of Planck's and Wien's laws are given in figure 3.1 on the next page. Two black bodies temperatures are considered: 6 000 K and 288 K. They correspond to a typical temperature of the solar photosphere and the Earth's mean surface temperature.

Figure 3.2 on page 46 shows the comparison of the solar radiation at the top of the atmosphere and at sea level versus the irradiance of a black-body at 6 000 K. It appears that the Sun can be seen, in a first approach, as a black-body since the plotted spectral irradiances are very close. Nevertheless, the difference between the solar irradiance at the top of the atmosphere and the one at sea level highlights the role played by the atmosphere, and more particularly by the water vapour, in

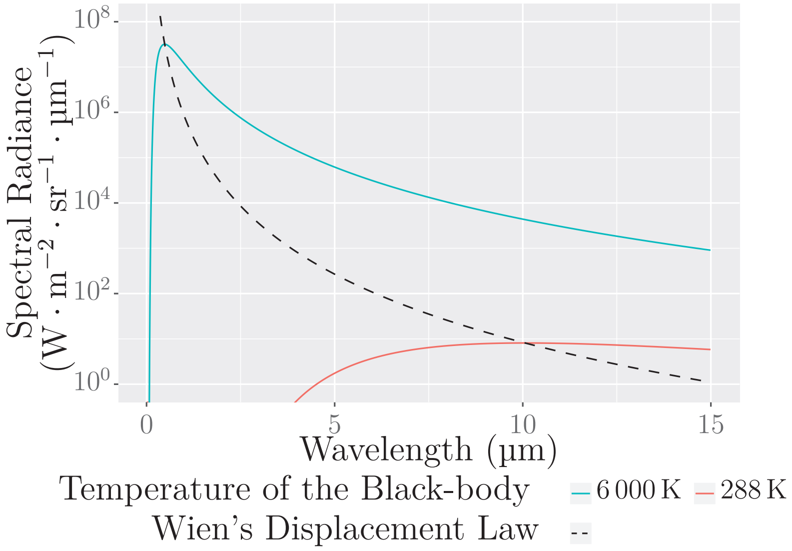

Figure 3.1.: Spectral Radiance of Black Bodies for $T = 6\,000\,\mathrm{K}$ (a Typical Temperature of the Solar Photosphere) and $T = 288\,\mathrm{K}$ (the Earth's Mean Surface Temperature)

the radiative phenomena. This justifies the need for ENVI-met to take them into consideration, as discussed in the next section.

In the field of urban micro-climate simulation, radiation is often separated into two groups: shortwave and longwave radiations. According to Wien's law (equation (3.20) on the preceding page), the higher the temperature, the lower the peak wavelength. Therefore, the shortwave radiation is related to the high temperatures, which is the solar radiation in the context of urban area. Its temperature is about 6 000 K, namely a peak wavelength around 500 nm. Thus, this radiation is in the visible range.
The longwave radiation is related to lower temperatures. In urban context, it corresponds to the temperature of buildings' and ground's surfaces. They can be assumed with a temperature of around 288 K.

Figure 3.3 on the following page shows that the wavelength of 4 µm splits almost completely the short- and longwave radiations. This supports the assumption of splitting the radiation into two distinct wavebands.

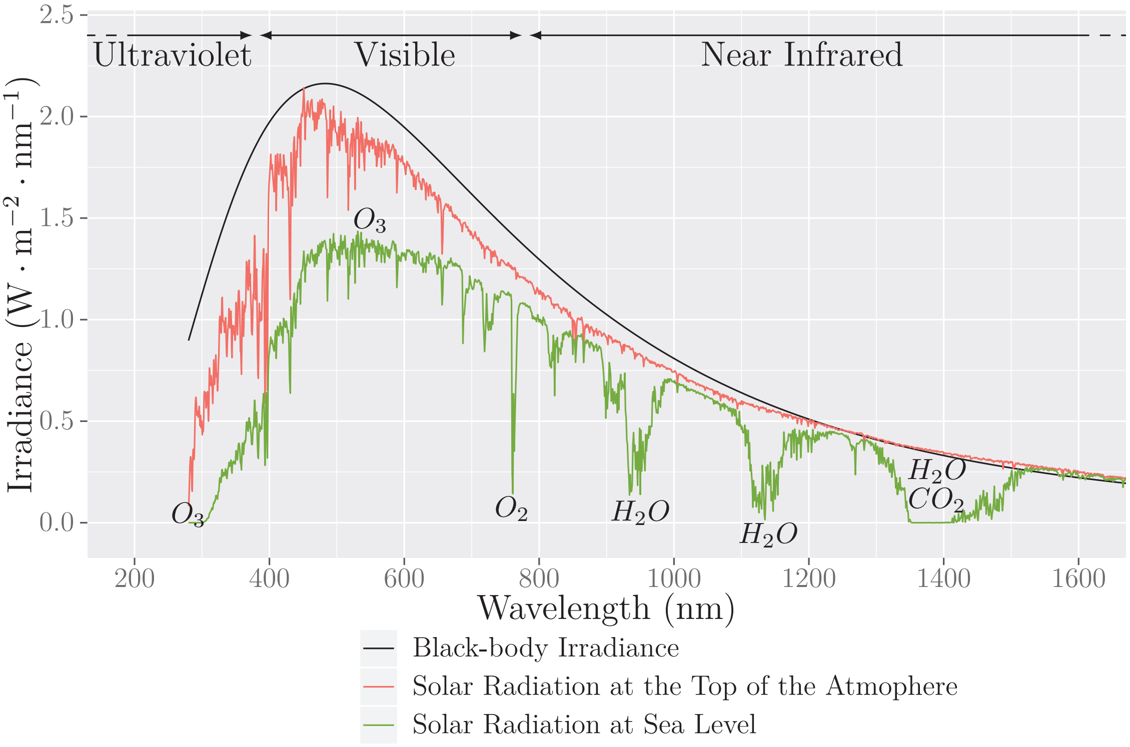

Figure 3.2.: Irradiance Spectrum of Solar Radiation at the Top of the Atmosphere and at Sea Level Compared with the Black Body Irradiance Spectrum at a Temperature of 6 000 K

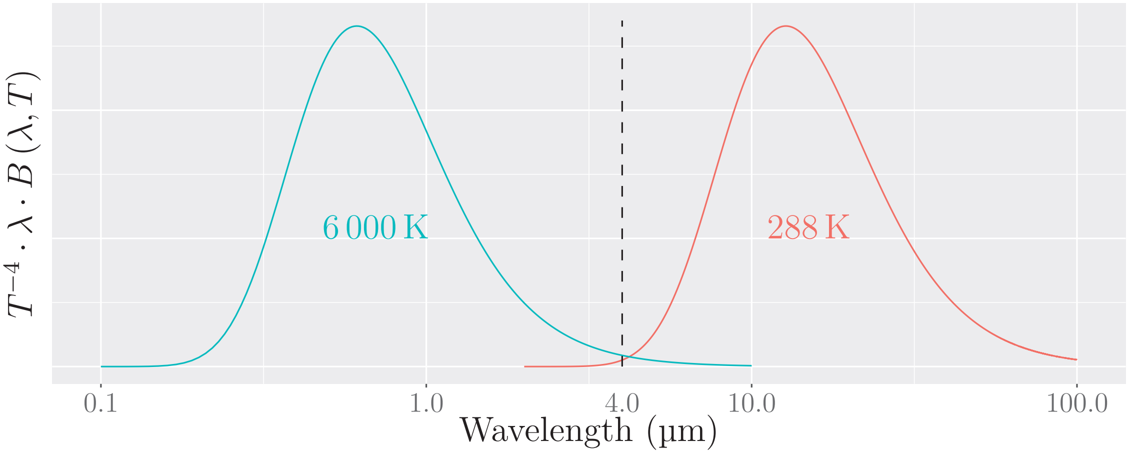

Figure 3.3.: Separation of the Solar and the Thermal Radiation

3.2.2 *Shortwave Radiation*

The SW radiation fluxes at the upper edge of the model (see figure 1.5 on page 9) are determined by integration of the radiation intensity of the Sun I_0 over the wavelength range calculated from $\lambda = 0.29\,\mu\text{m}$ to $\lambda = 4.0\,\mu\text{m}$:

$$Q^*_{sw} = \int_{0.29}^{4.0} I_0\left(\lambda\right) \exp\left(-\alpha_R\left(\lambda\right) m + \alpha_M\left(\lambda\right) m\right) \mathrm{d}\lambda \tag{3.21}$$

where Q^*_{sw} $[\mathrm{W} \cdot \mathrm{m}^{-2}]$ is the shortwave radiation at the top of the modeled domain (see figure 1.5 on page 9), I_0 $[\mathrm{W} \cdot \mathrm{m}^{-2} \cdot \mathrm{nm}^{-1}]$ is the radiation intensity of the Sun, m is the optical air mass [-], α_R and α_M are the Rayleigh and Mie scattering, respectively, and λ is the wavelength [µm].

The upper integration limit is in accordance with the separation domain of SW radiation, as seen in figure 3.3 on the preceding page. The integral in the equation (3.21) can be solved numerically by calculating the area of each considered waveband.

The energy content in the individual wavelength ranges can be derived from the table B.1 on page IV from (Houghton, 1977). Figure 3.4 on the following page shows the similarity between the radiation intensity of the Sun and that of a black body at a temperature of 6 000 K. The Houghton coefficients make easier the calculation of the integral in the equation (3.21) from a numerical point of view, whilst giving a reliable evaluation of the solar radiation.
The Earth is continuously irradiated by the Sun at a level of about $1.74 \cdot 10^{14}$ kW. In relation to the Earth's diameter, the mean value of total solar radiation incident on surface just outside Earth's atmosphere normal to solar beam is equal to $1\,370\,\mathrm{W} \cdot \mathrm{m}^{-2}$. The integral of Planck's law for a black body at a temperature of 5 780 K (surface temperature of the Sun) and for wavelengths from 100 nm to 85 000 nm is equal to $1\,371\,\mathrm{W} \cdot \mathrm{m}^{-2}$. On their side, the Houghton coefficients give an integral of $1\,375\,\mathrm{W} \cdot \mathrm{m}^{-2}$ for the same range of wavelengths.

The optical air mass m is a function of the height of the Sun h [°]:

$$m = \begin{cases} \dfrac{1}{\sin h} & ;\ \text{if } h > 10° \\ 1.22 \times \left(\dfrac{1.0144}{\sin\left(h + 1.44\right)} - 0.49\right) & ;\ \text{if } h \leq 10° \end{cases} \tag{3.22}$$

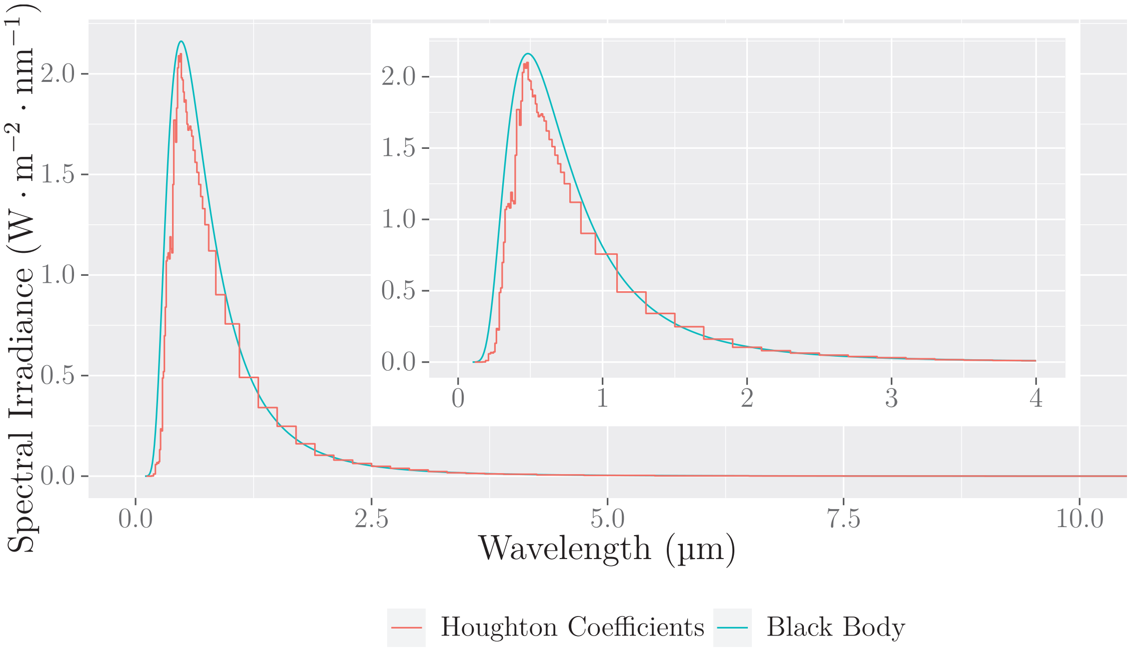

Figure 3.4.: Plot of the Houghton Coefficients Compared with the Spectral Radiation of a Black Body at a Temperature of 6 000 K

The coefficients for Rayleigh and Mie scattering (α_R and α_M) are:

$$\alpha_R(\lambda) = 0.00816 \cdot \lambda^{-4} \tag{3.23}$$

$$\alpha_M(\lambda) = \lambda^{-1.3}\beta_{tr} \tag{3.24}$$

where β_{tr} is the turbidity coefficient according to Ångström. It lies in the range between 0.0040 for clear air and 0.1 for cloudy air and can be taken from tables. However, the influence of this factor on the final result is small under normal atmospheric conditions.

The absolute amount of the short-wave direct radiation at the model upper edge is obtained after subtracting the amount of energy absorbed by the water vapor in the atmosphere:

$$Q^0_{sw_{dir}} = Q^*_{sw} - Q_{sw_{abs}} \tag{3.25}$$

The amount of energy absorbed by the water vapor in the atmosphere is given by (Liljequist, 1979):

$$Q_{sw_{abs}} = 70 + 2.8 \cdot e_{2m} \cdot m \tag{3.26}$$

where e_{2m} [hPa] is the vapor pressure at a height of two meters and m is the optical air mass. The distance between the Earth and the Sun, which varies slightly over the course of the year, is neglected when calculating the radiation.

With a cloud-free sky, the diffuse radiation component can be derived from the direct component and the Sun's height h as follows, according to (Brown, 1974):

$$Q^0_{sw_{diff}} = Q^0_{sw_{dir}} \cdot \sin h \cdot \left(\frac{\Upsilon(h)}{1-\Upsilon(h)} \right) \tag{3.27}$$

where

$$\Upsilon(h) = \frac{1}{1+8(\sin h)^{0.7}} \tag{3.28}$$

Under cloudy weather, the radiation conditions change, since the absolute amount of energy is reduced and the diffuse radiation receives a larger proportion of the remaining radiation energy. The cloud influence is integrated into the model simulation using the method of (Taesler and Andersson, 1984). The relationship for the direct component results from this:

$$Q^0_{sw_{dir}}(covered) = Q^0_{sw_{dir}} \cdot \left(1 - \frac{N_{clo}}{8}\right) \tag{3.29}$$

The change in the diffuse component is more complex, since reflections between the ground and the underside of the cloud must also be taken into account. According to (Taesler and Andersson, 1984), this is where the relationship arises:

$$Q^0_{sw_{diff}}(covered) = \left(\frac{Q^0_{sw_{dir}} \times \sin h}{1-\Upsilon(h)} \right) \cdot \left(\frac{a_{so}-1}{a_w \cdot a_{so}-1} \right) - Q^0_{sw_{dir}}(covered) \cdot \sin h \tag{3.30}$$

The albedo of the various cloud layers a_w is averaged as follows:

$$a_w = \frac{0.75N_l + 0.45N_m + 0.40N_h}{N_{ges}} \tag{3.31}$$

A value averaged over the model area is used for the albedo of soil a_{so}.

3.2.3 *Longwave Radiation*

The long wave radiation directed downwards from the sky is at one cloud-free atmosphere depending on the temperature, and the absorption and emissivity of the individual air layers. The actual absorption and emission rate of the air in the different wavelength ranges depends on the concentration of the main radiation absorbers, such as water vapor, carbon dioxide and ozone. Due to the complex relationships between the partially overlapping absorption bands and the lack of information about the vertical distribution of carbon dioxide and ozone it is common to consider the absorption and emissivity of the individual atmospheric layers exclusively as a function of the water vapor content (Gross, 1991; Paltridge and Platt, 1976)).

The downwardly directed long-wave radiation without modifying components such as vegetation layers is a function of the temperature and the emission and absorption capacity of all upwardly adjoining atmospheric layers up to the edge of the water vapor atmosphere, which is assumed here at $z_v = 15\,\mathrm{km}$. The downward radiation flux at a height z can be represented by the following integral:

$$Q_{lw}^{\downarrow}(z) = \int_{z}^{z_v} \sigma T^4(z') \frac{\partial \varepsilon(z', z)}{\partial z'} \mathrm{d}z' \tag{3.32}$$

where σ is the Stefan-Boltzmann constant, T the temperature and ε the emissivity.

To solve the integral it is necessary to discretize the term $\frac{\partial \varepsilon}{\partial z}$ by finite atmospheric layers with a determinable emissivity. Up to the upper edge of the one-dimensional model at $z = H$, the already defined vertical grid structure can be used for this. Above the model space, a linear decrease in temperature of 3.0 kelvin per kilometer and a linear decrease in specific humidity up to $q(z_v) = 0$ are assumed (Gross, 1991).

According to (Paltridge and Platt, 1976) the integral equation (3.32) can be approximated by N_{at} single layers:

$$Q_{lw}^{\downarrow}(z) = \sum_{n_{at}=1}^{N_{at}} \sigma T^4(n_{at}) \left[\varepsilon_{n_{at}}(m_{vap} + \Delta m_{vap}) - \varepsilon_{n_{at}}(m_{vap})\right] \tag{3.33}$$

Here, m_{vap} is the amount of absorbing water vapor between the height z and the lower edge of the layer n_{at}, $m_{vap} + \Delta m_{vap}$ is the amount of absorbing water vapor including the layer n_{at}.

The amount of water vapor m_{vap_i} in a layer i at the mean height z_i with the thickness Δz_i is given as:

$$m_i = \int_{z_i}^{z_i + \Delta z_i} \left(\frac{p(z_i)}{p_0}\right)^{0.85} \rho q_i \mathrm{d}z_i \tag{3.34}$$

Here $p\left(z_i\right)$ is the air pressure at height z_i and q_i is the specific humidity in layer i. The barometric altitude formula is used to simplify the calculation of the air pressure:

$$p\left(z\right) = p_0 \cdot \exp\left(-\frac{z}{z^*}\right) \tag{3.35}$$

with $z = 8\,000\,\mathrm{m}$. The relationship between the amount of absorbing water vapor and the emissivity of the layer under consideration can be parameterized as follows on the basis of the measurement data from (Kuhn, 1963 and (Piekle, 1984)):

$$\varepsilon_{n_{at}}\left(z, z+\Delta z\right) = \begin{cases} 0.113 \log\left(1 + 12.6 \cdot m_g\right) ; & \text{if} \qquad \log\left(m_g\right) \leq -4.0 \\ 0.104 \log\left(m_g\right) + 0.440 ; & \text{if} \; -4.0 < \log\left(m_g\right) \leq -3.0 \\ 0.121 \log\left(m_g\right) + 0.491 ; & \text{if} \; -3.0 < \log\left(m_g\right) \leq -1.5 \\ 0.146 \log\left(m_g\right) + 0.527 ; & \text{if} \; -1.5 < \log\left(m_g\right) \leq -1.0 \\ 0.161 \log\left(m_g\right) + 0.542 ; & \text{if} \; -1.0 < \log\left(m_g\right) \leq 0 \\ 0.136 \log\left(m_g\right) + 0.542 ; & \text{if} \qquad \log\left(m_g\right) > 0 \end{cases} \tag{3.36}$$

The amount of absorbing water vapor m_g is to be given in $\mathrm{g} \cdot \mathrm{cm}^{-2}$. It should be noted that due to the non-linear relationship between the water vapor content, the emissivity and the empirical data basis, the following must be observed:

$$\varepsilon_n\left(m_{vap} + \Delta m_{vap}\right) - \varepsilon_n\left(m_{vap}\right) \neq \varepsilon_n\left(\Delta m_{vap}\right) \tag{3.37}$$

The procedure presented here is only valid for a cloud-free sky. In the presence of clouds, especially warm, low-hanging clouds, the long-wave radiation exchange between the layers of the atmosphere and between the atmosphere and the ground changes significantly.

Since the quantification of the radiation flux is complex under these conditions, the long-wave radiation at the upper edge of the model is parameterized using a simple empirical approach (Oke, 1987):

$$Q_{lw}^{\downarrow,0} = \sigma\left(T_{2m}\right)^4 \cdot \left[1 - c \cdot \exp\left(-d \cdot \left(273 - T_{2m}\right)^2\right)\right] \tag{3.38}$$

$$Q_{lw}^{\downarrow,0}\,(covered) = Q_{lw}^{\downarrow,0} \cdot \left(1 + \omega_{clo} \cdot \left(\frac{N_{clo}}{8}\right)\right) \tag{3.39}$$

$Q_{lw}^{\downarrow,0}\,(covered)$ is the long-wave downward radiation at the top of the model when it is cloudy, T_{2m} is the air temperature at a height of two meters, $c = 0.261$ and $d = 7.77 \cdot 10^{-4}$ apply to the constants. The mean influence of the cloud cover on the long-wave radiation (ω_{clo}) is determined by the relationship:

$$\omega_{clo} = \frac{0.22N_l + 0.185N_m + 0.06N_h}{N_{clo}} \tag{3.40}$$

where N_l, N_m, N_h and N_{clo} are the degree of coverage with low, medium and high clouds or the total degree of coverage in eighths (Bruse, 1999).

3.3 PHOTOVOLTAIC POWER GENERATION MODELS

3.3.1 *Solar Cell Modeling*

3.3.1.1 *Current-voltage Characteristic*

As its name implies, photovoltaic is the direct conversion of sunlight (photo-) to electricity (-voltaic) using solar cells. Without illumination, a solar cell has the same electrical characteristics as a large diode. The current-voltage (IV) curve of an ideal diode is shown in figure 3.5b on the next page. Under a given value of voltage, no current is allowed to flow – it is called the threshold. Above this value, the ideal diode allows current to flow in one direction. Due to the non-ideality of a diode, this change of behavior occurs in a range of voltage, which leads to the differences between the IV curves of ideal and real diodes (see figure 3.5b to figure 3.5c on the facing page).

Under illumination, the IV curve shifts as the solar cell begins to generate power. The higher the light intensity, the greater the amount of shift (see figure 3.5d to figure 3.5e on the next page). By convention, given that the solar cell delivers current, the curve is flipped (see figure 3.5f on the facing page).

The equation of the IV curve is:

$$I = I_L - I_0 \exp\left[\exp\left(\frac{qV}{nkT}\right) - 1\right] \tag{3.41}$$

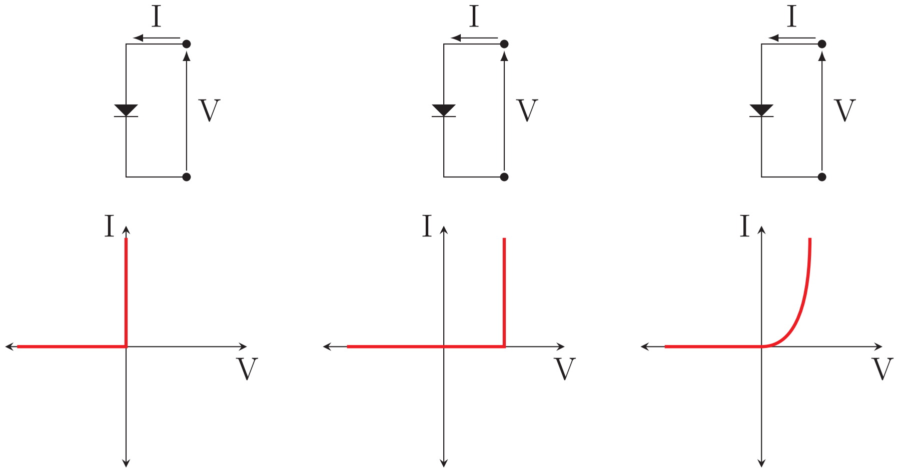

(a) Ideal No-threshold Diode

(b) Ideal Diode

(c) Real Diode

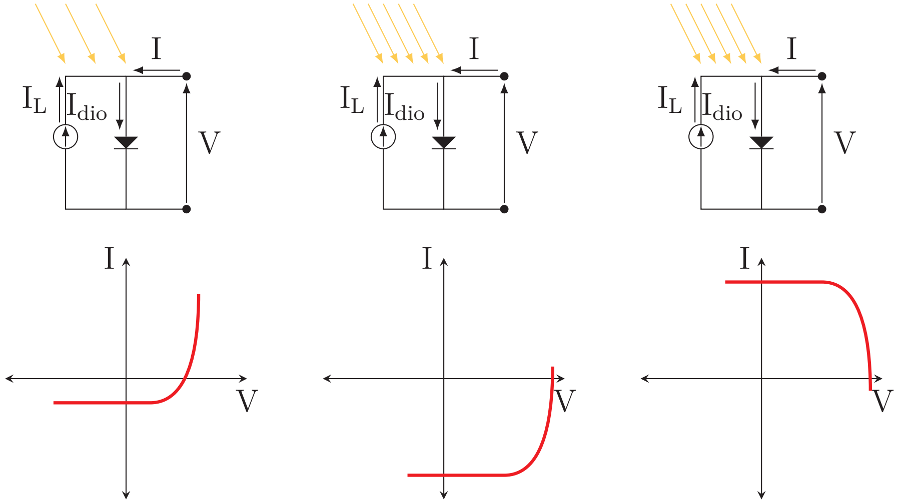

(d) Diode Under Low Illumination

(e) Diode Under High Illumination

(f) Conventional Current-voltage Curve

Figure 3.5.: Schematic Representation of a Diode and its Associated Current-voltage Characteristics

The plot of this equation is given in figure 3.6 on the next page. It makes the relevant points appear:

1. The short-circuit current $\mathrm{I_{sc}}$. It is the current through the solar cell when the voltage across it is zero. According to the graphical representation of a solar cell in figure 3.5b on the preceding page it means that the solar cell is short circuited (hence the name).
2. The open-circuit voltage $\mathrm{V_{oc}}$. It is the maximum available voltage from a solar cell and it occurs when the current flowing through it is equal to zero. According to the graphical representation of a solar cell in Figure 3.5b on the previous page it means that the circuit is opened (hence the name).
3. The maximum power point $\mathrm{P_{mp}}$ which is the maximum output power that can be delivered by the solar cell. It occurs at a voltage of $\mathrm{V_{mp}}$ and $\mathrm{I_{mp}}$.

3.3.1.2 *Fill Factor*

For an ideal solar cell:

$$\begin{aligned} I_{mp} &= I_{sc} \\ V_{mp} &= V_{oc} \end{aligned} \tag{3.42}$$

For a real solar cell:

$$\begin{aligned} I_{mp} &< I_{sc} \\ V_{mp} &< V_{oc} \end{aligned} \tag{3.43}$$

It means that the maximum power of a solar cell is strictly less than the product $I_{sc} \times V_{oc}$. The ratio between the maximum power and this product is the fill factor (FF) (equation (3.44)):

$$\begin{aligned} FF &= \frac{P_{mp}}{V_{oc} I_{sc}} \\ &= \frac{V_{mp} I_{mp}}{V_{oc} I_{sc}} \end{aligned} \tag{3.44}$$

The figure 3.7 on the next page shows that the higher the fill factor, the closer to ideal the solar cell. Graphically, FF can be evaluated by the squareness of the IV curve.

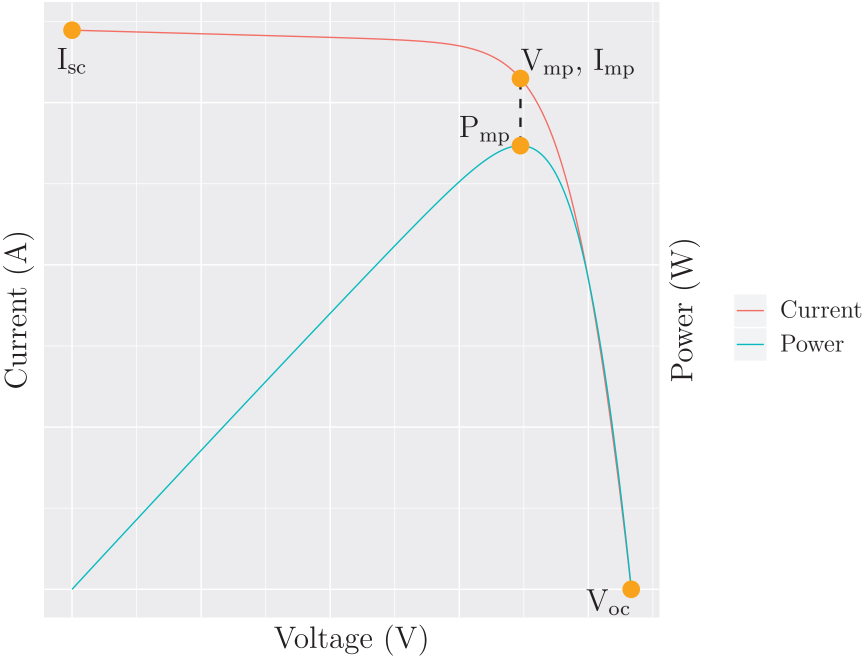

Figure 3.6.: Current-voltage Curve of a Solar Cell

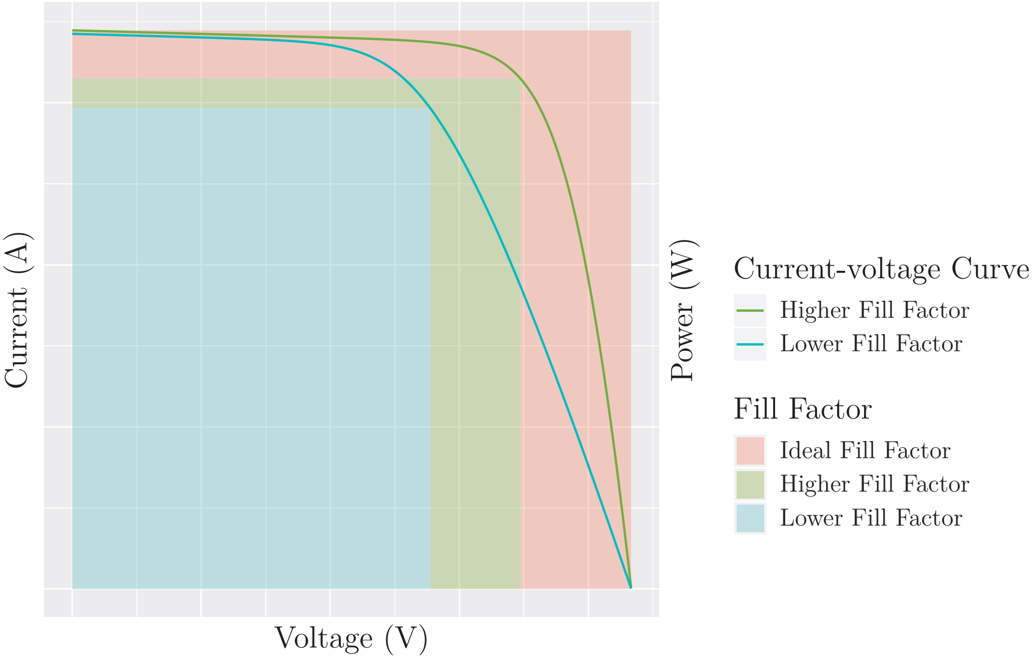

Figure 3.7.: Fill Factor

3.3.1.3 *Resistive Effects of a Solar Cell*

Nevertheless a solar cell presents resistive effects which alter its functioning and deviates it from an ideal behavior. The two main parasitic resistances are series resistance and shunt resistance. The inclusion of these resistive effects in the modeling of a solar cell leads to the implementation of a single-diode model whose the equivalent-circuit is shown in figure 3.10 on page 58.

SERIES RESISTANCE

Series resistance in a solar cell has three causes:

1. the movement of current through the emitter and base of the solar cell;
2. the contact resistance between the metal contact and the silicon;
3. the resistance of the top and rear metal contacts

The main impact of series resistance is to reduce the FF (see figure 3.8 on the next page, although excessively high values may also reduce the short-circuit current (see the blue line which corresponds to an extremely high series resistance value).

SHUNT RESISTANCE

Significant power losses caused by the presence of a shunt resistance are typically due to manufacturing defects, rather than poor solar cell design. Low shunt resistance causes power losses in solar cells by providing an alternate current path for the light-generated current. Such a diversion reduces the amount of current flowing through the solar cell junction and reduces the voltage from the solar cell. The effect of a shunt resistance is particularly severe at low light levels, since there will be less light-generated current. The loss of this current to the shunt therefore has a larger impact. In addition, at lower voltages where the effective resistance of the solar cell is high, the impact of a resistance in parallel is large.

Like the series resistance, the shunt resistance has an impact on the IV curve of the solar cell, as shown in figure 3.9 on the facing page.

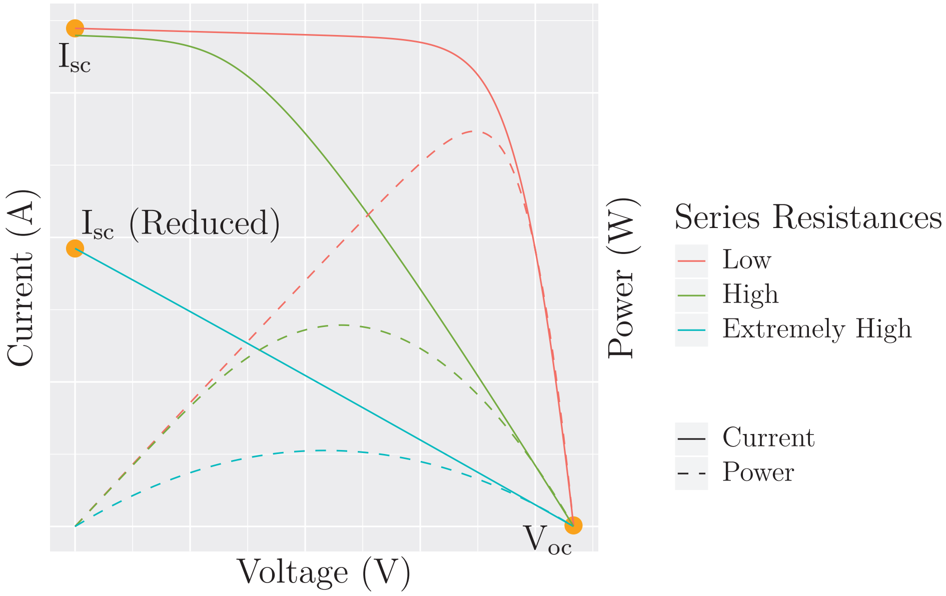

Figure 3.8.: Effect of the Series Resistance on the Current-voltage Curve

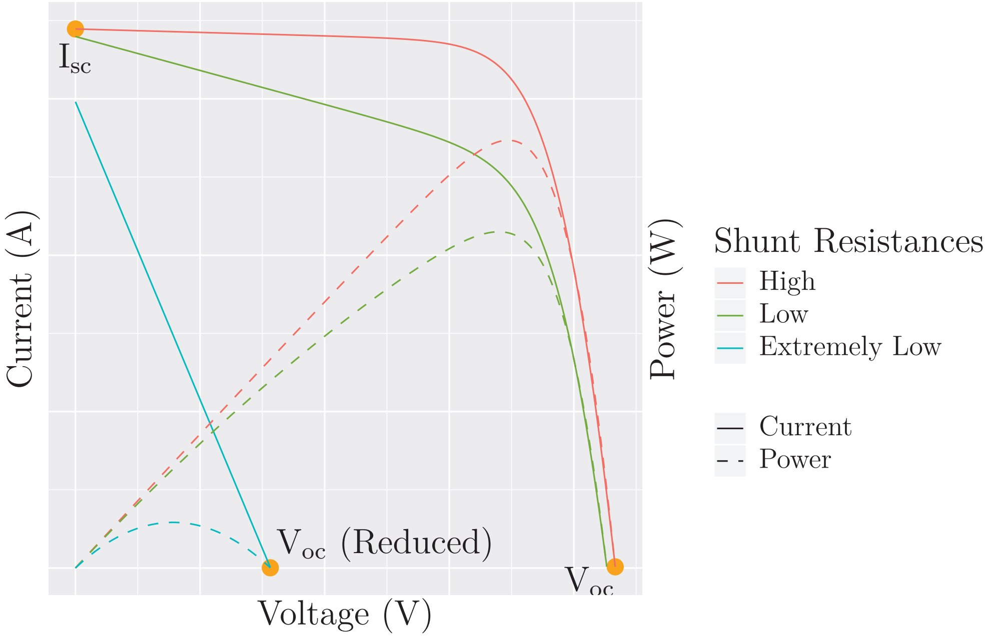

Figure 3.9.: Effect of the Shunt Resistance on the Current-voltage Curve

3.3.2 *Diode-based Models*

The electrical response of a PV cell can be modeled through representing it with an equivalent electrical circuit. This equivalent circuit is able to faithfully represent the entire IV curve of a solar cell, module or array. The representation of a solar cell with a basic equivalent circuit model is derived from physical principles (Gray, 2003). A common way to model a solar cell with an equivalent circuit is the single- or the double-diode model, as discussed in the following.

3.3.2.1 *Single-diode Model*

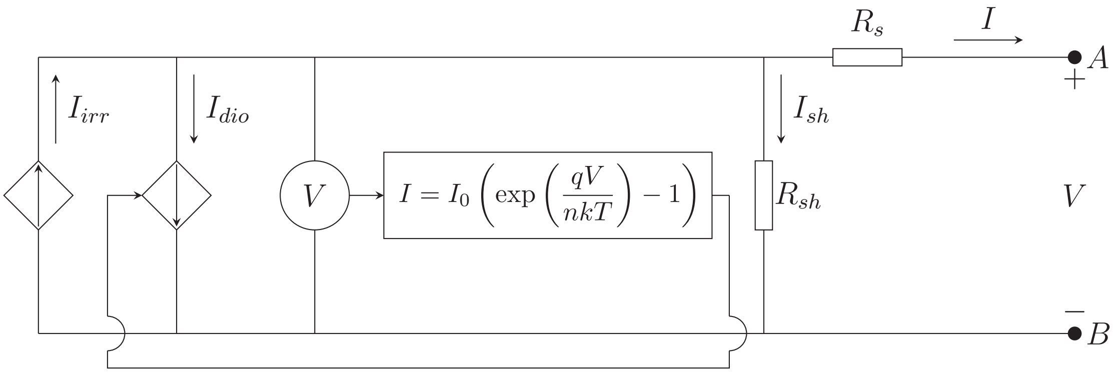

Figure 3.10.: Single-diode Model Equivalent-Circuit

The single-diode model, thanks to its electric design (figure 3.10), takes into account the non-linear behaviour of the PV panel (Chin et al., 2015b).

According to Kirchoff's current law:

$$I = I_{irr} - I_{dio} - I_{sh} \tag{3.45}$$

where I is the output current, I_{irr} is the light-generated current, I_{dio} the current through the diode and I_p the current through the shunt resistance. Substituting expressions of the current through the diode and the shunt resistance leads to the following equation:

$$I = I_{irr} - I_0 \left[\exp\left(\frac{q\,(V + IR_s)}{nkT} \right) - 1 \right] - \frac{V + IR_s}{R_{sh}} \tag{3.46}$$

where I is the output current, I_{irr} is the light-generated current I_0 is the saturation current of the diode, q is the elementary electrical charge, V is the output voltage, R_s is the series resistance, n is the ideality factor, k is the Boltzmann's constant, T is the surface temperature of the cell and R_{sh} is the shunt resistance.

The resolution of the model involves the assessment of five parameters:

1. I_{irr}: the photo current;
2. I_0: the saturation current of the diode;
3. n: the ideality factor;
4. R_s: the series resistance;
5. R_{sh}: the shunt resistance.

The five parameters can be extracted from real measurements (Toledo et al., 2018; Toledo and Blanes, 2014). A distinction can be made between the different methods, with some that try to fit an actual IV curve by minimizing the error between the measured data and the theoretical values (Cárdenas et al., 2017; Easwarakhanthan et al., 1986; Lim et al., 2015; Lo Brano et al., 2010) and those which neglect or approximate some term by a quantity obtained empirically (Chan et al., 1986; Ortiz-Conde et al., 2006; Phang et al., 1984; Toledo et al., 2012a). Finally, other methods are able to assess the five parameters from four arbitrary points (Toledo et al., 2012b).

The main advantages and drawbacks of the different solving methods have been investigated (Shongwe and Hanif, 2015). Other methods (Deihimi et al., 2016; Majdoul et al., 2015; Park and Choi, 2015; Villalva et al., 2009; Yıldıran and Tacer, 2016), as the one considered in this work (Tian et al., 2012), use only the manufacturer's datasheet. They assess the five parameters with only three remarkable points:

1. where the voltage across the solar cell is zero and the current through it is maximum ($\mathrm{I_{sc}}$). It corresponds to a short-circuited;
2. where the current through the solar cell is zero and the voltage across it is maximum ($\mathrm{V_{OC}}$). It corresponds to an open circuit;
3. where the output power is maximum ($\mathrm{P_{mp}}$).

An additional equation is given by the last point. Indeed, at this point, the derivative of power with respect to voltage is zero. Nonetheless, the knowledge of these equations is not enough to characterize the IV curve of the solar module. On the one hand, assumptions are made to analytically solve the the set of equations (Celik and Acikgoz, 2007; Tian et al., 2012). The method proposed by (Tian et al.,

2012) has been selected in this work. The method of resolution for this model is detailed in chapter C on page VII. On the other hand, the use of the manufacturer's datasheet alone may not be sufficient, because of the dependence on the irradiance of the temperature coefficients supplied by the manufacturer's datasheet (Li et al., 2020).

3.3.2.2 *Double-diode Model*

Regarding the lack of accuracy of the single-diode model for low radiation levels (Chin et al., 2015b), an improvement of the method of resolution is needed. This can be accieved by the use of a double-diode model. Indeed, the single-diode model is based on assumptions regarding the flowing through the cell which is assumed as the superposition of two currents: one due to junction bias and the other due to illumination (Mohamed et al., 2013). In addition, the behavior of the single-diode model is different than that of the measured data near the open-circuit voltage, as shown in section E.1.3 on page XLIX (Ishaque et al., 2011). Thus, shading may have a significant impact on the values predicted by the single-diode model. On the other hand, this model assumes that the recombination loss can be neglected in the depletion region, whereas it can be substantial in an actual solar cell, especially at low voltages (Gow and Manning, 1999).

The double-diode model makes it possible to increase the accuracy of the predicted values. This passes through adding a second diode, as shown in figure 3.11 on the facing page. The presence of a second diode add two paramaters to assess (equation (3.48) on the next page). Indeed, instead of a single diode saturation current and an ideality factor, two are to be assessed (one for each diode). Usually, the diode saturation current of the second diode is 3 to 7 orders of magnitude larger than the one of the first diode (Chan et al., 1986; Chin et al., 2016). This leads to a greater value for the ideality factor of the second diode than for the first one (Yahya-Khotbehsara and Shahhoseini, 2018).

$$I = I_{irr} - I_{d1} - I_{d2} - I_{sh} \tag{3.47}$$

where I is the output current, I_{irr} is the light-generated current, I_{dio} the current through the diode and I_p the current through the shunt resistance. Substituting

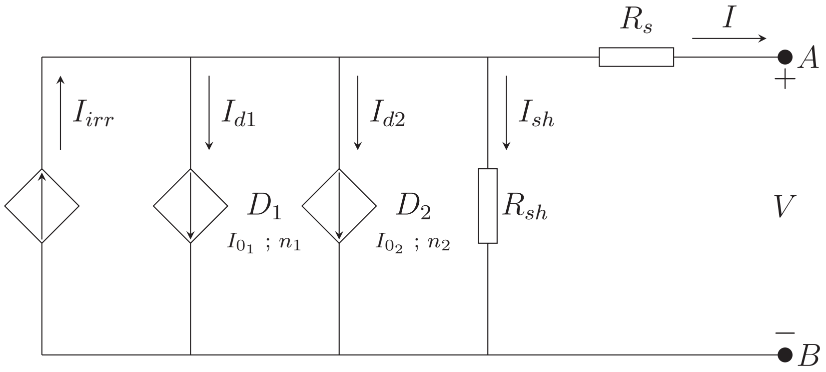

Figure 3.11.: Double-diode Model Equivalent-circuit

expressions of the current through the diode and the shunt resistance leads to the following equation:

$$I = I_{irr} - I_{0_1}\left[\exp\left(\frac{q\,(V+IR_s)}{n_1 kT}\right)-1\right] - I_{0_2}\left[\exp\left(\frac{q\,(V+IR_s)}{n_2 kT}\right)-1\right] - \frac{V+IR_s}{R_{sh}} \qquad (3.48)$$

where I is the output current, I_{irr} is the light-generated current I_0 is the saturation current of the diode, q is the elementary electrical charge, V is the output voltage, R_s is the series resistance, n is the ideality factor, k is the Boltzmann's constant, T is the surface temperature of the cell and R_{sh} is the shunt resistance.

Adding a second diode makes solving the system of equations more complex and increases the cost of calculation. Two types of methods to assess the seven parameters of the solar cell are usually used: analytical and numerical approach (Chin et al., 2015b). The analytical resolution method is fast but the nonlinearity of the IV curve makes it difficult to determine the parameters accurately without assumptions and simplifications (Majdoul et al., 2015).

A way to increase the accuracy of the results is to use recent numerical approach, based on artificial intelligence (Chin et al., 2015a; Chin et al., 2016; Jacob et al., 2015; Muhsen et al., 2015). However, these methods are difficult to implement and highly resource intensive. They are therefore far beyond the scope of the integrated methodology proposed here.

In the proposed integrated methodology, the time of calculation is a crucial issue. A compromise between time of calculation and accuracy is therefore a crucial issue.

A combination between analytical resolution and associated assumptions has been selected, based on the model developed by (Et-torabi et al., 2017). In this model, seven parameters are to be assessed. In order to reduce the cose of computation, the ideality factors are assumed as equal to $n_1 = 1$ and $n_2 = 2$ (Allam et al., 2016; Ishaque et al., 2011), respectively. This assumption, which is an approximation of the Schokley-Read-Hall recombination in the space charge layer in the photodiode, is also widely used. Despite the slight loss of accuracy, under extreme conditions, due to this assumption, this method of resolution is able to simulate the diffusion process of the minority carriers into the depletion layer, as well as the carrier recombination in the space charge region of the junction (Attivissimo et al., 2013; Gao et al., 2016).

3.3.3 *Power Model*

Diode-based models design have a physical meaning because of the similarities between the IV curves of a solar cell and a diode. Nonetheless, their cost of computing can be high and their accuracy quite poor, depending on the weather conditions. Other available alternatives, discussed in the next section, can be used to reduce the computational time.

The power model is given as a simple algebric equation where the output power is proportional to the irradiation level and inversely proportional to the temperature[1]. The maximal output power is assessed under reference conditions. These assumptions lead to the equation (3.49).

$$P_{out} = P_{MAX_{ref}} \times \frac{G}{G_{ref}} \times (1 + \gamma \times (T - T_{ref})) \tag{3.49}$$

The usually considered reference conditions are standard test conditions (STC) and nominal operating cell temperature (NOCT). Their details are given in the table 3.1 on the next page. When the STC are taken as a reference:

$$P_{out} = P_{MAX_{STC}} \times \frac{G}{G_{STC}} \times (1 + \gamma \times (T - T_{STC})) \tag{3.50}$$

---

[1] The temperature coefficient of the maximum power γ is negative.

Table 3.1.: Details of Standard Test Conditions and Nominal Operating Cell Temperature

	STC	NOCT
Irradiation [$W \cdot m^{-2}$]	1 000	800
Temperature [°C]	25 (cell)	20 (air)
Air mass	1.5	1.5
Wind velocity [$m \cdot s^{-1}$]		1

The main advantage of this model is its simplicity of implementation because it relies on a single equation. As a counterpart, it assumes a linear relationship between the maximal STC panel output power, and the solar irradiation and the surface temperature. This assumption can become particularly strong under extreme weather conditions.

This chapter presents three main families of models needed for assessing the photovoltaic potential of buildings while taking into account the specific features of the urban microclimate. The aeraulic and radiative models make it possible to provide data, used as input for the photovoltaic production model.

The methods of resolution chosen by ENVI-met for the aeraulic and radiative models are not those providing the most accurate results, for each of the phenomena considered independently. Nevertheless, it is a question of compromise, making it possible to consider the inter-relation between these phenomena whilst reducing the computation cost, and thus to increase the spatial study scale.

A positioning of the different models, taken into consideration by ENVI-met and related to the evaluation of the photovoltaic potential, is then necessary, to demonstrate the ability of ENVI-met to be used for this purpose. Similarly, the strengths and drawbacks of the different photovoltaic generation models have to be highlighted. This is the theme of the chapter chapter 5 on page 83.

REFERENCES RELATED TO THE EXISTING MODELS

Allam, D., Yousri, D. A., & Eteiba, M. B. (2016). Parameters extraction of the three diode model for the multi-crystalline solar cell/module using Moth-Flame Optimization Algorithm. *Energy Conversion and Management*, *123*, 535–548. https://doi.org/https://doi.org/10.1016/j.enconman.2016.06.052 (Cited on page 62)

Attivissimo, F., Adamo, F., Carullo, A., Lanzolla, A. M. L., Spertino, F., & Vallan, A. (2013). On the performance of the double-diode model in estimating the maximum power point for different photovoltaic technologies. *Measurement*, *46*(9), 3549–3559. https://doi.org/https://doi.org/10.1016/j.measurement.2013.06.032 (Cited on page 62)

Brown, G. I. E. (1974). *Solar irradiation and sun shading devices* (tech. rep.). National Swedish Council for Building Research. Stockholm. (Cited on page 49).

Bruse, M. (1999). *Die Auswirkungen kleinskaliger Umweltgestaltung auf das Mikroklima*. Univeristy of Bochum. (Cited on pages 42, 52).

Bruse, M., & Fleer, H. (1998). Simulating surface–plant–air interactions inside urban environments with a three dimensional numerical model. *Environmental Modelling & Software*, *13*(3), 373–384. https://doi.org/https://doi.org/10.1016/S1364-8152(98)00042-5 (Cited on page 42)

Cárdenas, A. A., Carrasco, M., Mancilla-David, F., Street, A., & Cárdenas, R. (2017). Experimental Parameter Extraction in the Single-Diode Photovoltaic Model via a Reduced-Space Search. *IEEE Transactions on Industrial Electronics*, *64*(2), 1468–1476. https://doi.org/10.1109/TIE.2016.2615590 (Cited on page 59)

Celik, A. N., & Acikgoz, N. (2007). Modelling and experimental verification of the operating current of mono-crystalline photovoltaic modules using four- and five-parameter models. *Applied Energy*, *84*(1), 1–15. https://doi.org/https://doi.org/10.1016/j.apenergy.2006.04.007 (Cited on page 59)

Chan, D. S. H., Phillips, J. R., & Phang, J. C. H. (1986). A comparative study of extraction methods for solar cell model parameters. *Solid-State Electronics*, *29*(3), 329–337. https://doi.org/https://doi.org/10.1016/0038-1101(86)90212-1 (Cited on pages 59, 60)

Chin, V. J., Salam, Z., & Ishaque, K. (2015a). An accurate two diode model computation for CIS thin film PV module using the hybrid approach. *2015 4th International Conference on Electric Power and Energy Conversion Systems (EPECS)*, 1–6. https://doi.org/10.1109/EPECS.2015.7368493 (Cited on page 61)

Chin, V. J., Salam, Z., & Ishaque, K. (2015b). Cell modelling and model parameters estimation techniques for photovoltaic simulator application: A review. *Applied Energy*, *154*, 500–519. https://doi.org/https://doi.org/10.1016/j.apenergy.2015.05.035 (Cited on pages 58, 60, 61)

Chin, V. J., Salam, Z., & Ishaque, K. (2016). An accurate modelling of the two-diode model of PV module using a hybrid solution based on differential evolution. *Energy Conversion and Management*, *124*, 42–50. https://doi.org/https://doi.org/10.1016/j.enconman.2016.06.076 (Cited on pages 60, 61)

Deihimi, M. H., Naghizadeh, R. A., & Meyabadi, A. F. (2016). Systematic derivation of parameters of one exponential model for photovoltaic modules using numerical information of data sheet. *Renewable Energy*, *87*, 676–685. https://doi.org/https://doi.org/10.1016/j.renene.2015.10.066 (Cited on page 59)

Đugum, A., & Hanjalić, K. (2019). Numerical simulation of coal-air mixture flow in a real double-swirl burner and implications on combustion anomalies in a utility boiler. *Energy*, *170*, 942–953. https://doi.org/10.1016/J.ENERGY.2018.12.121 (Cited on page 39)

Easwarakhanthan, T., Bottin, J., Bouhouch, I., & Boutrit, C. (1986). Nonlinear Minimization Algorithm for Determining the Solar Cell Parameters with Microcomputers. *International Journal of Solar Energy*, *4*(1), 1–12. https://doi.org/10.1080/01425918608909835 (Cited on page 59)
doi: 10.1080/01425918608909835

Et-torabi, K., Nassar-eddine, I., Obbadi, A., Errami, Y., Rmaily, R., Sahnoun, S., El fajri, A., & Agunaou, M. (2017). Parameters estimation of the single and double diode photovoltaic models using a Gauss–Seidel algorithm and analytical method: A comparative study. *Energy Conversion and Management*, *148*, 1041–1054. https://doi.org/https://doi.org/10.1016/j.enconman.2017.06.064 (Cited on page 62)

Gao, X., Cui, Y., Hu, J., Xu, G., & Yu, Y. (2016). Lambert W-function based exact representation for double diode model of solar cells: Comparison on fitness and parameter extraction. *Energy Conversion and Management*, *127*, 443–460. https://doi.org/https://doi.org/10.1016/j.enconman.2016.09.005 (Cited on page 62)

Gow, J. A., & Manning, C. D. (1999). Development of a photovoltaic array model for use in power-electronics simulation studies. *IEE Proceedings - Electric Power Applications*, *146*(2), 193–200. https://doi.org/10.1049/ip-epa:19990116 (Cited on page 60)

Gray, J. L. (2003). The Physics of the Solar Cell. https://doi.org/https://doi.org/10.1002/0470014008.ch3. (Cited on page 58)
https://doi.org/10.1002/0470014008.ch3

Gross, G. (1991). Anwendungsmöglichkeiten mesoskaliger Simulationsmodelle dargestellt am Beispiel Darmstadt. I : Wind- und Temperaturfelder; On the application of mesoscale models with Darmstadt as an example. I: Wind and temperature. *Meteorologische Rundschau*, *43*(4), 97–112 (Cited on page 50)
Classification: 001E02F: Géophysique. Techniques, méthodes, appareillage et modèles / Geophysics. Techniques, methods, instrumentation and models Inist-CNRS record number 5007626.

Houghton, J. T. (1977). *The physics of the atmophere* (tech. rep.). Camnridge University Press. New York, New York. (Cited on page 47).

Huttner, S. (2012). *Further development and application of the 3D microclimate simulation ENVI-met* (Doctoral dissertation). Mainz. (Cited on page 42).

Ishaque, K., Salam, Z., Taheri, H., & Syafaruddin. (2011). Modeling and simulation of photovoltaic (PV) system during partial shading based on a two-diode model. *Simulation Modelling Practice and Theory*, *19*(7), 1613–1626. https://doi.org/https://doi.org/10.1016/j.simpat.2011.04.005 (Cited on pages 60, 62)

Jacob, B., Balasubramanian, K., Babu, T. S., & Rajasekar, N. (2015). Parameter extraction of solar PV double diode model using artificial immune system. *2015 IEEE International Conference on Signal Processing, Informatics, Communication and Energy Systems (SPICES)*, 1–5. https://doi.org/10.1109/SPICES.2015.7091390 (Cited on page 61)

Kuhn, P. M. (1963). Radiometersonde Observations of Infrared Flux Emissivity of Water Vapor. *Journal of Applied Meteorology*, *2*(3), 368–378. https://doi.org/10.1175/1520-0450(1963)002<0368:ROOIFE>2.0.CO;2 (Cited on page 51)

Launder, B. E., & Spalding, D. B. (1974). The numerical computation of turbulent flows. *Computer Methods in Applied Mechanics and Engineering*, *3*(2), 269–289. https://doi.org/10.1016/0045-7825(74)90029-2 (Cited on page 43)

Li, B., Migan, A., & Delpha, C. (2020). *Irradiance Dependence of the Short-Circuit Current Temperature Coefficient of sc-Si PV Module.* (Cited on page 60).

Liang, Y. Y., Fimbres Weihs, G., & Fletcher, D. F. (2018). CFD study of the effect of unsteady slip velocity waveform on shear stress in membrane systems. *Chemical Engineering Science*, *192*, 16–24. https://doi.org/10.1016/J.CES.2018.07.009 (Cited on page 39)

Liljequist, G. H. (1979). *Meteorology* (tech. rep.). Univerisity of Uppsala. Uppsala. (Cited on page 48).

Lim, L. H. I., Ye, Z., Ye, J., Yang, D., & Du, H. (2015). A Linear Identification of Diode Models from Single I– V Characteristics of PV Panels. *IEEE Transactions on Industrial Electronics*, *62*(7), 4181–4193. https://doi.org/10.1109/TIE.2015.2390193 (Cited on page 59)

Liu, L., Yang, J., Lu, H., Tian, X., & Lu, W. (2019). Numerical simulations on the motion of a heavy sphere in upward Poiseuille flow. *Ocean Engineering*, *172*, 245–256. https://doi.org/10.1016/J.OCEANENG.2018.11.041 (Cited on page 39)

Lo Brano, V., Orioli, A., Ciulla, G., & Di Gangi, A. (2010). An improved five-parameter model for photovoltaic modules. *Solar Energy Materials and Solar Cells*, *94*(8), 1358–1370. https://doi.org/https://doi.org/10.1016/j.solmat.2010.04.003 (Cited on page 59)

Majdoul, R., Abdelmounim, E., Aboulfatah, M., Touati, A. W., Moutabir, A., & Abouloifa, A. (2015). Combined analytical and numerical approach to determine the four parameters of the photovoltaic cells models. *2015 International Conference on Electrical and Information Technologies (ICEIT)*, 263–268. https://doi.org/10.1109/EITech.2015.7162977 (Cited on pages 59, 61)

Mohamed, N., Yahaya, N. Z., & Singh, B. (2013). *Single-diode model and two-diode model of PV modules: A comparison*. https://doi.org/10.1109/ICCSCE.2013.6719960. (Cited on page 60)

Muhsen, D. H., Ghazali, A. B., & Khatib, T. (2015). Parameter extraction of photovoltaic module using hybrid evolutionary algorithm. *2015 IEEE Student Conference on Research and Development (SCOReD)*, 533–538. https://doi.org/10.1109/SCORED.2015.7449393 (Cited on page 61)

Oke, T. R. (1987). Boundary Layer Climates, Methuen: London. *New York*, *435* (Cited on page 51).

Ortiz-Conde, A., García Sánchez, F. J., & Muci, J. (2006). New method to extract the model parameters of solar cells from the explicit analytic solutions of their illuminated I–V characteristics. *Solar Energy Materials and Solar Cells*, *90*(3), 352–361. https://doi.org/https://doi.org/10.1016/j.solmat.2005.04.023 (Cited on page 59)

Paltridge, G. W., & Platt, C. M. R. (1976). Radiative processes in meteorology and climatology (Cited on page 50)
Classification: 001E02F: Géophysique. Techniques, méthodes, appareillage et modèles / Geophysics. Techniques, methods, instrumentation and models Inist-CNRS record number PASCAL7730074104.

Park, J.-Y., & Choi, S.-J. (2015). A novel datasheet-based parameter extraction method for a single-diode photovoltaic array model. *Solar Energy*, *122*, 1235–1244. https://doi.org/https://doi.org/10.1016/j.solener.2015.11.001 (Cited on page 59)

Phang, J. C. H., Chan, D. S. H., & Phillips, J. R. (1984). Accurate analytical method for the extraction of solar cell model parameters. *Electronics Letters*, *20*(10), 406–408. https://doi.org/10.1049/el:19840281 (Cited on page 59)

Piekle, R. A. (1984). Mesoscale meteorological modelling. (Cited on page 51).

Rago, G., Rossiello, G., Dadduzio, R., Giani, T., Saponaro, A., Cesareo, F., Lacerenza, M., Fornarelli, F., Caramia, G., Fortunato, B., Camporeale, S., Torresi, M., & Panebianco, V. (2018). CFD analysis of a swirl stabilized coal combustion burner. *Energy Procedia*, *148*, 703–711. https://doi.org/10.1016/J.EGYPRO.2018.08.160 (Cited on page 39)

Shongwe, S., & Hanif, M. (2015). Comparative Analysis of Different Single-Diode PV Modeling Methods. *IEEE Journal of Photovoltaics*, *5*(3), 938–946. https://doi.org/10.1109/JPHOTOV.2015.2395137 (Cited on page 59)

Silva, J., Teixeira, J., Teixeira, S., Preziati, S., & Cassiano, J. (2017). CFD Modeling of Combustion in Biomass Furnace. *Energy Procedia*, *120*, 665–672. https://doi.org/10.1016/j.egypro.2017.07.179 (Cited on page 39)

Sun, D., & Zhang, Y. (2018). Influence of avenue trees on traffic pollutant dispersion in asymmetric street canyons: Numerical modeling with empirical analysis. *Transportation Research Part D: Transport and Environment*, *65*, 784–795. https://doi.org/10.1016/J.TRD.2017.10.014 (Cited on page 39)

Taesler, R., & Andersson, C. (1984). A method for solar radiation computations using routine meteorological observations. *Energy and Buildings*, *7*(4), 341–352. https://doi.org/https://doi.org/10.1016/0378-7788(84)90080-X (Cited on page 49)

Tian, H., Mancilla-David, F., Ellis, K., Muljadi, E., & Jenkins, P. (2012). *Detailed performance model for photovoltaic systems* (tech. rep.). National Renewable Energy Lab.(NREL), Golden, CO (United States). (Cited on page 59).

Toledo, F. J., Blanes, J. M., & Galiano, V. (2018). Two-Step Linear Least-Squares Method For Photovoltaic Single-Diode Model Parameters Extraction. *IEEE Transactions on Industrial Electronics*, *65*(8), 6301–6308. https://doi.org/10.1109/TIE.2018.2793216 (Cited on page 59)

Toledo, F. J., & Blanes, J. M. (2014). Geometric properties of the single-diode photovoltaic model and a new very simple method for parameters extraction. *Renewable Energy*, *72*, 125–133. https://doi.org/https://doi.org/10.1016/j.renene.2014.06.032 (Cited on page 59)

Toledo, F. J., Blanes, J. M., Garrigós, A., & Martínez, J. A. (2012a). Analytical resolution of the electrical four-parameters model of a photovoltaic module using small perturbation around the operating point. *Renewable Energy*, *43*, 83–89. https://doi.org/https://doi.org/10.1016/j.renene.2011.11.037 (Cited on page 59)

Toledo, F. J., Blanes, J. M., Garrigós, A., & Martínez, J. A. (2012b). Analytical resolution of the electrical four-parameters model of a photovoltaic module using small perturbation around the operating point. *Renewable Energy*, *43*, 83–89. https://doi.org/https://doi.org/10.1016/j.renene.2011.11.037 (Cited on page 59)

Vassilev, A., Ben Hadid, H., El Hajem, M., & Botton, V. (2007). Experimental and numerical investigation of an air pocket immersed and immobilized in a horizontal water duct flow. *International Journal of Heat and Fluid Flow*, *28*(4), 673–682. https://doi.org/https://doi.org/10.1016/j.ijheatfluidflow.2007.02.005 (Cited on page 39)

Villalva, M. G., Gazoli, J. R., & Ruppert Filho, E. (2009). Comprehensive approach to modeling and simulation of photovoltaic arrays. *IEEE Transactions on power electronics*, *24*(5), 1198–1208 (Cited on page 59).

Yahya-Khotbehsara, A., & Shahhoseini, A. (2018). A fast modeling of the double-diode model for PV modules using combined analytical and numerical approach. *Solar Energy*, *162*, 403–409. https://doi.org/https://doi.org/10.1016/j.solener.2018.01.047 (Cited on page 60)

Yamada, T., & Mellor, G. (1975). A Simulation of the Wangara Atmospheric Bourndary Layer Data. *Journal of the Atmospheric Sciences*, *32*, 2309–2329 (Cited on page 43).

Yıldıran, N., & Tacer, E. (2016). Identification of photovoltaic cell single diode discrete model parameters based on datasheet values. *Solar Energy*, *127*, 175–183. https://doi.org/https://doi.org/10.1016/j.solener.2016.01.024 (Cited on page 59)

Zhang, H., Wang, F., Wang, Y., & Wang, H. (2017). CFD Simulation of Cooking Particle Distribution and Motion. *Procedia Engineering*, *205*, 1800–1806. https://doi.org/10.1016/J.PROENG.2017.10.234 (Cited on page 39)

Zhao, R., Zhou, L., & Ma, J. (2018). CFD design of ventilation system for large underground bus terminal in Macau Barrier Gate. *Journal of Wind Engineering and Industrial Aerodynamics*, *179*, 1–13. https://doi.org/10.1016/J.JWEIA.2018.05.010 (Cited on page 39)

4

NUMERICAL DEVELOPMENTS FOR THE CHAINING BETWEEN ENVI-MET AND THE PHOTOVOLTAIC POWER GENERATION MODELS

> *Work keeps at bay three great evils: boredom, vice and need.*
>
> Voltaire

As a urban microclimate (UMC) modeling software, ENVI-met is able to evaluate the phenomena that occur in an urban context and the associated physical values. To do so, local weather conditions are required as input for the simulations.

The input data for the simulation has to follow a particular format for ENVI-met to be able to use it. Then, this format is detailed first, as well as the required process to meet this format.

The ENVI-met output format is also fixed. It is oriented for the data to be easily visualized by the user with Leonardo. Nevertheless, this format is not suitable for the evaluation of the photovoltaic (PV) potential of buildings' facades. Thus, a new output format was developed. This format is based on a relational database system. It is detailed in the second section of this chapter.

ENVI-met is able to calculate the surface temperature and the irradiance level for each cell of the modeled domain. Thus, the spatial heterogeneity and the time variability can be taken into consideration, as well as the intermittency, in a certain way. The simulation output data can therefore be used as input data for the PV power generation models.

The software ENVI-met has been selected to carry out simulations taking into consideration the local microclimate. The goal of the work is to evaluate the PV potential of buildings' facades. As shown in the previous chapter, the diode-based photovoltaic (PV) power generation models require two parameters related to the weather conditions: the surface temperature and the irradiance level. These data are part of the ENVI-met output. Nonetheless, their original format is not suitable for the evaluation of the solar potential. Thus, the latter has been modified, and the new developed output format is described in 4.2.2 on page 76.

The input data format is also an issue in the simulations carried out with ENVI-met. Indeed, they have to follow a format, which is the same as the one used in EnergyPlus weather files (`.epw`). However, the measured data may not follow the same format, because of the sensors used in the experiment or the sample time. Since the use of on-site measurements is the way to get the most reliable results regarding taking into consideration the local microclimate, the format of the measurements has to be adjusted to the ENVI-met input data format. The required adjustments are highlighted in section 4.1 on the facing page.

Finally, a focus is put on the developed framework used to analyze and visualize the results obtained with the developed format.

4.1 INPUT DATA FORMATTING

At the time of writing, ENVI-met provides several options for the input data:

1. Beginner;
2. Intermediate;
3. Advanced.

Both Intermediate and Advanced offers the Full Forcing option, which offers to provide the simulation with local measurements as input data. These inputs have to follow a specific structure, in a coma-separated values (CSV) file (`.csv`).

4.1.1 *Format Used by ENVI-met*

The format used by ENVI-met to provide the simulation with local measurements data is the same as the one used by the EnergyPlus weather files or the typical representative year data files (see table 4.1 on the next page). Thanks to this format, local weather conditions can be provided to the simulation. Thus, the accuracy of the results is increased.

The provided data cover the different phenomena (aeraulic or radiative) presented in the chapter 2 on page 15, as well as the different methods of resolution associated to them. Thus, depending on available measurements, the different components of the solar radiation (beam normal irradiance (BNI) or beam horizontal irradiance (BHI), shortwave (SW) diffuse, longwave (LW)) or the ones of the cloud cover can be used as input data.

The choice for user to select different data as input highlights the ability and the flexibility of ENVI-met to adapt to the different methods of measurements. Nevertheless, a formatting is necessary for the user measurements to match the data structure expected by ENVI-met.

Table 4.1.: Input Data Format from Coma-separated Values

Data	Date	Time	SW Direct / Low Clouds	SW Diffuse / Medium Clouds	LW / High Clouds	Absolute Temperature	Relative Humidity	Wind Speed	Wind Direction	Precipitation
Format	[DD.MM.YYYY]	[hh:mm:ss]	$[\mathrm{W} \cdot \mathrm{m}^{-2}]$ / [0-8]	$[\mathrm{W} \cdot \mathrm{m}^{-2}]$ / [0-8]	$[\mathrm{W} \cdot \mathrm{m}^{-2}]$ / [0-8]	[K]	[%]	$[\mathrm{m} \cdot \mathrm{s}^{-1}]$	[°]	[mm]

4.1.2 *Process to Meet the ENVI-met Input Data Format*

As aforementioned, the ENVI-met input data follow a structure in terms of physical quantities that can be provided to the simulation core. In addition, the time step for the input data is set: 30 minutes. This time step may not match with the data acquisition frequency, which requires them to be adjusted.

The measurements used in the presented work have been carried out in the framework of the project RESSOURCES (1.1.2.2 on page 6). Plenty of sensors are installed on both of the prototypes, including pyranometers, thermocouples and anemometers. The weather stations provide information on the local weather conditions, including the local temperature or humidity.

Regarding the solar radiation measurements, two sensors are installed. They are able to measure the total and the direct SW radiation, respectively. Then, the diffuse part of the solar radiation has to be calculated from these two measurements, with the following equation:

$$\begin{aligned} Q_{sw_{tot}} &= Q_{sw_{dir}} + Q_{sw_{diff}} \\ \Leftrightarrow Q_{sw_{diff}} &= Q_{sw_{tot}} - Q_{sw_{dir}} \end{aligned} \tag{4.1}$$

where $Q_{sw_{dir}}$ and $Q_{sw_{diff}}$ are the direct and the diffuse components of the total SW radiation $Q_{sw_{tot}}$, respectively. As the radiation is measured horizontally in both cases, the direct SW radiation is the BHI.

A second adjustment is necessary to use the measurements carried out on the prototypes of the RESSOURCES project. Indeed, the measurements where carried out every minute. To match the ENVI-met input data structures, the measurements are averaged over a 30-minute period.

4.2 OUTPUT DATA FORMATTING

The results of the simulations carried out with ENVI-met are intended to be visualized with Leonardo. The way in which the output data are sorted is discussed first, prior to detailing the new developed format used to ease the use of the simulations output in the evaluation of the PV potential of buildings' facades.

4.2.1 *ENVI-met Format*

For every time step, specified by the user, ENVI-met writes output files on the disk. In general, ENVI-met output files are found in pairs (Bruse and the ENVI-met team, 2020):

1. An EDX file;
2. An EDT file.

The EDX files contain the metadata and take advantage of the ENVI-met markup language (EML), which is a XML-based self-describing file format. They contain information on how to read the associated EDT file. The binary files follow the Intel Float format, according to the IEEE Standard 754. Thus, each packet of information is represented by four bytes. Complete information on how to read the EDT binary files is given on the ENVI-met official website: https://envi-met.info/doku.php?id=filereference:edx_edi.

At the time of writing, the output files are stored in eleven folders:

1. atmosphere;
2. buildings;
3. inflow;
4. log;
5. pollutants;
6. radiation;
7. receptors;
8. soil;
9. solar access;
10. surface;
11. vegetation.

These folders are intended to store output data and make them easy to visualize with Leonardo, according to the considered phenomenon. However, this data architecture has drawbacks. Indeed, some data are relevant for different phenomena. For example, the SW radiation received on the horizontal plan for each cell can be found in several folders: atmosphere, buildings, receptors (if any) and radiation.

Regarding the way in which the data are stored, it was not suitable for this work. Indeed, Leonardo is not able to extract data for several elements of a facade in a time series. It represents a lack in the evaluation of the PV potential of buildings facades over time. In addition, information are stored for every cell of the modeled domain, without any regard for the nature of the cell. Thus, where there is no building, the building surface temperature is stored as -999. In a classical modeled domain, the amount of buildings' cells do not exceed 10 %. Thus, a huge amount of irrelevant information is stored and makes reading a slow process. Then, a new output format was needed to be able to extract time series for several facade elements in a single file reading.

4.2.2 *Developed Format*

The main goal of the presented work is to evaluate the PV potential of buildings' facades, taking into consideration the local microclimate. This potential is usually expressed in terms of energy. However, the knowledge of instantaneous producible power is necessary to consider energy injection in a local grid, such as a smart-grid (Calderon et al., 2018). Taking into consideration the intermittency requires small time steps for ENVI-met outputs. Thus, results are stored every five minutes, which is the smallest available time step. As a disadvantage, recording outputs every five minutes increases dramatically the amount of data stored and read.

The first target of the developed output format is to reduce the amount of data to read, by removing useless ones. In the case of the evaluation of the PV potential of buildings' facades these data are the values -999, which represent, for example, the building's facades temperature for the cells where there is no building. As abovementioned, it represents a major portion of the stored data.

The first value added in the developed output format is to store a list of the spatial coordinates, which are common to all the output variables detailed in the previous section. In order to reduce the amount of stored data, the spatial coordinates have to be stored once and to stay accessible for every kind of variable. This highlights the need of a format based on a relational database. Indeed, the store of the spatial coordinates makes it possible to remove the useless data without loss of information.

The second value added is the reduction in the number of files to read. Indeed, the relational database format makes it possible to store values for the same cell at multiple time points, distinguishing them by time indices.

The final output format is represented in figure 4.1 on page 79. Only four tables are represented, but the same process could be extended to the other output folders, such as radiation or vegetation. The *Spatial dimensions* and *Datetimes* are the tables used to store the spatial coordinates and datetimes to reduce both the amount of data per file and the amount of files. The format presented here has proved its efficiency by reducing the size of the output files from several gigabytes for a typical simulation to a few hundreds of megabytes, which represents a reduction in the order of 80 % to 90 %.

This format takes advantage of the entity-relationship models for handling huge amounts of data. The selected database management system (DBMS) is SQLite. Unlike other widely used DBMS, such as MySQL or PostgreSQL, SQLite is not based on a client-server system, which makes it easier for users to implement and handle.

The developed format offers a new framework for analyzing the ENVI-met simulation outputs. This could be used with almost any programming language. Nonetheless, R has been selected for its ability to handle large quantities of data. These data are used as input data for the PV power generation models, detailed in the following.

The developed output format can also be used in other frameworks. Indeed, some building professionals are not used to work with databases or programming languages. A R package *REnviMET* has been developed to resolve the issue of the inability of Leonardo to help the user to analyze quantitatively the simulation outputs. Indeed, the extraction of a time series of the evaluation of the mean surface temperature of a building is complicated to accomplish with Leonardo. To help users in their analysis, *REnviMET* offers the possibility to convert the binary output files into readable and widely used formats, such as `.csv` or `.xlsx`. The complete documentation of the package is contained in appendix chapter D on page XIII.

4.3 SIMULATION OUTPUT DATA AS INPUT DATA FOR THE PV POWER GENERATION MODEL

As seen in section 3.3 on page 52, the PV power generation models require, besides the PV module electrical characteristics, two weather data as input: the irradiance level and the surface temperature. These data are part of the physical values assessed by ENVI-met, as highlighted in figure 4.1 on the next page. In this case, the building's surface temperature is considered to be representative of that of the PV cells. Thus, the PV power generation model can be applied with the chaining presented in figure 1.8 on page 13.

The output format presented in the previous section makes it possible to assess the PV potential of each considered cell for every time step. Indeed, the surface temperature and the irradiance level are calculated for every cell at every time step. Thus, time series of the PV potential of buildings' facades can be worked out. For a 24-hour simulation with a time step of five minutes, it represents 289 recordings for each considered cell, which is a huge amount of data. For this reason, R has been selected for the analysis of the data because of its ability to handle huge data sets.

The graphical representation of the analyzed data plays an important part in the communication of information. This was a major reason for adopting the R language for the work presented here. Indeed, R allows the creation of clean, elegant and efficient graphics thanks to the package *ggplot2*. Its efficiency is based on the grammar of graphics. Other languages provide other packages which are able to create efficient graphics as well. Nevertheless, combined use of *ggplot2* and *tikzDevice* packages allows to create homogeneous graphics, which integrate perfectly with the text compiled with LaTeX. The perspective of writing this thesis dissertation was taken into account when setting up this framework.

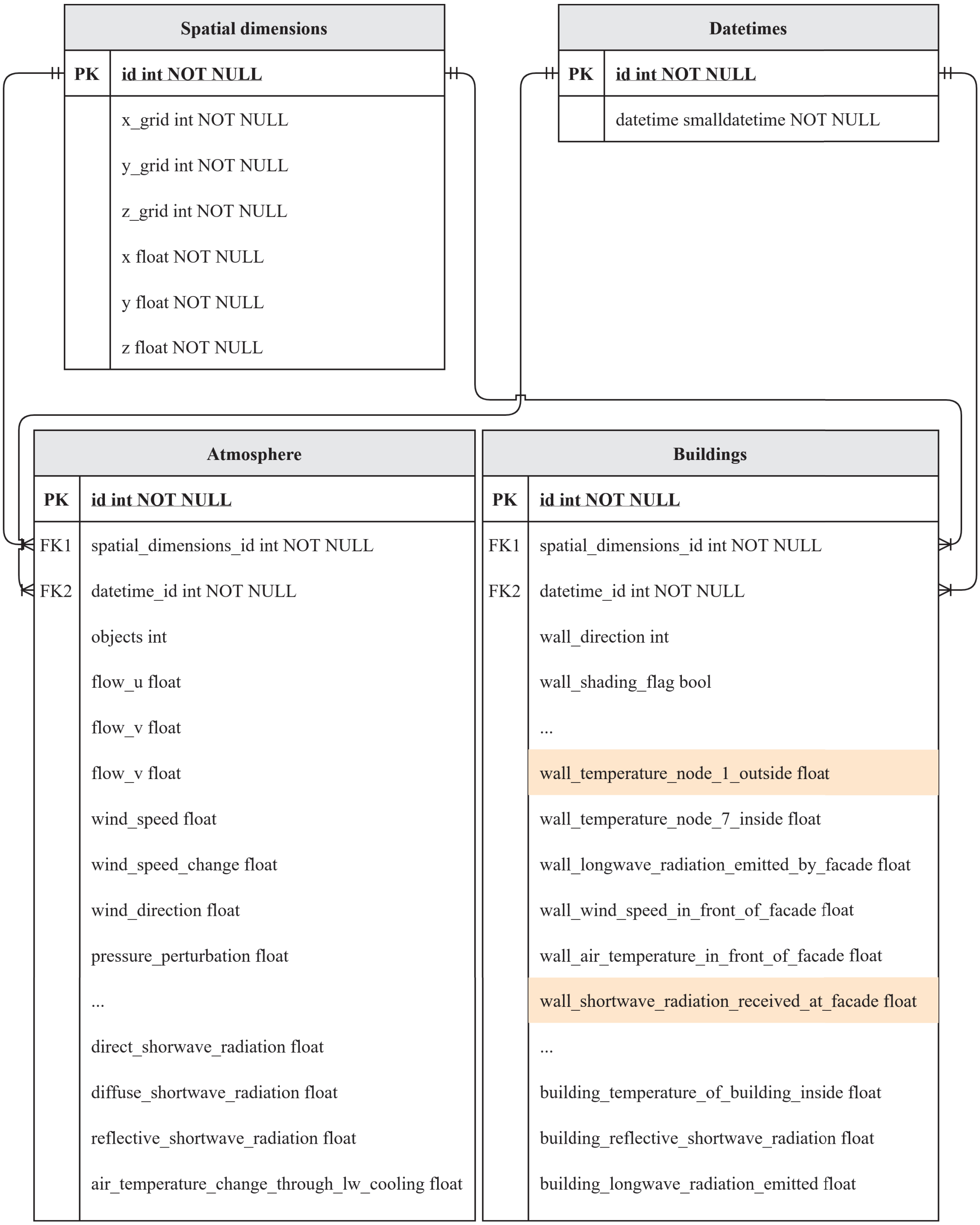

Figure 4.1.: Entity Relationship Diagram for the ENVI-met Output

Accurate simulation of the urban microclimate (UMC) using ENVI-met requires compliance with the data entry format. Since the latter is based on typical weather data, it is often slightly different from the available measured data. A rearrangement of the latter is therefore a first step necessary for the use of results from measurements as input for simulations. Nevertheless, this preliminary work makes it possible to take into account the conditions specific to the simulated neighborhood (unlike typical weather data), which increases the precision and reliability of the results obtained.

Regarding the format of the output data, the one developed during this work has proven its advantage over the format used by ENVI-met, within the framework of the evaluation of the PV potential of buildings. Indeed, it makes it possible to contain the same data as the initial format, while occupying approximately 10 times less space on the hard disk. This reduction in the quantity of data to be read makes it possible to consider carrying out temporal studies on large surfaces (here, building facades), and not only on isolated cells.

REFERENCES RELATED TO THE NUMERICAL DEVELOPMENTS

Bruse, M., & the ENVI-met team. (2020). ENVI-met Output Files [Online; accessed 17-October-2020]. (Cited on page 75).

Calderon, F., Anvari-Moghaddam, A., Badosa, J., Guerrero, J., Vasquez, J. C., Migan, A., & Bourdin, V. (2018). *Dealing with Uncertainty in PV-Powered Microgrids: An Optimal Corrective Approach.* (Cited on page 76).

5

INDEPENDENT STUDIES OF RESOLUTION METHODS AND PHENOMENA TAKEN INTO CONSIDERATION BY ENVI-MET

> *When the Sun disappears,*
> *we see its greatness.*
>
> Seneca

ENVI-met is software including a large number of models, aiming to represent as faithfully as possible the various phenomena relating to the urban context. Concerning the evaluation of the photovoltaic (PV) potential of building facades, two main families of phenomena play an essential role: radiative and aeraulic models. The following chapter aims to position the different models of ENVI-met in order to reveal their strengths as well as their limits.

The aeraulic model is positioned using a comparison between numerical results and experimental data. This study aims to highlight the ability of ENVI-put to model air flow in urban areas, despite the modeling assumptions introduced in order to limit the computation cost. Regarding the radiative model, a comparison between the results obtained with two resolution methods proposed by ENVI-met is carried out. This study aims both to highlight the influence of the choice of the resolution method on the results obtained, as well as the improvements brought by recent developments of this software. Finally, the influence of taking wind velocity into account on the PV production potential is studied, through a parametric study carried out on a theoretical district.

Finally, a comparison is made between the results obtained using two models of PV production. This study aims to demonstrate, through a real case, the importance of the choice of the production model on the evaluation of its potential.

5.1 POSITIONING OF THE ENVI-MET MODELS

5.1.1 *ENVI-met Airflow Model: Results Obtained by Following the Best Practice Guidelines*

5.1.1.1 *Best Practice Guidelines Reminder*

A first approach to evaluate the aerodynamics model of ENVI-met has been carried out following the guidelines. Firstly, these guidelines are presented before detailing the studied configurations. As a final step, a discussion about the application of the guidelines with ENVI-met is held. The main goal of the following is not to pinpoint the weaknesses of ENVI-met to faithfully reproduce all to turbulent phenomena. Indeed, the required compromise in terms of computational cost in order to allow the study of a large spatial area, symbolized by the use of Reynolds-averaged Navier-Stokes (RANS) methods, as well as the typical spatial resolution, used in ENVI-met, of the order of one meter, do not make it possible to represent turbulent phenomena on a small spatial scale. However, to the best of my knowledge, no evaluation of the ENVI-met aeraulic model, aginst measurements carried out under controlled conditions, has been referenced so far. This is a first step in the implementation of the integrated methodology for the assessment of PV potential on a city scale.

The positioning of the ENVI-met airflow model is carried out with a comparison between numerical results and experimental data. The experimetal data are from measurements made in the Blasius wind tunnel in Hambourg University (see in appendix, figure A.1 on page II). This wind tunnel is a small conventional type

Table 5.1.: Spatial Dimensions of the Wind Tunnel and the ENVI-met Modeled Domain

	Wind Tunnel	ENVI-met
Domain of Calculation / Measurement		
Width	1.5 m	300 m
Height	1.0 m	200 m
Depth	4.0 m	800 m
Buildings		
Width	150 mm	30 m
Height	125 mm	25 m
Depth	100 mm	20 m

boundary layer wind-tunnel whose test section is 4 m long (x-axis), 1.5 m wide (y-axis) and 1 m high (z-axis). The domain simulated with ENVI-met is in accordance with the spatial dimensions of the wind tunnel. The spatial dimensions of the wind tunnel and the modeled domain are presented in table 5.1. They include the model scale of 1:200.

Two main indicators have been used to ensure that there was no numerical bias induced by the modeled domain. These are:

1. the blockage ratio;
2. the spacing between the obstacle and the domain borders.

The blockage ratio (BR) is the proportion between the free flow area and the domain area. It can be a global BR or a directional one. Their definition are given in equation (5.1) to equation (5.3) on the next page, as well as their illustration in figure 5.1 on the facing page. To ensure not to get any numerical bias in the results, directional BR should be between 17 % to 22 %. It ensures a global BR between 3 % and 5 %.

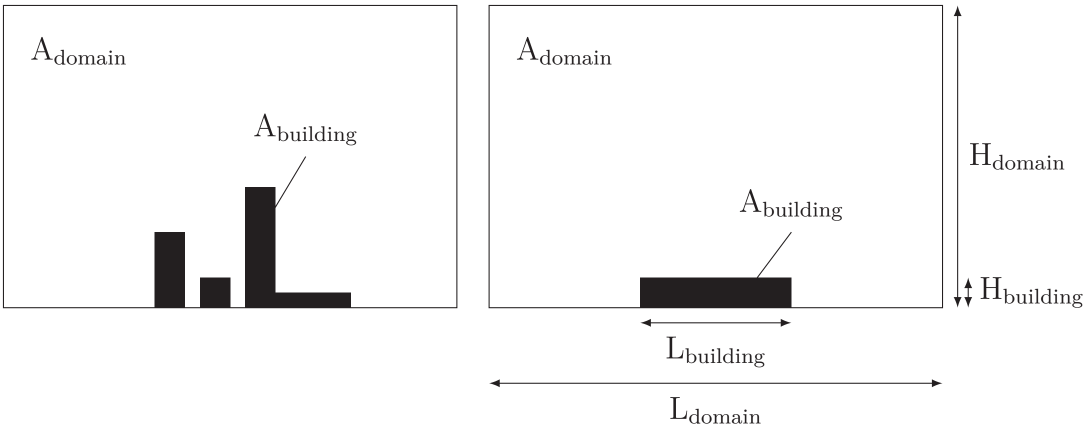

(a) Maximum Allowed Blockage Ratio (b) Directional Blockage Ratio

Figure 5.1.: Blockage Ratios

$$BR = \frac{A_{building}}{A_{domain}} = \frac{L_{building} \times H_{building}}{L_{domain} \times H_{domain}} < 3 - 5\ \% \tag{5.1}$$

$$BR_L = \frac{L_{building}}{L_{domain}} < 17 - 22\ \% \tag{5.2}$$

$$BR_H = \frac{H_{building}}{H_{domain}} < 17 - 22\ \% \tag{5.3}$$

Figure 5.2 on the next page presents the recommended distances between the obstacle and the domain borders. This three dimensional sketch matches with the BR recommended values for the cross section of the flow. In addition, it highlights the need of free space for the flow upstream and downstream of the obstacle. Due to disturbances of the flow around the obstacle, flow features can be generated and need space to be dissipated. An illustration of those features are given in figure 5.3 on page 89. Thus, numerical errors can be introduced if the spacing between the obstacle and the domain border is insufficient. This explains the large downstream area in figure 5.2 on the next page.

Regarding the flow features presented in figure 5.3 on page 89, they can be grouped into four regions, according to the associated phenomena:

1. Upstream recirculation;

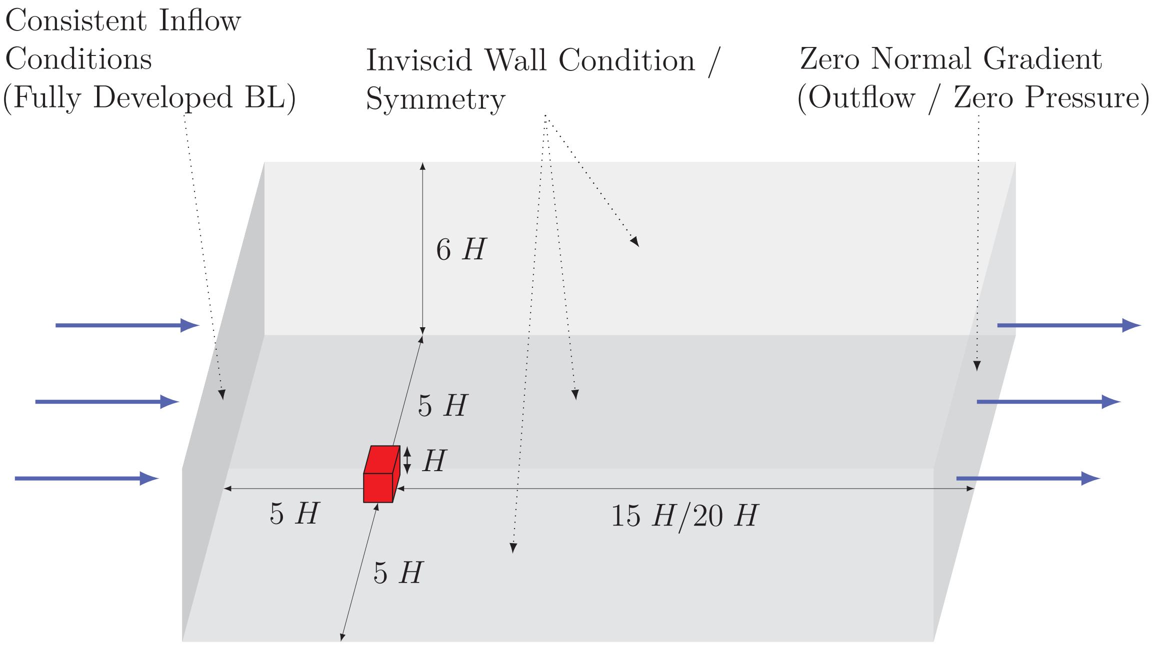

Figure 5.2.: 3D Representation of the Best Practice Guidelines for Computational Fluid Dynamics

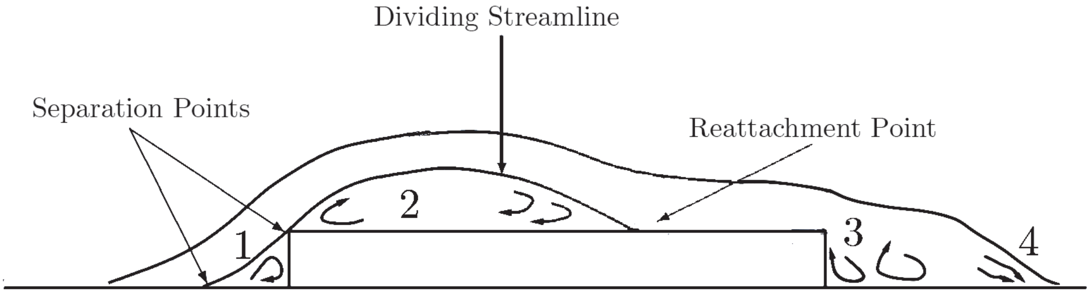

Figure 5.3.: Flow Features Over a Cubicoidal Obstacle

2. Above the obstacle recirculation;
3. Downstream recirculation;
4. Flow reestablishment.

These guidelines are applied in the two cases of study in the following section.

5.1.1.2 *Studied Cases*

Two standard cases are considered to evaluate the performance of the airflow model of ENVI-met:

1. An isolated cube put in the center of a wind-tunnel;
2. A finite array of cubes put in the center of a wind-tunnel.

Those two standard cases makes it possible to evaluate the accuracy of the ENVI-met airflow model in a simple case and in a case closer to an urban morphology.

ISOLATED CUBE

The first studied case is composed of a single rectangular obstacle in the middle of the domain. A 3D representation of this configuration is given in figure 5.4 on the next page. This configuration makes it possible for the flow structure to be freely developed around the cubicoidal building.

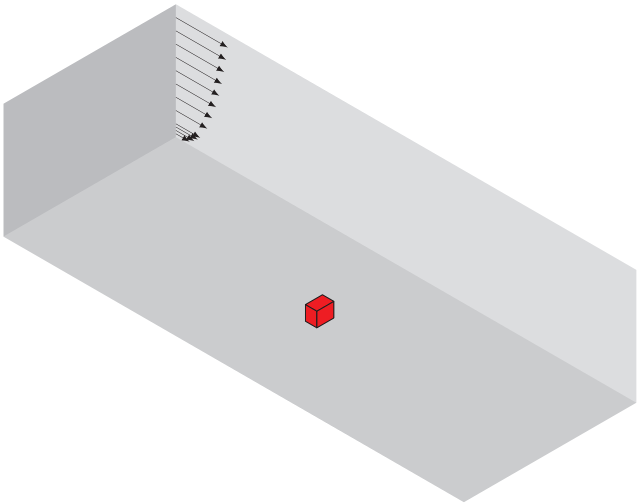

Figure 5.4.: 3D Representation of the Isolated Cube in the Blasius Wind-Tunnel

Verification of Compliance with the Best Practice Guidelines Targets

The figure 5.5 on the facing page shows the 2D representation of the isolated obstacle in the domain, as well as the considered dimensions. These dimensions allow to calculate the BR in this configuration. They are given in table 5.2 on page 92. With values of 1.25 %, 10 % and 12.5 % for the global, the horizontal and the vertical BR, respectively, the best practice guidelines in terms of blockage ratios are perfectly followed.

Regarding the spacing between the obstacle and the domain borders, four distances have to be checked: the distance between the building and the borders in the cross-section, the up- and downstream free distances and the height of the modeled domain. Their values are given in table 5.3 on page 92. As with the BRs, the targets for the spacings with the domain borders are respected.

The BRs and the spacings with the domain borders recommended by the best practice guidelines being respected, it ensures that no numerical bias is introduced by the modeled area. Thus, the differences between the numerical results and the experimental data are mainly attributable to the airflow model of resolution; the velocity measurements being carried out with laser Doppler vibrometer, the measured values are ponctual and still contain uncertainties and imprecision (especially regarding the recirculation zones).

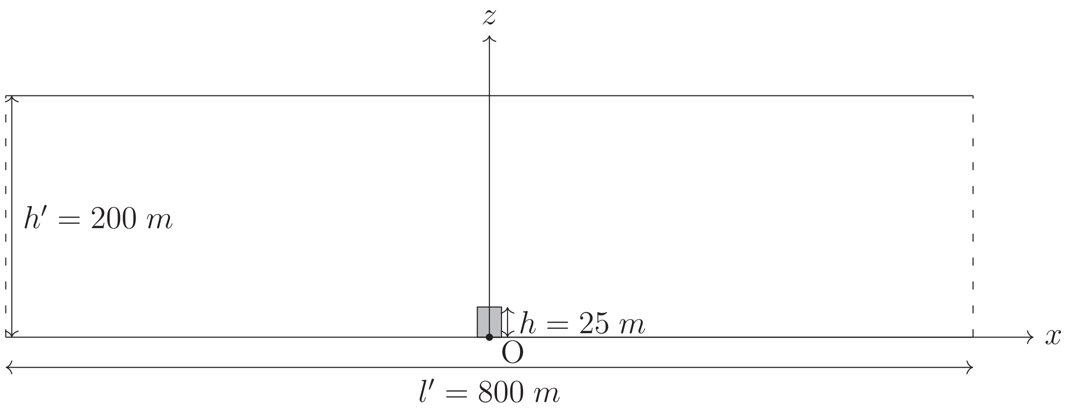

(a) Side View

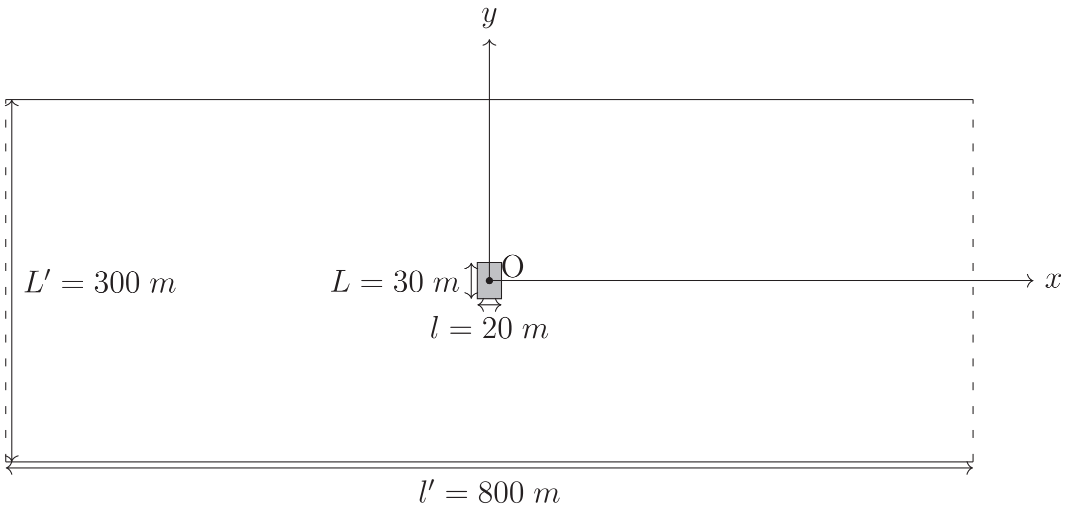

(b) Top View

Figure 5.5.: Simulation Setup for a Single Cube

Table 5.2.: Blockage Ratios for the Isolated Cube Case Study

BR	1.25 %
BR_L	10.00 %
BR_H	12.50 %

Table 5.3.: Best Practice Guidelines Checks for the Isolated Cube Case Study

	Actual Value	Ratio to the Obstacle Height	Best Practice Guidelines Target
Distance in cross-section	285 m	11.4 H	5 H
Upstream free distance	390 m	15.6 H	5 H
Downstream free distance	390 m	15.6 H	15 H
Height of the modeled domain	200 m	8 H	6 H

Comparison Between the Numerical Results and the Experimental Data

As shown in figure 5.3 on page 89, flow structures can develop around the obstacle. They can occur in every spatial directions. Thus, two plans of measurements are used to visualize the flow structures due to the cube in the wind-tunnel :

1. a horizontal plan at a height equal to one half of the building height: plan (xOy) with $z = 0.5\ H$ (see figure 5.6 on the facing page);
2. a vertical plan, intersecting the middle of the wind-tunnel: (xOz) with $y = 0$ (see figure 5.7 on page 96).

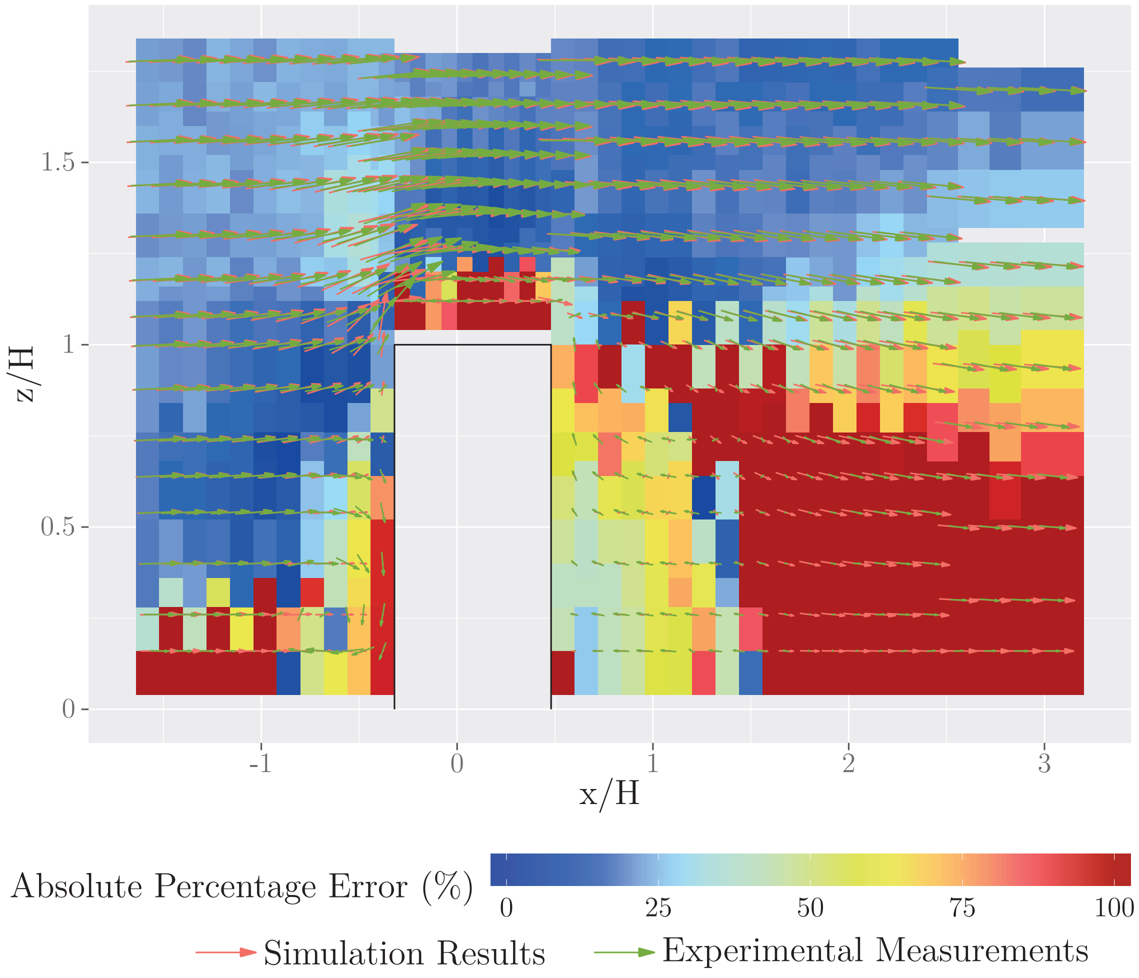

Figure 5.6.: Comparison of Vertical Profiles, Experimental and Numerical, for the Isolated Cube

In figure 5.6 on the preceding page, the measured values are plotted in green and the numerical results are in red. The background color highlights the absolute percentage error between the numerical results and the experimental data calculated as follows:

$$APE = \left| \frac{X_{exp} - X_{sim}}{X_{exp}} \right| \tag{5.4}$$

The mean values of the absolute percentage error (APE), the mean absolute percentage error (MAPE), are given in table 5.4 on the next page. They are given according to the studied region.

The large part in blue, presenting a MAPE of 17.40 %, highlights the accuracy of the numerical model for the fully developed and slightly disrupted flows. The APE sharply increases in the regions where turbulence-related structures develop. Three different regions appear in red in figure 5.6 on the preceding page, corresponding to the regions numbered 1, 2 and 3 in figure 5.3 on page 89.

The first region, corresponding to the upstream recirculation, is not well described by the ENVI-met model. Indeed, the recirculation zone that appears in the measurements is not reproduced in the simulation results. This lead to a MAPE of 70.12 % for this region.

Regarding the second region, where the flows separate at the sharp corners, the perturbations are taken into consideration and reproduced by the model. However, the magnitude of these perturbations is not as high as that of the measurements. Due to the spatial resolution, the recirculation close to the buildig's surface is not reproduced, as shown by the value of 173.06 % for the MAPE. This may question the tha way in which ENVI-met evaluates the air flow very close to the buildings.

Finally, the region after the obstacle presents a double reading. The cavity zone, the region number 3 in figure 5.3 on page 89, is reproduced quite acccurately (appears in yellowish in figure 5.6 on the previous page). Thus, the MAPE for this region is moderatly high (53.01 %). Regarding the region where the flow returns to undisturbed, the simulated wind velocity is much greater than the measured one. This is especially true near the ground surface and lead to a sharp increase of the MAPE which raises 293.53 %. As with the region above the building, it questions the proximity approximation of the ENVI-met airflow model.

The horizontal profiles in figure 5.7 on page 96 show the flow structures which have a main horizontal direction. As with the figure 5.6 on the previous page the slightly disturbed regions are accurately modeled by ENVI-met. These regions appear in

Table 5.4.: Mean Absolute Percentage Error for the Regions Around the Isolated Cube in the Vertical Plan

Region	MAPE
Region 1	70.12 %
Region 2	173.06 %
Region 3	53.01 %
Region 4	293.53 %
Slightly Disturbed Region	17.40 %
Overall Domain	75.58 %

blueish and have a low MAPE. The other regions of interest have a similar behavior as that observed in the vertical plan.

The lower value of MAPE in the horizontal plan (at a height equals to a half of the building's height) also highlights the less accurate near the ground surface. Indeed, the most of the areas that are less precisely modeled are below the building's top and nearly all the first cells in the vertical dimensions have an MAPE value exceeding 100 %. This demonstrates the need for an enhancement in the hypothesis of the proximity approximation.

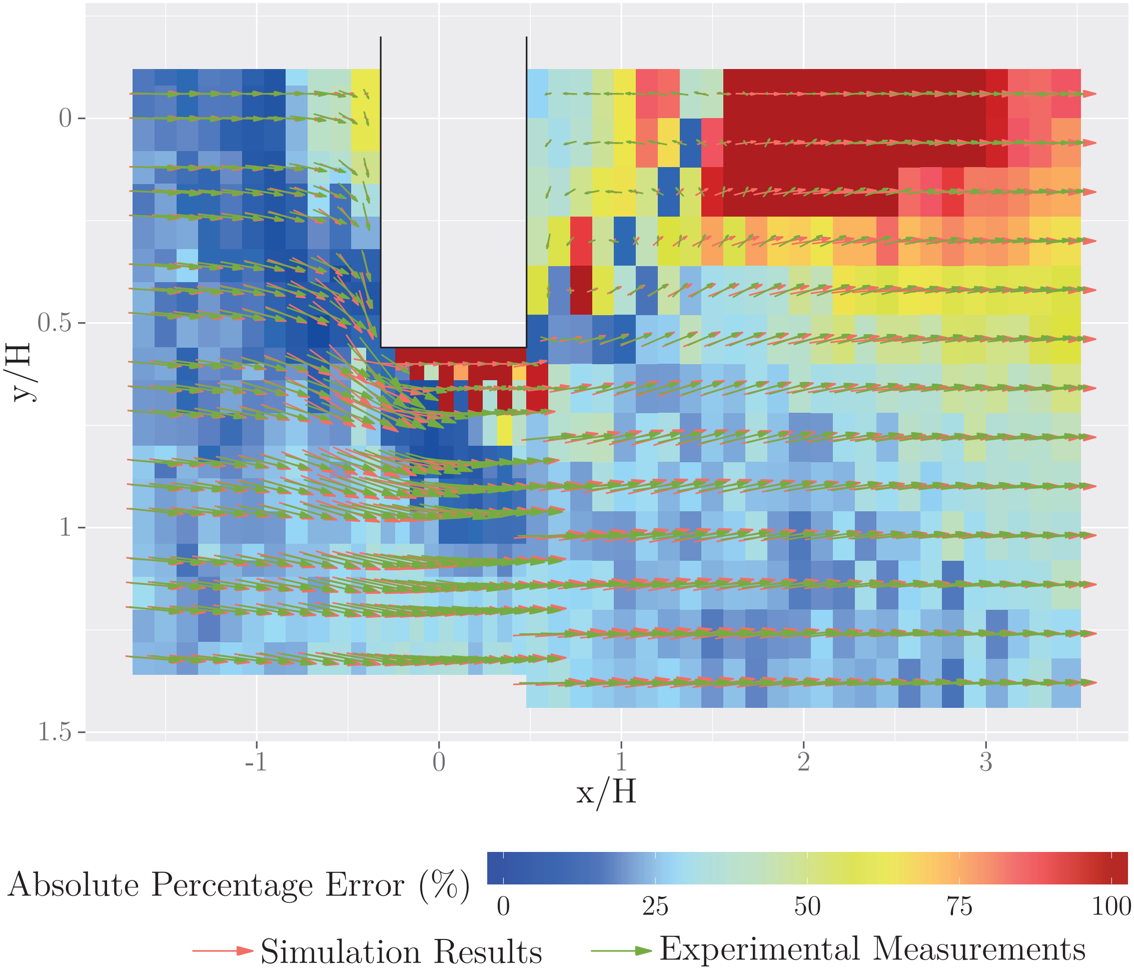

Figure 5.7.: Comparison of Horizontal Profiles, Experimental and Numerical, for the Isolated Cube

Table 5.5.: Mean Absolute Percentage Error for the Regions Around the Isolated Cube in the Horizontal Plan

Region	MAPE
Region 1	66.85 %
Region 2	197.23 %
Region 3	45.84 %
Region 4	130.53 %
Slightly Disturbed Region	25.50 %
Overall Domain	47.58 %

FINITE ARRAY OF CUBES

An isolated cube is not enough to demonstrate the accuracy of the ENVI-met airflow model. Indeed, while this tool aims to simulate urban micro-climates, such a configuration is not representative of an urban area. Indeed, an urban area is composed of several buildings, located on regular or irregular grids. To overcome this lack, a second configuration is studied, as shown in figure 5.8 on the following page.

Instead of an isolated cube in the middle of the wind-tunnel, an array of cubicoidal buildings is placed. It is composed of 3 rows of 7 buildings, giving a total of 21 buildings. It corresponds to the case study B1-1 of the CEDVAL data sets[1]. The details of this configuration are given in figure 5.9 on page 99. The considered buildings are the same as the one considered in the previous section. The red building is the one where the measurements are carried out.

As for the previous case study, measurements are made according to a horizontal plan at a height equals to a half of the buildings' height (figure 5.10 on page 100). However, instead of a single vertical plan of measurements, four are used. They are at a distance equals to 0, 0.4 H, 0.6 H and H (with H the height of the buildings),

---

[1] CEDVAL stands for Compilation of Experimental Data for Validation of Microscale Dispersion Models

The data are accessible on: https://mi-pub.cen.uni-hamburg.de/index.php?id=432 (last accessed on 16/11/2020)

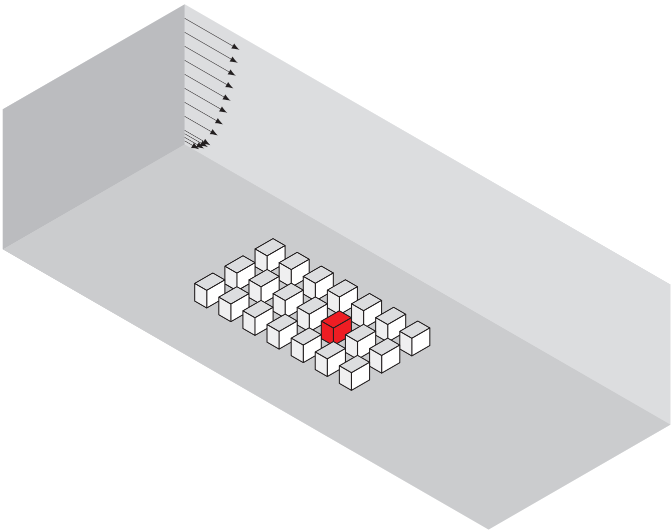

Figure 5.8.: 3D Representation of the Finite Array of Cubes in the Blasius Wind-Tunnel

from the center of the wind-tunnel. The comparison of the wind-speed profiles are given in figure 5.11 on page 102.

The results presented in figure 5.10 on page 100 show a high MAPE, exceeding 100 %. The region of flow recirculation is better predicted as shown in the lower part of the figure. Nevertheless, the MAPE remains quite high with a value of 74.42 %. This highlights the effects of the turbulence of the air flow between the buildings and the non-ability of the ENVI-met model to reproduce these phenomena, which occur at low spatial scales.

The results observed on the horizontal plan of measurements are also to be found in figure 5.11c to figure 5.11d on page 102. Indeed, these plans are parallel to the airflow and located between two rows of buildings. Thus, the magnitude for the wind velocity in these plans and for the heights lower than the buildins' height is overestimated as well.

For the vertical plans of measurements intersecting the buildings, the observed results are closer than that of the isolated building. Indeed, as seen in figure 5.11a and figure 5.11b on page 101, the part above the buidlings is accurately described. The recirculation region between the buildings is less precisely simulated but the MAPEs remain quite low: 59.46 % and 58.61 % for the plans $y = 0$ and $y = \frac{2}{5}\,H$, respectively.

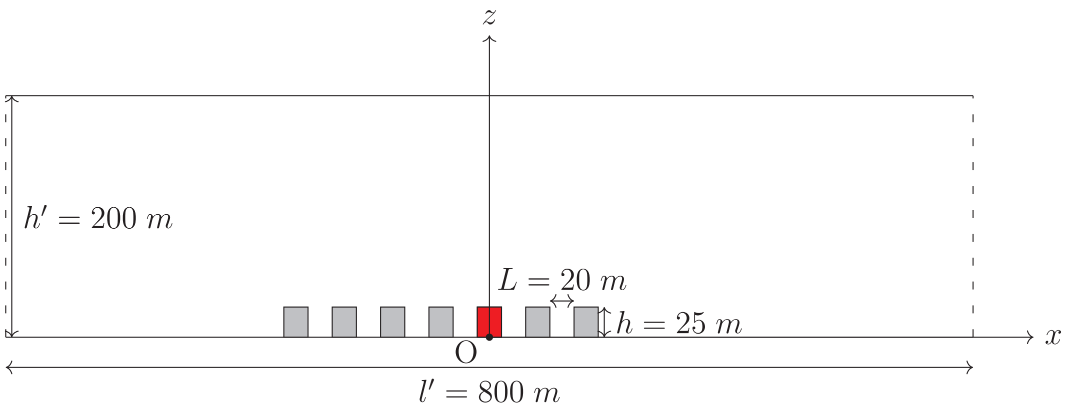

(a) Side View

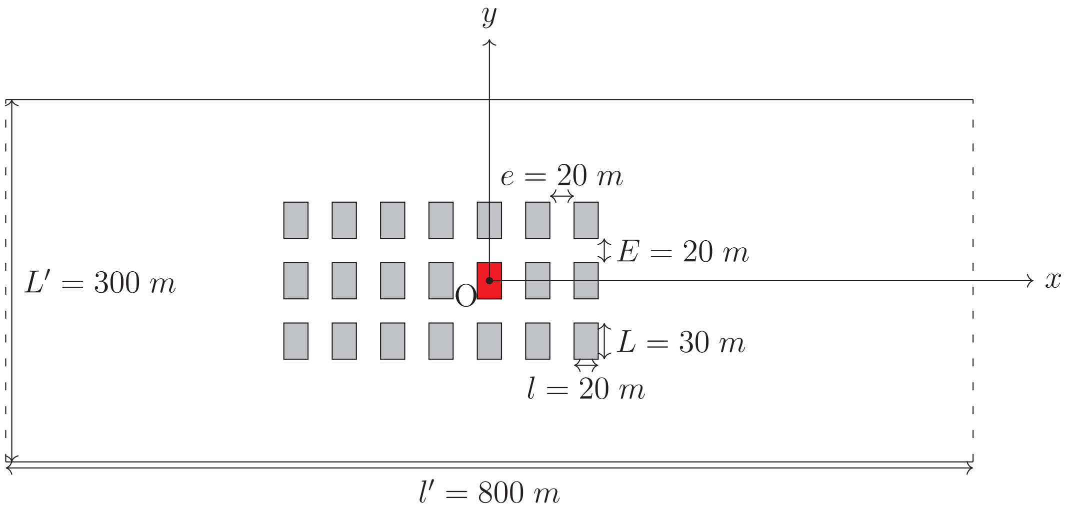

(b) Top View

Figure 5.9.: Simulation Setup for a Finite Array of Cubes

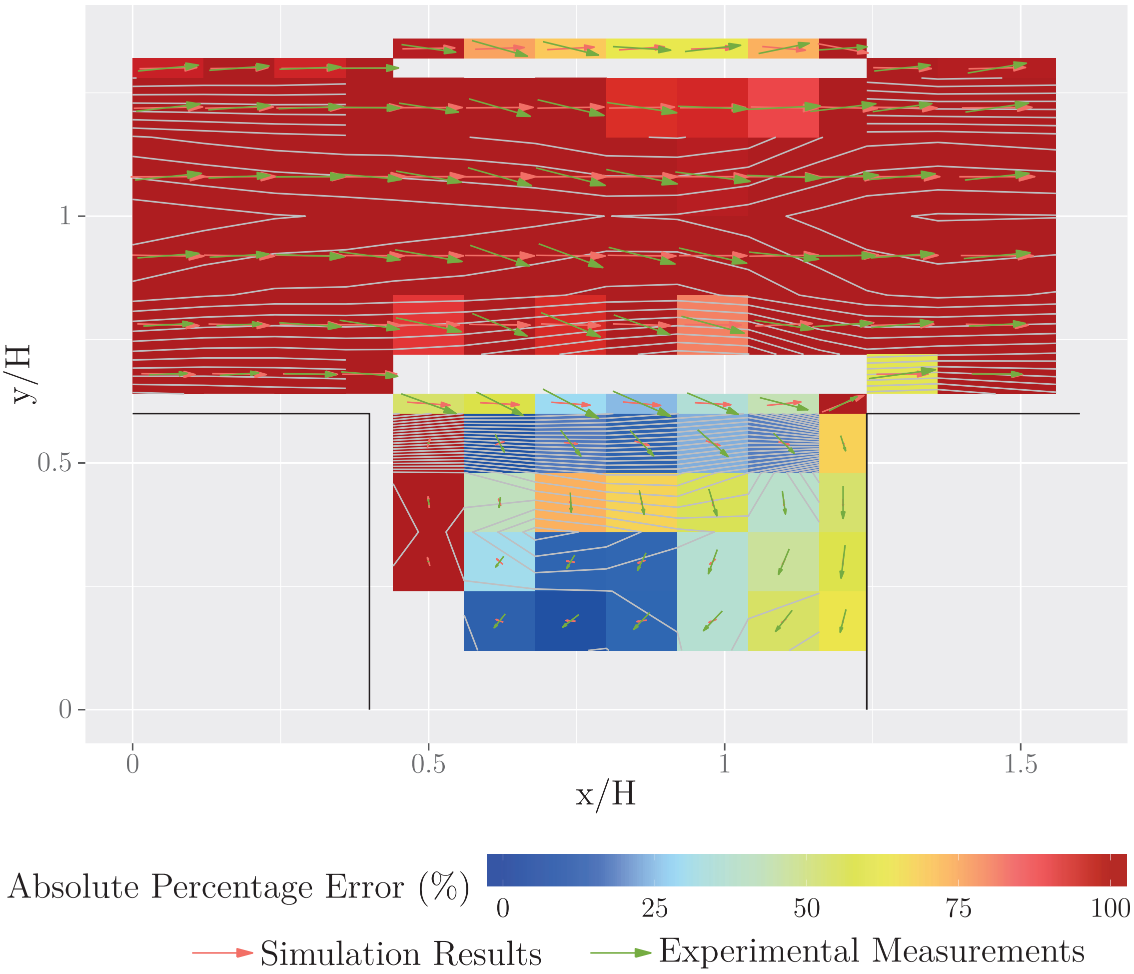

Figure 5.10.: Comparison of Horizontal Profiles, Experimental and Numerical, for the Array of Cubes

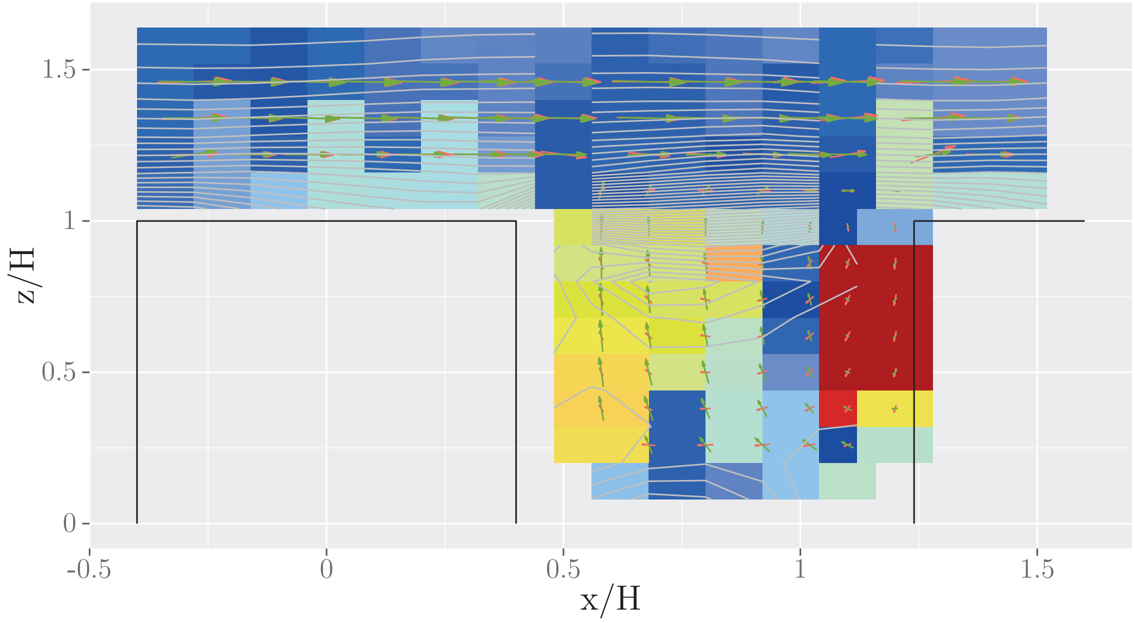

(a) $y = 0$

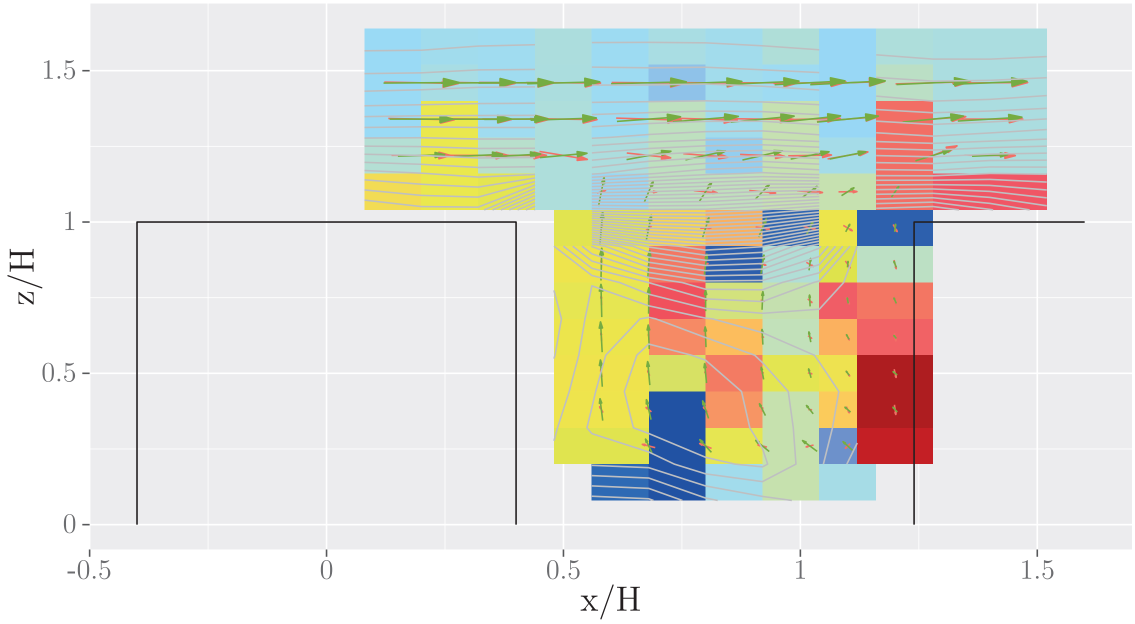

(b) $y = \frac{2}{5}H$

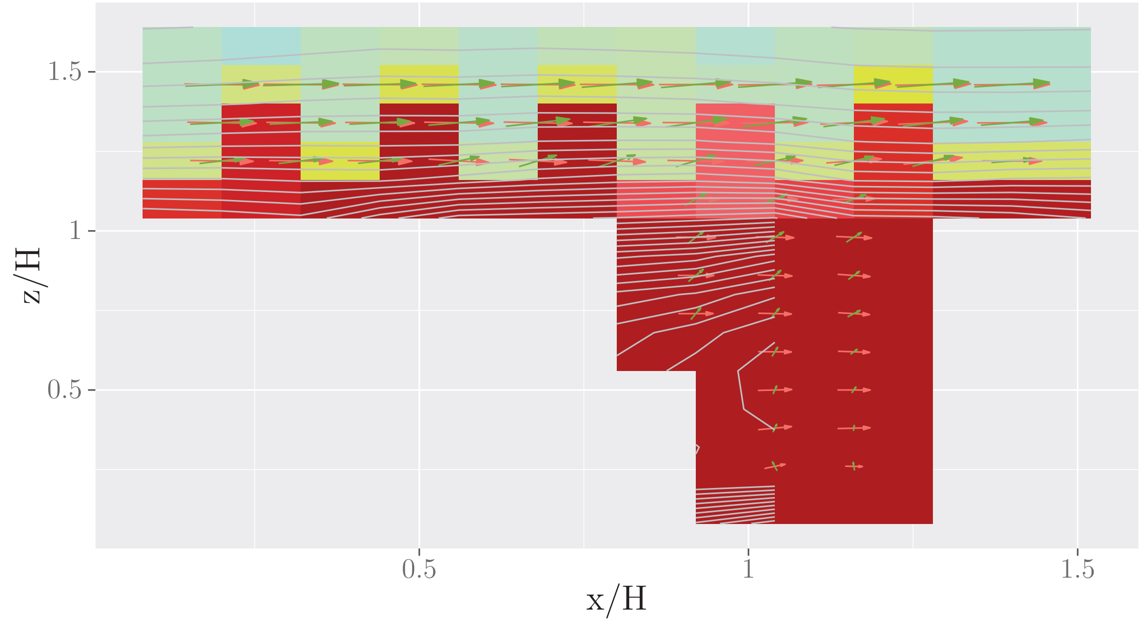

(c) $y = \frac{3}{5}H$

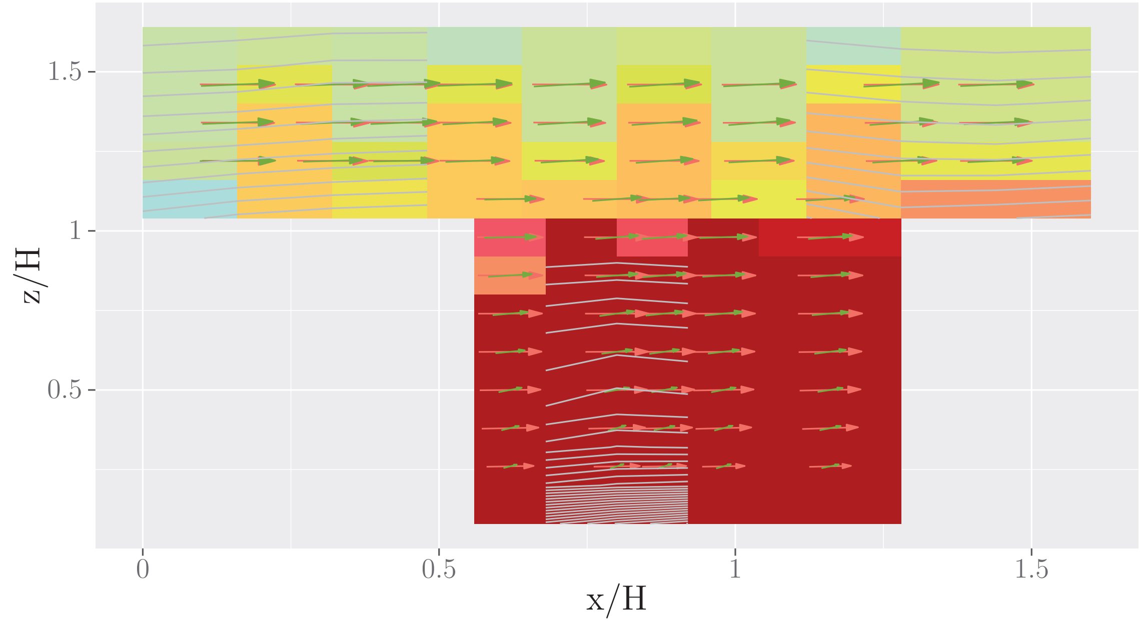

(d) $y = H$

Figure 5.11.: Comparison of Vertical Profiles, Experimental and Numerical, for the Array of Cubes

5.1.2 *Positioning of ENVI-met Radiative Model*

The work presented here has been carried out first in the framework of the ORCHIDEE project, presented in 1.1.2.1 on page 5, aiming at assessing the outdoor thermal comfort with different numerical tools. It has then been expanded to the assessment of the different methods of resolution for the radiative phenomena available in ENVI-met.

5.1.2.1 *Studied District*

The studied area is the Vauban district, located in Saint-Denis, on the Reunion Island (southern hemisphere). Located in the Indian Ocean, the Reunion Island benefits from a tropical climate with a long hours of daylight[2], which can reach 2 524 hours per year. In terms of temperature, Saint-Denis supports a good weather with a slight variation of the temperature over the year. Thus, the minimal temperatures vary between 18 °C in July and August, and 24 °C in February, while the maximal temperature vary from 25 °C in July and August and 30 °C between January and March.

The Vauban district is mainly residential, with just a few commercial buildings. In particular, residential buildings are mostly apartments, the rest being detached houses. All buildings have a height of about 12 m. An overview of the district is given in figure 5.12 on the following page.

Local climates may vary on the Reunion Island depending on the location but since the Vauban district is located near the coastline, it benefits from annual temperatures roughly between 20 °C and 30 °C. Regarding the solar irradiation, the sunniest period lasts from January to March. February 21st, 2017 has been selected for the study performed (and described later) as it presents the advantages of being one of the sunniest days of the year along with the drawbacks of being the warmest one.

---

[2] The annual daylight hours is defined as the number of hours of the year for which direct or non-diffused solar irradiation is of an intensity strictly greater than $120\,\mathrm{W \cdot m^{-2}}$.

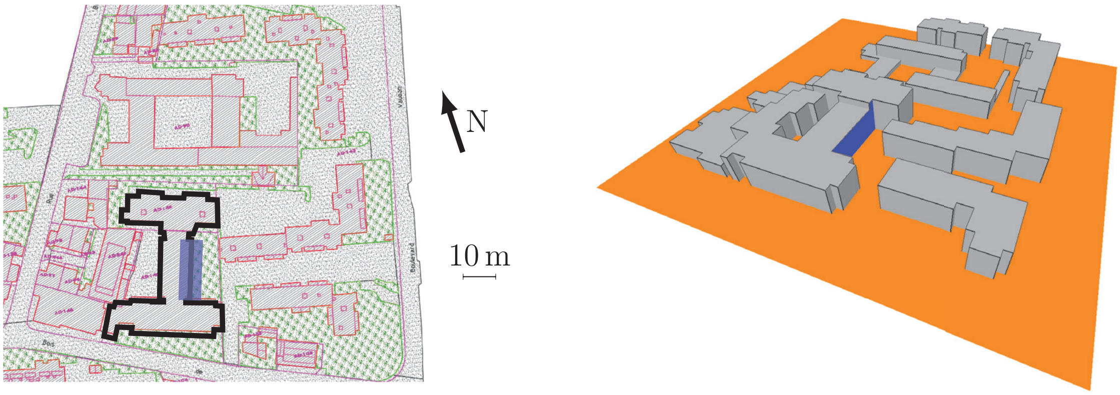

(a) District Area Map

(b) ENVI-met Modeled Domain

Figure 5.12.: District Vauban – Saint-Denis, Reunion Island

5.1.2.2 *Input Data for the Model*

The studied day is February 21st, 2017 which was the hottest and one of the sunniest days of that year on the Reunion Island (figure 5.13a on page 106). This day has been considered to provide with a sufficiently high solar potential for energy production. The weather data used were provided by the nearest meteorological station located in the Saint-Denis airport. Thus, the meteorological conditions are entered in the ENVI-met model, as given in table 5.6 on page 107. There are two reasons to the quite high wind velocity at 10 m height:

- the weather conditions are measured at the airport, which is an open space, located 5 km from the Vauban district;
- Saint-Denis is located on the coast of the Reunion Island.

While these two parameters lead to a high measured wind velocity, these measurements are not strictly representative of the wind velocity in the Vauban district but they were the best source of data at the time of the study.

The roughness length is the height at which the wind velocity theoretically becomes zero. The adjustment factor allows the maximum irradiation value to be set between $500\,\mathrm{W \cdot m^{-2}}$ (adjustment factor: 0.5) and $1\,500\,\mathrm{W \cdot m^{-2}}$ (adjustment factor: 1.5). The cover of clouds is defined on a scale of 8 values. 0 represents a completely clear sky and 8 represents a fully covered sky.
Regarding the solar radiation profile, no on-site measurements were available at the

time of study. Thus, the input profile is based on a theoretical evolution. Nevertheless, even though it introduces a bias in the absolute results reported subsequently, it was not a crucial issue for the project. Indeed, as aformentionned in section 1.1.2.1 on page 5, the goal of the ORCHIDEE project's was to evaluate the results predicted by various urban microclimate (UMC) tools.

The total modeling time was 48 hours. As recommended (Bruse, 2015), the first 24 hours were used to spin up the model in order to get reliable results that would have been influenced by the initialization parameters. Only the last 24 hours were used for the analysis.

Particular focus will be made on the facade outlined in blue on figure 5.12 on the facing page. The interest of this facade lies in the fact it has a direct exposure to sunlight during the first part of the day. However, a small part of the studied wall (16 m high) gets partially shaded by the facing wall (15 m high). Thus, it is possible to evaluate the heterogeneity and time variability of solar irradiation over this facade.

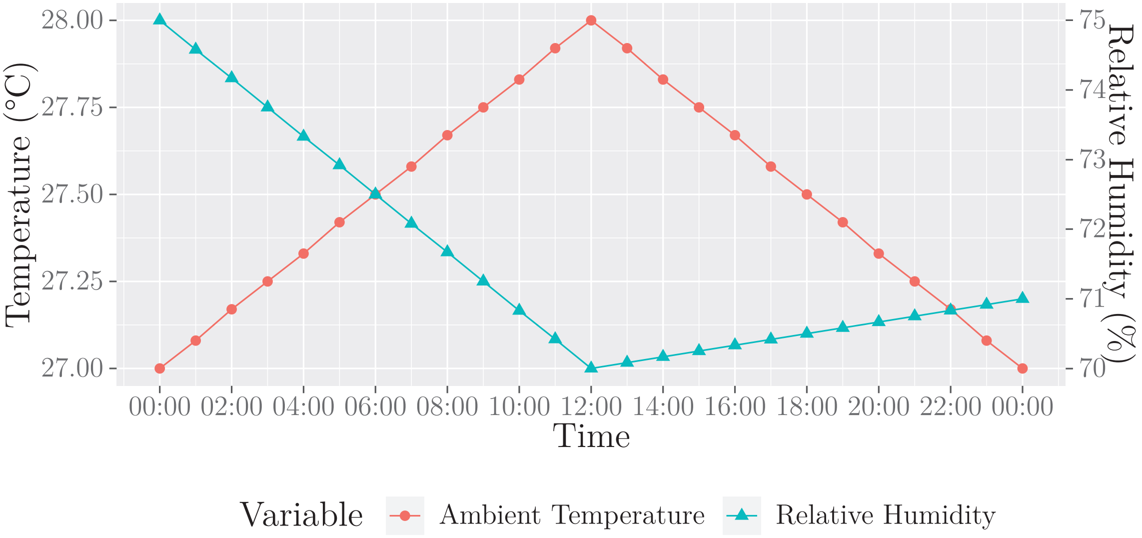

(a) Ambient Temperature and Relative Humidity

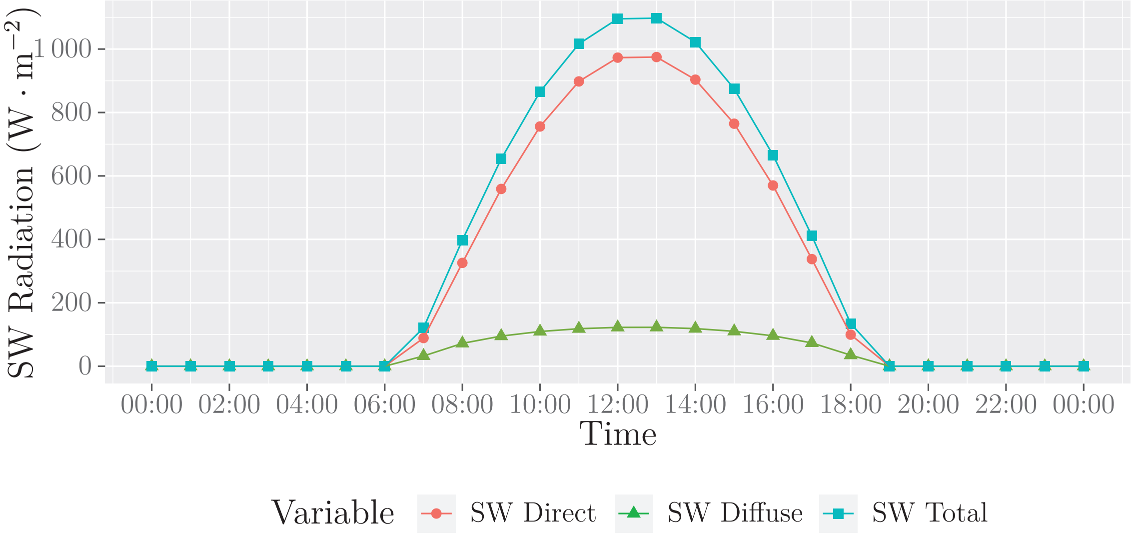

(b) Shortwave Radiation

Figure 5.13.: Evolution of Weather Conditions of the Vauban District on February 21st, 2017

Table 5.6.: Input Configuration Data Applied in ENVI-met for the Vauban District on February 21st, 2017

Position		
Longitude	[°]	55.45
Latitude	[°]	-20.88
Start and Duration of the Model		
Date of Simulation		02/20/2017
Start Time		00:00 am
Total Simulation Time	[h]	48
Initial Meteorological Conditions		
Wind Speed Measured at 10 m Height	$[\mathrm{m} \cdot \mathrm{s}^{-1}]$	5.1
Wind Direction	[°]	45
Roughness Length at Measurement Site	[m]	0.01
Specific Humidity at Calculation Domain Upper Bound (2 500 m)	$[\mathrm{mg} \cdot \mathrm{kg}^{-1}]$	17.4
Relative Humidity at 2 m height	[°]	78
Solar Radiation and Clouds		
Adjustment Factor for Solar Radiation		1.0
Cover of Low Clouds	[octas]	0.0
Cover of Medium Clouds	[octas]	0.0
Cover of High Clouds	[octas]	0.0
Soil Data		
Initial Temperature in All Layers	[K]	1.0
Relative Humidity Upper Layer ([0; -20]cm)	[%]	50
Relative Humidity Middle Layer ([-20; -50]cm)	[%]	60
Relative Humidity Deep Layer (<-50 cm)	[%]	60

5.1.2.3 *Comparison of the Results Obtained with the Indexed View Sphere and the Averaged View Factor Methods*

Two different radiative models are available in ENVI-met :

1. the AVF method;
2. the IVS method.

The indexed view sphere (IVS) method is the most recent one. Its aim is to increase the accuracy of the ENVI-met radiative model by modeling multiple interactions that occur between buildings in urban areas. To do so, it considers the actual state of each element of the facade instead averaged values for incoming shortwave and longwave radiation and reflections (averaged view factor (AVF) method). Thus, the results obtained with the IVS method are be more accurate than the ones obtained with the AVF method (Bruse and the ENVI-met Team, 2020).

Two outputs from ENVI-met are used to calculate the PV power generation on the building facades:

- the outer surface temperature;
- the received radiation.

The double-diode model (see section 3.3.2.2 on page 60) is then applied with the the parameters corresponding to the PV panel (see table 5.7 on page 114).

The calculated surface temperature is considered to be representative of the building integrated photovoltaic (BIPV) panel. Taking into consideration this temperature is crucial to evaluate the PV potential of the facade. Indeed, the higher the PV panel temperature, the lower its efficiency.

Figure 5.14 on page 111 shows the values predicted by ENVI-met with the IVS model in terms of received shortwave (SW) radiation, surface temperature and potential of PV power generation of the east facade (highlighted in blue in figure 5.12 on page 104). The same results obtained under the same conditions with the AVF model are presented in figure 5.15 on page 112. It appears that the overall shape of the results are the same for both of the methods and for the three considered hours.

The three considered hours (08:00 am, 09:00 am and 10:00 pm) are used to illustrate the influence of the Sun position on the solar-related values. The darker spots on the facades are due to the shading induced by the buildings (the facing one for the spot in the center of the facade and the building itself for the darker spot on the right edge).

Although the shape of the results are similar for both of the IVS and AVF methods, the considered method of calculation has an appreciable influence on the evaluation of the PV potential. Thus, the absolute difference between the results obtained with both of the methods has to be highlighted. This difference is defined as follows:

$$X = X_{\mathrm{IVS}} - X_{\mathrm{AVF}} \tag{5.5}$$

As shown in figure 5.16 on page 113, the range of difference between the results predicted by the IVS and the AVF methods exceeds 15 W. It represents almost 20 % of the nominal power of the PV panel. This difference in terms of power generation is attributable to the difference in terms of SW radiation and surface temperature predictions. These are $200\,\mathrm{W} \cdot \mathrm{m}^{-2}$ and 10 °C, respectively.

In terms of spatial heterogeneity, it appears that the AVF method tends to overestimate the PV potential of facade that are not directly facing the Sun. Indeed, as can be seen on figure 5.16c on page 113, the right part of the facade turns to darker colors, which correspond to negative values. On the contrary, the left part has yellowish colors. This observation is particularly true for SW radiation and PV power generation. The predicted surface temperature is then less impacted by the considered method of calculation.

The darker colors (the right part of the facade) highlights that the AVF method tends to overestimate the SW radiation received by shaded facade. On the contrary, the IVS method better renders the influence of the inter-building reflections, as shown with the lighter spots in figure 5.16b on page 113. The latter are due to the reflection of the sunrays on surrounding buildings' facades.

In addition to having an impact on the prediction of the instantaneous values and their spatial heterogeneity, the differences between the results of the two methods have an influence on the overall PV potential of the building facade. Indeed, the choice of the method of calculation may lead to a difference of almost 15 % in terms of energy capacity over the whole day. The difference in terms of predicted PV power generation, hour by hour, is given in table 5.8 on page 115. It appears that except for the very beginning and the very end of the day (07:00 am and 07:00 pm), the AVF method overestimates the PV potential of the building's facade. This overestimation depends on the time of the day. Nonetheless, the predicted PV power generation is particularly overestimated in the afternoon, when the received SW radiation is purely diffuse.

The observed difference in terms of estimation of the PV potential of the building's facade brings to light the importance of the choice of the method of calculation in the evaluation of the solar potential with ENVI-met. In terms of accuracy of the results obtained, the IVS method is to be preferred over the AVF method. Nevertheless, taking into account the computing power that the IVS method requires (especially in terms of amount of RAM), the IVS method can be privileged within the framework of a preparatory work or during studies not focusing on the radiative phenomena.

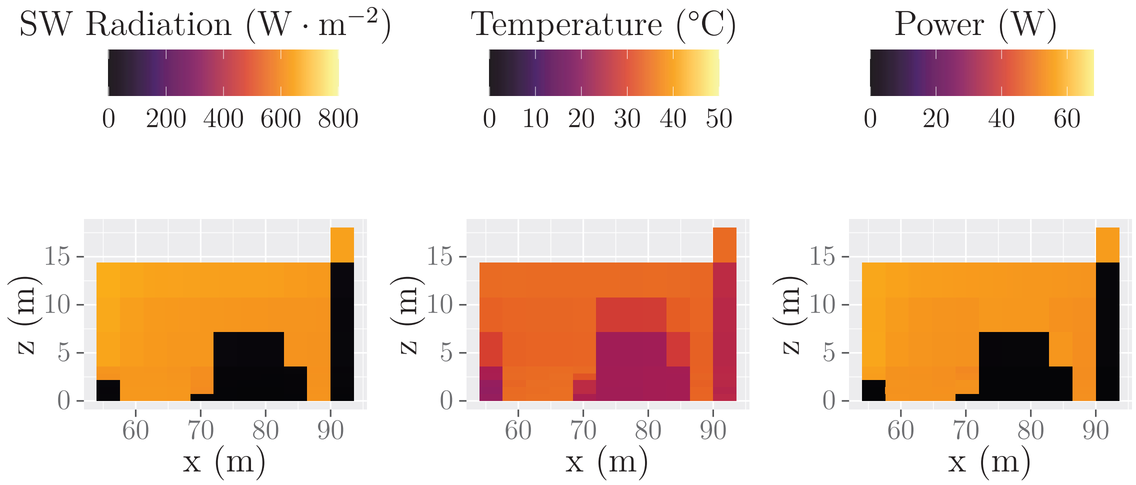

(a) 08:00 am

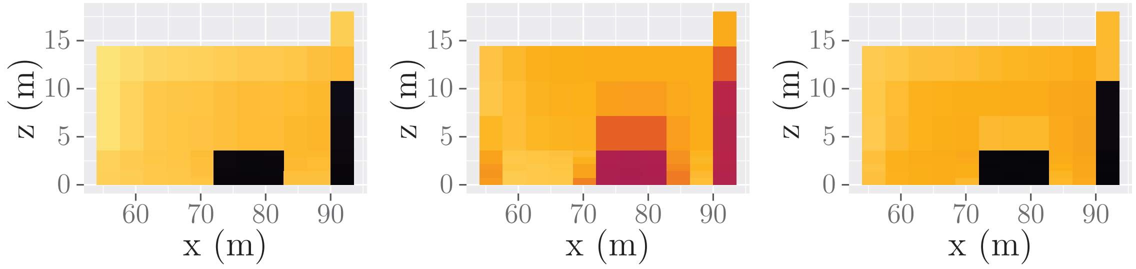

(b) 09:00 am

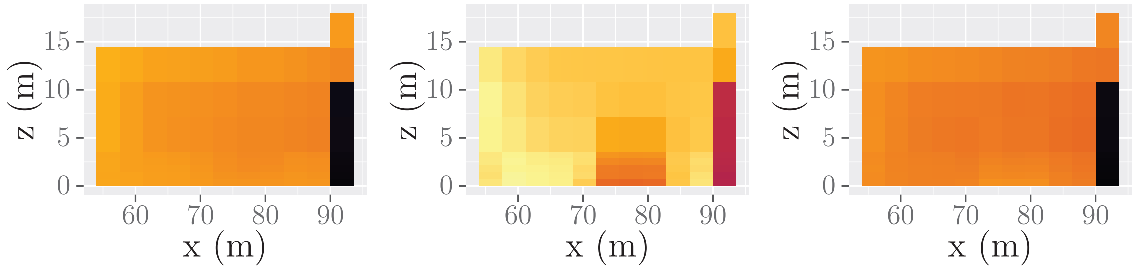

(c) 10:00 am

Figure 5.14.: Evolution of the Physical Values (Shortwave Radiation, Surface Temperature and Photovoltaic Power Generation) on the East Facade Predicted by the Indexed View Sphere Method

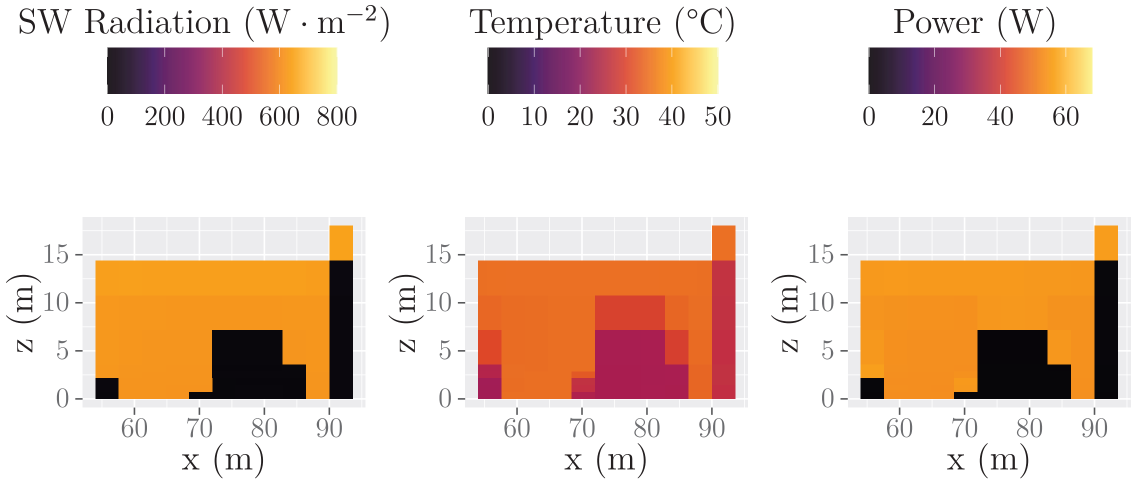

(a) 08:00 am

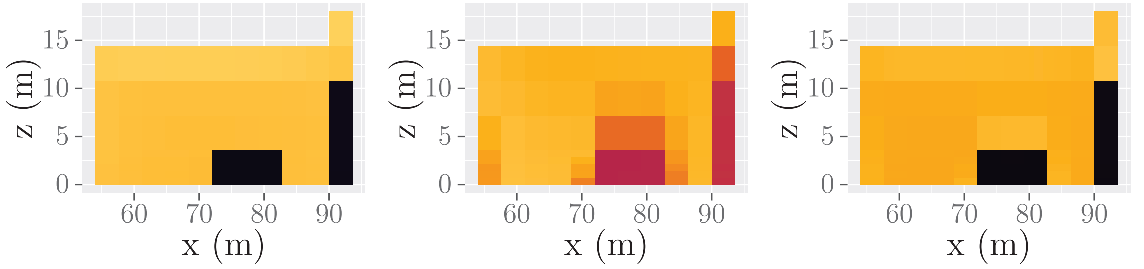

(b) 09:00 am

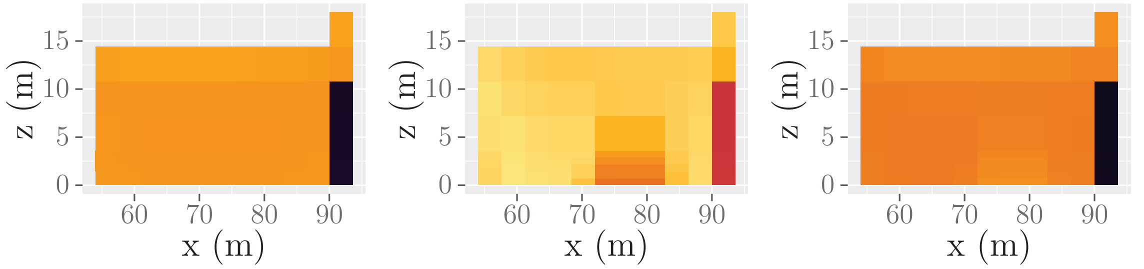

(c) 10:00 am

Figure 5.15.: Evolution of the Physical Values (Shortwave Radiation, Surface Temperature and Photovoltaic Power Generation) on the East Facade Predicted by the Averaged View Factor Method

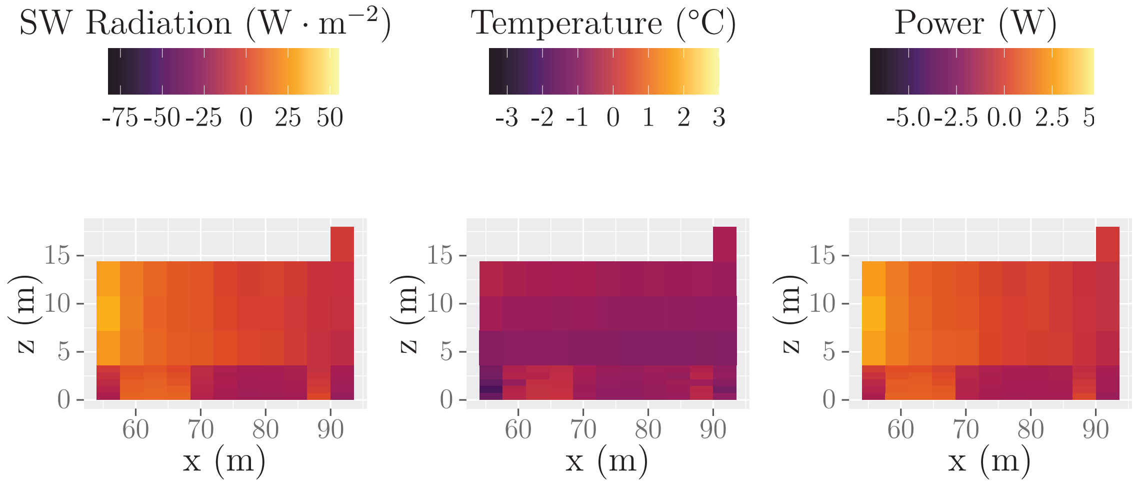

(a) 08:00 am

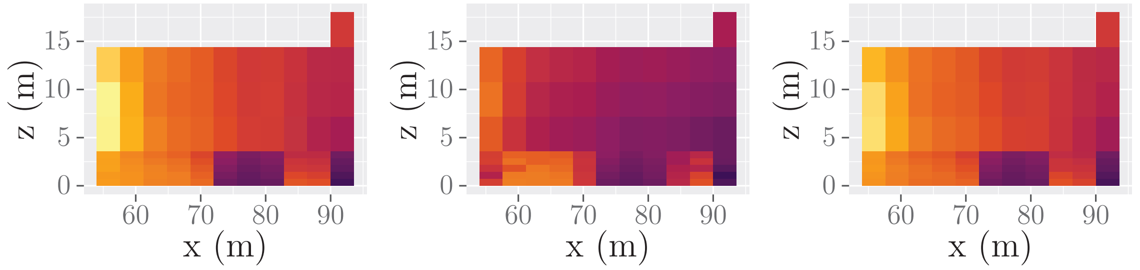

(b) 09:00 am

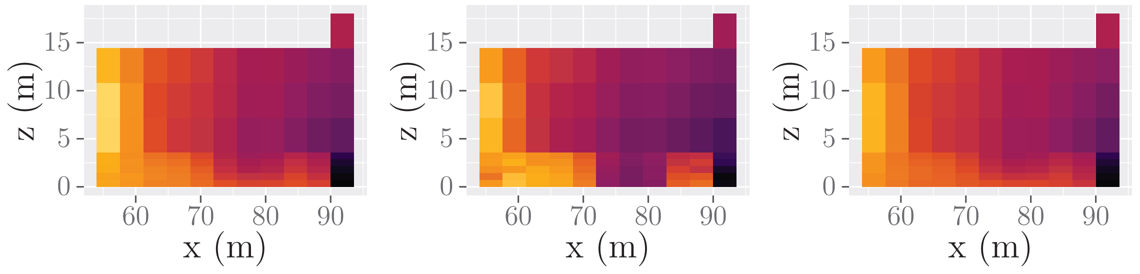

(c) 10:00 am

Figure 5.16.: Differences Between the Predicted Values by the Indexed View Sphere and Averaged View Factor Methods (Shortwave Radiation, Surface Temperature and Photovoltaic Power Generation)

Table 5.7.: Parameters of the Solar Module TEX854

Electrical Parameters			
Maximum Power Rating	P_{max}	[W]	92.5
Minimum Power Rating	P_{min}	[W]	87.5
Rated Current	I_{mp}	[A]	5.0
Rated Voltage	V_{mp}	[V]	18.0
Short Circuit Current	I_{SC}	[A]	5.4
Open Circuit Voltage	V_{OC}	[V]	22.2
Thermal Parameters			
Nominal Operating Cell Temperature	NOCT	[°C]	45
Temperature Coefficient of I_{SC}	α	$[\mathrm{mA} \cdot {}^{\circ}\mathrm{C}^{-1}]$	+1.53
Temperature Coefficient of V_{OC}	β	$[\mathrm{mV} \cdot {}^{\circ}\mathrm{C}^{-1}]$	-76.32
Temperature Coefficient of P_{max}	γ	$[\% \cdot {}^{\circ}\mathrm{C}^{-1}]$	-0.43
Physical Parameters			
Number of Series Cells			36 (4×9)
Length		[mm]	1157
Width		[mm]	512

Table 5.8.: Hour by Hour Differences of Predicted Photovoltaic Power Generation of the Facade

Hour	Difference of PV Power Generation (%)	Hour	Difference of PV Power Generation (%)
00:00	0	12:00	−15.13
01:00	0	13:00	−39.80
02:00	0	14:00	−138.34
03:00	0	15:00	−146.74
04:00	0	16:00	−105.17
05:00	0	17:00	−92.88
06:00	0	18:00	−140.24
07:00	+0.37	19:00	+78.02
08:00	−0.93	20:00	0
09:00	−0.36	21:00	0
10:00	−1.11	22:00	0
11:00	−4.19	23:00	0
Total −14.73 %			

5.1.2.4 *Evaluation of the Impact of the Inter-building Reflections on the Photovoltaic Potential of Buildings' Facades*

Taking into consideration the close surrounding of buildings has an important influence on the evaluation of their solar energy production potential. So far, models of energy production only consider close buildings as masks. In the following section, the influence of the inter-building reflections in the evaluation of the PV potential of buildings' facades is assessed. To do so, the same geometry as the one presented in figure 5.12 on page 104 is used. The only modified parameter is the reflectivity of the outer surfaces of the walls. To set the reflectivity to a value of 0 allows not to take into account the inter-building reflections.

Figure 5.17 on the next page shows the difference in terms of SW radiation, surface temperature and PV power generation on the studied facade considering the inter-building reflections or not.

As with the figure 5.16 on page 113, the results obtained with the IVS method is taken as the reference for the calculation. Thus, the differences are calculated as follows:

$$X = X_{\mathrm{IVS}} - X_{\mathrm{IVS\ without\ reflection}} \tag{5.6}$$

As all the values presented in figure 5.17 on the next page are greater than zero, it appears that not taking into consideration the surrounding buildings leads to an underestimation in terms of SW radiation, surface temperature and predicted PV power generation. This observation is valid for any time of the day and each and every facade's element. This underestimation reaches 16.76 % of the predicted PV energy production over the whole day. Thus, taking into consideration the inter-building reflections in the evaluation of the solar potential of buildings is a crucial issue.

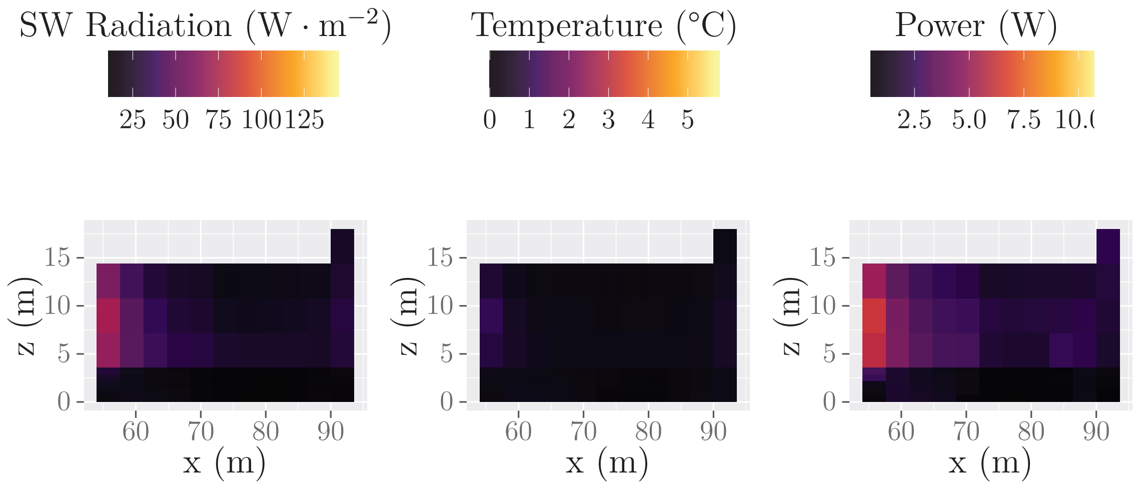

(a) 08:00 am

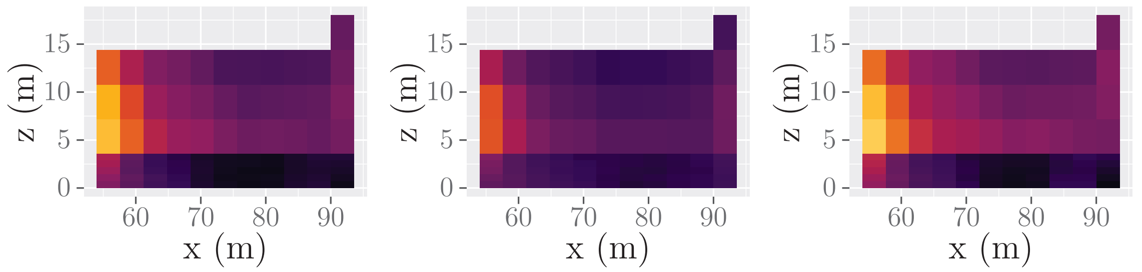

(b) 09:00 am

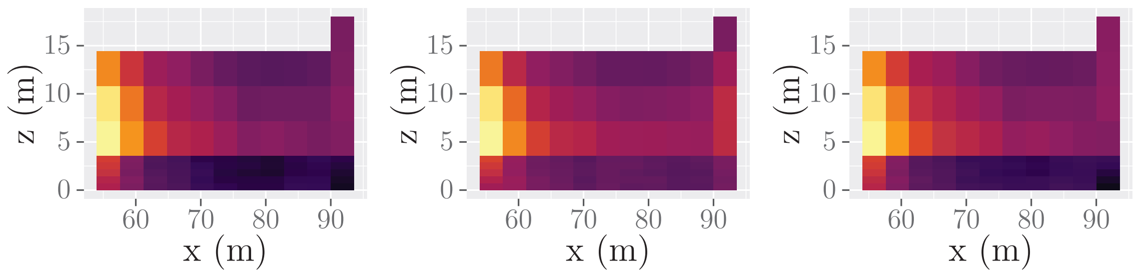

(c) 10:00 am

Figure 5.17.: Differences Between the Predicted Values by the Indexed View Sphere Method Taking the Inter-building Reflections into Consideration or not (Shortwave Radiation, Surface Temperature and Photovoltaic Power Generation)

5.1.3 *Evaluation of the Influence of the Wind Speed on the Photovoltaic Potential of Buildings' Facades*

The PV power generation models need two input values: the received SW radiation and the surface temperature of the PV cells. However, these required data are impacted by the airflow around the PV panels. Indeed, the airflow has an impact on the heat transfer between the PV surface and the air. Hence the specified temperature in the nominal operating cell temperature (NOCT) ($1\,\mathrm{m}\cdot\mathrm{s}^{-1}$). In addition, the turbulences further increase the heat transfer between the buildings surfaces and the air. The appearance of the turbulence are facilitated by the proximity between the buildings in urban areas. The wind velocity appears then as a key parameter to get more accurate results in terms of prediction of PV power generation.

By taking into consideration all the phenomena that occur in urban areas, ENVI-met makes it possible to assess the actual influence of the wind velocity on the building's surfaces temperatures and then to evaluate its influence on the PV potential. A theoretical neighborhood is considered to position the ENVI-met tool in relation to this issue. This neighborhood is presented as a first step. Then, the simulated results in terms of buildings' surface temperature and predicted PV power generation are plotted in accordance with the evolution of the wind velocity.

5.1.3.1 *Studied Neighborhood*

As aforementioned, taking the surrounding environment into consideration has a huge impact on the solar potential of buildings at district scale. Taking into account physical phenomena that occurs in urban environment includes both negative impacts (such as shading or shadowing) and positive impacts (such as inter-building reflections or wind channeling) in terms of PV potential of the buildings' facades.

The main goal of the following section is to demonstrate the influence of the wind velocity on the potential of PV power generation on buildings' facades. The influence is due to surrounding buildings and more precisely the turbulences due to the narrow space between buildings.

The studied case is a theoretical neighborhood composed of 3 rows and 3 columns of identical cubicoidal buildings.

The studied days are the representative average days of the months of February and June. The representative average day of the month is defined, according to the equation (5.7), as the day for which the meteorological conditions (including: irradiation level, temperature, wind speed and direction) for each hour are equal to the average of these conditions over all the days of the month. Carrying out the study for two different months allows to evaluate the influence of various weather conditions. Thus, the month of February provides results for a cold month with a low wind flow, while the month of June is warmer and windier.

$$X_{RAD}\left(t\right) =< X_i\left(t\right) >_{N_{day}} \tag{5.7}$$

LAYOUT OF THE NEIGHBORHOOD

The modeled district is a fictional district, positioned at a location corresponding to the city of Geneva, Switzerland. It is shown in figure 5.18. This neightborhood is studied within the project G2 solaire (see 1.1.2.3 on page 8) and a benchmark carried out with the International Energy Agency.

The building of interest is the building number 5. The results concern the south facade. Buildings 1, 2 and 3 can create shadows or reflections on this facade of the building. In addition, the narrow space between the buildings can create a wind channeling, which may have an influence on the building's surface temperature.

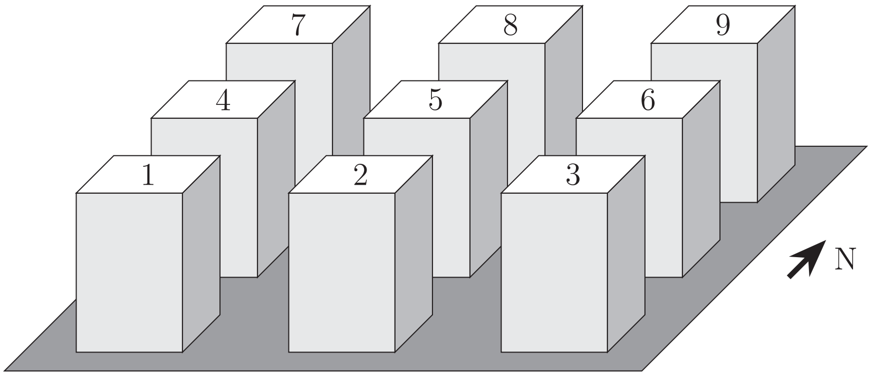

Figure 5.18.: Fictional Homogeneous Neighbourhood – Geneva

All the buildings are 20 meters wide and 30 meters high. They are separated from each other by 20 meters. The layout of this neighborhood is shown in figure 5.19 on the next page. The spatial resolution is set to 1 meter in every spatial direction.

Even if it leads to a very high computational cost, this resolution provides results of a greater precision in terms of spatial heterogeneity.

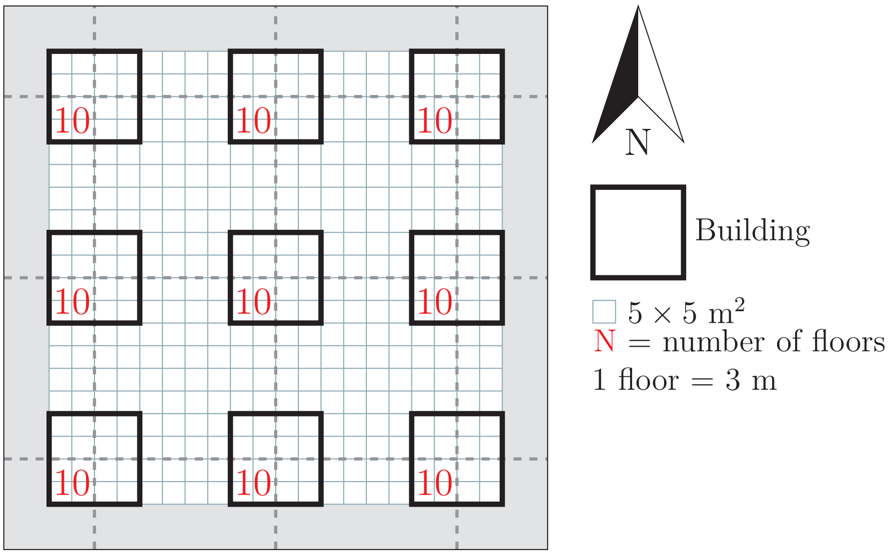

Figure 5.19.: Fictional Homogeneous Neighbourhood (Top View) – Geneva

INPUT DATA: REPRESENTATIVE AVERAGED DAYS

As aforementionned, the representative averaged day is a fictive day based on the actual weather conditions averaged over the month. It allows to get a global overview for a month when simulating a single day.

Two different representative days are considered to evaluate the influence of the wind velocity on the potential of PV power generation:

1. the month of February, which is a cold day, with temperatures ranging from 1 °C to 7.5 °C,
2. the month of June, which is a warm day, with temperatures ranging from 15 °C to 25 °C.

Regarding the temperature, the month of June appears warmer than the month of February. This difference is due to the higher level of SW radiation, as shown in figure 5.20c on page 122. However, both days have similar profiles in terms of wind speed and direction (figure 5.20b on page 122) with a mean wind speed around $1.5\,\mathrm{m}\cdot\mathrm{s}^{-1}$.

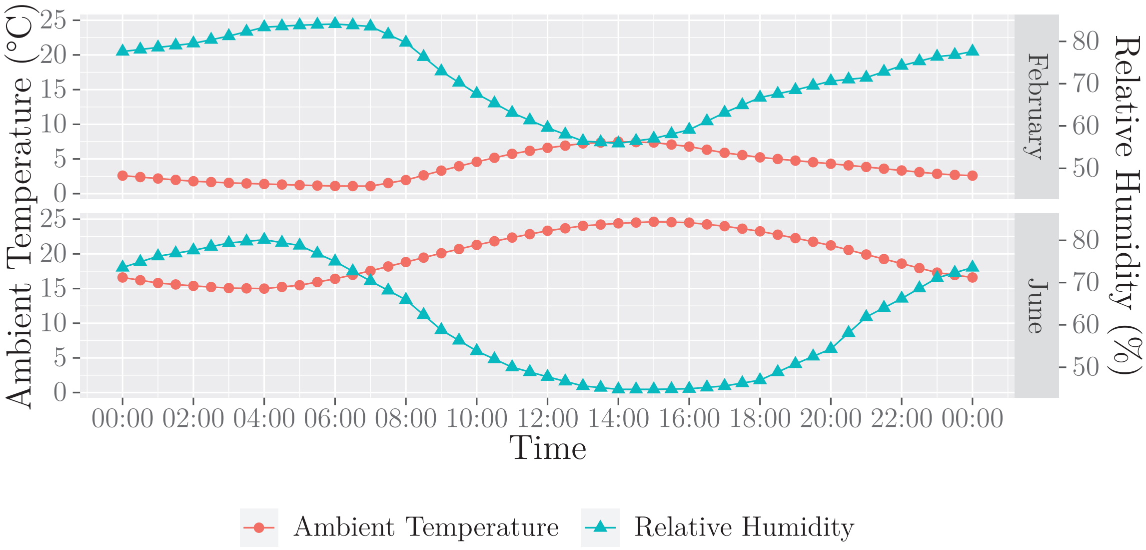

(a) Ambient Temperature and Relative Humidity

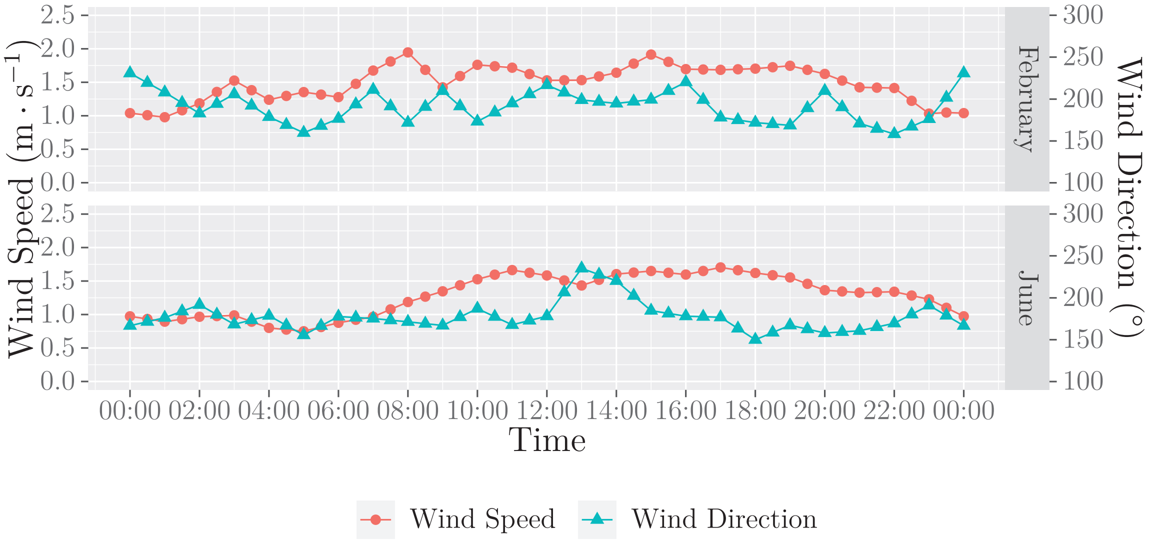

(b) Wind Speed and Direction

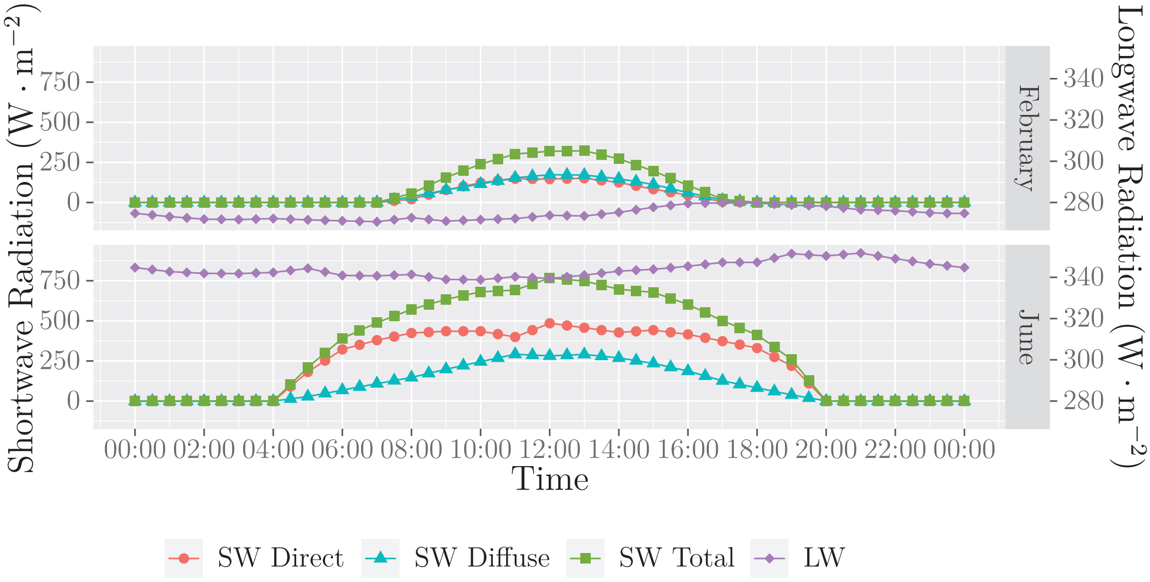

(c) Shortwave Radiation

Figure 5.20.: Representative Averaged Day of the Months of February and June in Geneva

5.1.3.2 *Instantaneous Results*

Three physical values are compared: two outputs from ENVI-met simulation and the output power predicted by the PV power generation model. As solar-related values, they evolve over time. A sample of three hours is selected to demonstrate this evolution and evaluate the variation of the predicted output power for both studied days, with the weather conditions given in figure 5.20 on the facing page.

As expected, the maps of data for the months of February and June are very different, for three main reasons. Indeed, the levels of SW radiation, surface temperature and PV power generation are higher in June than in February (see figure 5.21 on the next page and figure 5.22 on page 125). In addition, the days being longer in June than in February for the city of Geneva, these higher levels last longer over the day. Finally, the values are more homogeneous in June than in February, the latter being more subject to shading phenomena.

Three hours have been selected to demonstrate the aforementioned characteristics for the studied days. Naturally, these differences being found for every hour, they have an impact on the production of energy throughout the day, as discussed in the following.

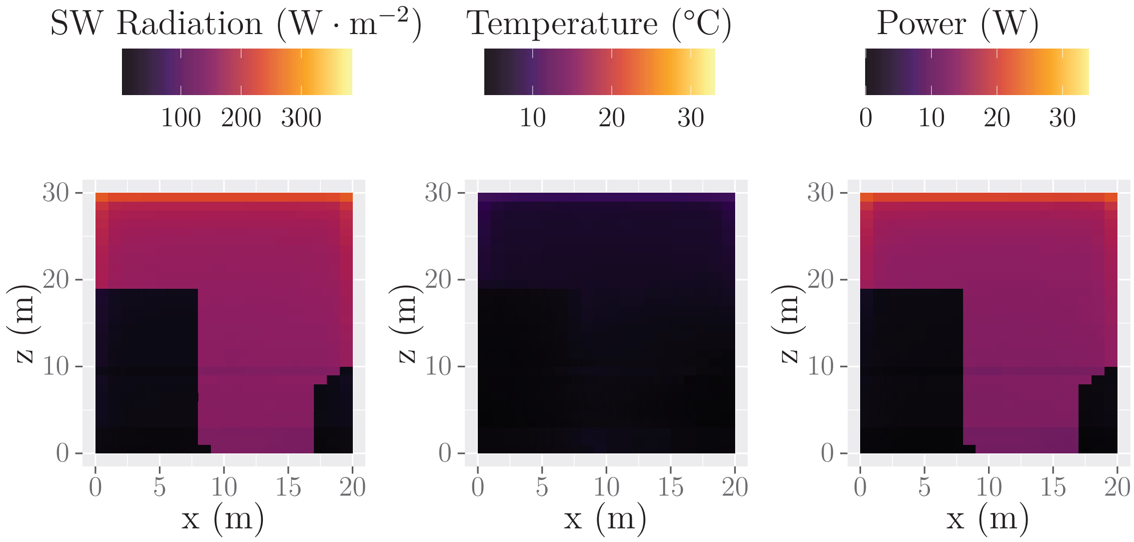

(a) 11:00 am

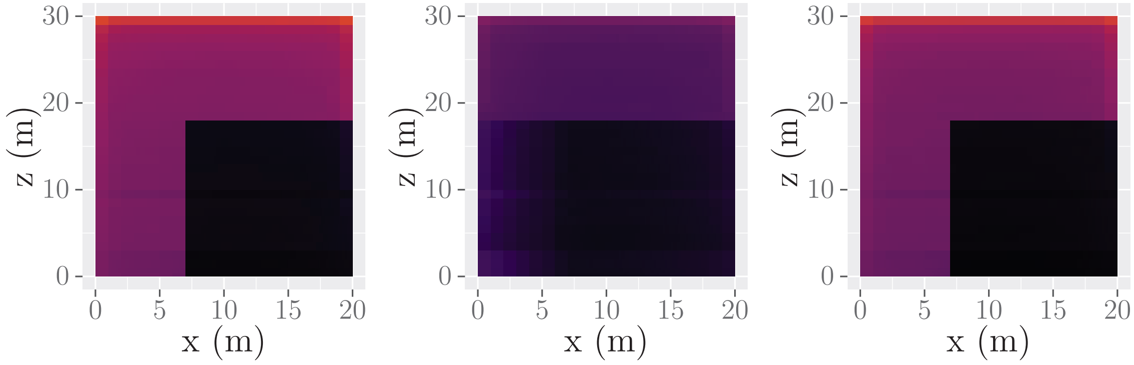

(b) 02:00 pm

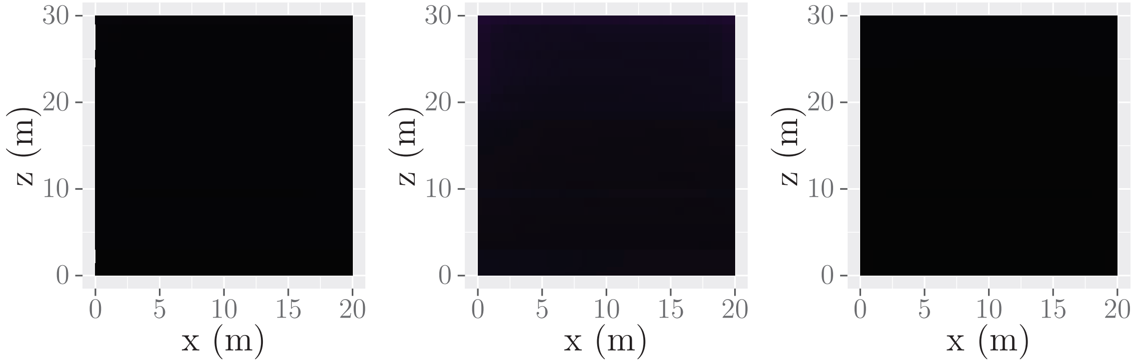

(c) 05:00 pm

Figure 5.21.: Weather Conditions on the Building's Facade at Different Times of the Day – February

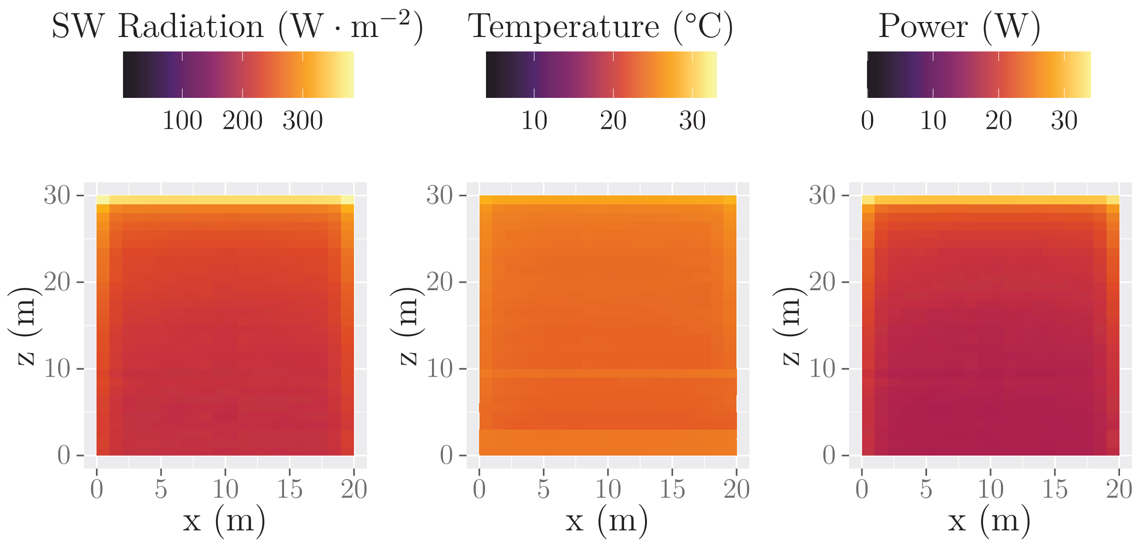

(a) 11:00 am

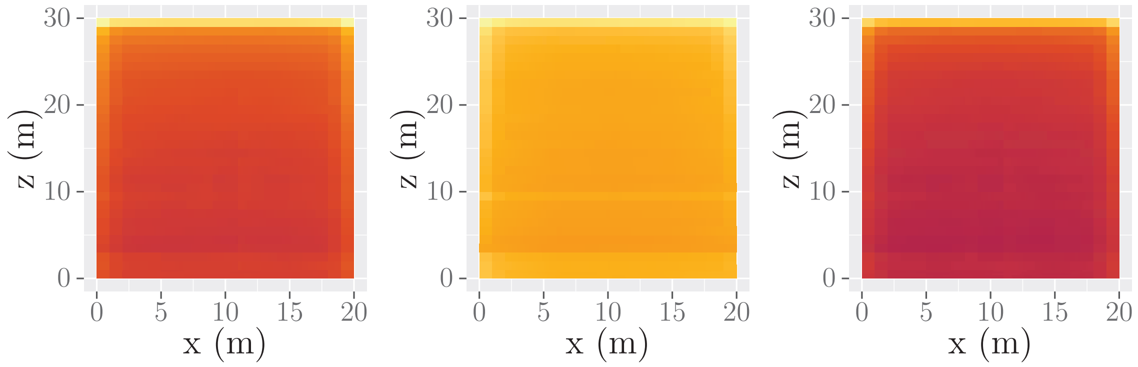

(b) 02:00 pm

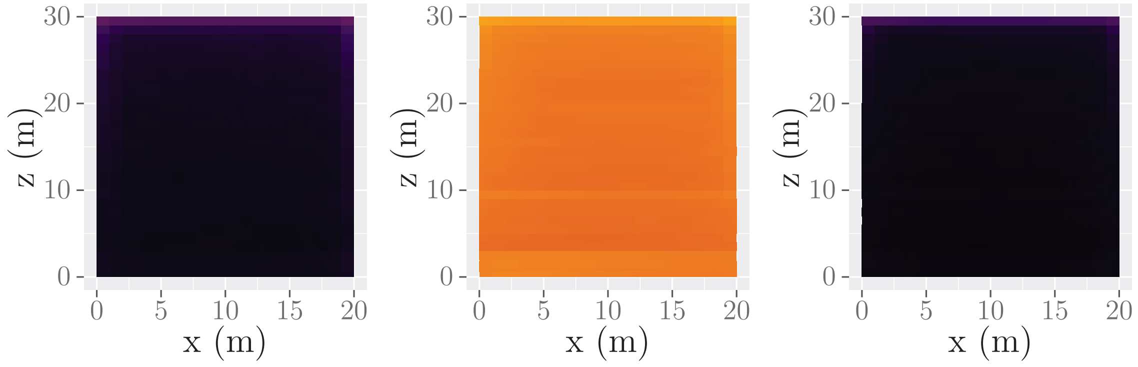

(c) 05:00 pm

Figure 5.22.: Weather Conditions on the Building's Facade at Different Times of the Day – June

5.1.3.3 *Energy Production*

ENVI-met makes it possible to evaluate the output at a fixed time steps. For this study, a time step of one hour has been set. As previously said, the instantaneous differences in the profiles for the weather conditions and the PV output power lead to differences for the profile of the energy production throughout the days. These differences are highlighted in figure 5.23 on the next page.

Two main differences may be noted:

1. Due to higher levels of solar radiation, the energy production is more important in June than in February;
2. Due to longer days in summer than in winter, the energy production has a non-null value for a longer period in June (between 06:00 am and 07:00 pm) than in February (between 09:00 am and 04:00 pm).

The results presented figure 5.23 on the facing page are obtained for the weather conditions presented in figure 5.20 on page 122. They are considered as the reference case for the study of the following section, aiming at evaluating the influence of taking into consideration the wind velocity in the evaluation of the PV potential of buildings' facades.

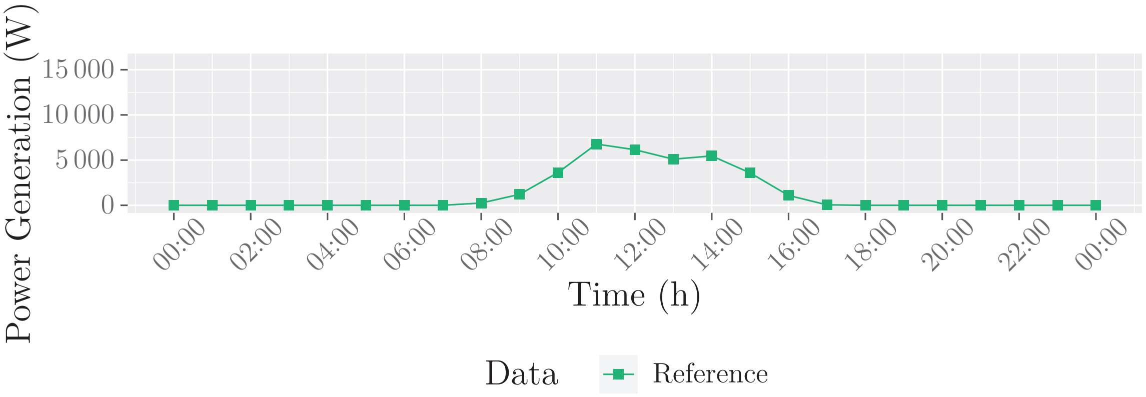

(a) February

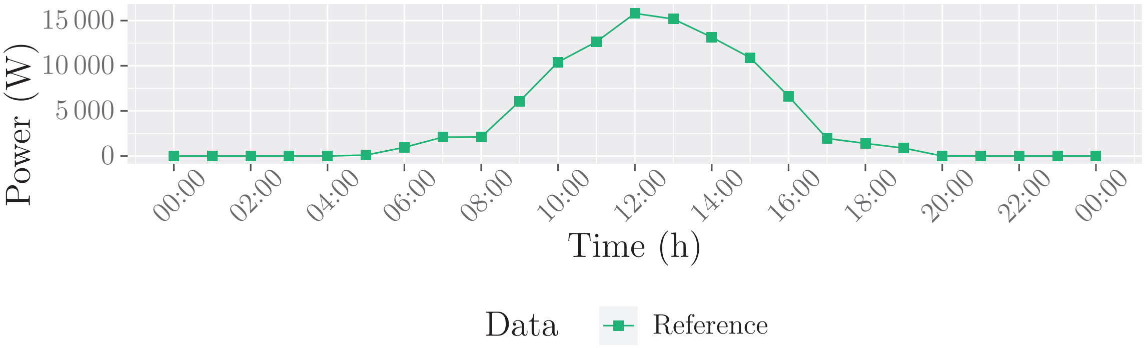

(b) June

Figure 5.23.: Evolution of the Photovoltaic Power Generation Over the Day

5.1.3.4 *Influence of the Wind Speed Variation*

The wind velocity is an often overlooked parameter in the radiative and PV production models because it requires to take into consideration the aeraulic phenomena, as well as the radiative ones. Nonetheless it brings more information for the facade because it makes it possible to calculate its thermal balance.

In order to evaluate the influence of the wind velocity on the potential of PV energy production, variation cases have been studied, for the months of February and June, with different simulations carried out with ENVI-met. All factors being equal (see figure 5.20a on page 121 and figure 5.20c on page 122), different values of inflow wind velocity are used. These values are given in table 5.9 on the following page. For the reference case, the inflow wind velocity is the one calculated for the representative average day (RAD). Four other cases are considered, for the two months, with wind velocity 10 % and 25 % lower and higher, respectively. The evolution of the wind velocity for the ten studied cases is given in figure 5.24 on the next page.

Table 5.9.: Mean Wind Speeds for the Months of February and June to Evaluate the Influence of the Wind Speed on the Photovoltaic Potential

Mean Wind Speed ($m \cdot s^{-1}$)	February	June
−25 %	1.12	0.96
−10 %	1.34	1.15
Reference	1.49	1.28
+10 %	1.64	1.41
+25 %	1.87	1.60

The variation of the inflow wind velocity has an influence on the observed wind speed at the building's facade. Nonetheless, the relationship between the variation of the inflow wind speed and the one at the building's facade is not linear, in particular because of the surrounding buildings influencing the air flow around the building (see figure 5.18 on page 119).

The maps of the instantaneous differences between the wind velocity at the building's facade and at different times of the day for the months of February and June are given in figure 5.25 on page 130. Three main differences appear from these maps.
First, although very homogeneous, the differences are not the same all over the facade. Indeed, the left side of the facade is less impacted in February. The wind speed is even higher, whereas the comparison is made between the reference case and the one with an inflow wind velocity 10 % lower. This observation can be extended to the other cases, and more particularly to the month of June, at 02:00 pm (figure 5.25e on page 130). Despite a decrease of the inflow wind speed, a slight increase of the wind speed near the building's facade can be observed on the left side. This is due to the surrounding buildings, which have an influence on the air flow. This behaviour demonstrates the importance of the description of the air flow near the buildings, as mentioned in section 5.1.1.2 on page 97.
Finally, the magnitude of the difference in terms of wind velocity near the building's

facade varies over the day. Thus, the latter is more important at the beginning of the afternoon (02:00 pm) than at its end (05:00 pm).

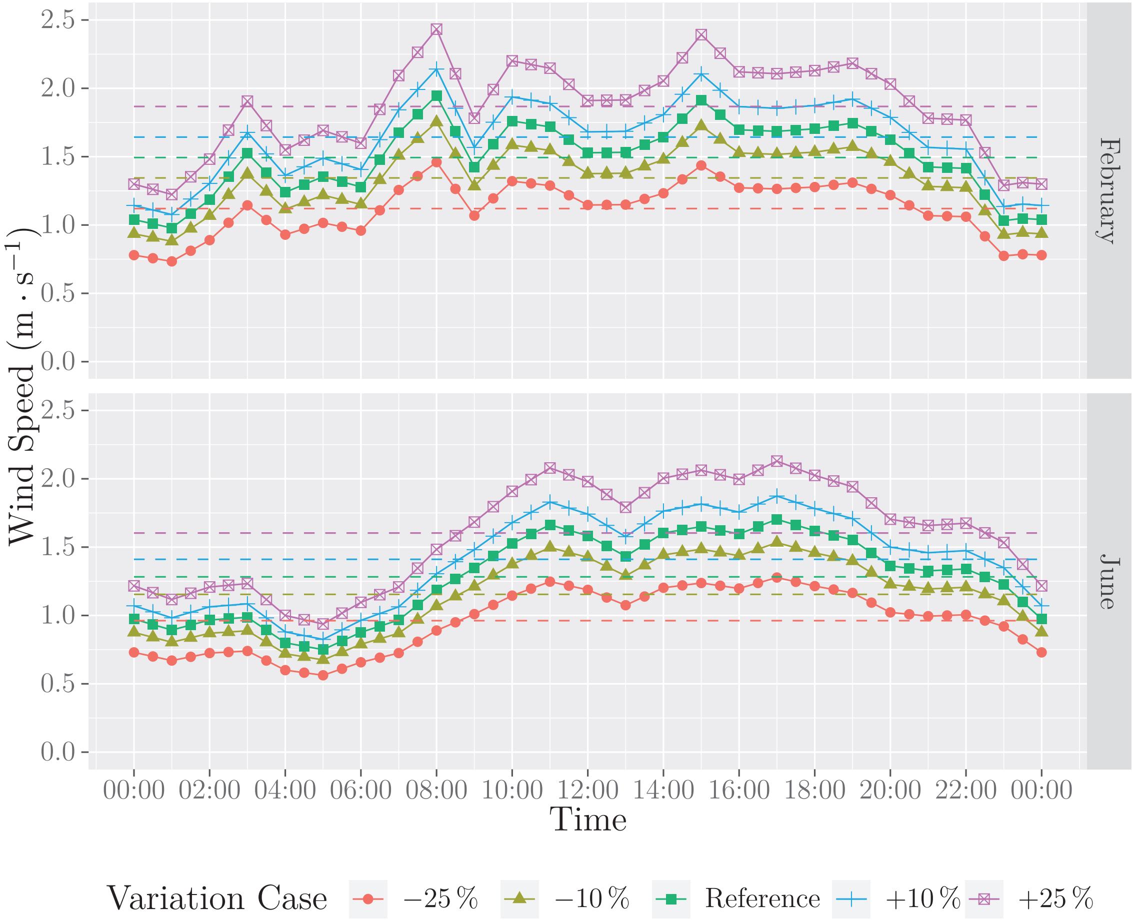

Figure 5.24.: Variation of the Inflow Wind Speed

Although low in terms of magnitude, the wind speed difference observed between the different cases has an influence on the physical values used as input for the PV power generation model as well as on its output.

By keeping all other factors equal, only the wind velocity influences the differences observed in the results. Thus, the observed differences in terms of SW radiation and surface temperature in figure 5.26 to figure 5.27 on pages 133–134 are only due to the variation of the wind speed.

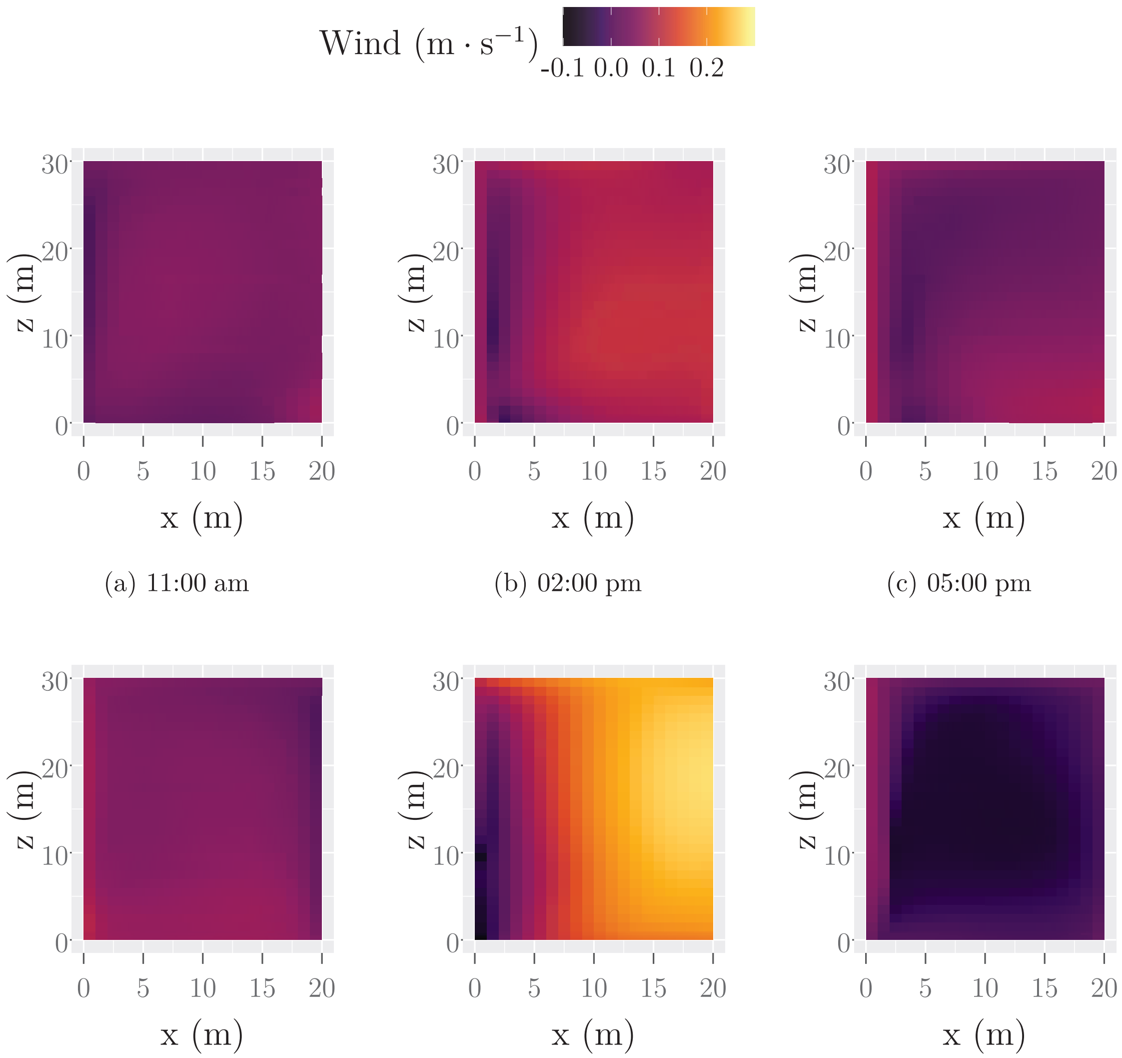

(a) 11:00 am

(b) 02:00 pm

(c) 05:00 pm

(d) 11:00 am

(e) 02:00 pm

(f) 05:00 pm

Figure 5.25.: Instantaneous Differences for the Wind Speed Between the Results Obtained in the Reference Case and With a Wind Speed 10 % Lower for the Months of February and June

The observed differences in terms of surface temperature are due to the modification of the heat transfer between the building's facade and the atmosphere. As can be seen in both of the figures, the difference in terms of temperature remains low with differences ranging from 0 °C to 0.06 °C for the month of February and −0.36 °C to

0.15 °C for the month of June (this pinpoints the possible increase of temperature, despite the increase of the inflow wind velocity).

The difference in terms of SW radiation received by the facade is due to the consideration of the pressure in the calculation of the diffuse SW radiation. The difference is higher than that of temperature, with differences ranging from $0\,\mathrm{W}\cdot\mathrm{m}^{-2}$ to $1.39\,\mathrm{W}\cdot\mathrm{m}^{-2}$ for the month of February to $0\,\mathrm{W}\cdot\mathrm{m}^{-2}$ to $1.04\,\mathrm{W}\cdot\mathrm{m}^{-2}$.

The differences in terms of both SW radiation and surface temperature have an impact on the output PV power. Nevertheless, the maximum difference does not exceed 0.3 W, which is less than 0.3 % of the maximal output power on the facade.

The slight observed differences in terms of PV power generation occur for each time step, resulting in differences in terms of energy production over the day. Nevertheless, the differences being very slight, the total energy productions are very close for each studied case, as shown in figure 5.28 on page 135.

The cumulative differences for the ten studied cases are given in table 5.10 on page 136. The variation of the wind velocity appears to have a low influence on the potential of the PV production. Indeed, the variation in terms of PV energy production is about a hundred times lower than that of the wind speed magnitude. However, the observed differences due to the variation of the wind velocity between the studied scenarios are very low compared to the results demonstrated for BIPV on double-skin facades (Gaillard et al., 2014). Indeed, the variation of the wind velocity near the building's facade may have a significant impact on the heat balance between the building and the atmosphere. Moreover, a higher wind velocity may have an influence on the accuracy of the predicted power generation, as shown in section 6.2 on page 173.

These demonstrated differences question the thoroughness of the presented study. Indeed, it is a first approach of the study of the influence of the wind velocity on the assessement of the PV potential. Several parameters may have an influence on the results and would need to be studied further. Among them, the morphology and the location of the fictitious neighborhood. This district is located in Geneva and the variation of the wind velocity has been selected according to the seasonal average of this location. Another location with a higher variation of wind velocity could lead to more significant differences in terms of PV power generation. In addition, the studied building is the one located in the center of the district. Thus, a variation of 25 % in terms of inflow wind velocity leads to a lower variation of the wind velocity near the building's facade. The surrounding buildings give protection against the wind for this building, regardless of wind direction. Finally, only two months have been studied so far. They have been selected as representative days for cold and warm seasons. Nonetheless, different weather conditions could also lead to different results, regarding the influence of the wind velocity. For example, a cold wind can cool down a PV panel more than a hot wind.

A way to complete the proposed study on the importance of taking into consideration the wind velocity in the assessement of the PV potential of buildngs' facades would then be to enlarge the context of study by:

1. studying several districts at different locations;
2. expanding the range of the variation of the wind velocity;
3. studying representative days at different seasons.

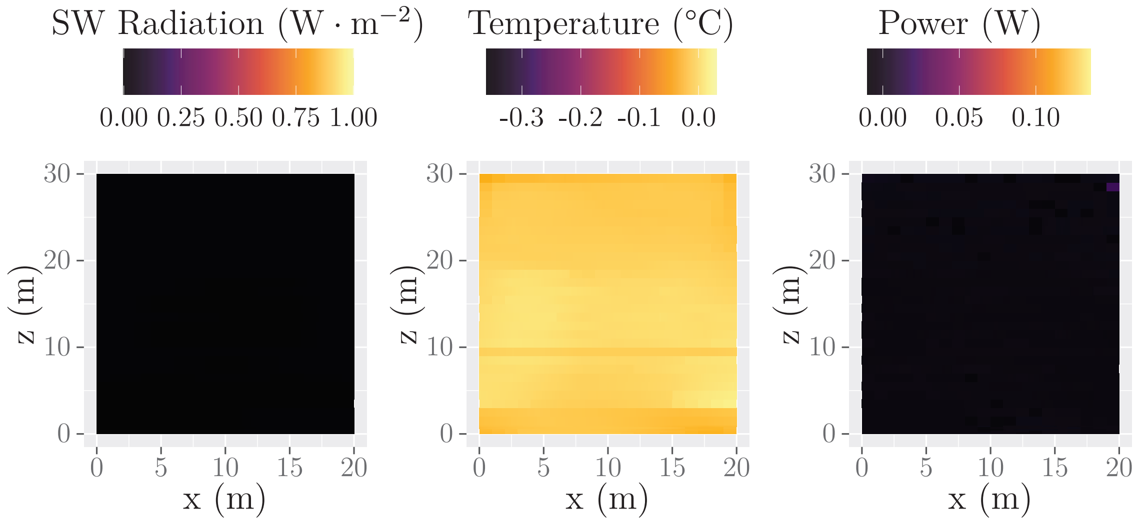

(a) 11:00 am

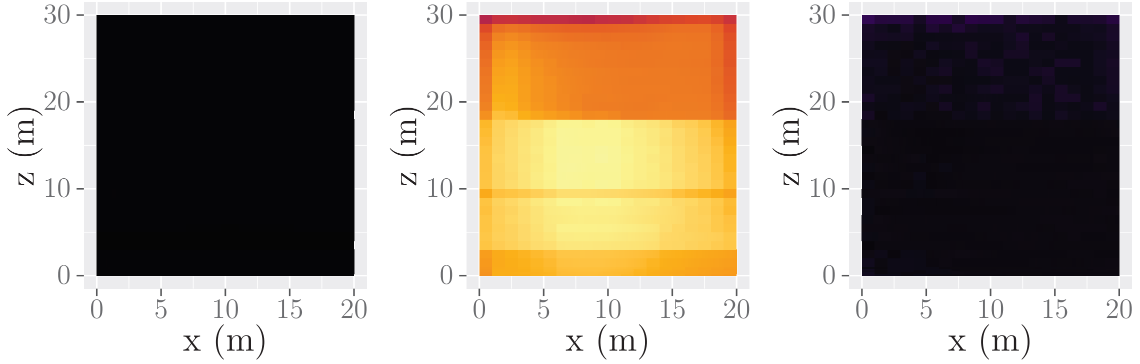

(b) 02:00 pm

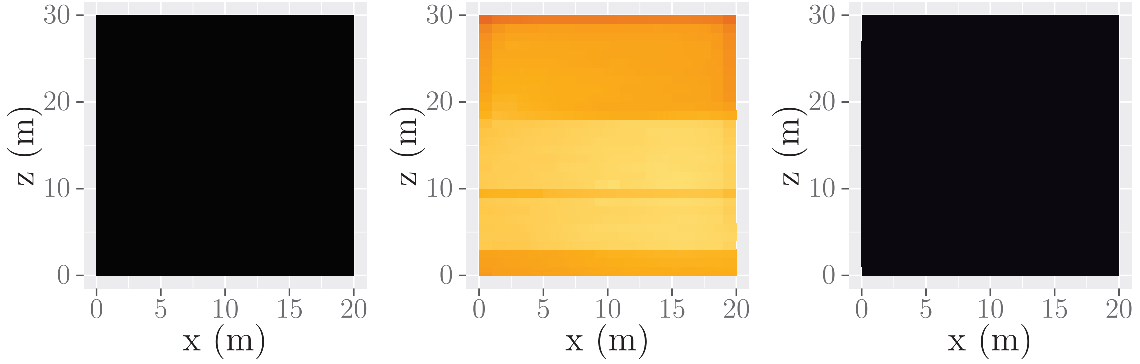

(c) 05:00 pm

Figure 5.26.: Instantaneous Differences for the Input and Output of the Photovoltaic Power Generation Model Between the Results Obtained in the Reference Case and With a Wind Speed 10 % Lower for the Month of February

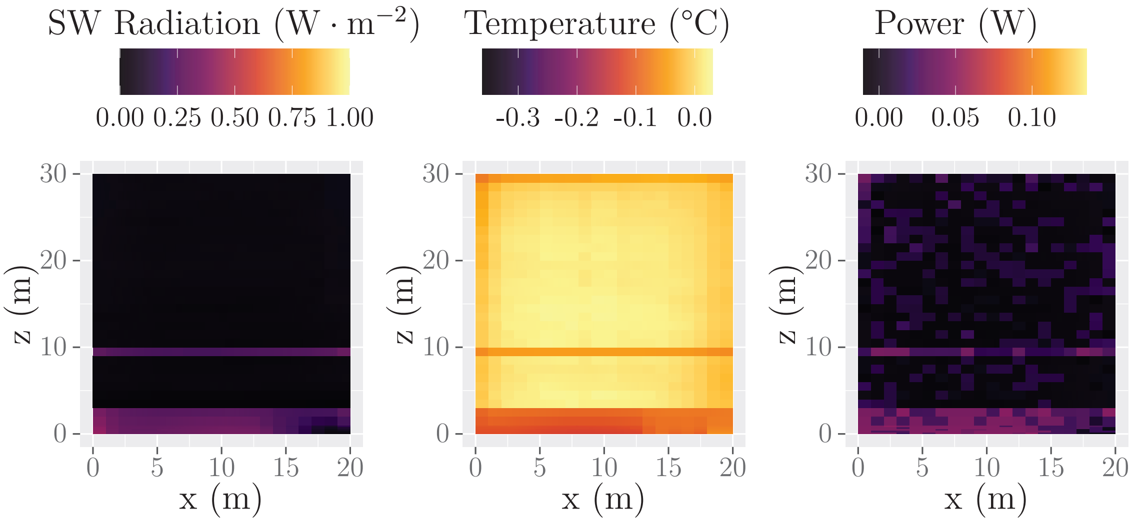

(a) 11:00 am

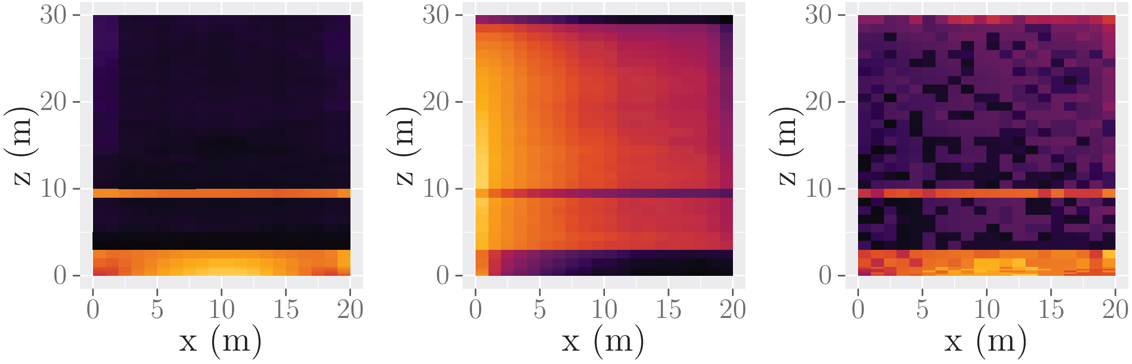

(b) 02:00 pm

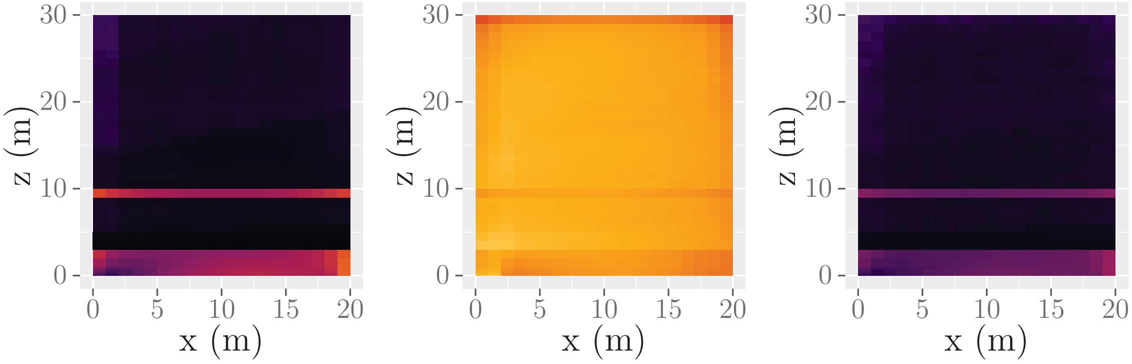

(c) 05:00 pm

Figure 5.27.: Instantaneous Differences for the Input and Output of the Photovoltaic Power Generation Model Between the Results Obtained in the Reference Case and With a Wind Speed 10 % Lower for the Month of June

(a) February

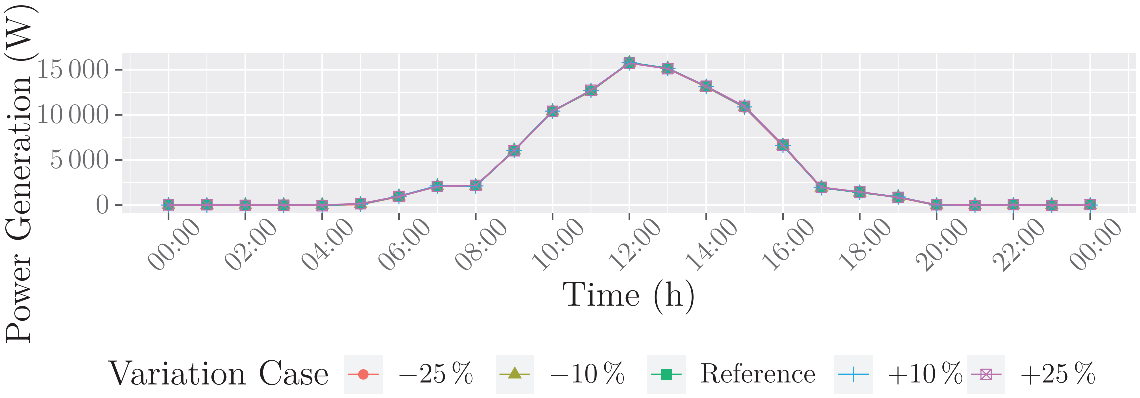

(b) June

Figure 5.28.: Evolution of the Photovoltaic Power Generation Over the Day

Table 5.10.: Gain / Loss of Photovoltaic Energy Production Against the Wind Speed Variation[3]

Gain / Loss of Photovoltaic Energy Production	February	June
−25 %	−0.028 %	−0.155 %
−10 %	−0.025 %	−0.140 %
+10 %	+0.025 %	+0.117 %
+25 %	+0.053 %	+0.247 %

5.2 COMPARISON OF THE PERFORMANCES OF THE SINGLE-DIODE MODEL AND THE POWER MODEL

The diode-based models and the power model are based on very different assumptions. Their strengths and drawbacks are set out in section 3.3.2.1 on page 58 and 3.3.3 on page 62. The goal of the following section is to evaluate and compare the accuracy of those models under actual operating conditions. This study involves a comparison between the numerical results predicted by the single-diode and power models, and the experimental measurements.

5.2.1 *Studied Building*

The study builds on a test building located in the R&D Laboratory of EDF[4] in the southeast of the Greater Paris region. The actual building is represented in the figure 5.29a on the next page and the modeled one is shown in figure 5.29b on the facing page. This domain includes surrounding buildings which may constitute a solar mask – see the grey building in the figure 5.29b on the next page is about 25 m south of the ETNA building. It may have an influence on the solar potential of the facades, depending on the length of the shadow, which varies according to the time of day and the day of year.

---

[3] The reference case is taken as the reference for the calculation.

[4] EDF is the main electricity producer in France.

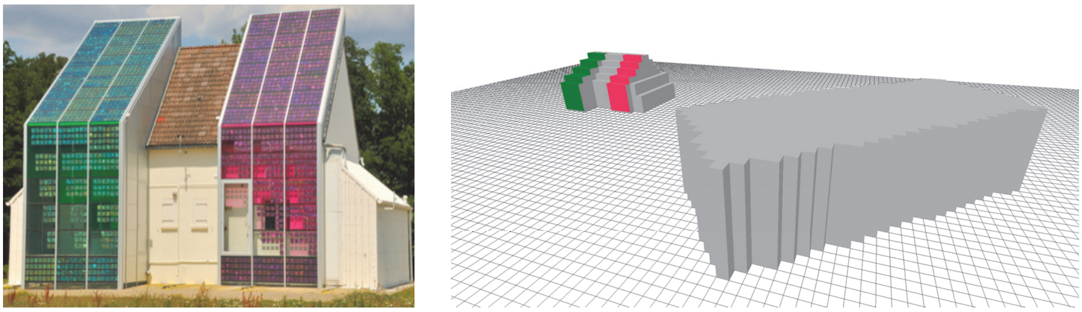

(a) Real Building ETNA (b) Modeled Domain in ENVI-met

Figure 5.29.: Test Building ETNA – EDF R&D Laboratory

Many sensors are installed on the building, among others twenty thermocouples on the vertical and slanted walls, as wells as pyranometers. On the top of the building, a weather station is installed to get local climatic conditions, such as air temperature, wind velocity and direction, solar irradiance (total and direct, what enables to deduce the diffuse irradiance).

The use of local meteorological measurements is important to evaluate more precisely the PV potential of the facades. Indeed, as demonstrated (Kyriakodis and Santamouris, 2018), the urban heat island (UHI) effect may exceed 6 °C to 7 °C. The weather stations usually used for weather forecast, installed in rural areas (typically airports), are then not affected by this effect. The use of forecasted temperatures instead of measured may induce by themselves a bias in the power generation assessment of several percent.

In addition, on-site measurements can be used as inputs of ENVI-met simulations. Thus, the more accurate the measurements, the more accurate the comparison between numerical results and experimental measurements.

5.2.2 *Input Data for the Photovoltaic Power Generation Models*

In this study, the simulations were done with the version 4.4 of the software ENVI-met. The computational domain (shown in the figure 5.29b) has a spatial resolution of 1 m in all directions. Despite the high computational cost that it implies, this resolution is a necessity in the evaluation of the PV potential of a facade as it allows getting precise results in terms of spatial heterogeneity regarding values such as surface temperature and solar irradiance.

The input data for air temperature and humidity, wind speed and direction and solar irradiation for the day of the 15th October 2012 are presented in the figure 5.30 on page 140. The solar radiation is broken into two parts:

1. The SW radiation, with wavelengths ranging betweeen 290 and 400 nm;
2. The longwave (LW) radiation, with wavelengths ranging between 400 and 2 500 nm.

The day of Monday 15th October 2012 appears as a sunny and not windy day, given the season of the year, with a peak of SW solar radiation measured on the vertical facade which exceeds $750\,\mathrm{W \cdot m^{-2}}$ and a wind velocity between $1.5\,\mathrm{km \cdot h^{-1}}$ and $7.2\,\mathrm{km \cdot h^{-1}}$. Yet the temperature level stays low, ranging between 1.4 °C and 13.4 °C, while the relative humidity stays relatively high (between 60 % and 100 %).

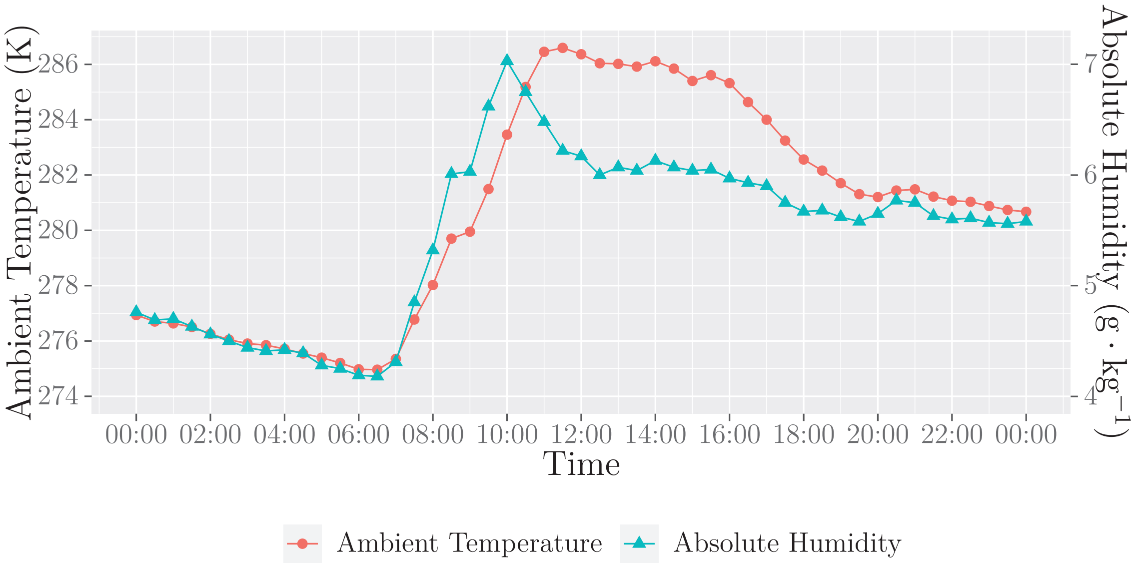

(a) Evolution of Ambient Temperature and Absolute Humidity During the Day

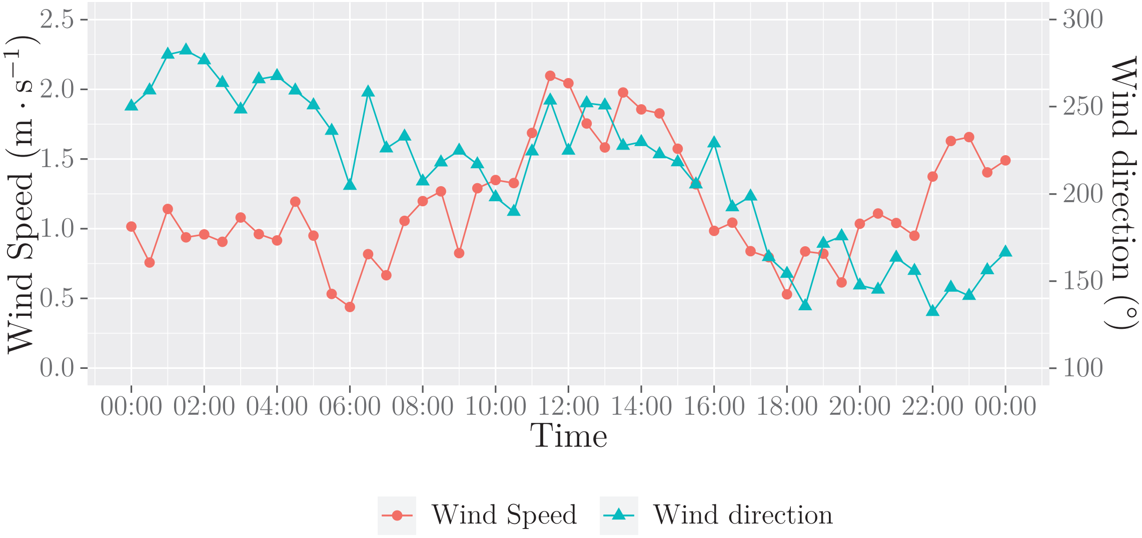

(b) Evolution of Wind Speed and Direction During the Day

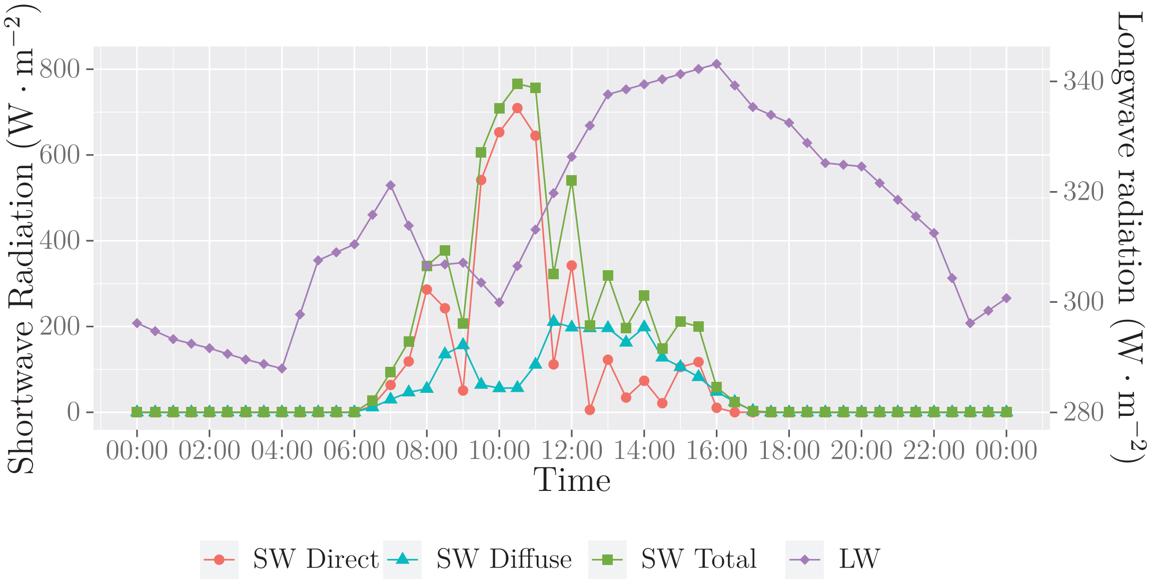

(c) Evolution of Shortwave and Longwave Radiation During the Day

Figure 5.30.: On-site Weather Conditions on Monday 15th October 2012

5.2.3 *Application of the Photovoltaic Power Generation Models to the Facade Measurements*

The figure 5.31 on the following page compares the measured PV power generation on the facades to the modeled ones. The models are applied to the local measurements of surface temperature and solar irradiation recorded on the prototype. Measurements are carried out every minute. This short time lapse between two records makes it possible to assess the accuracy of the models regarding the evolution of actual operating conditions (i.e.: intermittency). Figure 5.31 on the next page shows that both models react to high frequency changes in surface temperature and solar irradiation. It highlights the ability of these models to give full account of the variations in operating conditions. However, it can be noticed a global overestimation of the power generation by the power model (in red in the figure 5.31 on the following page) and, albeit to a lesser extent, by the single-diode model (in blue in the figure 5.31 on the next page). This is particularly marked before 9:00 am. Nevertheless, this overestimation is not due to the production models themselves but to the operating and regulating modes of the PV facade. Indeed, the estimated power is consistent with the solar radiation curve (see figure 5.33 on page 145). The shortwave solar radiation starts rising at 6:00 am with a first peak at $380\,\mathrm{W}\cdot\mathrm{m}^{-2}$ at 8:30 am, corresponding to the first peak of predicted production of about 200 W.

Regarding the comparison of the two models, according to the table 5.11 on page 143, the single-diode model is more accurate than the power model. Indeed, the lower the root mean squared error (RMSE) and MAPE, the more accurate the model. RMSE and MAPE are defined in equation (5.8) and equation (5.9).

$$RMSE = \sqrt{\frac{\sum_{i=1}^{N} (y_m - y_s)^2}{N}} \tag{5.8}$$

where y_m is the measured value and y_s is the predicted one, respectively. N is the number of items in the sample.

$$MAPE = \frac{1}{N} \sum_{i=1}^{N} \left| \frac{y_m - y_s}{y_m} \right| \tag{5.9}$$

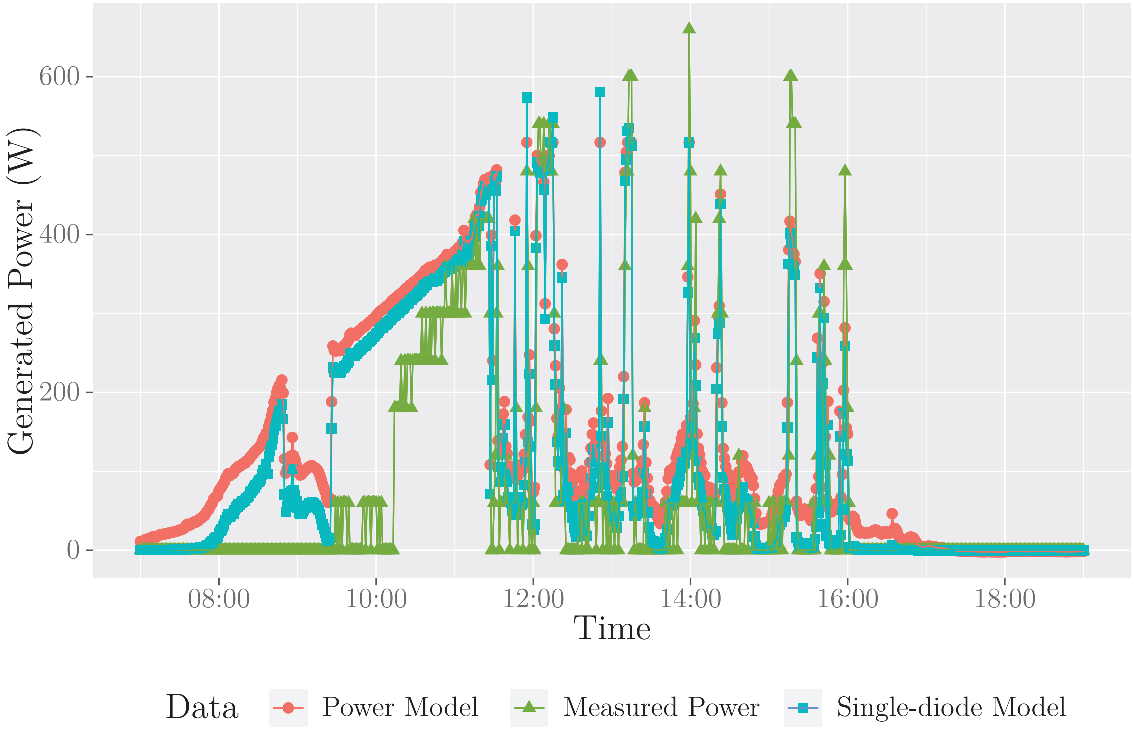

Figure 5.31.: Comparison of the Single-diode and Power Models Applied to Short-wave Radiation Measured on Building Facade versus Power Generation Measurements

The absolute values of these two indicators appear to be pretty high. Nonetheless, a main part of these values are attributable to the predicted values in the morning, particularly before 9:30 am. Indeed, as shown in table 5.12 on the next page, RMSE and MAPE decrease when considering the measurements only after 9:30 am, and even more so when considering only the values on the afternoon. This cutting in terms of calculation is to highlight the questionable operation of the prototype at the beginning of the day.

Table 5.11.: Comparison of the Root Mean Squared Error and the Mean Absolute Percentage Error of the Two Photovoltaic Production Models with Facade Measurements as Input Data

Production Model	RMSE	MAPE
Power Model	106.39 W	85.98 %
Single-diode Model	91.79 W	70.44 %

Table 5.12.: Comparison of the Root Mean Squared Error and Mean Absolute Percentage Error for Different Time Lapses

Start of Calculation	Production Model	RMSE	MAPE
9:30 am	Power Model	115.00 W	85.04 %
	Single-diode Model	109.08 W	69.62 %
12:00 pm	Power Model	97.26 W	68.59 %
	Single-diode Model	98.35 W	54.59 %

5.2.4 *Application of the Photovoltaic Power Generation Models to the Simulation Results*

As solar irradiance is measured in a single spot, the results of simulation carried out with the meteorological tool ENVI-met are aggregated over the whole green facade (see the figure 5.29a on page 137). On the other hand, measured data are averaged in bouts of five minutes. This corresponds to the shortest time period allowed by ENVI-met for the values outputs.

The comparison between the predicted power generation from the simulated data and the measured one is presented in figure 5.32 on the next page.

The figure 5.32 on the following page compares the measured PV power generation on the facades to the modeled ones. The models are applied to the local results of simulation for surface temperature and solar irradiation. As in the previous case, it appears that both single-diode and power model are able to react to high frequency

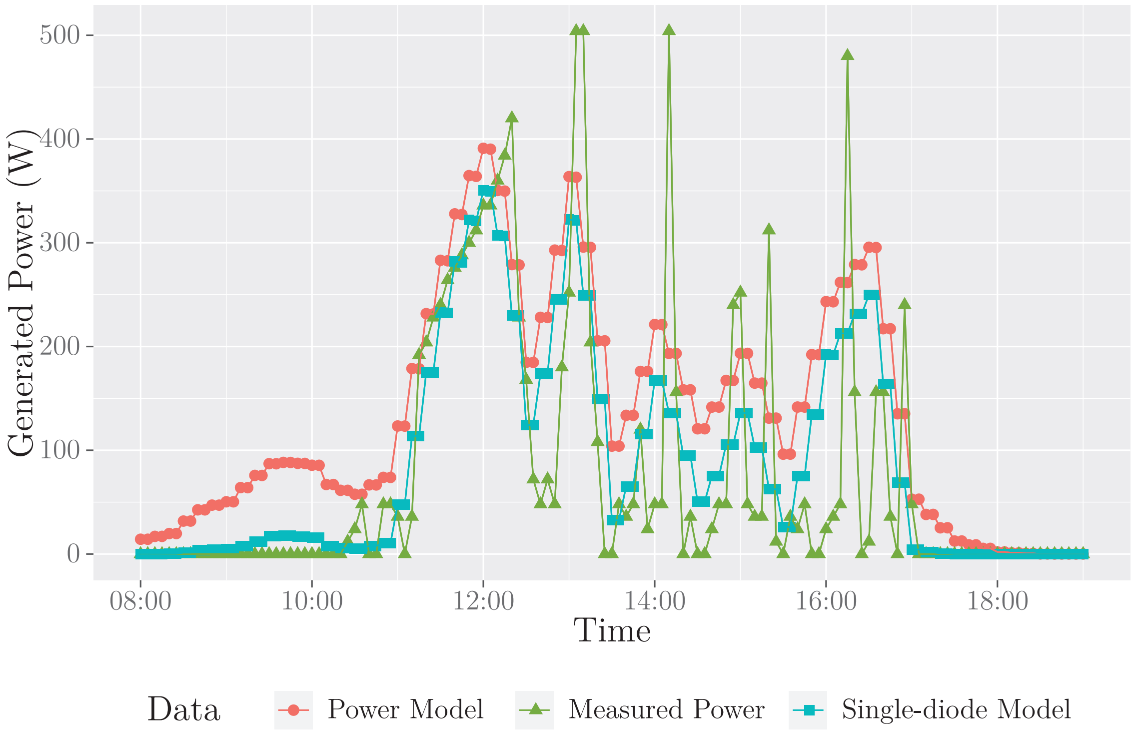

Figure 5.32.: Comparison of the Single-diode and Power Models Versus the Measured Power

changes in terms of weather conditions. It highlights the ability of these models to give full account of the variations in operating conditions.

The estimated production before 9:00 am does not reflect any bias in the model since it is consistent with the solar radiation on the facade (see figure 5.33 on the next page). The single-diode model appears as being more accurate than the power model, as shown in table 5.13 on the facing page. Indeed, both RMSE and MAPE are around 20 % and 40 % lower for the single-diode model than for the power model. However, the power generation results from the simulated data seem less accurate than the one from measurements, as evidenced by the increase in MAPE (respectively +131 % for the power model and +68 % for the single-diode model). This is due to the time interval of the data (five minutes for simulated data against one minute for measurements). This underlines the need to take the intermittency of solar radiation into account in order to improve the accuracy of the power generation prediction.

Table 5.13.: Comparison of the Root Mean Squared Error and Mean Absolute Percentage Error of the Two Photovoltaic Production Models with Facade Simulated Data as Input Data

Production Model	RMSE	MAPE
Power Model	105.48 W	217 %
Single-diode Model	84.85 W	138 %

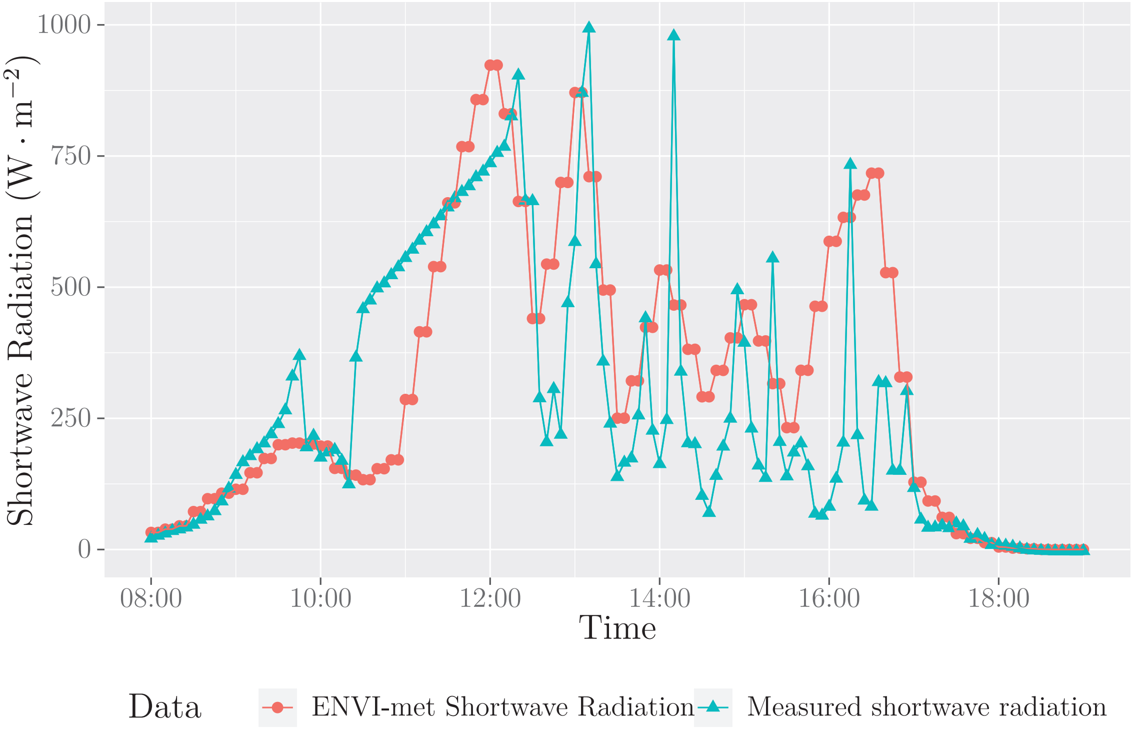

Figure 5.33.: Comparison of the Measured Shortwave Radiation on Building's Facade and the One Predicted by ENVI-met

A second parameter of influence that can partly explain the observed difference between the measured and the predicted values in terms of PV power generation is the difference between the predicted and the measured SW radiation. Figure 5.34 on page 147 shows the comparison between the simulated and measured values of shortwave radiation on the building's roof. The calculated values on the horizontal part of the building appear much more accurate than the one on the vertical wall. Indeed, the MAPE of the predicted values on the roof is one-quarter the one on the facade (see table 5.14).

Table 5.14.: Comparison of the Root Mean Squared Error and Mean Absolute Percentage Error for the Predicted Shortwave Radiation on Building's Facade

Wall	RMSE	MAPE
Facade	$203.54\,\mathrm{W} \cdot \mathrm{m}^{-2}$	$86.88\,\%$
Roof	$53.87\,\mathrm{W} \cdot \mathrm{m}^{-2}$	$20.35\,\%$

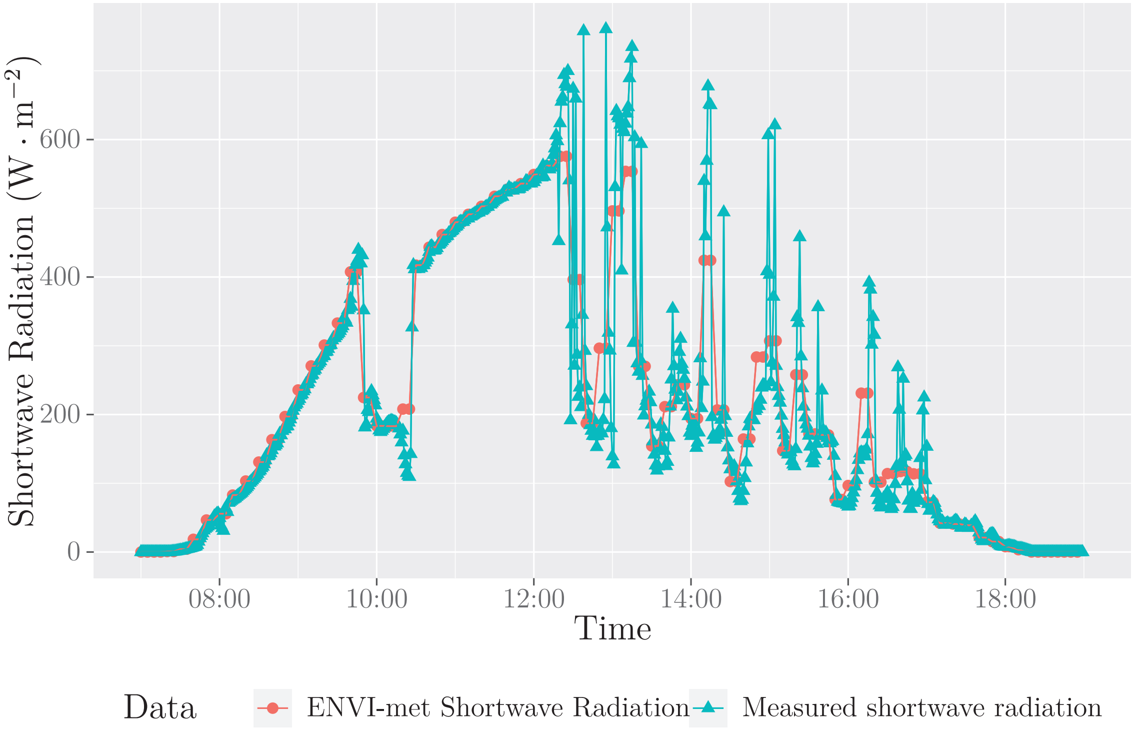

Figure 5.34.: Comparison of the Measured Shortwave Radiation on Building's Roof and the One Predicted by ENVI-met

This chapter highlights the ability of ENVI-met to both accurately simulate the different phenomena that occur in an urban context as well as to be used for the evaluation of the PV potential of buildings' facades.

The studies of each phenomenon, considered independently, pinpoints the fact that ENVI-met is not the software to use for the study of an isolated phenomenon. Indeed, the accuracy of each of the models used by ENVI-met is not the highest that can be obtained. Nonetheless, ENVI-met has the advantage of considering the inter-relation between the different families of phenomena, and then to simulate a urban microclimate as a set of phenomena interacting together and not as a sum of phenomena independent of each other. In this way, ENVI-met appears as a solution to simulate an UMC, by faithfully representing the various related phenomena, while maintaining bearable computing time.

Regarding, the evaluation of the PV potential of buildings' facades, ENVI-met has demonstrated its ability to provide accurate and reliable data used as input for the PV power generation models. Indeed, the values predicted by the models, based on input data from ENVI-met simulation, are in accordance with the measurements.

REFERENCES RELATED TO THE POSITIONING OF EXISTING MODELS

Bruse, M. (2015). Envi-met 4: A microscale urban climate model. *Available online: www. envi-met. com (accessed on 19 December 2019)* (Cited on page 105).

Bruse, M., & the ENVI-met Team. (2020). Advances in simulating radiative transfer in complex environments. https://www.envi-met.com/wp-content/uploads/2020/11/201119-530_06_201116-CaseStudy_IVS-1-1.pdf (Cited on page 108)

Gaillard, L., Ménézo, C., Giroux, S., Pabiou, H., & Le-Berre, R. (2014). Experimental Study of Thermal Response of PV Modules Integrated into Naturally-ventilated Double Skin Facades. *Energy Procedia*, *48*, 1254–1261. https://doi.org/https://doi.org/10.1016/j.egypro.2014.02.142 (Cited on page 131)

Kyriakodis, G.-E., & Santamouris, M. (2018). Using reflective pavements to mitigate urban heat island in warm climates - Results from a large scale urban mitigation project. *Urban Climate*, *24*, 326–339. https://doi.org/https://doi.org/10.1016/j.uclim.2017.02.002 (Cited on page 137)

6

IMPLEMENTATION OF NEW PHOTOVOLTAIC POWER GENERATION MODELS

> *All models are wrong, but some are useful.*
>
> George Box

The main goal of the presented work is to evaluate the ability of ENVI-met to assess the potential of photovoltaic (PV) power generation, taking into consideration the urban microclimate. The following section puts a focus on two different studies, which use the ENVI-met simulation outputs as input for the proposed PV power generation model.

The first study focuses on the influence of the series connections on the potential of PV energy production. This study relies on fictional neighborhoods located in Geneva. The fictional neighborhoods have the advantage that their layout can be thoroughly controlled. This makes it possible to study both the influence of the direction of the series connections on the potential of production over the year and the influence of the morphology.

The second study aims at characterizing the seasonal behavior of PV power generation model. This passes through a comparison between the numerical results obtained with simulations carried out with ENVI-met and experimental data from measurements on HBS building (RESSOURCES project (1.1.2.2 on page 6)). Four days have been selected to assess the influence of the evolution of the weather conditions on the accuracy of the proposed model. Three parameters have been selected: shortwave radiation, temperature and wind velocity. This comparison makes it possible to highlight the accuracy of the proposed model as well as the weather conditions under which this accuracy decreases.

6.1 INFLUENCE OF THE SERIES CONNECTIONS ON THE POTENTIAL OF PHOTOVOLTAIC POWER GENERATION

6.1.1 *Context of Study*

As aforementioned, taking the surrounding environment into consideration has a huge impact on the solar potential of buildings at district scale. Taking into account physical phenomena that occurs in urban environment includes both negative impacts (such as shading or shadowing) and positive impacts (such as inter-building reflections or wind channeling) in terms of PV potential of the buildings' facades.

The main goal of the following section is to demonstrate the influence of the series connections on the potential of photovoltaic (PV) power generation on buildings' facades. The influence is due to surrounding buildings and more precisely both the shadows projected on each other and the inter-building reflections.

Two cases are studied:

1. a homogeneous neighborhood (section 6.1.2);
2. a heterogeneous neighborhood (section 6.1.3 on page 166).

The studied days are the representative average days of each month of the year. The representative average day of the month is defined, according to the equation (6.1), as the day for which the meteorological conditions (including: irradiation level, temperature, wind speed and direction) for each hour are equal to the average of these conditions over all the days of the month. Carrying out the study over the whole year makes it possible to assess the evolution of the impact of the surrounding environment on the solar potential.

$$X_{RAD}\left(t\right) = < X_i\left(t\right) >_{N_{day}} \tag{6.1}$$

6.1.2 *Homogeneous Neighborhood*

The studied building is the same as the one presented in section 5.1.3.1 on page 118.

6.1.2.1 *Irradiation Maps on South Facade*

Some examples of the irradiation profiles on the south facade of building 5 at different times of the year and at different times of the day are shown in figure 6.1 on page 156. The figure presents the total direct and diffuse solar radiation incident on the facade, including sky diffuse and ground reflected components. The lower levels of irradiation on the facade are due to the shadow of close buildings located on the southern row. The mask that they create have an influence on the production profile, as discussed in section 6.1.2.2 on page 157.

The evolution of the radiation profiles over the year and for the same time of the days are due to the Sun's path. Indeed, because of the Earth's rotation, the Sun's position varies over the year. Its course over Geneva is given in figure 6.2 on page 157. This course leads to a variation in terms of shape of solar radiation on the facade, as well as of level of irradiation. Thus, the irradiation profile for the month of June appears both as much more homogeneous and higher than the months of February and October. The homogeneous side of the solar radiation in June is because the Sun gets high enough in the sky to pass over the southern buildings. Thus, no shading effect occurs on this facade.

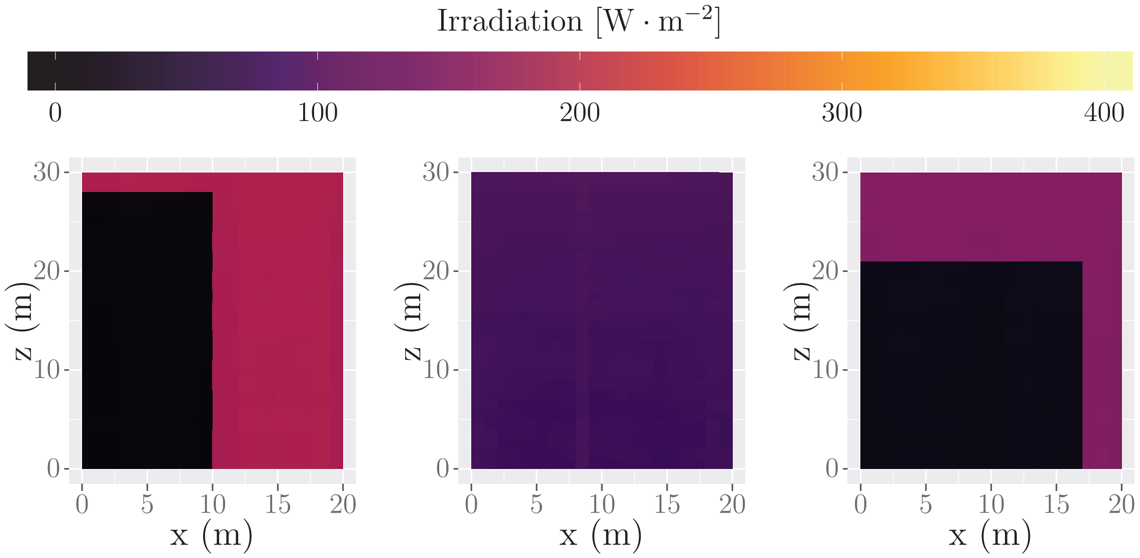

(a) February – 08:00 am (b) June – 08:00 am (c) October – 08:00 am

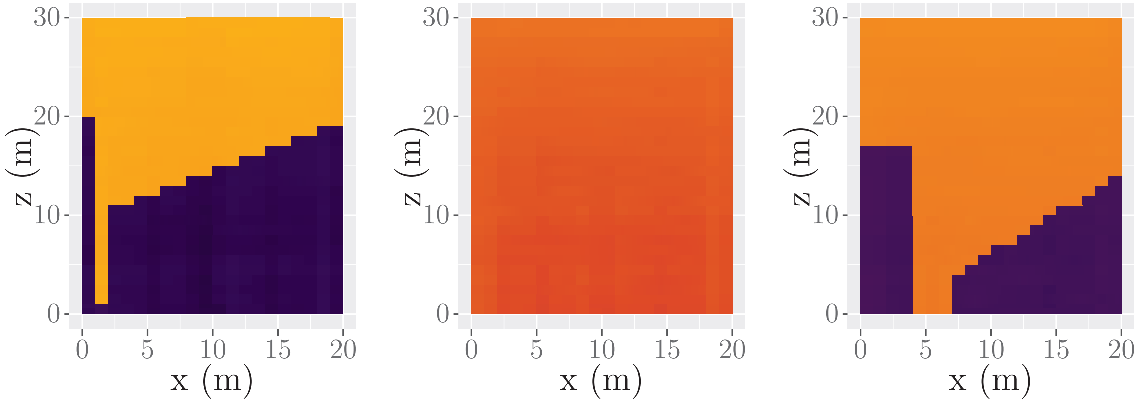

(d) February – 10:00 am (e) June – 10:00 am (f) October – 10:00 am

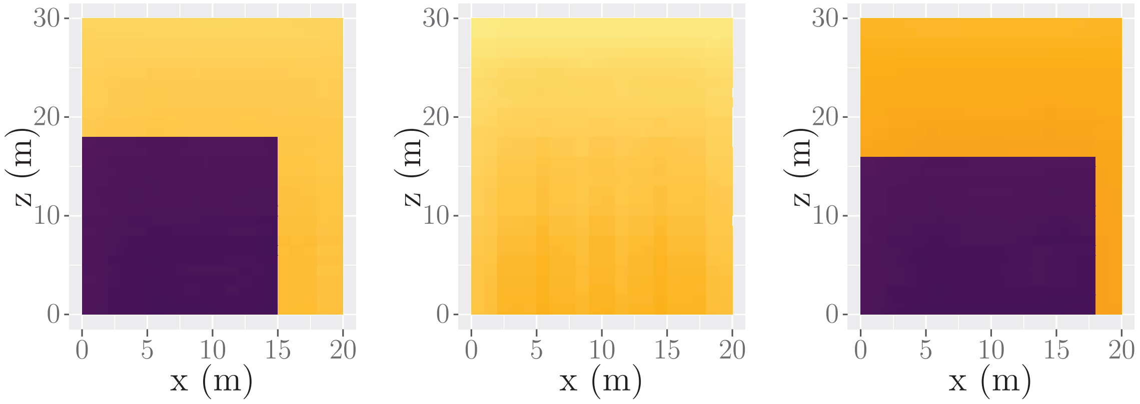

(g) February – 12:00 pm (h) June – 12:00 pm (i) October – 12:00 pm

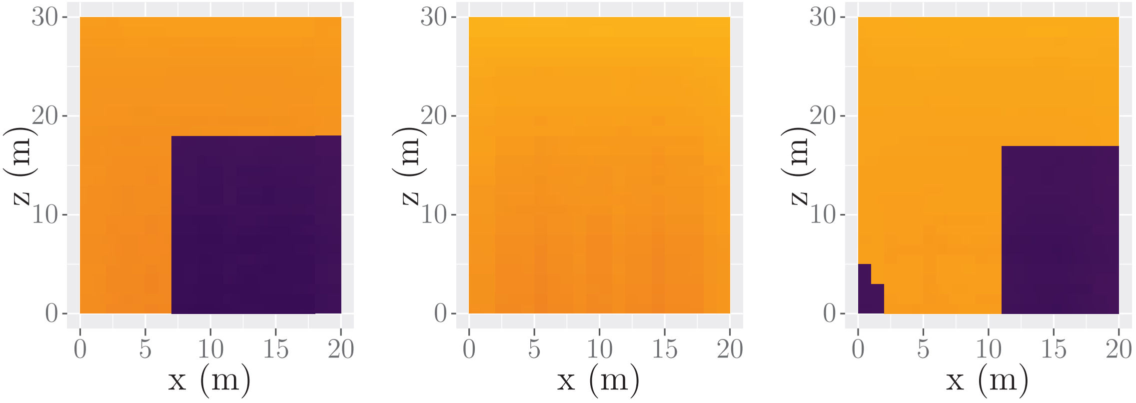

(j) February – 02:00 pm (k) June – 02:00 pm (l) October – 02:00 pm

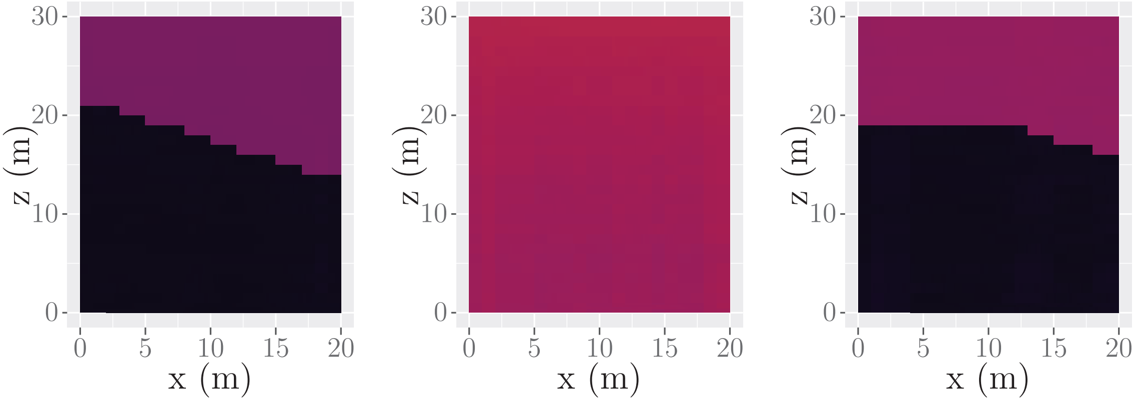

(m) February – 04:00 pm (n) June – 04:00 pm (o) October – 04:00 pm

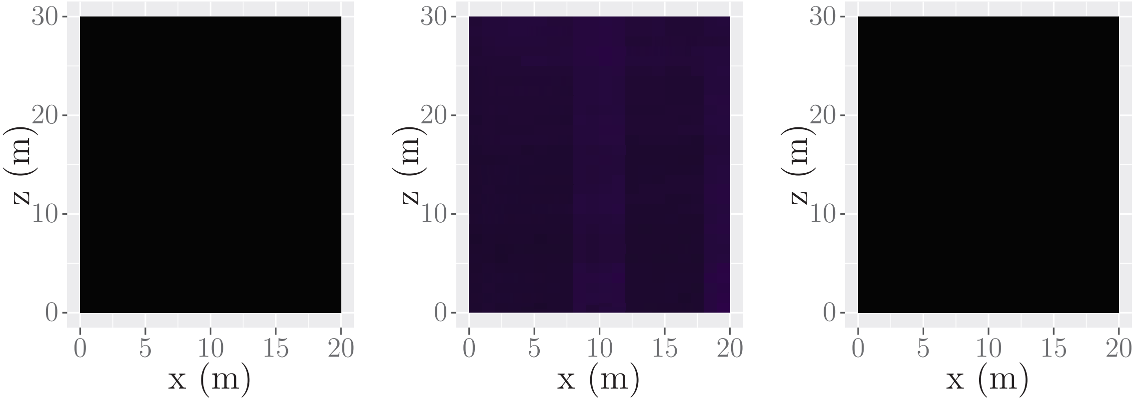

(p) February – 06:00 pm (q) June – 06:00 pm (r) October – 06:00 pm

Figure 6.1.: Comparison of Irradiation Maps of South Facade at Different Months

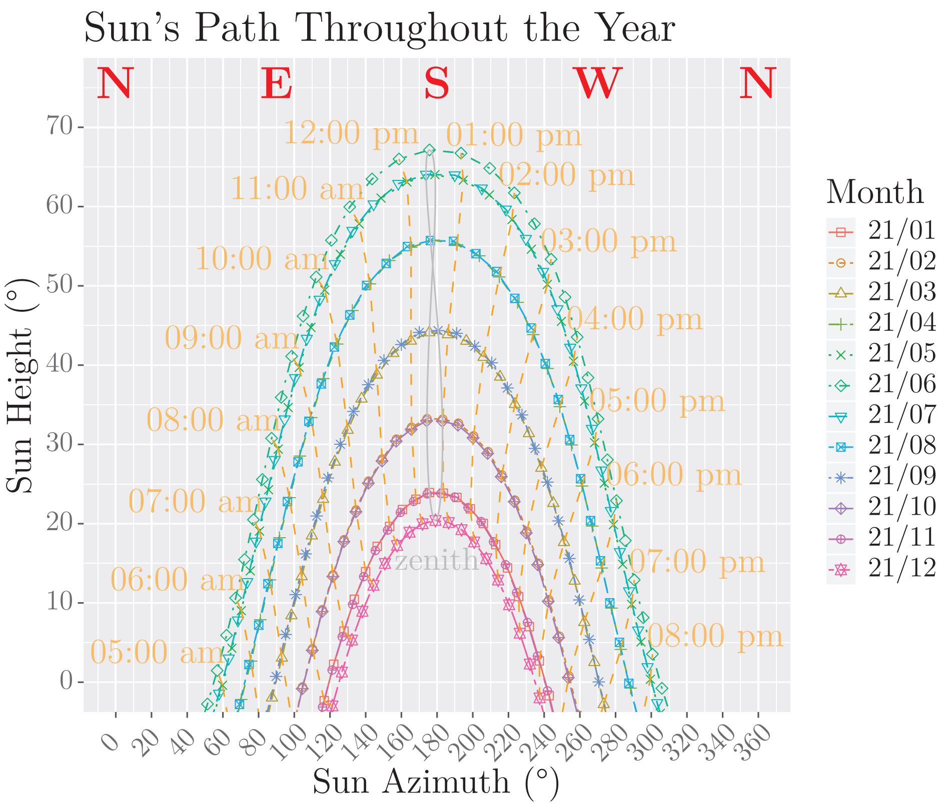

Figure 6.2.: Sun's Path Throughout the Year Over Geneva, Switzerland

6.1.2.2 *Photovoltaic Power Generation Map*

The evolution of the solar radiation profile on the facade, over the days and over the year, leads to an evolution of the potential of PV power generation of the building's facades. The generated PV power is assessed with the multicrystalline solar module TEX854. Its characteristics are given in the table 5.7 on page 114.

Connecting the panels in series affects the current flowing through them. In the case of micro-inverters, each panel is electrically independent. Thus, the current-voltage couple of the PV panel is only dependent on its level of irradiation and its temperature. However, in the case of a series connection of several PV panels, the current flowing through them is equal to the lowest current flowing through all these panels. Different connection configurations are considered:

1. one micro-inverter per PV panel;

2. one inverter for all PV panels;
3. one inverter for each vertical row;
4. one inverter for each horizontal row.

The results of these different configurations obtained from the irradiation profiles (figure 6.1 on page 156) are shown in figure 6.3 to figure 6.4 on pages 159–160. They correspond to a situation where the entire facade would be covered with PV panels. The case of micro-inverters (figure 6.3a on the next page and figure 6.4a on page 160) are the most favorable from the point of view of energy production. Indeed, only the area of the facade that is effectively hidden is affected. Thus, this case is taken as a reference for the calculation of the power generation drop. The case where all the panels are connected in series (figure 6.3b on the next page and figure 6.4b on page 160) are the least favorable cases. This is because the area of the facade, which is shaded also impacts the non-shaded area. The instantaneous production profile is like the case where the entire wall was shaded. Finally, the cases of vertical and horizontal connections (respectively figure 6.3c and figure 6.4c, and figure 6.3d and figure 6.4d) have an intermediate impact on the level potential PV power generation. Indeed, the panels impacted by the shading are those effectively hidden, as well as those connected in accordance with the direction of the series connection.

The drop of power generation due to shadowing is depending on the time of the day. Indeed, on October 16th, 2018, this drop is higher in the case of a vertical series connection. The potential of instantaneous PV power generation for the case of the micro-inverters reaches 13.39 kW. This is reduced by 20.8 % with horizontal series connection (10.60 kW) and up to 40.0 % with vertical series connection (8.04 kW). Nonetheless, the drop of power generation due to the horizontal series connection is more important than that of vertical series connection the same day at 2:00 pm. Indeed, the drop of power generation reaches 27.3 % for the horizontal series connection against 20.5 % for the vertical series connection.

Thus, it appears that, depending on the time of the day, the option to be preferred for the series connection may either be horizontal or vertical. This observation highlights the need of carrying out the comparison between the different series connection cases over the whole year to optimize the potential of PV energy production of the building.

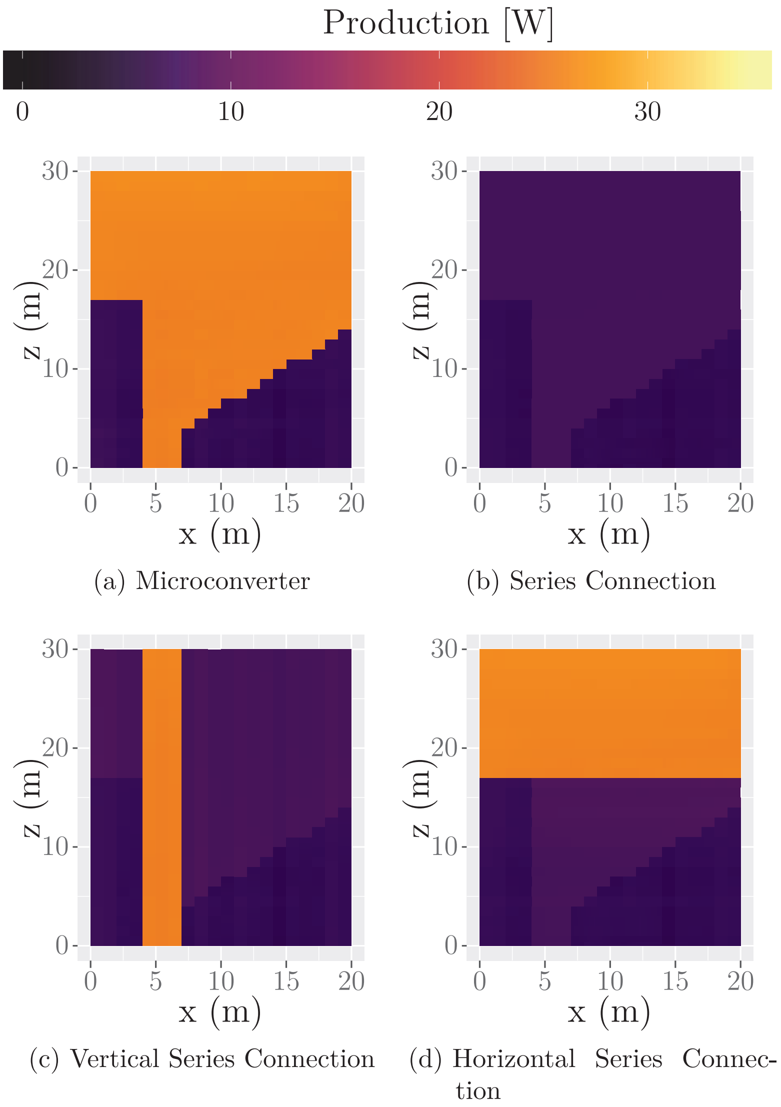

(a) Microconverter

(b) Series Connection

(c) Vertical Series Connection

(d) Horizontal Series Connection

Figure 6.3.: Comparison of Power Generation Maps
October – 10:00 am

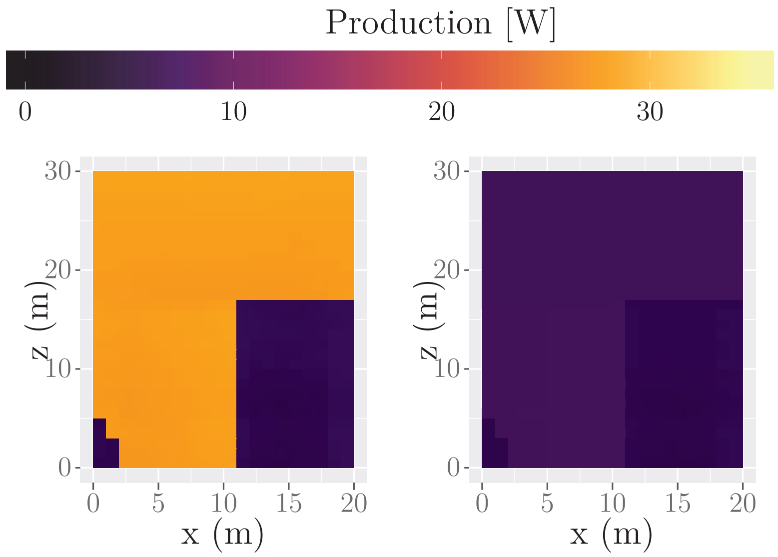

(a) Microconverter (b) Series Connection

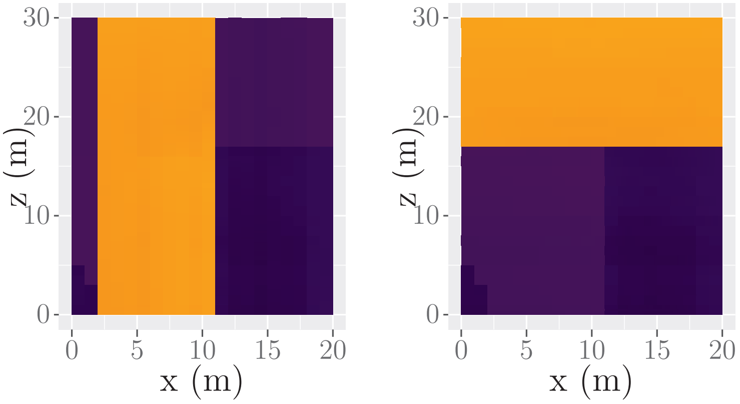

(c) Vertical Series Connection (d) Horizontal Series Connection

Figure 6.4.: Comparison of Power Generation Maps
October – 02:00 pm

6.1.2.3 *Daily Power Generation*

As seen in the previous section, the PV power generation of the building's facade depends on the type of connection of the PV panels, as well as on the time of day. This leads to an evolution of the potential of power generation over the day. This evolution for the homogeneous neighborhood and for each representative average day of the month is given in figure 6.5 on page 164.

The first reading of this figure is about the magnitude of the PV power generation over the year. Indeed, the maximum of daily power generation depends on the considered month. Thus, for the sunniest days of the year, the total amount of power may exceed 22 kW, while the one for the least sunny days is lower than 10 kW. This predictible results draws the attention to the need of taking into consideration the evolution of the weather conditions over the year to evaluate the instantaneous capacity of power generation.

The second reading is about the series connections of the PV panels, and more particularly the evolution of their influence over the year. Indeed, for the months between May and August (figure 6.5e to figure 6.5h on pages 163–164), the series connection of the PV modules only have a slight impact on the power generation potential. This is because the Sun's course of these days is high enough for the Sun to pass over the buildings (see figure 6.2 on page 157). Thus, as can be seen in figure 6.6 on page 165, the drop of power generation, compared with the reference case, is very low for these months.

The drop of PV power generation due to the series conections is much higher for the rest of the year. Indeed, the drop of power generation in the case of the series connection exceeds 40 % for the months between September and April. It can reach more than 80 % in January. This latter appears as a particular month. Indeed, it is the only one - with the month of December - for which the potential of energy production is greater for the vertical series connection. As can be seen in table 6.1 on the following page, the drop of PV power generation is lower for the vertical series connection than for the other cases.

Finally, an hour-by-hour comparison between the different types of connections can be carried out. As seen in the previous section, the option to be preferred for the series connection depends on the time of the day (the vertical connections offer a greater potential at 10:00 m on October, 16th and a smaller one the same day at 2:00 pm). This observation may also be valid for other days, such as January and February but for other days, such as March or September, the horizontal series conection offers a greater potential of power generation, whatever the considered time of the day.

Table 6.1.: Drop of Photovoltaic Power Generation According to the Connection Type

Month	Connection Type		
	Vertical Series Connection	Horizontal Series Connection	Series Connection
01 – January	−35.27 %	−36.83 %	−80.97 %
02 – February	−35.56 %	−24.49 %	−62.71 %
03 – March	−38.06 %	−15.00 %	−62.79 %
04 – April	−18.87 %	−4.46 %	−42.99 %
05 – May	−1.68 %	−0.44 %	−2.94 %
06 – June	−1.92 %	−0.51 %	−3.36 %
07 – July	−1.92 %	−0.58 %	−3.41 %
08 – August	−1.15 %	−0.38 %	−2.02 %
09 – September	−29.48 %	−9.67 %	−53.13 %
10 – October	−36.56 %	−17.90 %	−58.47 %
11 – November	−28.47 %	−27.4 %	−61.65 %
12 – December	−24.57 %	−35.20 %	−66.05 %

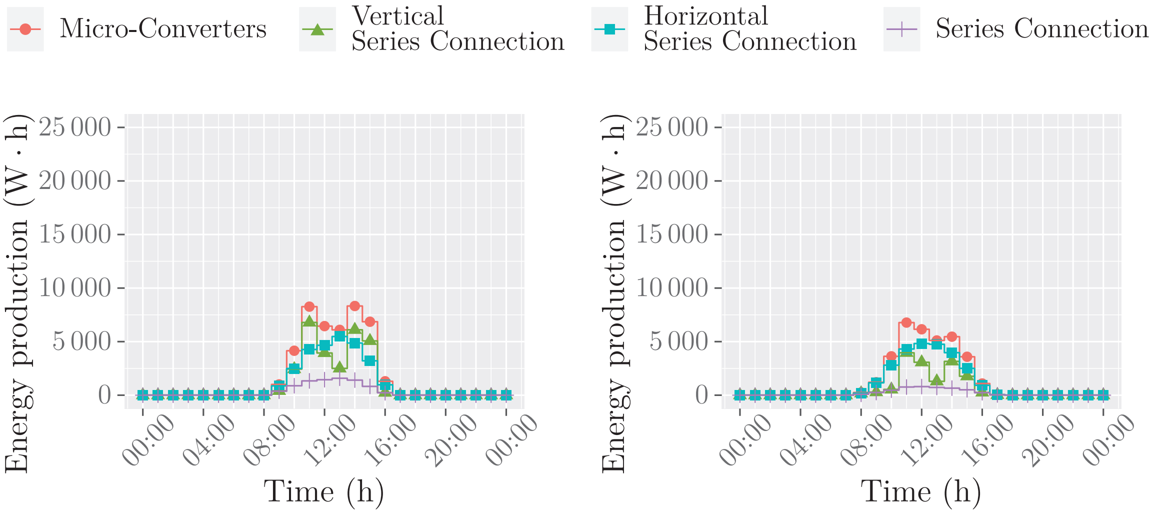

(a) January (b) February

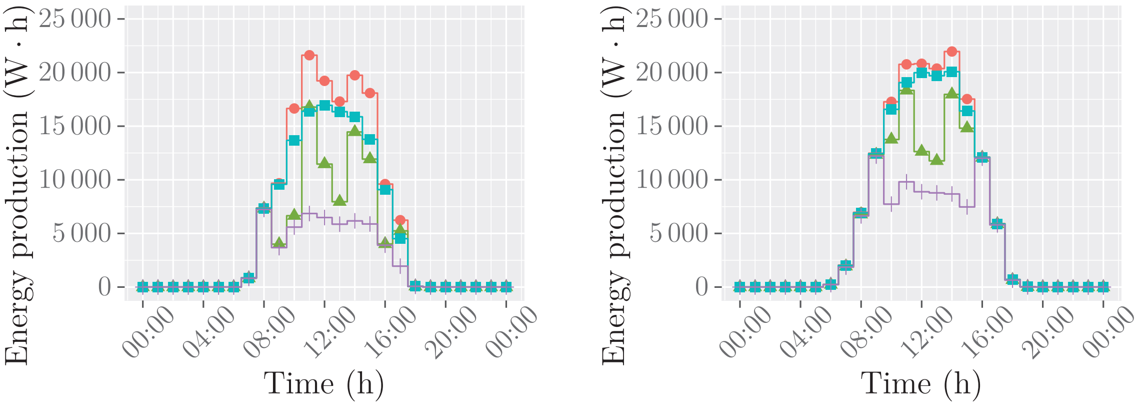

(c) March (d) April

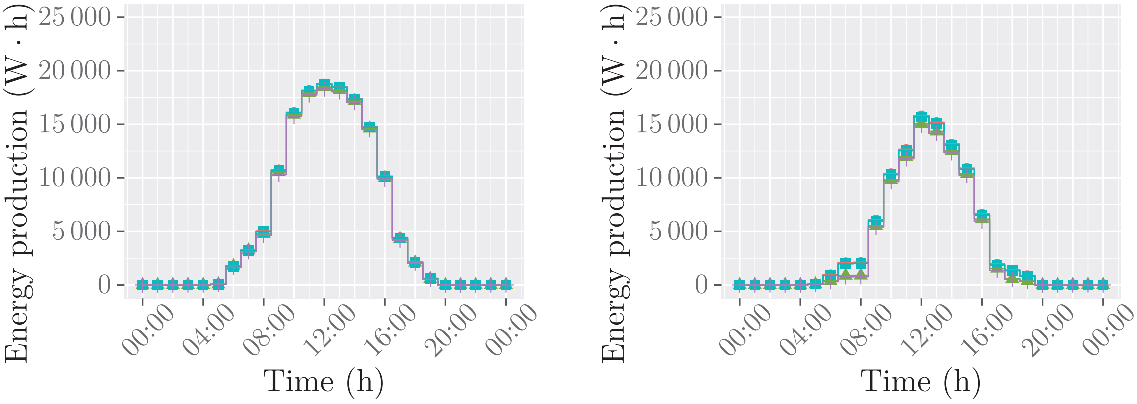

(e) May (f) June

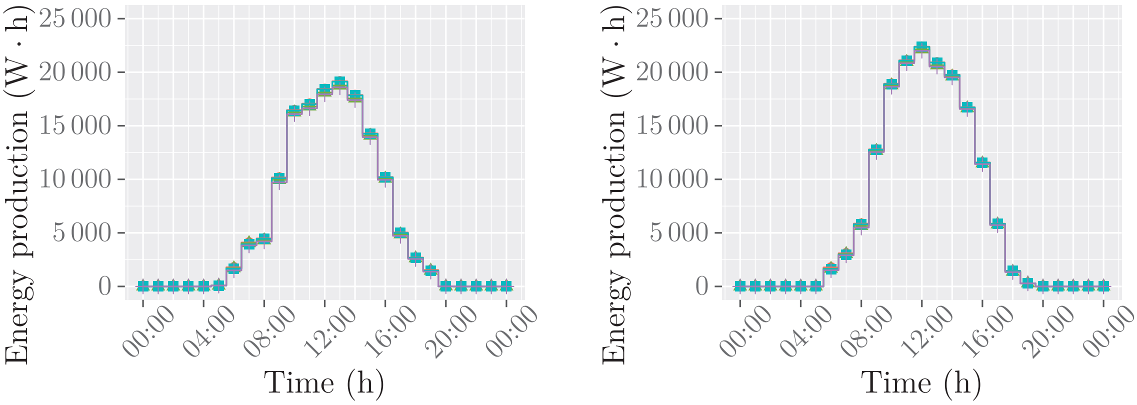

(g) July

(h) August

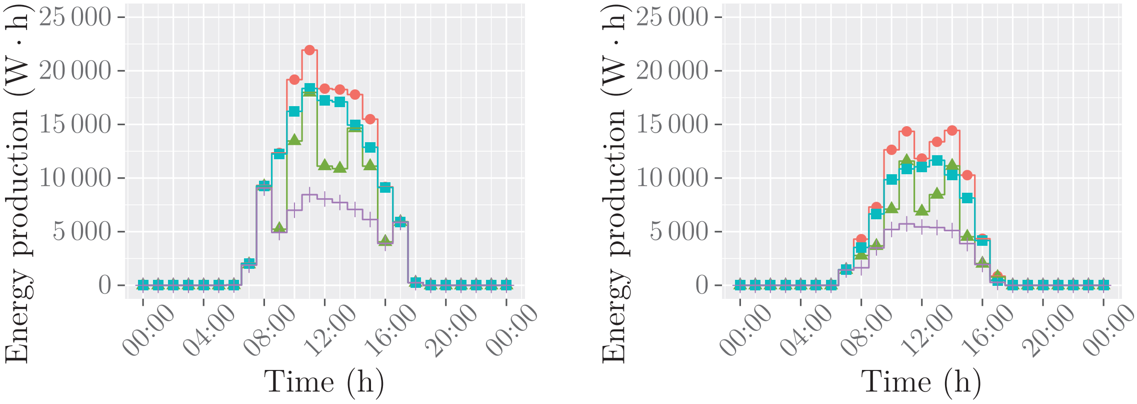

(i) September

(j) October

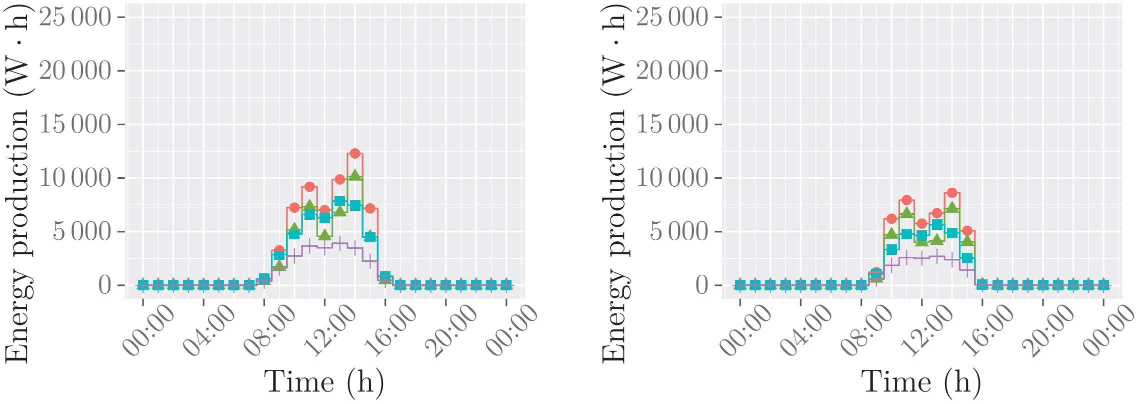

(k) November

(l) December

Figure 6.5.: Energy Production Over South Facade of Central Building

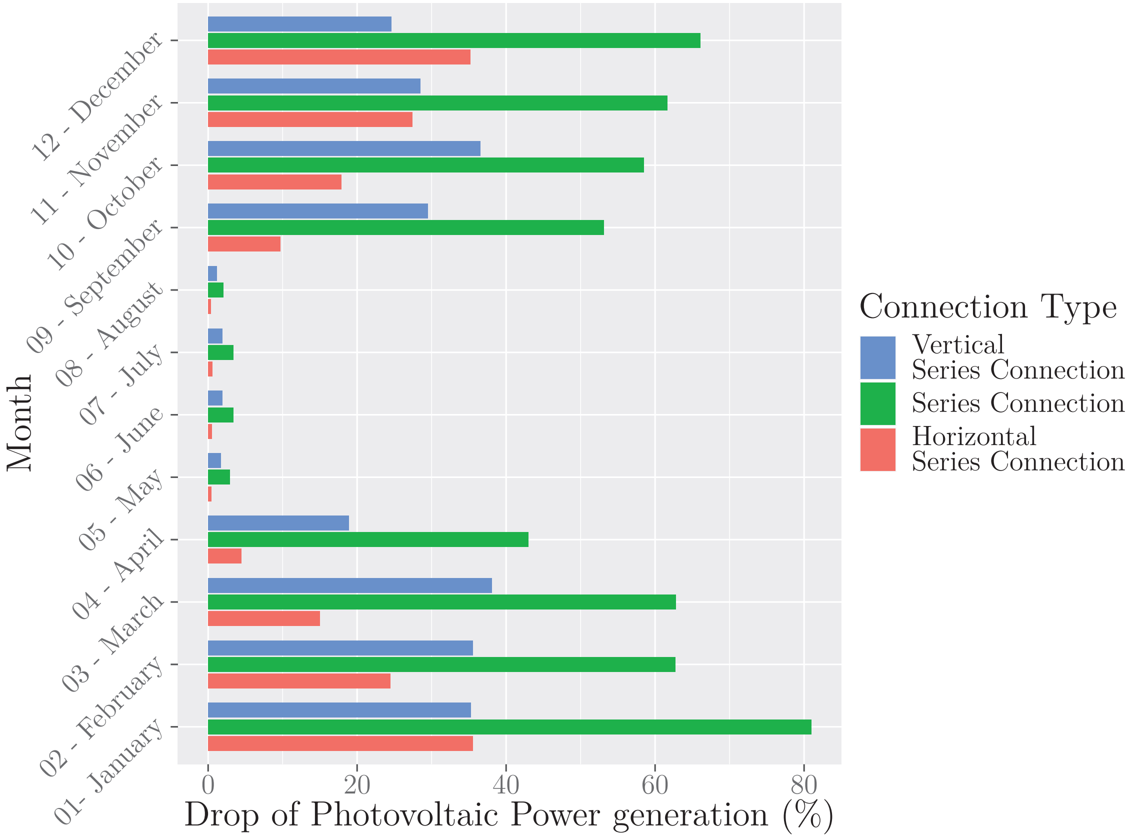

Figure 6.6.: Comparison of the Drops of Photovoltaic Power Generation

6.1.3 *Heterogeneous Neighborhood*

The previous neighborhood makes it possible to evaluate the influence of the series connections of the PV panels in a theoretical case, where all the buildings are the same as well as the distance between each of them. Nonetheless, the layout of this neighborhood is not close to an actual dristrict and then not enough to evaluate the influence of the series connection in an actual situation. Albeit this case can be used to get reference results for comparisons, an heterogeneous is needed to get results closer to the one of an actual case.

6.1.3.1 *Presentation of the Layout*

A second neighborhood is considered to overcome the gaps identified in the homogeneous neighborhood. This neighborhood, intended to be closer to an actual district because of its heterogeneity, is given in figure 6.7. In this case, the buldings' heights vary from 18 m to 42 m. The building 5, meanwhile, is 18 m high. Regarding the distances between the buildings, instead of an unique gap of 10 m, they are between 5 m and 25 m (see figure 6.8 on the facing page). This layout is more representative of an actual district, with randomly located buildings presenting different heights.

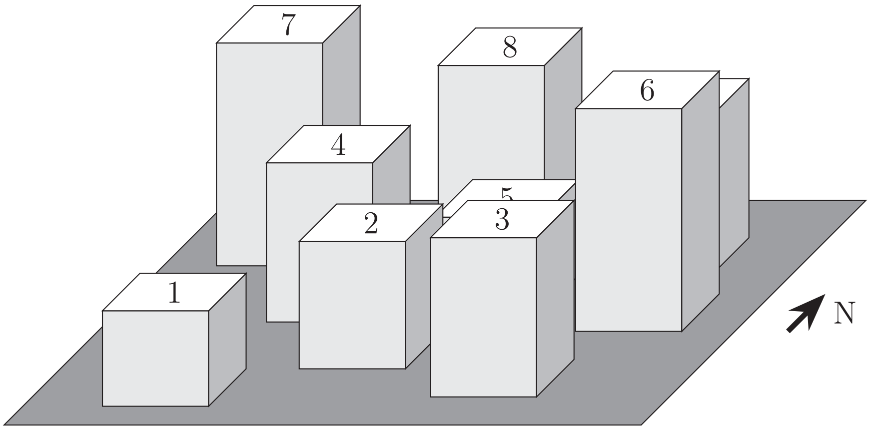

Figure 6.7.: Fictional Heterogeneous Neighbourhood – Geneva

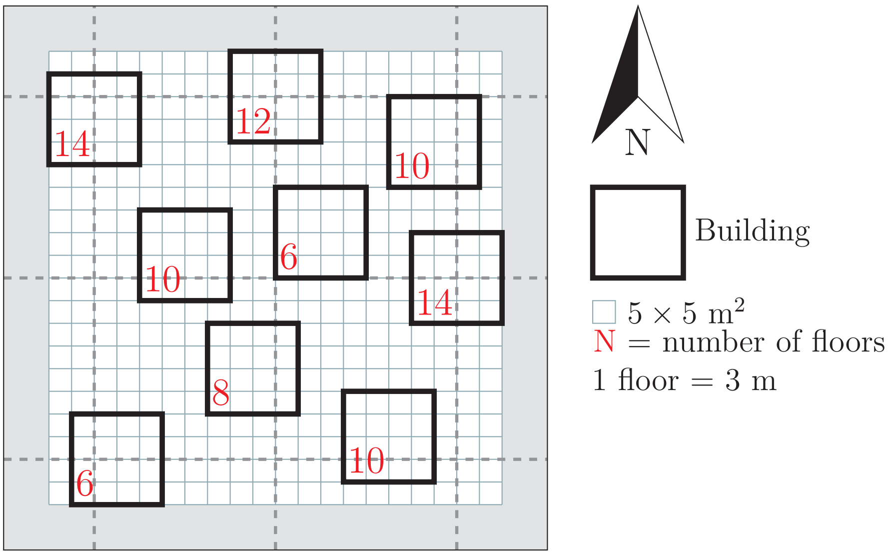

Figure 6.8.: Fictional Heterogeneous Neighbourhood (Top View) – Geneva

6.1.3.2 *Impact of the Layout on the Instantaneous Photovoltaic Power Generation*

The heterogeneity of the neighborhood has an impact on the profile of solar radiation on the facade. Indeed, unlike the previous case, the studied building is not as high as the surrounding buildings in the heterogeneous neighborhood. Thus, the building in the middle of the area is shaded for a longer time. The result in terms of instantaneous solar radiation on the facade is given in figure 6.9 on page 170.

Instead of presenting the months of February, June and October like in the case of the homogeneous neighborhood (see figure 6.1 on page 156), the months of February, May and August are plotted. Thus, the profiles of solar radiation for the month of February can be compared. The months of May and August tend to highlight the importance of the location and the height of the surrounding buildings on the spatial heterogeneity of the solar radiation on the facade.

The observed differences in terms of solar radiation profile between the homogeneous and the heterogenous neighborhood are only due to the difference of the two layouts. Indeed, every other weather conditions are the same for both of the cases: shortwave (SW) or longwave (LW) radiation, air temperature and humidity, or wind speed and direction. For the month of February, the amount of shaded area is similar for both the homogeneous and the heterogeneous cases. The shades are a bit larger in the latter case, though. The slight difference is due to the course of the Sun, which is lower in February (see figure 6.2 on page 157).

The solar radiation profiles of the months of May and August were homogeneous in the previous case of study, since the daily power generation profiles were the same for the four types of series connections. This is not the case anymore for the heterogeneous neighborhood. Indeed, as can be seen in the two columns on the right side of the figure 6.9 on page 170, parts of the facade is shaded in this case. This shading is due to the fact that the surrounding buildings are taller than the studied building. This difference in terms of solar radiation also has an influence on the daily power generation profile, as discussed in the next section.

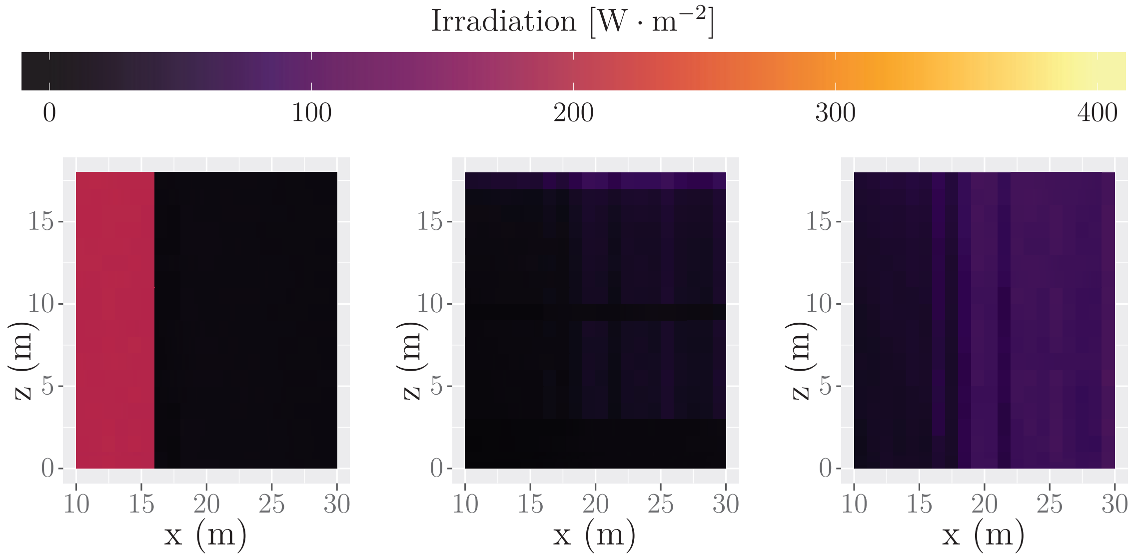

(a) February – 08:00 am (b) May – 08:00 am (c) August – 08:00 am

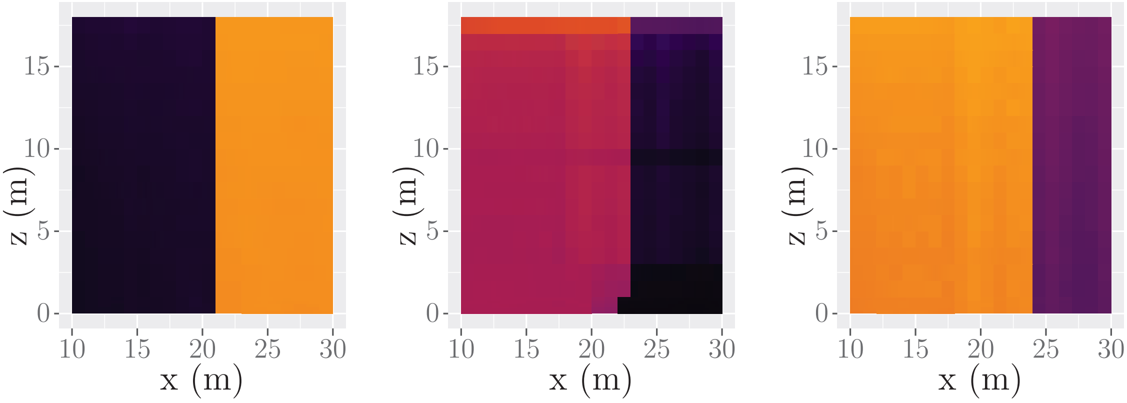

(d) February – 10:00 am (e) May – 10:00 am (f) August – 10:00 am

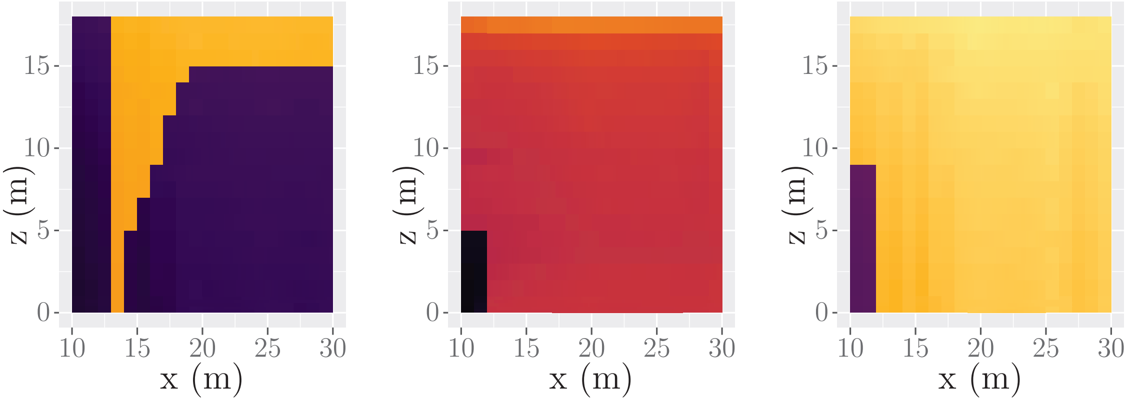

(g) February – 12:00 pm (h) May – 12:00 pm (i) August – 12:00 pm

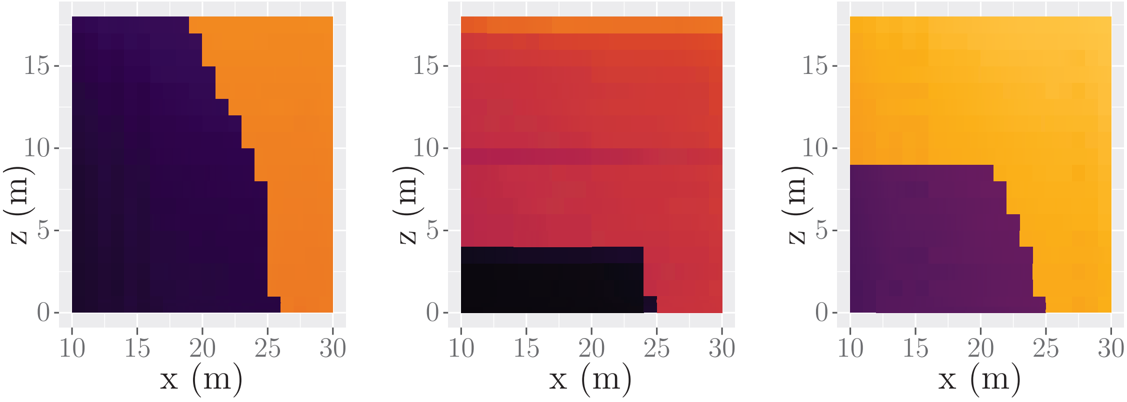

(j) February – 02:00 pm (k) May – 02:00 pm (l) August – 02:00 pm

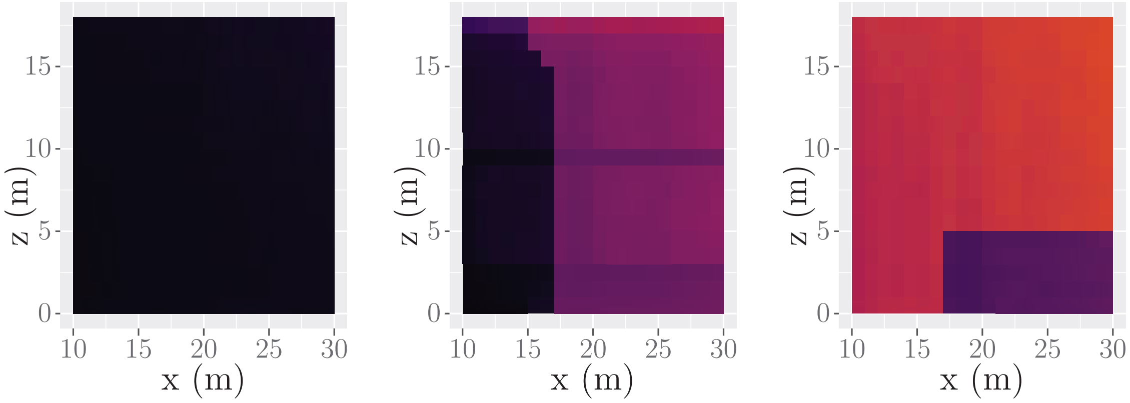

(m) February – 04:00 pm (n) May – 04:00 pm (o) August – 04:00 pm

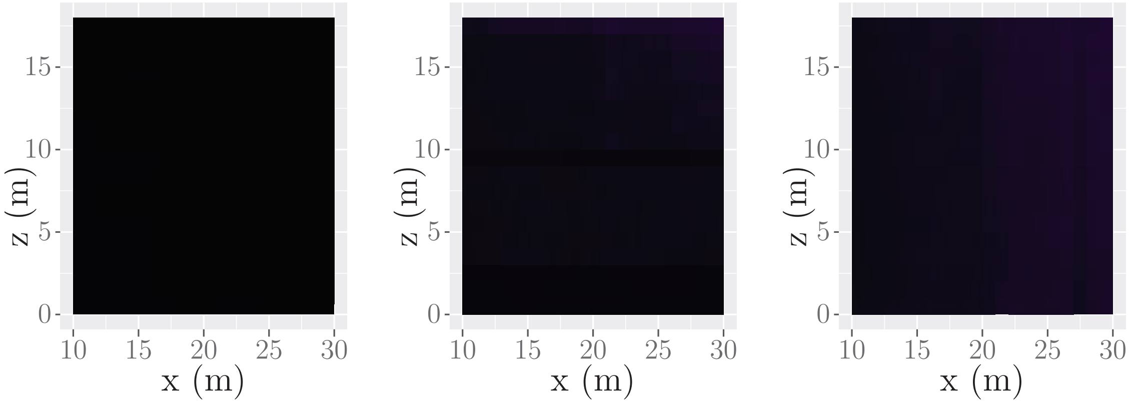

(p) February – 06:00 pm (q) May – 06:00 pm (r) August – 06:00 pm

Figure 6.9.: Comparison of Irradiation Maps of South Facade at Different Months

6.1.3.3 *Influence on the Daily Power Generation*

The evolution of the solar radiation on the facade involves an evolution of the power generation over the day. The power generation is predicted as for the homogeneous neighborhood (see figure 6.3 on page 159 and figure 6.4 on page 160). Thus, the difference between the two cases of study are only due to the difference in terms of layout.

Four months are considered for the evolution of the daily power generation: February, May, August and September (see figure 6.10 on the next page). In the previous case of study, May and August are not subject to shading. Thus, the profiles of power generation are the same for all the types of series connections. February and September are differently impacted by shadings. Nonetheless, for the homogeneous neighborhood, the horizontal series connection appears as the option to be preferred to optimize the potential of PV energy production for both months.

The first reading of the figure 6.10 on the following page is about the overall shape of the energy production profile. They are different than the one of the homogeneous neighborhood. This is due to the difference between the layouts of the two districts. Regarding the month of February (figure 6.10b on the next page), a sharp decrease can be observed in the middle of the day. This is due to the buildings 2 and 3, which are taller than the building 5 (see figure 6.7 on page 166). This configuration, combined with a low course of the Sun (see figure 6.2 on page 157) leads to a temporarily fully shaded facade. Thus, the potential of PV power generation decreases, for all of the four cases of series connections.

The case of September is slightly different. Indeed, this sharp drop of power generation is not present for the case of the micro-converters (see figure 6.10e on the following page). However, the profiles for the horizontal and vertical connections complement one another. Indeed, the vertical series connection has a sharp decrease in potential of PV power generation, while the horizontal series connection potential of production increases dramatically (almost up to the potential of the micro-converter case).

The cases of May and August are totally different than the one of the homogeneous neighborhood. Indeed, the predicted profile of energy production depend on the type of the series connections. Both micro-converters and series connections appear as the solution with the highest and the lowest potential of production, respectively. Regarding, the vertical and horizontal series connection, the solution that offers the highest potential depends on the time of the day. This is especially true for May,

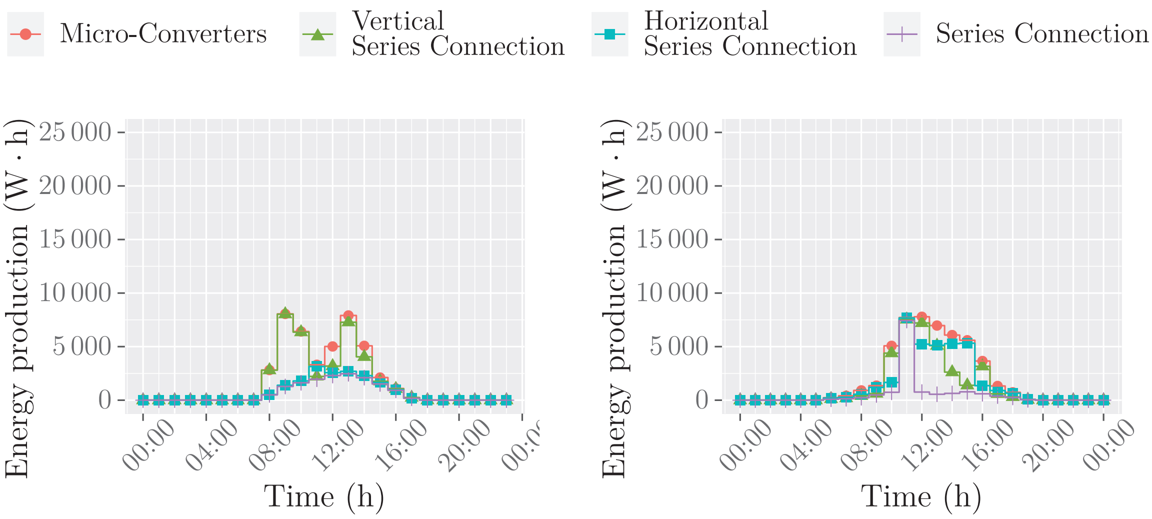

(b) February (c) May

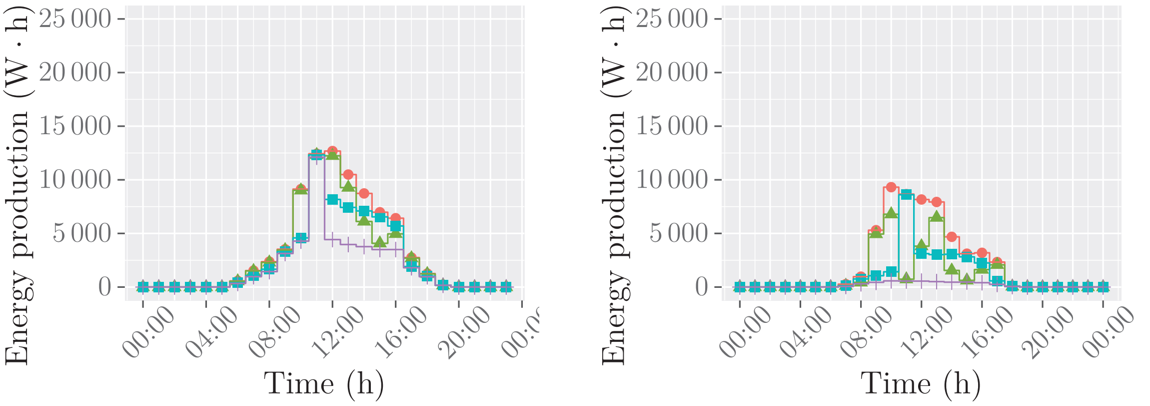

(d) August (e) September

Figure 6.10.: Energy Production Over South Facade of Central Building – Heterogeneous Neighborhood

where the curves of both cases intersect several times during the day. Considering the potential of production of the entire day, the difference between the two cases is less than 4 %, while the difference in terms of instantenous power generation can exceed 300 %.

6.2 SEASONAL BEHAVIOR OF THE PHOTOVOLTAIC GENERATION MODELS

The electrical response of a photovoltaic (PV) panel depends on weather conditions. As these vary throughout the year, the PV power that can be produced also varies. It is therefore important that the PV production models are able to provide accurate results, taking into account the evolution of these weather conditions.

6.2.1 *Context of Study*

The main goal of the following study is to evaluate the seasonal behavior of the proposed PV power generation model. In this context, a comparison between experimental data and numerical results is carried out. The numerical results are obtained by applying the double-diode model on data issued from simulation carried out with ENVI-met. The experimental data are from measurements carried out within the framework of the RESSOURCES project (see 1.1.2.2 on page 6), throughout 2012.

The details of the vertical productive facade is given in figure 6.11 on the following page. It is composed of semi-transparent PV modules, divided into three blocks (see figure 6.11b on the next page). This layout makes it possible to take into consideration the spatial heterogeneity in terms of PV power generation in accordance with the considered height.

Among the parameters that influence the PV power generation, there are: the shortwave (SW) radiation, the surface temperature of the PV module and, indirectly, the wind. Thus, the influence of these three parameters are studied in the following.

In order to limit the time of simulation in the context of the characterization of the seasonal behavior of the PV power generation model, while studying the influence of the aforementioned parameters, four days have been selected, regarding the levels of solar irradiation, the air temperature and the wind velocity:

1. January, 12th;

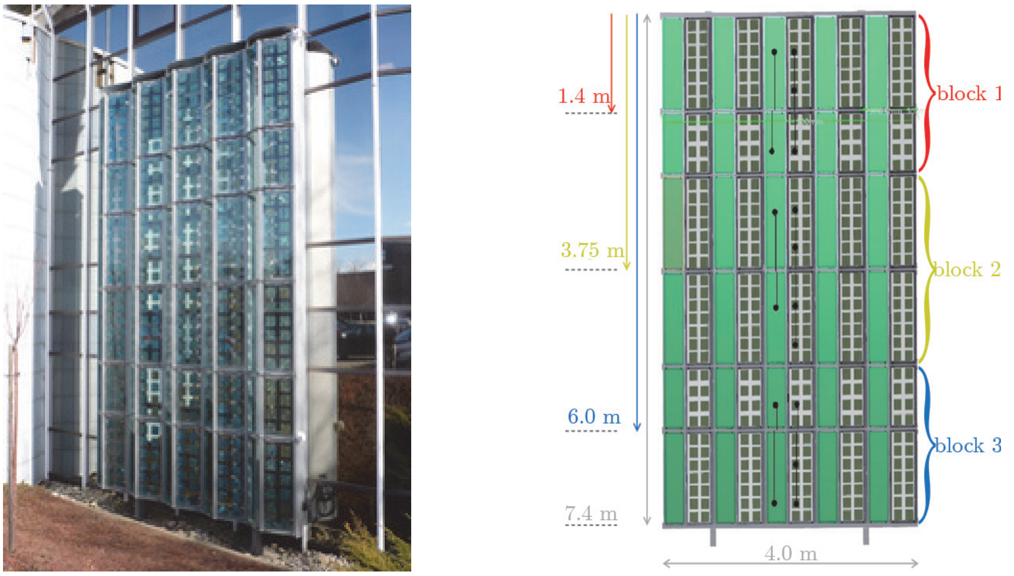

(a) Solar Modules on the Vertical Facade

(b) Layout of the Blocks Composing the Facade

Figure 6.11.: Facade of the HBS-Technal Headquarter Building

2. June, 28th;
3. August, 20th;
4. September 23th.

The weather conditions of these days are given in table 6.2 on the facing page. For each of these days, the predicted PV power is compared with the measured values.

Table 6.2.: Weather Conditions of the Selected Days for the Study of the Seasonal Behavior of the Photovoltaic Power Generation Model

Day	Warm / Cold Day	Sunny / Cloudy Day	Windy Day
January, 12th	Cold	Cloudy	Not Windy
June, 28th	Warm	Sunny	Windy
August, 20th	Warm	Sunny	Not Windy
September, 23rd	Warm	Moderately Sunny	Windy

6.2.2 *Comparison Between Experimental Data and Numerical Results*

The characterization of the seasonal behavior of the proposed PV power generation model is carried out with a comparison between the measured and the predicted values for the output PV power, regarding the level of SW radiation, the surface temperature or the wind velocity near the building's facade. In addition, the agreement between the measurements and the results is also checked, in order to verify the sources of bias in the production model.

6.2.2.1 *Correspondence Between the Predicted and the Measured Photovoltaic Power*

For each studied day, the predicted power is plotted against the measured power. Thus, a perfect correspondence between the numerical results and the experimental data would lead to a straight line along the first bisector.

To evaluate the influence of the weather parameters (SW radiation, surface temperature and wind velocity) on the accuracy of the PV power generation model, the points of evaluation are colored in accordance with their levels. These graphs are given in figure 6.12 to figure 6.15 on pages 178–181.

The results for the four days can be broken into two groups in accordance with the way with which their results match:

1. June, 28th and August, 20th, with a good accordance between the predicted and the measured values;

2. January, 12th and September, 23rd, where the predicted value is always overestimated.

The quality of the correspondence between the predicted and the measured values, regarding the day of study and the block of the facade, is given in table 6.3. Two parameters are considered to evaluate the correspondence between the predicted and the measured values:

1. The slope: the closer to one, the better the correspondence between the predicted and the measured values;
2. The coefficient of determination (R^2): the closer to one, the closer the linear relationship between the predicted and the measured values.

Table 6.3.: Quantitative Analysis of the Correspondence Between the Predicted and the Measured Photovoltaic Power Generation

Day	Block 1	Block 2	Block 3
January, 12th	$slope = 1.717$ $R^2 = 0.614$	$slope = 1.803$ $R^2 = 0.652$	$slope = 2.760$ $R^2 = 0.591$
June, 28th	$slope = 0.964$ $R^2 = 0.883$	$slope = 0.722$ $R^2 = 0.885$	$slope = 0.729$ $R^2 = 0.800$
August, 20th	$slope = 0.890$ $R^2 = 0.761$	$slope = 0.667$ $R^2 = 0.724$	$slope = 0.736$ $R^2 = 0.649$
September 23rd	$slope = 3.764$ $R^2 = 0.893$	$slope = 3.016$ $R^2 = 0.869$	$slope = 4.756$ $R^2 = 0.822$

Regarding the first group of results, no clear influence of the irradiation and the temperature on the accuracy of the results appears. Indeed, the higher the level of irradiation, the higher the predicted and the measured powers. The accuracy for the same level of irradiation varies, though. This observation is also valid for the temperature (see figure 6.13 on page 179 and figure 6.14 on page 180). Nevertheless, the wind velocity seems to have an influence on the accuracy of the PV power generation model.

Indeed, the days of June, 28th and August, 20th are both warm and sunny. The only difference between these two days is about the wind velocity. The average wind speed of June, 28th is $3.16\,\mathrm{m} \cdot \mathrm{s}^{-1}$, while the one of August, 20th is $1.04\,\mathrm{m} \cdot \mathrm{s}^{-1}$. It appears that a higher wind speed provides more accurate results in terms of predicted PV power, as shown by the higher coefficient of determination for June than for August.

These observations are also valid for the second group of results: January, 12th and September, 23rd. Indeed, the correlation between the predicted and the measured values are better for the windy days. September, 23rd, with an average wind velocity of $5.31\,\mathrm{m \cdot s^{-1}}$, has a better correspondence between the predicted and the measured PV power than January, 12th, with an average wind speed of $0.65\,\mathrm{m \cdot s^{-1}}$.

The accuracy of the predicted values can also be evaluated with two indicators: the mean absolute percentage error (MAPE) and the root mean squared error (RMSE) as defined in equation (5.9) on page 141 and equation (5.8) on page 141. They are given in table 6.4.

The PV power generation model is proving to be accurate. Indeed, except for the block 3 and the day of January, 12th, the MAPE stays below 60 %. The accuracy of the model decreases for the block 3, which is the lowest one. For the blocks 1 and 2 (the upper part of the facade), the MAPE stays below 50 %, which is a good score and highlights the ability of the PV power generation model to predict accurately the PV power generation for the sunny days.

Regarding the January, 12th, the MAPE is higher than the ones for the other days. This is not due to some specific points for which the predicted values are not accurate but to an overall overestimation as can in figure 6.16 on page 182.

Table 6.4.: Mean Absolute Percentage Error and Root Mean Squared Error per Block of Measurement for the Four Studied Days

Day	Block 1		Block 2		Block 3	
	MAPE (%)	RMSE (W)	MAPE (%)	RMSE (W)	MAPE (%)	RMSE (W)
January, 12th	83.78	28.262	108.73	29.523	121.86	34.512
June, 28th	40.70	17.706	31.22	25.664	110.55	29.243
August, 20th	42.91	16.687	36.36	22.310	99.13	21.780
September 23rd	57.09	13.447	44.91	10.863	86.03	12.234

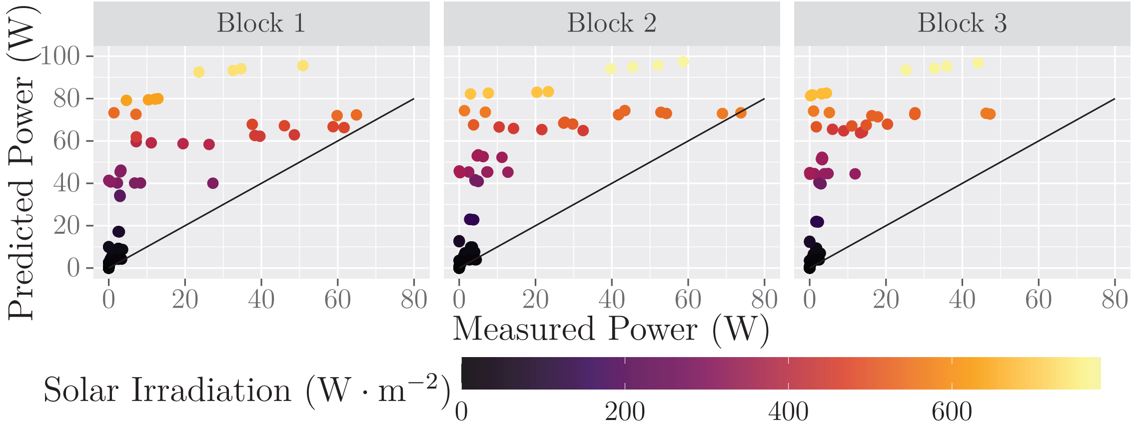

(a) Irradiation

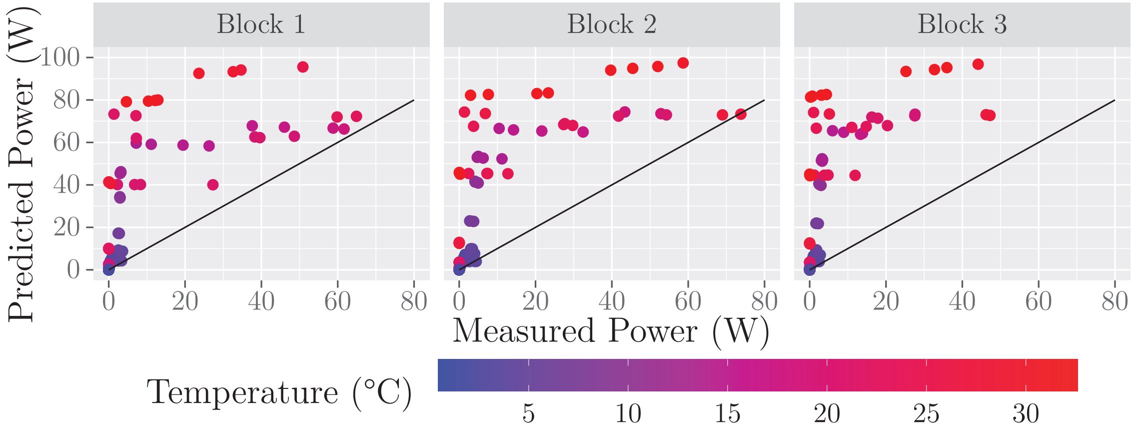

(b) Temperature

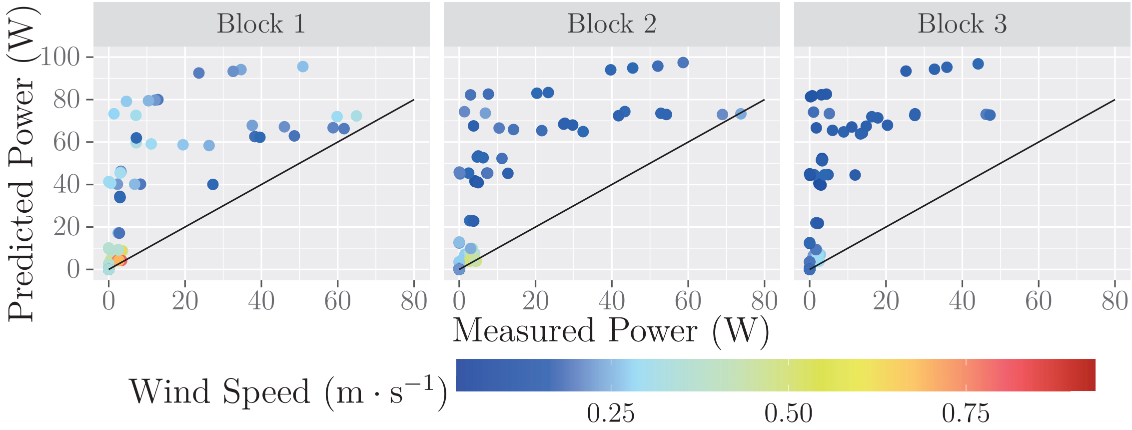

(c) Wind Speed

Figure 6.12.: Correspendence Between the Predicted and the Measured Power Generation – January, 12th

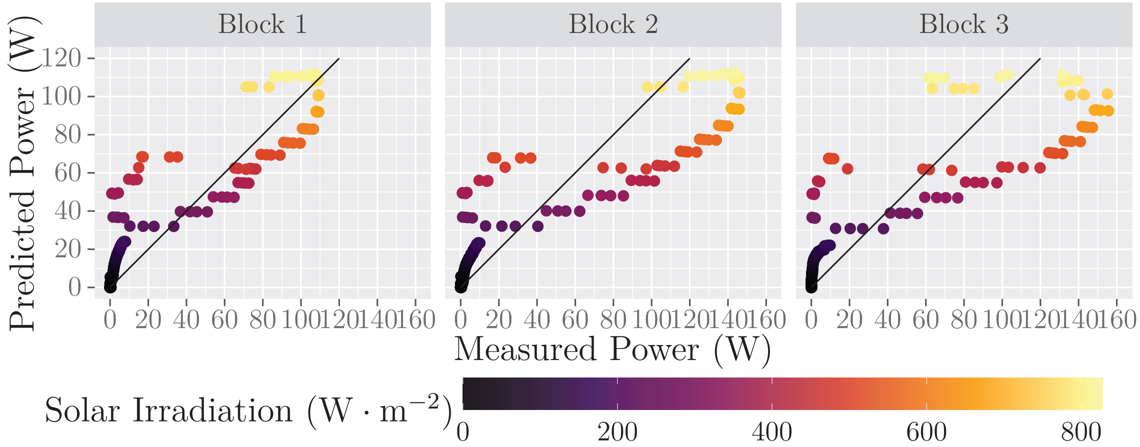

(a) Irradiation

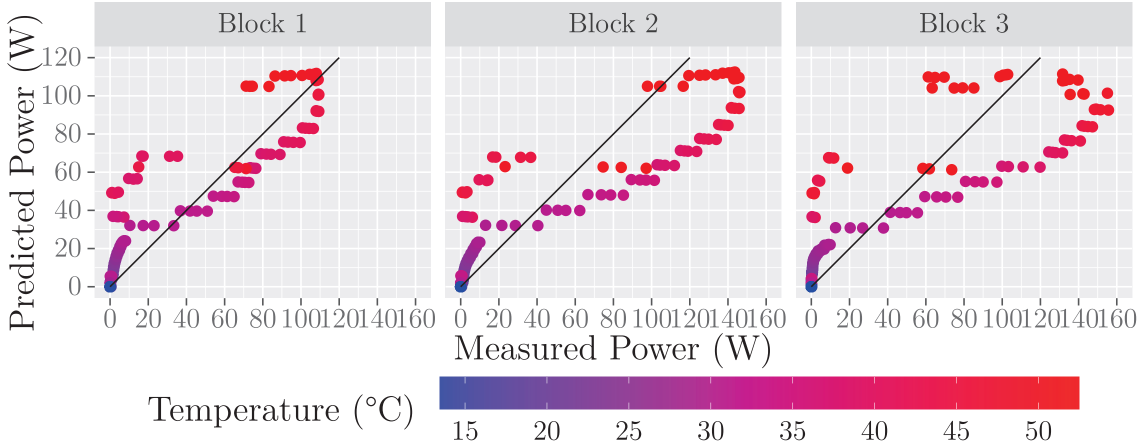

(b) Temperature

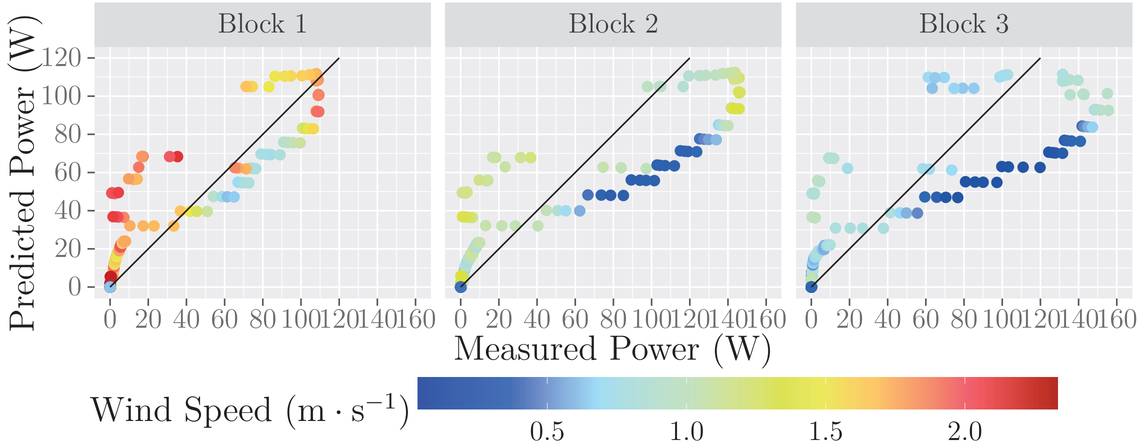

(c) Wind Speed

Figure 6.13.: Correspondence Between the Predicted and the Measured Power Generation – June, 28th

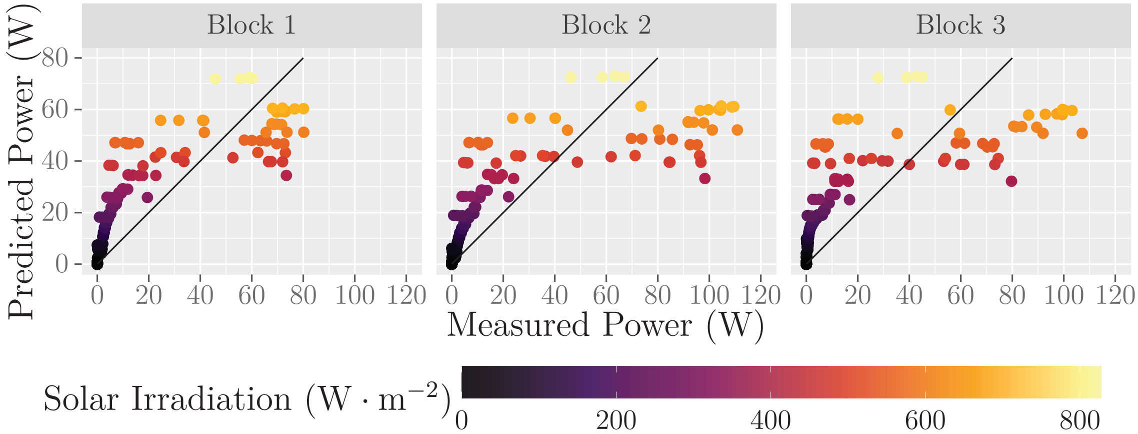

(a) Irradiation

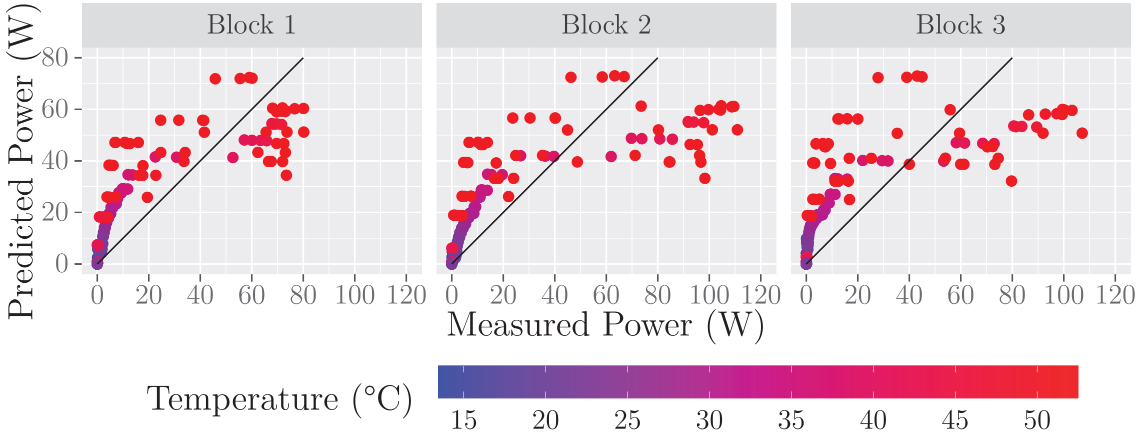

(b) Temperature

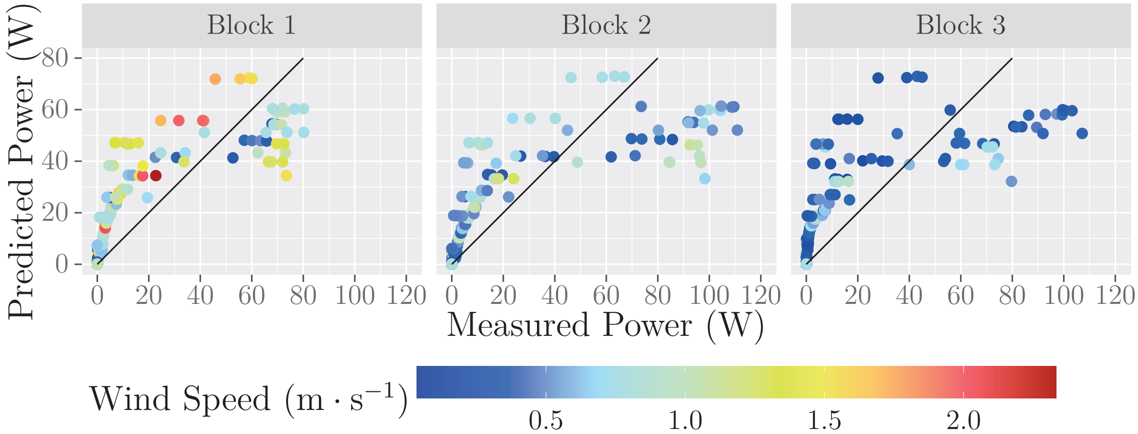

(c) Wind Speed

Figure 6.14.: Correspondence Between the Predicted and the Measured Power Generation – August, 20th

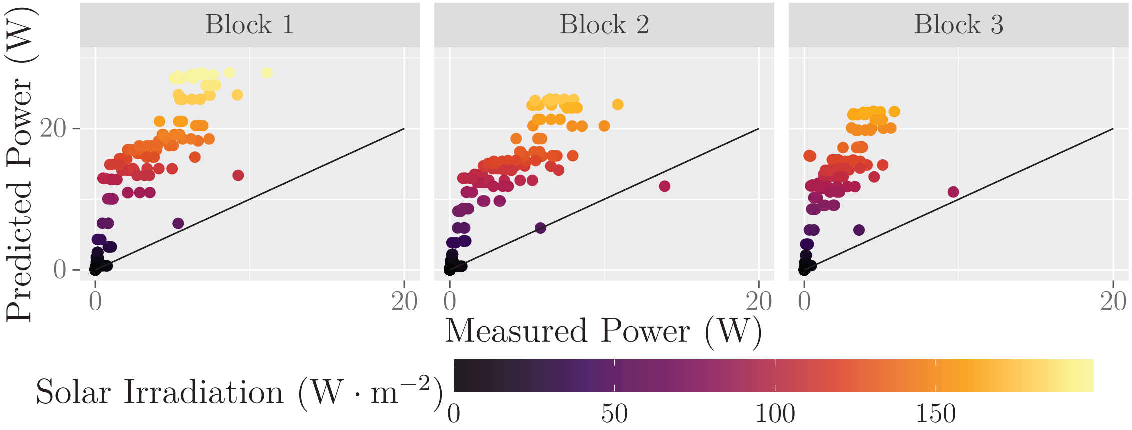

(a) Irradiation

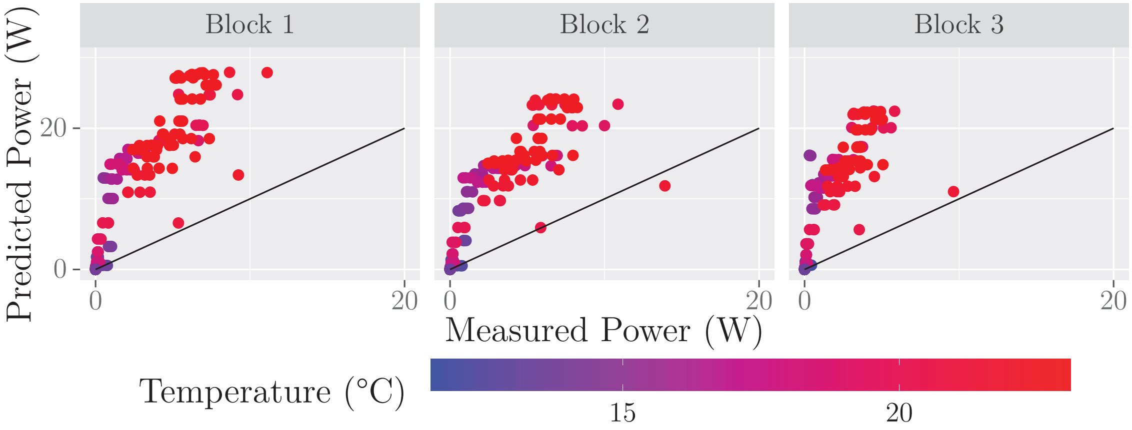

(b) Temperature

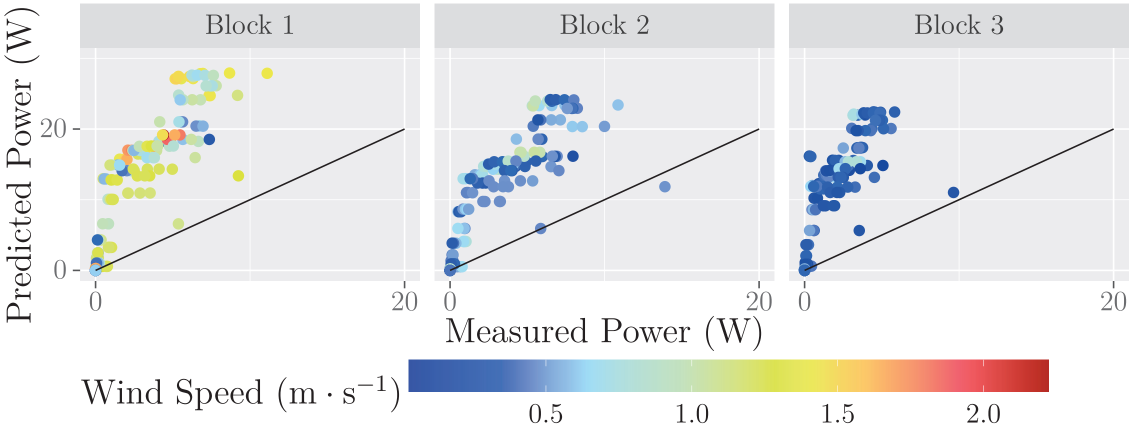

(c) Wind Speed

Figure 6.15.: Correspondence Between the Predicted and the Measured Power Generation – September, 23th

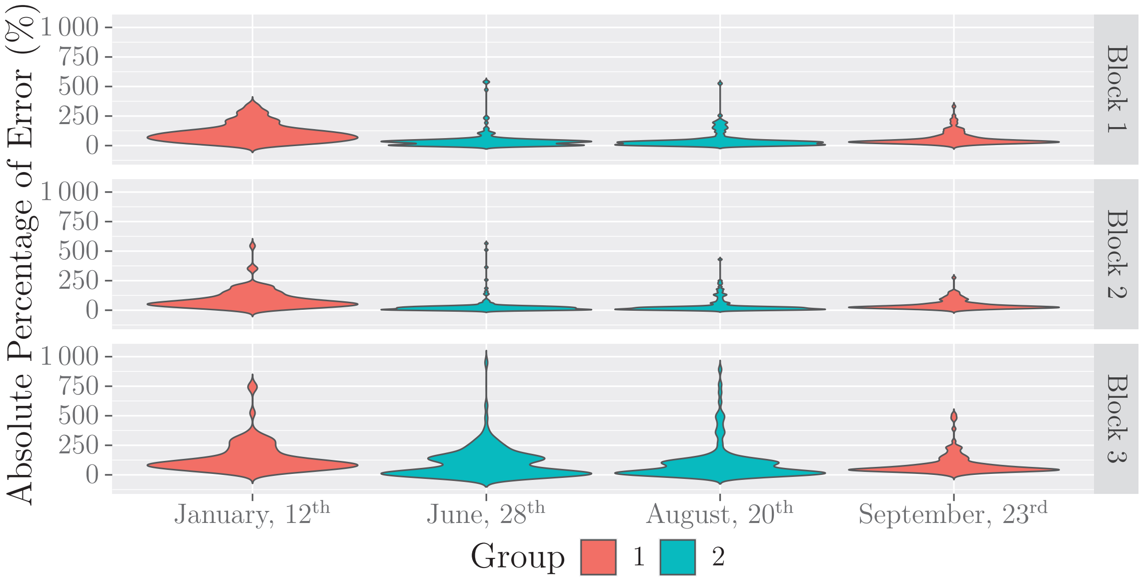

Figure 6.16.: Distribution of the Absolute Percentage Error for the Four Studied Days

Regarding the results of the block 3, several parameters can explain the observed difference. First, the lower part of the facade is closer to the ground. Thus, a part of the solar radiation can be reflected by the ground to the facade, and by so can increase the amount of SW radiation received by the facade. Secondly, vegetation is close to the actual building but is not taken into consideration in the simulation. The shading that it causes is therefore not taken into account, which leads to an overestimation of the PV power produced.

The trend emerging for the block 3 for the days of June 28th and August, 20th is also valid for the days of January, 12th and September, 23rd. Indeed, the MAPE and the RMSE are the highest in each case.

Regarding the results for the day of September, 23rd the predicted power is overestimated. Nevertheless, the MAPE remain low for both of the blocks 1 and 2 (around 50 %). Thus, even if the predicted PV power is overestimated, the accuracy of the model is acceptable. This is not the case for the day of January, 12th.

The results for the cold and cloudy day are not as accurate as the ones for the other days. Indeed, the MAPE exceed 80 %. The distribution of the absolute percentage error for the day of January, 12th figure 6.16 shows that the errors are globally larger for this day. This overestimation of the predicted PV power generation can be due to the height of the Sun. Indeed, as seen in figure 6.2 on page 157 (with the example of Geneva), the Sun's course is lower at this time of the year. Thus, inaccuracies in terms of geometry for the modeled district may lead to an overestimation of the SW radiation received by the facade. A check of the correspondence between the measured and the predicted values on the building's facade is therefore necessary in order to distinguish the sources of bias of the proposed PV power generation model.

6.2.2.2 *Correspondence Between the Predicted and Measured Weather Conditions*

The observed differences in terms of predicted power generation varies over the day. In addition, it is also due to the differences between the input data for the model (SW radiation and surface temperature) and the measured weather conditions. The following section puts a focus on the similarities and the differences, between the predicted and the measured values, which can partly be sources of inaccuracies for the PV power generation model.

ENVI-met makes it possible to use local measurements as inputs, in a format detailed in section 4.1 on page 73. Thus, the input data, and more particularly the direct SW radiation correspond to measurement carried out on buildings roofs. The accordance between the predicted and the measured values is therefore a key issue in the evaluation of the accuracy of the PV power model.

ON BUILDING'S ROOF

The comparison between the predicted and the measured SW radiation on the HBS building's roof is given in figure 6.17 on the next page. For the four considered days, the SW radiation is globally well reproduced by the ENVI-met model. Only the first hours of sunshine for the days of June, 28th and August, 20th can be questioned.

Regarding the intermittency, mainly observed on August, 20th, it can not be reproduced by ENVI-met, because of the time step of the input data (30 minutes). Nonetheless, the SW radiation is accurately reproduced by ENVI-met on the roofs. Therefore it can not be a source of inaccuracy for the proposed PV power generation model.

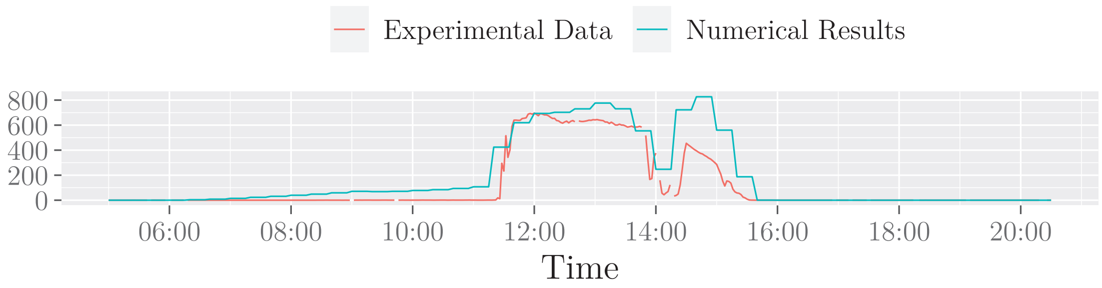

(a) January

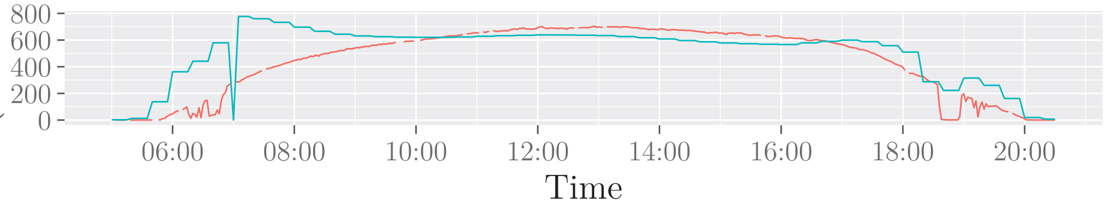

(b) June

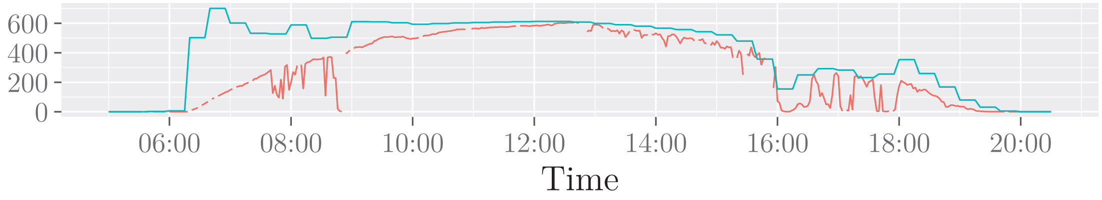

(c) August

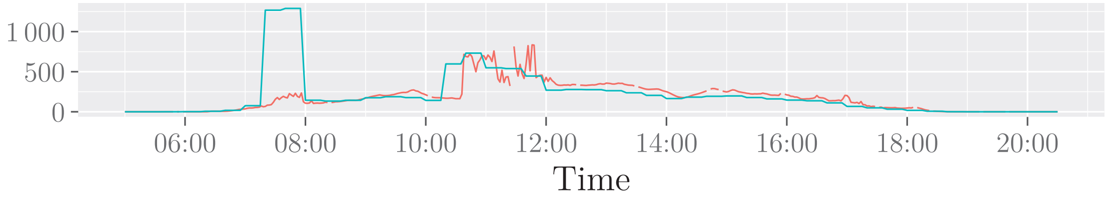

(d) September

Figure 6.17.: Correspondence Between the Predicted and the Measured Shortwave Radiation on Building’s Roof

ON BUILDING'S FACADE

ENVI-met makes it possible to use local measurements as inputs for the simulation. Nevertheless, the values which are entered are the one on the top of the modeled domain. In particular, the value of the direct SW radiation can either be the beam horizontal irradiance (BHI) or the beam normal irradiance (BNI). None of these are the same values as the one on the facade. Indeed, this latter is given by the radiative model of ENVI-met.

Two pyranometers are installed on the facade of the HBS building and are located on the block 1 and 3, as well as thermocouples. This makes it possible to assess the ability of the ENVI-met model to predict accurately the level of solar radiation and the surface temperature, over the days.

The significant differences observed for the day of January, 12th are mainly due to the inaccuracy in terms of predicted SW radiation (which has an impact on the surface temperature). The comparison between the predicted and the measured values for January, 12th are given in figure 6.18 on the following page. It appears that until 01:00 pm, the predicted values in terms of SW radiation and surface temperature are in accordance with the measured ones. After that, and until 06:00 pm, the SW radiation is highly overestimated on the facade. This leads to the significant overestimation of the PV power generation for this day. Nevertheless, the sharp decrease in terms of SW radiation between 03:00 pm and 05:00 pm is well reproduced by the ENVI-met as well as the one in terms of PV power generation by the double-diode model.

For the days of June, 28th and August, 20th, the predicted and measured values are in good accordance, in terms of both solar irradiance and surface temperature, as well as in terms of PV power generation. However, a remark can be made regarding the high-frequency phenomena. Indeed, the solar radiation has sharp evolution in the afternoon of June, 28th. This intermittency can not be accurately reproduced by ENVI-met because of the format of the input data (given with a time step of 30 minutes). Thus, the evolutions of the predicted SW radiation and PV power generation are smoothened.

A last point can be made about September, 23th. Indeed, aside from the small shift for the surface temperature (around 3 °C), the values predicted by ENVI-met are in good accordance with the measured ones. Despite this, the predicted PV power generation is more than twice higher than the measured one.

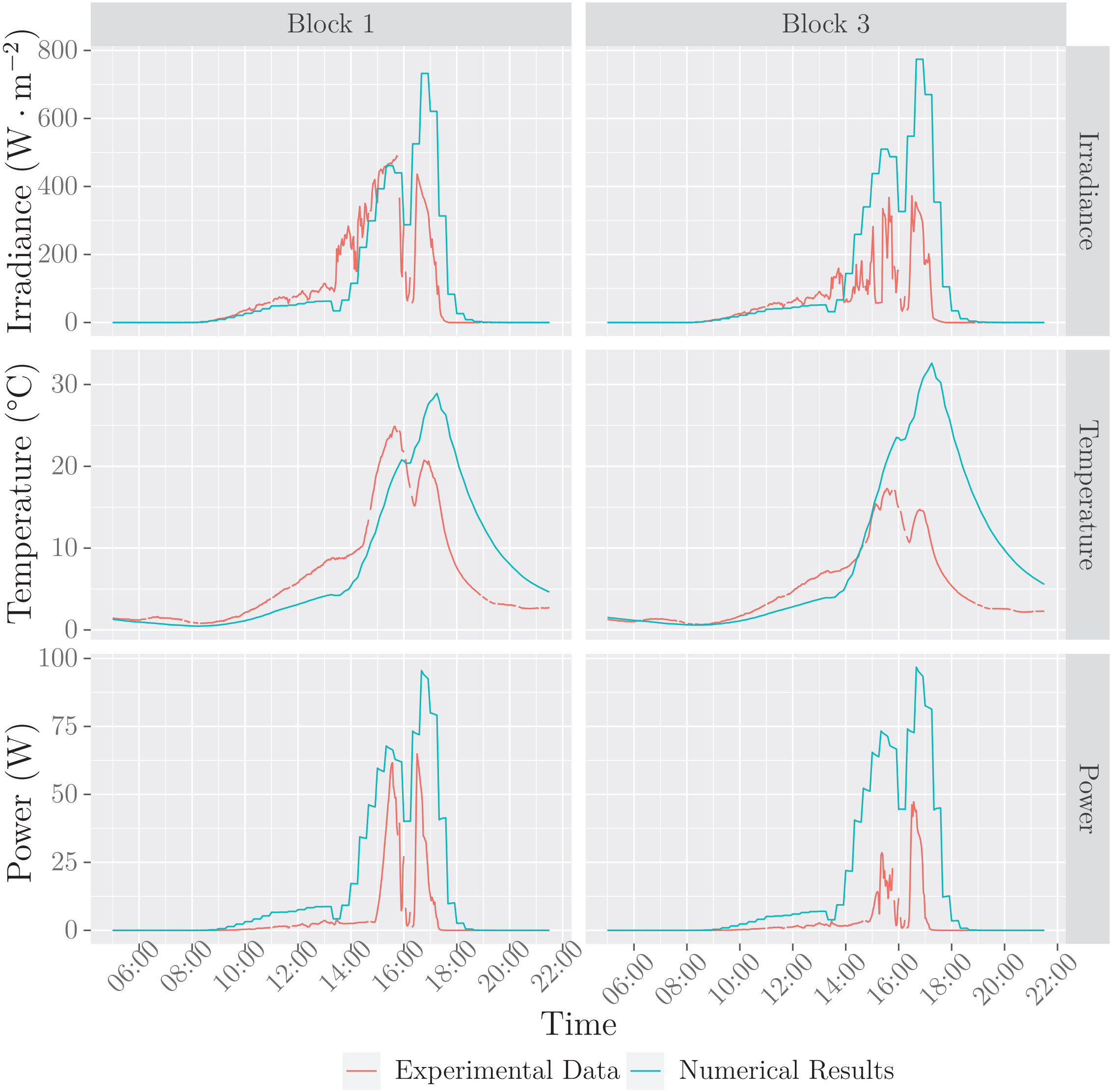

Figure 6.18.: Correspondence Between the Predicted and the Measured Values on the Building's Facade – January, 12th

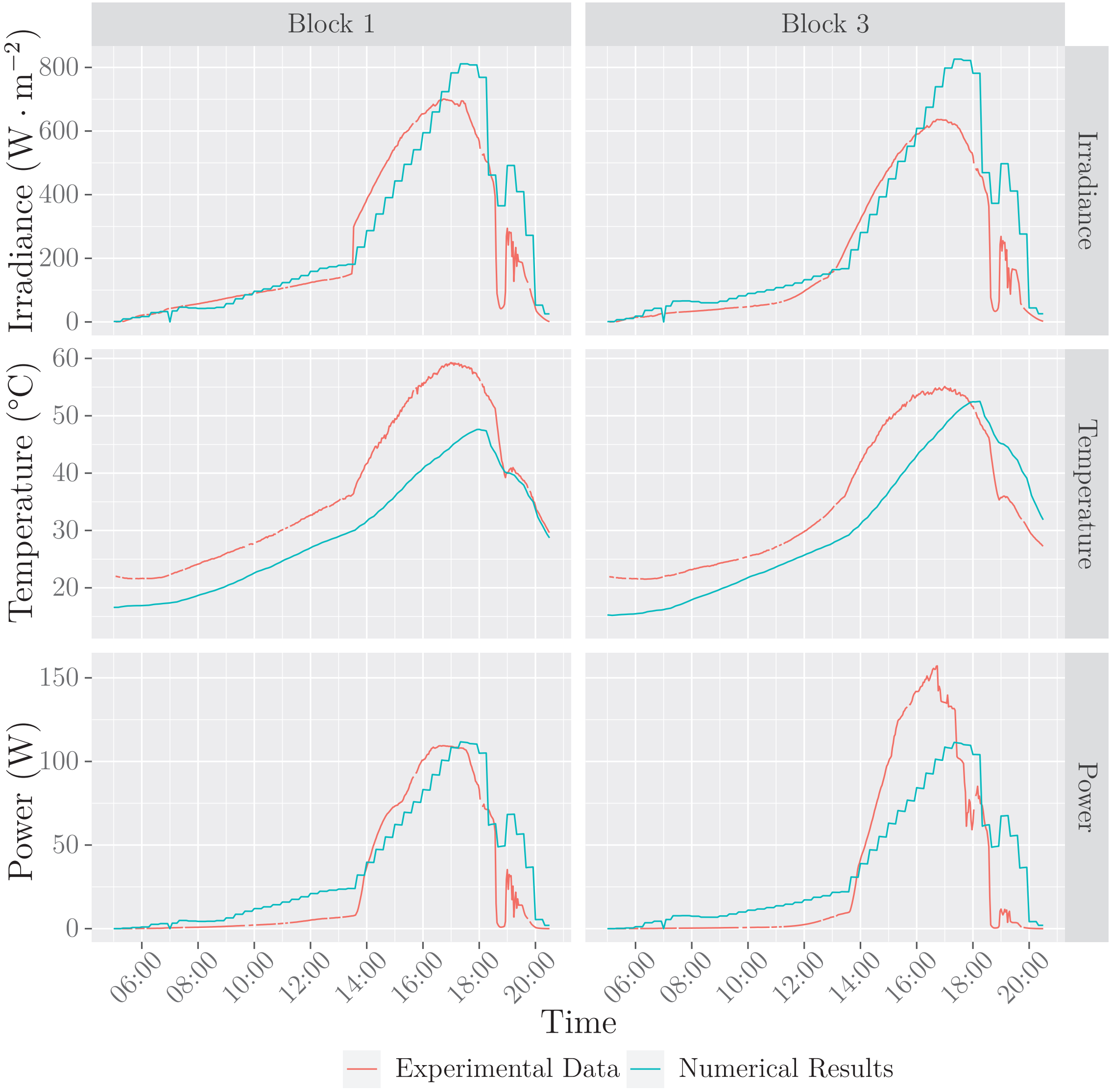

Figure 6.19.: Correspondence Between the Predicted and the Measured Values on the Building's Facade – June, 28th

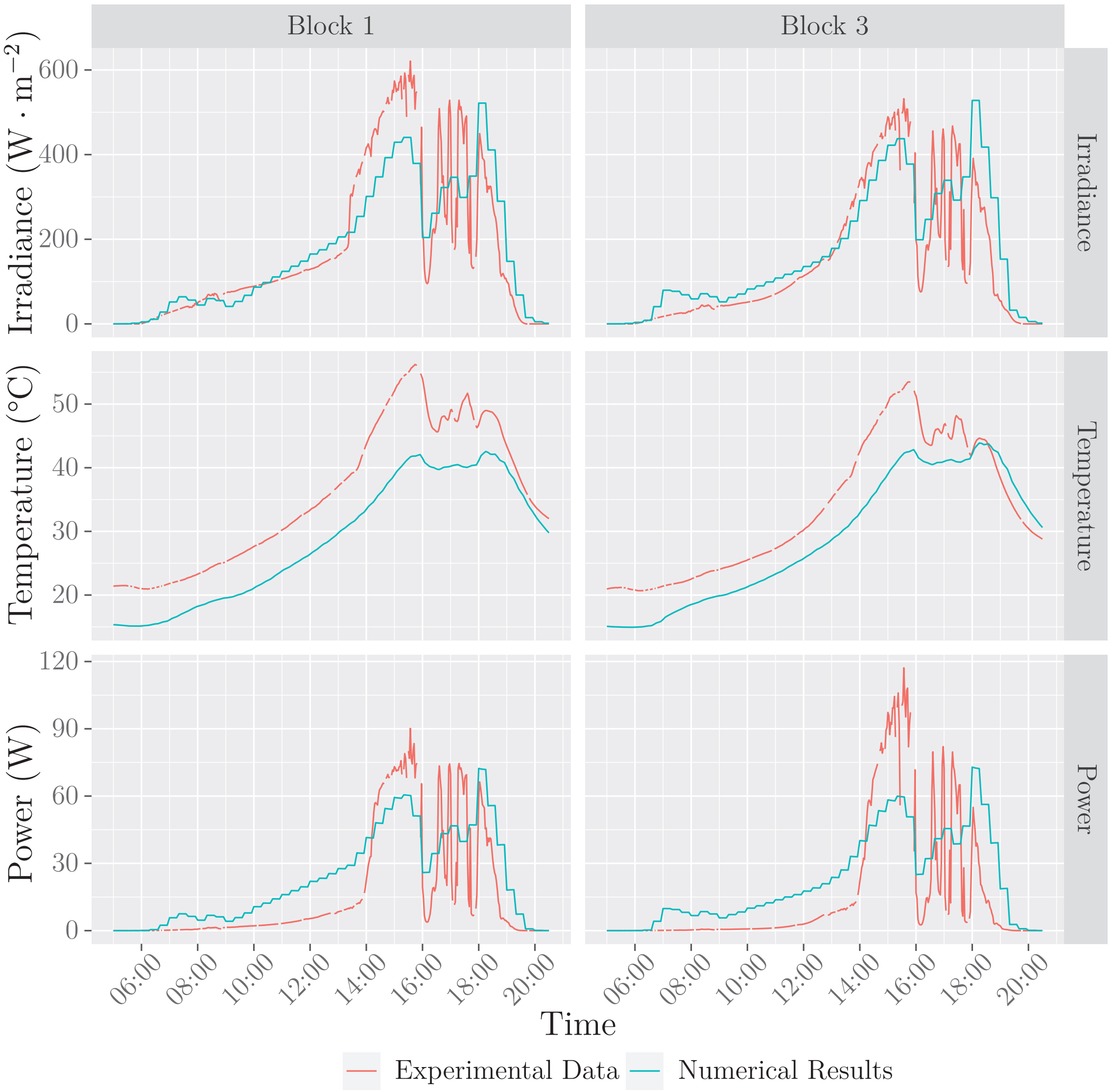

Figure 6.20.: Correspondence Between the Predicted and the Measured Values on the Building's Facade – August, 20th

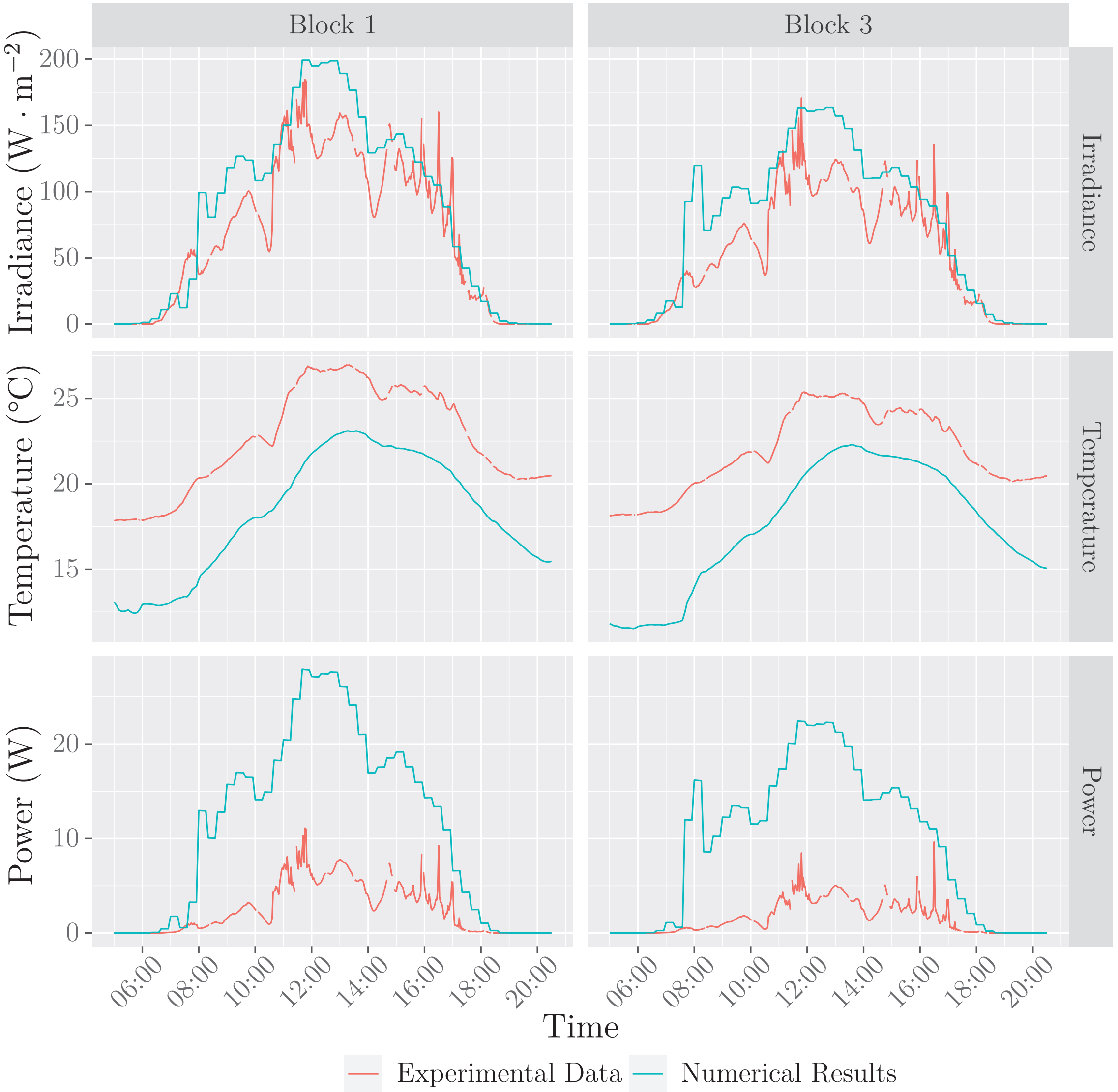

Figure 6.21.: Correspondence Between the Predicted and the Measured Values on the Building's Facade – September, 23th

Thanks to the two proposed studies, ENVI-met demonstrates its ability to assess the potential of PV power generation, taking into consideration the local urban microclimate (UMC).

Regarding the influence of the series connections on the PV potential, the proposed study on the two fictional neighborhood highlights the influence of the district morphology, as well as that of the day of the year and the time of the day, on the direction of the series connection to select in order to optimize the potential of PV production of the district. Thus, even if the horizontal series connection appears as the option to be selected to optimize the potential of PV production, this observation is not always valid. An adaptive solution regarding the direction would therefore help exploit the solar potential of facade to the maximum. The use of artificial intelligence would be part of this solution.

The second study focuses on the characterization of the seasonal behavior of the proposed PV power generation model. The electrical response of a PV module depending on the weather conditions, themselves evolving over the year, it is important to make sure that the proposed PV power generation remains accurate, whatever the operating conditions. Among them, three are studied: shortwave radiation, surface temperature and wind velocity. The accuracy of the model has been checked with a comparison between experimental data and numerical results.

With this study, ENVI-met demonstrates its ability to evaluate the potential of PV power generation on buildings' facades, despite a drop of accuracy under certain weather conditions. Indeed, sunny days provide a good match between experimental data and numerical results. The weather of more cloudy days, and more specifically days for which the Sun's course gets lower, would require more investigation and more development on the proposed PV power generation model in order to increase its accuracy under these weather conditions.

CONCLUSION AND PERSPECTIVES 7

It is only with the heart that we can see rightly, what is essential is invisible to the eye.

Antoine de Saint-Exupéry

These three years of thesis were the opportunity to study in depth the urban microclimate (UMC) simulation tool ENVI-met. The main objective of this work was to implement an integrated methodology for the evaluation of the photovoltaic (PV) potential of buildings' facades, taking into account the specific features of the UMC.

7.1 CONCLUSION ABOUT ENVI-MET

7.1.1 *Input and Output Format*

Despite the availability of different forms of documentation (online technical documentation, video tutorials, forums, etc.), getting started with the ENVI-met software for research purposes requires in-depth work, and was the preliminary part to the developments presented here. This required, in the first place, an understanding of the input and output data of the software, as well as the associated formats. Subsequently, an adaptation of the output format was necessary in order to assess the solar potential of building facades.

The development of the new output format necessitated rethinking what ENVI-met offered. Indeed, the latter, consisting of files arranged by categories of phenomena, and oriented for use with the software included with the ENVI-met software suite, Leonardo, is made up of EDX / EDT file pairs, i.e. a file XML-like and a binary file. This architecture aims to reduce the space occupied on the hard disk.

Nevertheless, the interrelation between different phenomena leads to redundancy in the writing of physical quantities in the output files. This is the case for example for direct short wavelength radiation, which can be accessed via the files contained in the atmosphere folder or the radiation folder. In addition, each cell of the simulated domain contains a value for each physical quantity considered by ENVI-met. In the event that this is not applicable (as is the case for a building surface temperature for a cell not containing a building), a default value is saved. This can lead to the writing of a large amount of avoidable data. The proposed output format, based on a relational database model, eliminates data redundancy as well as writing default values.

7.1.2 *Simulation of the Phenomena That Occur in Urban Context*

Regarding the evaluation of the PV potential of building facades on a city scale, taking into account the local urban environment requires the simulation of two large families of phenomena, simulated by ENVI-met: radiative and aeraulic phenomena . Rather than considering each phenomenon independently, ENVI-met makes it possible to simulate the interrelationships which exist between them, within the same computing core. This calculation structure requires the implementation of assumptions and models in order to limit the cost of calculation.

The models and methods of resolution implemented by ENVI-met do not allow us to describe with the same precision all the phenomena that occur in an urban environment. This is the case, for example, with turbulent aeraulic phenomena. Indeed, in order to limit the cost of computation, the turbulent phenomena are modeled and not resolved. This leads to a decrease in the accuracy of the results in areas where the air flow is strongly disturbed. Nevertheless, the precision of the results obtained is satisfactory for the application targeted by ENVI-met: the global simulation of the urban microclimate. For a more advanced purely aeraulics application, it is preferable to turn to software specialized in airflow simulation, such as Fluent or OpenFOAM, because of their large eddy scale (LES) models.

Concerning the modeling of radiative phenomena, no benchmark strictly speaking including ENVI-met has been carried out. During this work, a particular interest was focused on the influence of the choice of the resolution methods, as well as the taking into account of inter-reflections, on the simulation results. It is commonly accepted that taking them into account in an urban context is a crucial point in the precise evaluation of solar potential. Many radiative models applied to the urban environment, however, consider the surrounding buildings only as masks. The study presented here shows, however, that taking into account inter-reflections can lead to a difference of 15 %.

The method of resolution also has an impact on the evaluation of the PV potential. Indeed, two resolution methods are proposed by ENVI-met: AVF and IVS. The last, the most recent, aims to take better account of the state of the building (sun reflection, thermal radiation) by considering the real conditions of each of the cells instead of average values. The choice of the resolution method has an impact as important as that of the consideration of inter-reflections between buildings.

Numerical modeling of radiative phenomena, based on view factor calculations, is less precise than methods based on ray casting, in particular in the case of complex geometries. These methods are nevertheless much more costly in terms of calculation. The resolution methods proposed by ENVI-met therefore constitute a compromise between precision and calculation cost. For a purely radiative study, reference solutions such as Radiance appear as the preferred option.

7.1.3 *Personal Perspective on ENVI-met*

To conclude, ENVI-met appears as a solution including as much as possible the phenomena that occur at the city scale, with a need to compromise between precision of the results for each of the phenomena taken independently of one another and the cost of calculation. Thus, for a study focused on a single family of phenomena, ENVI-met is not the solution to adopt. On the other hand, if the aim is to consider all the phenomena, with equal importance, then ENVI-met is the tool to choose, because of the taking into account of the interrelationships between phenomena within a same computing core.

The results taken for each of the phenomena considered individually can be outperformed in terms of accuracy by other specialized tools. Nevertheless, the methods used by ENVI-met for the simulation of the UMC make it possible to obtain a good compromise and the most holistic approach of the UMC simulation.

7.2 CONCLUSION ABOUT THE RESULTS

The evaluation of the ability of ENVI-met to be used to accurately assess the PV potential of the buildings' facade is a two-step process. Indeed, ENVI-met makes it possible to use local measurements as simulation's input. It is therefore important to ensure that the data used as input match with the proposed data input format.

7.2.1 *Influence of the Input Data on the Results' Accuracy*

Through the various studies carried out during this work, ENVI-met has proven its ability to provide accurate data that can be used as input for PV power generation models. Indeed, diode-based models require two weather conditions as input: the shortwave (SW) radiation level on the facade and the surface temperature. These two are calculated by ENVI-met, from the values of the physical quantities given at the simulation input and from the resolution of the models.

The accuracy of the input data is a crucial issue in order to obtain an accurate simulation of the urban microclimate. Nonetheless, obtaining representative quantities with a limited number of measurements is a difficult task and the observed differences in the confrontation between numerical results and experimental data are not entirely attributable to the precision of the model but to the uncertainty of the measurements as well. Indeed, the measured values are often carried out locally. In addition, the measurements are frequently noisy and partial (loss of signal between the sensor and the data logger).

Among the inputs of ENVI-met, three appear to be the main ones in the framework of the evaluation of the PV potential taking into account the local environment: SW irradiation, temperature and wind speed.

Being directly impacted by radiative phenomena, the evaluation of the PV potential of facades requires precise measurements of solar irradiation, which can be difficult to measure accurately under actual conditions. These must be given as simulation input, with a distinction between direct and diffuse radiation. The preliminary work to match the measured data to the expected input format is a necessary and critical step. This is the main factor (apart from digital resolutions) that can cause differences between the numerical results and the experimental data.

The value of the temperature also has an impact on the accuracy of the results. Indeed, the electrical response of PV panels is sensitive to temperature variation. The wind velocity is a parameter of influence that is often neglected. Nonetheless, as aforementioned, the radiative phenomena are coupled with the aeraulic ones in ENVI-met. Thus, the surface temperature is based on the thermal balance between the building's facade and the outside air. A variation of the wind velocity leads to a variation of the heat transfer coefficient between the building's facade and the outside. The influence of the wind velocity on the evaluation of the PV potential of buildings in an urban context is demonstrated in this work. Nonetheless, its sensitivity is still poorly described and would need further studies. The measurement of a representative wind velocity near the buildings' facades is a complex work and will be the subject of studies for future projects.

Among the three input data directly related to the assessment of the PV potential of the buildings' facade, the measurement of the SW radiation has to be highly sensitive. Indeed, this is the main parameter to take into consideration in the evaluation of the PV power generation. Nevertheless, it is not sufficient to increase the accuracy of the predictive models of PV power generation Temperature and wind velocity, although having a lower sensitivity, have to be taken into account to get more accurate results in a context of UMC.

7.2.2 *Discussion About the Carried Out Studies*

Two studies have been carried out to assess the PV potential of buildings' facades at the district scale. In both of these studies, the output results from the simulations carried out with ENVI-met are used as input data for a double-diode model.

Regarding the influence of the series connections on the PV potential, the proposed study on the two fictional neighborhood highlights the influence of the district morphology, as well as that of the day of the year and the time of the day, on the direction of the series connection to select in order to optimize the potential of PV production of the district. Thus, even if the horizontal series connection appears as the option to be selected to optimize the potential of PV production, this observation is not always valid. An adaptive solution regarding the direction would therefore help exploit the solar potential of facade to the maximum. The use of artificial intelligence would be part of this solution.

The second study focuses on the characterization of the seasonal behavior of the proposed PV power generation model. The electrical response of a PV module depending on the weather conditions, themselves evolving over the year, it is important to make sure that the proposed PV power generation remains accurate, whatever the operating conditions. Among them, three are studied: shortwave radiation, surface temperature and wind speed. The accuracy of the model has been checked with a comparison between experimental data and numerical results.

With this study, ENVI-met demonstrates its ability to evaluate the potential of PV power generation on buildings' facades, despite a drop of accuracy under certain weather conditions. Indeed, sunny days provide a good match between experimental data and numerical results. The weather of more cloudy days, and more specifically days for which the Sun's course gets lower, would require more investigation and more development on the proposed PV power generation model in order to increase its accuracy under these weather conditions. This is an essential step in order to consider injecting energy produced by buildings into the grid. The information thus obtained could be useful to architects, electricity suppliers, or other energy stakeholders.

7.3 PERSPECTIVES AND FUTURE WORK

The work carried out during this thesis made it possible to answer many questions and in particular the main one which was to demonstrate the ability of ENVI-met to accurately assess the PV potential of building facades and the advantage of this model to take into account all the phenomena occurring on the scale of the city. However, they also raised other questions, still pending today.

Indeed, only the PV potential of the vertical facades has been evaluated. An interest was focused on this type of walls because they are less well characterized than the roofs. However, to the best of my knowledge, no study has been carried out on pitched roofs. It would therefore be interesting to carry out the same type of studies on this type of facade, in particular taking into account the limits of the geometric modeling of ENVI-met.

In addition, the integrated methodology developed here is only interested in PV energy. It would be possible to extend the evaluation of the potential to other technologies, such as solar thermal for example. Indeed, the integration of this technology could lead to different conclusions, in particular concerning the influence of wind velocity. Furthermore, the model used for the evaluation of the PV potential is only based on the manufacturer's datasheet, thus no ageing of the PV panel is considered. A way to extend the presented work would be to take into account the ageing of the PV panel in the evaluation of the PV potential of the buildings' facades.

Regarding the limitations of this study, the vegetation has not been taken into consideration. This assumption was made because of its semi-opaque nature, which makes it even more difficul to take into account accurately (especially with regard to the shading phenomena). Nevertheless, vegetation is present in the cities (and will be even more so in the years to come). It is therefore necessary to take it into account in order to simulate the UMC even more faithfully and obtain more precise results in terms of PV potential evaluation.

Finally, the methodology developed here is a chaining between the UMC simulation carried out with ENVI-met and the evaluation of the PV power generation with diode-based models. However, making building facades active in terms of energy production has an impact on the thermal balance of building walls. Indeed, the energy converted into electricity by PV technology is no longer dissipated in the form of heat through the walls. A coupling between ENVI-met and a PV production model, or even the integration of instantaneous PV production within the ENVI-met computing core would make it possible to further increase the precision of the results obtained.

A

BLASIUS WIND TUNNEL

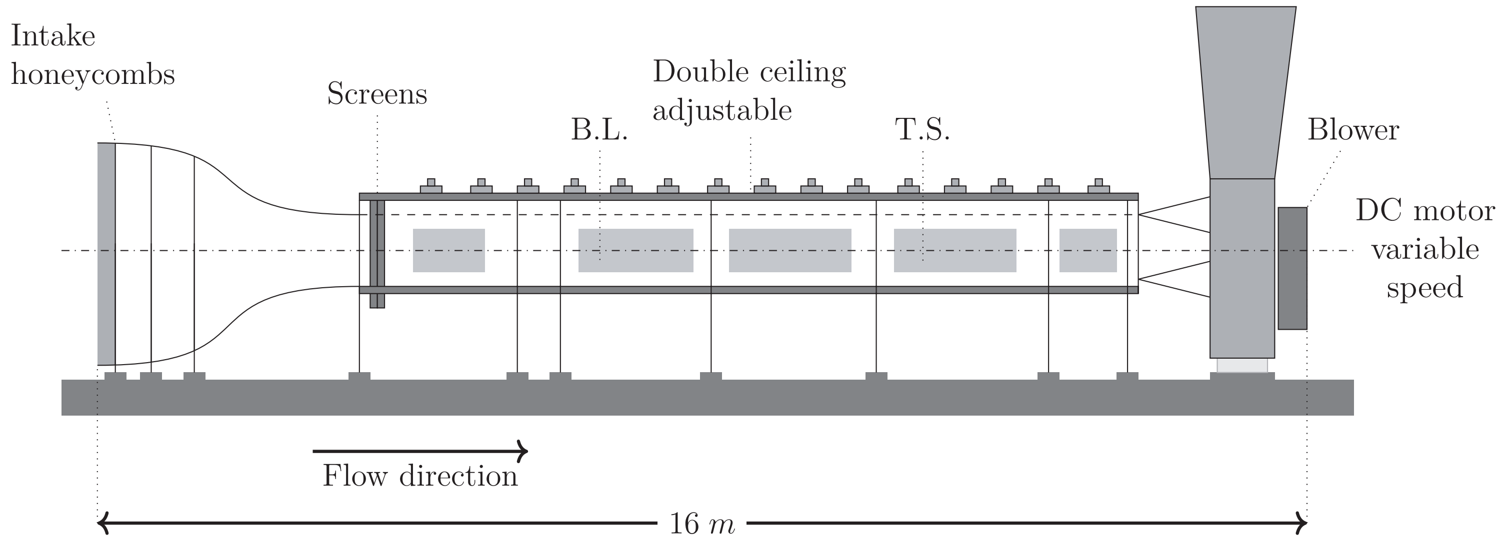

B.L : Boundary Layer development section (7.5 m long)
T.S : Test section with turntable (1.5 m wide, 1 m high, 4 m long)

Figure A.1.: Blasius Wind Tunnel

B

HOUGHTON COEFFICIENTS

Table B.1.: Solar Spectral Irradiance

λ[a]	I_λ[b]	$D_{0-\lambda}$[c]
0.115	$7 \cdot 10^{-6}$	$1 \cdot 10^{-4}$
0.14	$3 \cdot 10^{-5}$	$5 \cdot 10^{-4}$
0.16	$2.3 \cdot 10^{-4}$	$6 \cdot 10^{-4}$
0.18	0.001 27	$1.6 \cdot 10^{-3}$
0.20	0.010 8	$8.1 \cdot 10^{-3}$
0.22	0.058 2	0.05
0.23	0.067 5	0.10
0.24	0.063 8	0.14
0.25	0.071 8	0.19
0.26	0.132	0.27
0.27	0.235	0.41
0.28	0.225	0.56
0.29	0.488	0.81
0.30	0.520	1.21
0.31	0.698	1.66
0.32	0.840	2.22
0.33	1.072	2.93
0.34	1.087	3.72
0.35	1.107	4.52
0.36	1.081	5.32
0.37	1.190	6.15
0.38	1.134	7.00
0.39	1.112	7.82
0.40	1.447	8.73
0.41	1.773	9.92
0.42	1.770	11.22
0.43	1.660	12.47
0.44	1.833	13.73
0.45	2.031	15.14
0.46	2.092	16.65
0.47	2.059	18.17
0.48	2.100	19.68
0.49	1.975	21.15
0.50	1.966	22.60
0.51	1.906	24.01
0.52	1.856	25.38
0.53	1.865	26.74
0.54	1.805	28.08
0.55	1.747	29.38
0.56	1.716	30.65

[a] wavelength [µm]

[b] solar spectral irradiance averaged over small bandwidth centered at λ [$\mathrm{W} \cdot \mathrm{m}^{-2} \cdot \mathrm{nm}^{-1}$]

[c] percentage of the solar constant associated with wavelengths shorter than λ

λ[a]	I_λ[b]	$D_{0-\lambda}$[c]
0.57	1.734	31.91
0.58	1.737	33.18
0.59	1.721	34.44
0.60	1.687	35.68
0.62	1.622	38.10
0.64	1.563	40.42
0.66	1.505	42.66
0.68	1.445	44.81
0.70	1.386	46.88
0.72	1.331	48.86
0.75	1.251	51.69
0.80	1.123	56.02
0.90	0.902	63.37
1.00	0.757	69.49
1.2	0.491	78.40
1.4	0.341	84.33
1.6	0.248	88.61
1.8	0.161	91.59
2.0	0.104	93.49
2.2	0.080	94.83
2.4	0.063	95.86
2.6	0.049	96.67
2.8	0.039	97.31
3.0	0.031	97.83
3.2	0.022 9	98.22
3.4	0.016 8	98.50
3.6	0.013 7	98.72
3.8	0.011 2	98.91
4.0	0.009 6	99.06
4.5	0.006 0	99.34
5.0	0.003 8	99.51
6.0	0.001 8	99.72
7.0	0.001 0	99.82
8.0	$6.0 \cdot 10^{-4}$	99.88
10.0	$2.5 \cdot 10^{-4}$	99.94
15.0	$4.9 \cdot 10^{-5}$	99.98
20.0	$1.5 \cdot 10^{-5}$	99.99
50.0	$4.0 \cdot 10^{-7}$	100.00

[a] wavelength [µm]

[b] solar spectral irradiance averaged over small bandwidth centered at λ [$\mathrm{W} \cdot \mathrm{m}^{-2} \cdot \mathrm{nm}^{-1}$]

[c] percentage of the solar constant associated with wavelengths shorter than λ

C

RESOLUTION OF THE SINGLE-DIODE MODEL

This resolution is a two-step process. First, the parameters are assessed under standard conditions (see details in table 3.1 on page 63). Thereafter, the calculated values are adapted to the actual operating conditions.

The equation (3.46) on page 58 applies to a single cell. For an entire solar module, containing multiple cells connected in series or in parallel, this equation becomes:

$$I_M = N_p I_{irr} - N_p I_0 \left[\exp\left(\frac{q\left(V_M + I_M \dfrac{N_s}{N_p} R_s\right)}{N_s n k T} \right) - 1 \right] - \frac{V_M + I_M \dfrac{N_s}{N_p} R_s}{\dfrac{N_s}{N_p} R_{sh}} \tag{C.1}$$

where I_M is the output current of the module, V_M is the output voltage of the module, N_p is the number of cells connected in parallel and N_s is the number of cells connected in series

As an equation with five unknowns, it requires five equations to be solved. This needs to apply conditions to the equation (C.1). The first condition is to use the short-circuit hypothesis which implies that $I_M = I_{sc}$ and $V_M = 0$. Then comes the equation (C.3) on page VIII:

$$I_{SC_{ref}} = N_p \times I_{irr_{ref}} - N_p I_{0_{ref}} \left[\exp\left(\frac{q I_{SC_{ref}} R_{s_{ref}}}{N_p n_{ref} k T_{ref}} \right) - 1 \right] - \frac{I_{SC_{ref}} \dfrac{N_s}{N_p} R_{s_{ref}}}{\dfrac{N_s}{N_p} R_{sh_{ref}}} \tag{C.2}$$

where the subscripts ref refers to the reference conditions.

The second equation is given by the open-circuit condition, where $I_M = 0$ and $V_M = V_{oc}$. Then:

$$0 = N_p \times I_{irr_{ref}} - N_p \times I_{0_{ref}} \times \left[\exp\left(\frac{qV_{OC_{ref}}}{N_s n_{ref} k T_{ref}}\right) - 1\right] - \frac{V_{OC_{ref}}}{\frac{N_s}{N_p} R_{sh_{ref}}} \tag{C.3}$$

Considering that the solar module operates at the maximum power point comes the third equation:

$$\begin{aligned} I_{mp_{ref}} &= N_p \times I_{irr_{ref}} \\ &\quad - N_p \times I_{0_{ref}} \times \left[\exp\left(\frac{q\left(V_{mp_{ref}} + I_{mp_{ref}} \frac{N_s}{N_p} R_{s_{ref}}\right)}{N_s n_{ref} k T_{ref}}\right) - 1\right] \\ &\quad - \frac{V_{mp_{ref}} + I_{mp_{ref}} \frac{N_s}{N_p} R_{s_{ref}}}{\frac{N_s}{N_p} R_{sh_{ref}}} \end{aligned} \tag{C.4}$$

At the maximum power point (MPP), the derivative of power with respect to voltage is equal to zero:

$$\left.\frac{\partial P}{\partial V}\right|_{MPP} = \left.\frac{\partial\left(VI\right)}{\partial V}\right|_{MPP} = 0 \tag{C.5}$$

Then, the fourth equation is:

$$\frac{I_{mp_{ref}}}{V_{mp_{ref}}} = \frac{\frac{qN_p I_{0_{ref}}}{N_s n_{ref} k T_{ref}} \exp\left(\frac{q\left(V_{mp_{ref}} + I_{mp_{ref}} \frac{N_s}{N_p} R_{s_{ref}}\right)}{N_s n_{ref} k T_{ref}}\right) + \frac{1}{\frac{N_s}{N_p} R_{sh_{ref}}}}{1 + \frac{qI_{0_{ref}} R_{s_{ref}}}{n_{ref} k T_{ref}} \exp\left(\frac{q\left(V_{mp_{ref}} + I_{mp_{ref}} \frac{N_s}{N_p} R_{s_{ref}}\right)}{N_s n_{ref} k T_{ref}}\right) + \frac{R_{s_{ref}}}{R_{sh_{ref}}}} \tag{C.6}$$

The fifth and last equation is used to make sure that the assessment of the temperature coefficient of open-circuit is correct. This coefficient is defined as follows:

$$\beta_T = \frac{\partial V_{OC}}{\partial T} = \frac{V_{OC} - V_{OC_{ref}}}{T - T_{ref}} \tag{C.7}$$

As mentioned by (Tian et al., 2012), a cell temperature of $T = T_{ref} \pm 10\ K$ should be used. This assumption can now be used in equation (C.1) on page VII:

$$0 = N_p I_{irr} - N_p I_0 \left[\exp\left(\frac{qV_{OC}\left(T\right)}{N_s n k T}\right) - 1\right] - \frac{V_{OC}\left(T\right)}{\frac{N_s}{N_p} R_p} \tag{C.8}$$

When the standard test conditions (STC) (see details in table 3.1 on page 63) are taken as the reference, equation (C.3) to equation (C.8) on pages VIII–IX become:

$$0 = N_p \times I_{irr_{STC}} - N_p \times I_{0_{STC}} \times \left[\exp\left(\frac{qV_{OC_{STC}}}{N_s n_{STC} k T_{STC}}\right) - 1\right] - \frac{V_{OC_{STC}}}{\frac{N_s}{N_p} R_{p_{STC}}} \tag{C.9}$$

$$I_{SC_{STC}} = N_p \times I_{irr_{STC}} - N_p I_{0_{STC}} \left[\exp\left(\frac{qI_{SC_{STC}} R_{s_{STC}}}{N_p n_{STC} k T_{STC}}\right) - 1\right] - \frac{I_{SC_{STC}} \frac{N_s}{N_p} R_{s_{STC}}}{\frac{N_s}{N_p} R_{p_{STC}}} \tag{C.10}$$

$$\begin{aligned} I_{mp_{STC}} &= N_p \times I_{irr_{STC}} \\ &\quad - N_p \times I_{0_{STC}} \times \left[\exp\left(\frac{q\left(V_{mp_{STC}} + I_{mp_{STC}} \frac{N_s}{N_p} R_{s_{STC}}\right)}{N_s n_{STC} k T_{STC}}\right) - 1\right] \\ &\quad - \frac{V_{mp_{STC}} + I_{mp_{STC}} \frac{N_s}{N_p} R_{s_{STC}}}{\frac{N_s}{N_p} R_{p_{STC}}} \end{aligned} \tag{C.11}$$

$$\frac{I_{mp_{STC}}}{V_{mp_{STC}}} = \frac{\dfrac{qN_p I_{0_{STC}}}{N_s n_{STC} k T_{STC}} \exp\left(\dfrac{q\left(V_{mp_{STC}} + I_{mp_{STC}} \frac{N_s}{N_p} R_{s_{STC}}\right)}{N_s n_{STC} k T_{STC}}\right) + \dfrac{1}{\frac{N_s}{N_p} R_{p_{STC}}}}{1 + \dfrac{qI_{0_{STC}} R_{s_{STC}}}{n_{STC} k T_{STC}} \exp\left(\dfrac{q\left(V_{mp_{STC}} + I_{mp_{STC}} \frac{N_s}{N_p} R_{s_{STC}}\right)}{N_s n_{STC} k T_{STC}}\right) + \dfrac{R_{s_{STC}}}{R_{p_{STC}}}} \tag{C.12}$$

$$0 = N_p I_{irr} - N_p I_0 \left[\exp\left(\frac{qV_{OC}\left(T\right)}{N_s n k T}\right) - 1\right] - \frac{V_{OC}\left(T\right)}{\frac{N_s}{N_p} R_p} \tag{C.13}$$

Once the five aforementioned parameters assessed, the ones under actual operating conditions can be evaluated. To do so, five assumptions are needed. The first assumption is that the photo current is proportional to the irradiation level and inversely proportional to the temperature. Thus:

$$\begin{aligned} I_{irr} &= I_{irr_{ref}} \times \frac{G}{G_{ref}} \times [1 + \alpha_T (T - T_{ref})] \\ \Leftrightarrow I_{irr} &= I_{irr_{STC}} \times \frac{G}{G_{ref}} \times [1 + \alpha_T (T - T_{STC})] \end{aligned} \tag{C.14}$$

where G is the irradiation level, T is the surface temperature of the cell and α_T is the temperature coefficient of the short-circuit current.

Regarding the diode saturation current I_0, it mainly depends on the temperature of the module:

$$\begin{aligned} I_0 &= I_{0_{ref}} \times \left[\frac{T}{T_{ref}}\right]^3 \times \exp\left[\frac{E_{g_{ref}}}{kT_{ref}} - \frac{E_g}{kT}\right] \\ \Leftrightarrow I_0 &= I_{0_{STC}} \times \left[\frac{T}{T_{STC}}\right]^3 \times \exp\left[\frac{E_{g_{STC}}}{kT_{STC}} - \frac{E_g}{kT}\right] \end{aligned} \tag{C.15}$$

where E_g is the bandgap energy. For the silicon, (Kim et al., 2009) define it as:

$$E_g = 1.16 - 7.02 \cdot 10^{-4} \times \left(\frac{T^2}{T - 1108}\right) \tag{C.16}$$

The third parameter of the model, the ideality factor n, keeps the same in all conditions:

$$\begin{aligned} n &= n_{ref} \\ \Leftrightarrow n &= n_{STC} \end{aligned} \tag{C.17}$$

The last assumptions are about the resistances. Regarding the series resistance, it is assumed to be independent of temperature and irradiation (De Soto et al., 2006):

$$\begin{aligned} R_s &= R_{s_{ref}} \\ \Leftrightarrow R_s &= R_{s_{STC}} \end{aligned} \tag{C.18}$$

On the contrary, as highlighted by (De Soto et al., 2006), the shunt resistance is proportional to the irradiation level:

$$\begin{aligned} R_{sh} &= R_{sh_{ref}} \times \frac{G}{G_{ref}} \\ \Leftrightarrow R_{sh} &= R_{sh_{STC}} \times \frac{G}{G_{STC}} \end{aligned} \tag{C.19}$$

D

RENVIMET DOCUMENTATION

Package ‘REnviMet’

November 17, 2020

Type Package

Title Envi_MET Binary Files Manipulation with R

Version 0.8.0

Author Benjamin GOVEHOVITCH

Maintainer Benjamin GOVEHOVITCH `<benjamin.govehovitch@insa-lyon.fr>`

Description Provide access to data simulation results carried out with Envi_MET v4.x.
The EDT binary file is converted into a matrix.
The goal is to resolve the issue of the lack of features on LEONARDO, regarding the data analysis.

URL `https://gitlab.com/Spoutnik1337/renvimet`

BugReports `https://gitlab.com/Spoutnik1337/renvimet/issues/new`

License CeCILL-2

Encoding UTF-8

LazyData true

Depends R(>= 3.5.0), XML, openxlsx, lutz

RoxygenNote 7.1.1

R topics documented:

`renvimet-package` *Support for converting Envi-met binary files into matrices*

Description

The RenviMET package implements the readEDTFile, which converts the ENVI-met binary file into a matrix. The information about the binary (.EDT) and XML-like (.EDX) files and their structure are given in `http://envi-met.info/doku.php?id=filereference:edx_edi`.

Details

Package:	RenviMET
Type:	Package
Version:	0.8.0
Date:	2019-09-17
License:	CeCILL-2
LazyLoad:	yes

This package gives access to data simulation results carried out with Envi_MET v4.x. The EDT binary file is converted into a matrix that can be used with R.

Author(s)

Benjamin GOVEHOVITCH <benjamin.govehovitch@insa-lyon.fr>

See Also

readEDTFile

Examples

```
### Example 1: read data of atmosphere files
atmosphereEDT <- system.file(
  "extdata",
  "atmosphere/atmosphere.EDT",
  package = "REnviMet",
  mustWork = TRUE
)
atmosphere <- readEDTFile(atmosphereEDT)
atmosphere
```

```
### Example 2: read data of buildings files
buildingsEDT <- system.file(
  "extdata",
  "buildings/buildings.EDT",
  package = "REnviMet",
  mustWork = TRUE
)
buildings <- readEDTFile(buildingsEDT)
buildings
```

`data_atmosphere` *Example of atmosphere output file*

Description

A dataset representing the contents of the ENVI-met atmosphere binary file.

Usage

```
data_atmosphere
```

Format

A data frame with 21600 rows and 40 variables:

x Spatial coordinate.

y Spatial coordinate.

z Spatial coordinate.

Objects Single object IDs to visualize the model domain. Meaning of the different IDs is stored in LEONARDO Special Layer Definition Files.

Flow_u Wind speed. Vector component along the West-East axis (+: East, -: West).

Flow_v Wind speed. Vector component along the North-South axis (+: South, -: North).

Flow_w Wind speed. Vector component along the vertical axis (+: up, -: down).

Wind_Speed Wind speed. Vector sum over all 3 axis.

Wind_Speed_Change Wind speed change in percent referring to the undisturbed inflow profile at the same height level.

Wind_Direction Wind direction of horizontal component in geographic reference (0: N..90:E..180:S etc).

Pressure_Perturbation Dynamic pressure as a result of the wind field calculation. Pressure values will add up over time, use spatial difference values only if required.

Air_Temperature Potential air temperature at reference (and model default) pressure. For the 3D model, it can be treated like the absolute air temperature.

Air_Temperature_Delta Difference between the local air temperature and the reference air temperature at inflow at the same height level.

Air_Temperature_Change Changes of air temperature compared to the last _AT_ output file.

Spec._Humidity Specific air humidity.

Relative_Humidity Relative air humidity (Caution: Depends both on Specific air humidity and air temperature).

TKE Local Turbulent Kinetic Energy.

Dissipation Local dissipation rate of Turbulent Kinetic Energy.

Vertical_Exchange_Coef._Impuls Calculated vertical exchange coefficient for impulse.

Horizontal_Exchange_Coef._Impuls Calculated horizontal exchange coefficient for impulse (At the moment for microscale assumed to be equal to the vertical exchange coefficient).

Vegetation_LAD One-sided Leaf Area Density (Surface of leaf area per m^3 air).

Direct_Sw_Radiation Available direct solar radiation referring to a reference surface perpendicular to the incoming sun rays (maximum value before applying Lamberts' law).

Diffuse_Sw_Radiation Available diffuse solar radiation referring to a horizontal reference surface.

Reflected_Sw_Radiation Available reflected solar radiation from the environment referring to a horizontal reference surface.

Temperature_Flux Temperature Flux in K from leaf to atmosphere.

Vapour_Flux Evaportation and transpiration flux on leaf per leaf area unit.

Water_on_Leafes Liquid water on leaf per leaf area.

Leaf_Temperature Temperature Flux in K from leaf to atmosphere.

Local_Mixing_Length Local mixing length calculated from TKE model.

Mean_Radiant_Temp. The composed radiative fluxes and air temperature for a standing person.

TKE_normalised_1D Local TKE normlized to 1 with 1D reference model.

Dissipation_normalised_1D Local TKE dissiplation normlized to 1 with 1D reference model.

Km_normalised_1D Local Km normlized to 1 with 1D reference model.

TKE_Mechanical_Turbulence_Prod. Local TKE mechnical production normalized to 1 with 1D reference model.

Stomata_Resistance Actual resistance of stomata to vapour transfer.

CO2 Atmospheric CO2.

CO2 1 Atmospheric CO2.

Plant_CO2_Flux CO2 Flux at leaf per leaf area unit.

Div_Rlw_Temp_change Radiative cooling/heating rate of air due to longwave radiation divergence.

Building_Number Internal Building Number.

Source

`http://envi-met.info/doku.php?id=filereference:output:atmosphere`

`data_buildings` *Example of buildings output (dynamic subdirectory) file*

Description

A dataset representing the contents of the ENVI-met dynamic/buildings binary file.

Usage

```
data_buildings
```

Format

A matrix with 64800 rows and 54 variables:

x Spatial coordinate.

y Spatial coordinate.

z Spatial coordinate.

d Type of wall :

- **0** vertical facade in (yOz) plan (xWall);
- **1** vertical facade in (xOz) plan (yWall);
- **2** horizontal facade (zWall).

Wall_shading_flag Binary flag indicating if the wall is shaded or not.

Wall_Temperature_Node_1_outside Temperature of the wall at the interface between the first material and the atmosphere. See: `https://youtu.be/xor6_9-tVRc?t=1114`.

Wall_Temperature_Node_2 Temperature of the wall in the middle of the first material.

Wall_Temperature_Node_3 Temperature of the wall at the interface between the first and the second material.

Wall_Temperature_Node_4 Temperature of the wall in the middle of the second material.

Wall_Temperature_Node_5 Temperature of the wall at the interface between the second and the third material.

Wall_Temperature_Node_6 Temperature of the wall in the middle of the third material.

Wall_Temperature_Node_7_inside Temperature of the wall at the interface between the third material and the air inside the building.

Building_Sum_Humidity_Flux_at_facade Not Enough Information

Wall_Longwave_radiation_emitted_by_facade Longwave radiative flux emitted by the facade.

Wall_Wind_Speed_in_front_of_facade Wind speed in front of the facade.

Wall_Air_Temperature_in_front_of_facade Air temperature in front of the facade.

Wall_Shortwave_radiation_received_at_facade Shortwave radiation received by the facade.

Wall_Absorbed_direct_shortwave_radiation Absorbed direct shortwave radiation by the wall.

Wall_Incoming_longwave_radiation Incoming longwave radiation to the wall.

Wall_Reflected_shortwave_radiation_facade Reflected shortwave radiation by the wall.

Wall_Sensible_Heat_transmission_coefficient_outside Sensible heat transmission coefficient on the outside.

Wall_Longwave_Energy_Balance Longwave energy balance of the wall.

N.N_Building_Temperature_of_building_inside Building indoor temperature.

Building_Reflected_shortwave_radiation Reflected shortwave radiation by the building.

Building_Longwave_radiation_emitted Longwave radiation emitted by the building.

Greening_Temperature_Leafs Leaf temperature.

Greening_Air_Temperature_Canopy Air temperature of the canopy.

Greening_Air_Humidity_Canopy Air humidity of the canopy.

Greening_Longwave_radiation_emitted Longwave radiation emitted by the greening.

Greening_Wind_Speed_in_front_of_greening Wind speed in front of greening.

Greening_Air_Temperature_in_front_of_greening Air temperature in front of greening.

Greening_Shortwave_radiation_received_at_greening Shortwave radiation received by the greening.

Greening_Incoming_longwave_radiation Incoming longwave radiation to the greening.

Greening_Reflected_shortwave_radiation Reflected shortwave radiation by the greening.

Greening_Transpiration_Flux Transpiration flux.

Greening_Stomata_Resistance Stomata resistance.

Greening_Water_access_factor Water access factor.

Substrate_Temperature_Node_1_outside Temperature of the substrate at the interface between the first material and the atmosphere.

Substrate_Temperature_Node_2 Temperature of the substrate in the middle of the first material.

Substrate_Temperature_Node_3 Temperature of the substrate at the interface between the first and the second material.

Substrate_Temperature_Node_4 Temperature of the substrate in the middle of the second material.

Substrate_Temperature_Node_5 Temperature of the substrate at the interface between the second and the third material.

Substrate_Temperature_Node_6 Temperature of the substrate in the middle of the third material.

Substrate_Temperature_Node_7_inside Temperature of the substrate at the interface between the third material and the wall.

Substrate_Surface_humidity Surface humidity of the substrate.

Substrate_Humidity_Flux_at_substrate Humidity flux at the substrate.

Substrate_Longwave_radiation_emitted_by_substrate Longwave radiation emitted by the substrate.

Substrate_Wind_Speed_in_front_of_substrate Wind speed in front of the substrate.

Substrate_Air_Temperature_in_front_of_substrate Air temperature in front of the substrate.

Substrate_Shortwave_radiation_received_at_substrate Shortwave radiation received by the substrate.

Substrate_Absorbed_direct_shortwave_radiation Absorbed direction shortwave radiation by the substrate.

Substrate_Incoming_longwave_radiation Incoming longwave radiation to the substrate.

Substrate_Reflected_shortwave_radiation_substrate Reflected shortwave radiation by the substrate.

Source

`http://envi-met.info/doku.php?id=filereference:output:buildings`

`EDTToCSV` *Convert an EDT file into a CSV file*

Description

Converts the contents of an EDT file into a CSV file. The output file is written on disk.

`EDTToCSV` Converts the contents of an EDT file into a CSV file.

Usage

```
EDTToCSV(input, output, ...)
```

Arguments

`input`	The path of the EDT file, with or without its extension.
`output`	The path of the CSV file.
`...`	other parameters to pass to function write.csv

Examples

```
### Example 1: save atmosphere file into CSV file
atmosphereEDT <- system.file(
  "extdata",
  "atmosphere/atmosphere.EDT",
  package = "REnviMet",
  mustWork = TRUE
)
outputPath <- "atmosphere/file.csv"
EDTToCSV(atmosphereEDT, outputPath)

### Example 2: read data of buildings files
buildingsEDT <- system.file(
  "extdata",
  "buildings/buildings.EDT",
  package = "REnviMet",
  mustWork = TRUE
)
outputPath <- "buildings/file.csv"
EDTToCSV(buildingsEDT, outputPath)
```

`EDTToRData` *Convert an EDT file into an external representation of R object to the specified file (i.e. binary file)*

Description

Converts the contents of an EDT file into a binary file readable by R. The output file is written on disk.

`EDTToRData` Converts the contents of an EDT file into a RData file (binary file).

Usage

```
EDTToRData(input, output, ...)
```

Arguments

`input`	The path of the EDT file, with or without its extension.
`output`	The path of the XLSX file.
`...`	other parameters to pass to function save.

Examples

```
### Example 1: save atmosphere file into .RData file
atmosphereEDT <- system.file(
  "extdata",
  "atmosphere/atmosphere.EDT",
  package = "REnviMet",
  mustWork = TRUE
)
outputPath <- "atmosphere/file.RData"
EDTToRData(atmosphereEDT, outputPath)

### Example 2: read data of buildings files
buildingsEDT <- system.file(
  "extdata",
  "buildings/buildings.EDT",
  package = "REnviMet",
  mustWork = TRUE
)
outputPath <- "buildings/file.RData"
EDTToRData(buildingsEDT, outputPath)
```

`EDTToXLSX` *Convert an EDT file into a XLSX file*

Description

Converts the contents of an EDT file into a XLSX file. The output file is written on disk.

`EDTToXLSX` Converts the contents of an EDT file into a XLSX file.

Usage

```
EDTToXLSX(input, output, ...)
```

Arguments

`input`	The path of the EDT file, with or without its extension.
`output`	The path of the XLSX file.
`...`	other parameters to pass to function write.xlsx.

Examples

```
## Not run:
### Example 1: save atmosphere file into XLSX file
atmosphereEDT <- system.file(
  "extdata",
  "atmosphere/atmosphere.EDT",
  package = "REnviMet",
  mustWork = TRUE
)
outputPath <- "atmosphere/file.xlsx"
EDTToXLSX(atmosphereEDT, outputPath)

### Example 2: save buildings file into XLSX file
buildingsEDT <- system.file(
  "extdata",
  "buildings/buildings.EDT",
  package = "REnviMet",
  mustWork = TRUE
)
outputPath <- "buildings/file.xlsx"
EDTToXLSX(buildingsEDT, outputPath)

## End(Not run)
```

`EDXToXML` *Simple way to convert EDX file into XML file*

Description

`EDXToXML` converts an EDX file into a XML file. If the file passed as a parameter to the function is already a XML file, the conversion is simply skipped.

Usage

```
EDXToXML(EDXFile)
```

Arguments

`EDXFile`	The EDX file to be converted.

Value

The EDX file converted into a XML file.

Examples

```
### Example 1: actual conversion
atmosphereEDX <- system.file(
  "extdata",
  "atmosphere/atmosphere.EDX",
  package = "REnviMet",
  mustWork = TRUE
```

```
)
atmosphereXML <- EDXToXML(atmosphereEDX)
atmosphereXML

### Example 2: skipped conversion
atmosphereEDX <- system.file(
  "extdata",
  "atmosphere/atmosphere.EDX",
  package = "REnviMet",
  mustWork = TRUE
)
atmosphereXML <- xmlParse(atmosphereEDX, encoding = "ISO-8859-1")
atmosphereXML <- EDXToXML(atmosphereXML)
atmosphereXML

### Example 3: conversion of buildings file
buildingsEDX <- system.file(
  "extdata",
  "buildings/buildings.EDX",
  package = "REnviMet",
  mustWork = TRUE
)
buildingsXML <- EDXToXML(buildingsEDX)
buildingsXML
```

`ENVImetVersion` *Get the version of ENVI-met used for carrying out the simulation*

Description

Returns the version of ENVI-met used for carrying out the simulation.

Usage

```
ENVImetVersion(EDXFile)
```

Arguments

`EDXFile`	The EDX file from which the data are extracted.

Details

`ENVImetVersion` returns the version of ENVI-met used for carrying out the simulation.

Value

The version of ENVI-met used for carrying out the simulation.

Examples

```
### Example 1: get ENVI-met version from atmosphere files
atmosphereEDX <- system.file(
  "extdata",
  "atmosphere/atmosphere.EDX",
  package = "REnviMet",
  mustWork = TRUE
)
ENVImetVersion(atmosphereEDX)

### Example 2: get ENVI-met version from buildings files
buildingsEDX <- system.file(
  "extdata",
  "buildings/buildings.EDX",
  package = "REnviMet",
  mustWork = TRUE
)
ENVImetVersion(buildingsEDX)
```

`getDataPerVariable` *Get the number of data per variable in the EDX file*

Description

Returns the number of data per variable in the EDX file.

Usage

```
getDataPerVariable(EDXFile)
```

Arguments

`EDXFile`	The EDX file from which the data are extracted.

Details

`getDataPerVariable` returns the number of data per variable in the EDX file.

Value

Integer.

Examples

```
### Example 1: get the number of data per variable for atmosphere files
atmosphereEDX <- system.file(
  "extdata",
  "atmosphere/atmosphere.EDX",
  package = "REnviMet",
  mustWork = TRUE
)
getDataPerVariable(atmosphereEDX)
```

```
### Example 2: get the number of data per variable for buildings files
buildingsEDX <- system.file(
  "extdata",
  "buildings/buildings.EDX",
  package = "REnviMet",
  mustWork = TRUE
)
getDataPerVariable(buildingsEDX)
```

`getDateTime` *Extract datetime from file name*

Description

`getDateTime` extracts the datetime from a file name, depending on the version of ENVI-met.

Usage

```
getDateTime(filename, as="character", ...)
```

Arguments

`filename`	The file name (EDX or EDT) from which the datetime is extracted.
`as`	The type of the ouput ("POSIXct" "POSIXt" or character).
`...`	Further arguments to pass to function.

Value

The datetime of the file.

`getLatitude` *Get the latitude of the project area*

Description

Returns the latitude of the project area.

Usage

```
getLatitude(EDXFile)
```

Arguments

`EDXFile`	The EDX file from which the data are extracted.

Details

`getLatitude` returns the latitude of the project area.

Value

The latitude of the project area.

Examples

```
### Example 1: get latitude of the project area from atmosphere files
atmosphereEDX <- system.file(
  "extdata",
  "atmosphere/atmosphere.EDX",
  package = "REnviMet",
  mustWork = TRUE
)
getLatitude(atmosphereEDX)

### Example 2: get ENVI-met latitude of the project area buildings files
buildingsEDX <- system.file(
  "extdata",
  "buildings/buildings.EDX",
  package = "REnviMet",
  mustWork = TRUE
)
getLatitude(buildingsEDX)
```

`getLongitude` *Get the longitude of the project area*

Description

Returns the longitude of the project area

Usage

```
getLongitude(EDXFile)
```

Arguments

`EDXFile`	The EDX file from which the data are extracted.

Details

`getLongitude` returns the longitude of the project area.

Value

The longitude of the project area.

Examples

```
### Example 1: get longitude of the project area from atmosphere files
atmosphereEDX <- system.file(
  "extdata",
  "atmosphere/atmosphere.EDX",
  package = "REnviMet",
  mustWork = TRUE
)
getLongitude(atmosphereEDX)

### Example 2: get ENVI-met longitude of the project area buildings files
buildingsEDX <- system.file(
  "extdata",
  "buildings/buildings.EDX",
  package = "REnviMet",
  mustWork = TRUE
)
getLongitude(buildingsEDX)
```

`getNumberCellsX` *Get the number of cells along the X axis*

Description

Returns the number of cells along the X axis.

Usage

```
getNumberCellsX(EDXFile)
```

Arguments

`EDXFile`	The EDX file from which the data are extracted.

Details

`getNumberCellsX` returns the number of cells along the X axis.

Value

Integer.

Examples

```
### Example 1: get the number of cells along the x axis from atmosphere files
atmosphereEDX <- system.file(
  "extdata",
  "atmosphere/atmosphere.EDX",
  package = "REnviMet",
  mustWork = TRUE
)
getNumberCellsX(atmosphereEDX)
```

```
### Example 2: get the number of cells along the x axis from buildings files
buildingsEDX <- system.file(
  "extdata",
  "buildings/buildings.EDX",
  package = "REnviMet",
  mustWork = TRUE
)
getNumberCellsX(buildingsEDX)
```

`getNumberCellsY` *Get the number of cells along the Y axis*

Description

Returns the number of cells along the Y axis.

Usage

```
getNumberCellsY(EDXFile)
```

Arguments

`EDXFile`	The EDX file from which the data are extracted.

Details

`getNumberCellsY` returns the number of cells along the Y axis.

Value

Integer.

Examples

```
### Example 1: get the number of cells along the y axis from atmosphere files
atmosphereEDX <- system.file(
  "extdata",
  "atmosphere/atmosphere.EDX",
  package = "REnviMet",
  mustWork = TRUE
)
getNumberCellsY(atmosphereEDX)

### Example 2: get the number of cells along the y axis from buildings files
buildingsEDX <- system.file(
  "extdata",
  "buildings/buildings.EDX",
  package = "REnviMet",
  mustWork = TRUE
)
getNumberCellsY(buildingsEDX)
```

`getNumberCellsZ` *Get the number of cells along the Z axis*

Description

Returns the number of cells along the Z axis.

Usage

```
getNumberCellsZ(EDXFile)
```

Arguments

`EDXFile`	The EDX file from which the data are extracted.

Details

`getNumberCellsZ` returns the number of cells along the Z axis.

Value

Integer.

Examples

```
### Example 1: get the number of cells along the z axis from atmosphere files
atmosphereEDX <- system.file(
  "extdata",
  "atmosphere/atmosphere.EDX",
  package = "REnviMet",
  mustWork = TRUE
)
getNumberCellsZ(atmosphereEDX)

### Example 2: get the number of cells along the z axis from buildings files
buildingsEDX <- system.file(
  "extdata",
  "buildings/buildings.EDX",
  package = "REnviMet",
  mustWork = TRUE
)
getNumberCellsZ(buildingsEDX)
```

`getNumberOfVariables` *Get the number of variables in the XML file*

Description

Returns the number of variables in the XML file.

Usage

```
getNumberOfVariables(EDXFile)
```

Arguments

`EDXFile`	The EDX file from which the data are extracted.

Details

`getNumberOfVariables` returns the number of variables in the XML file.

Value

Integer.

Examples

```
### Example 1: get the number of data per variable for atmosphere files
atmosphereEDX <- system.file(
  "extdata",
  "atmosphere/atmosphere.EDX",
  package = "REnviMet",
  mustWork = TRUE
)
getNumberOfVariables(atmosphereEDX)

### Example 2: get the number of data per variable for buildings files
buildingsEDX <- system.file(
  "extdata",
  "buildings/buildings.EDX",
  package = "REnviMet",
  mustWork = TRUE
)
getNumberOfVariables(buildingsEDX)
```

`getSpacingX` *Get the spacings along the X axis*

Description

Returns the vector of spacings along the X axis.

Usage

```
getSpacingX(EDXFile)
```

Arguments

`EDXFile`	The EDX file from which the data are extracted.

Details

`getSpacingX` returns the vector of spacings along the X axis.

Value

Vector(numeric).

Examples

```
### Example 1: get the values of spacing along the x axis from atmosphere files
atmosphereEDX <- system.file(
  "extdata",
  "atmosphere/atmosphere.EDX",
  package = "REnviMet",
  mustWork = TRUE
)
getSpacingX(atmosphereEDX)

### Example 2: get the values of spacing along the x axis from buildings files
buildingsEDX <- system.file(
  "extdata",
  "buildings/buildings.EDX",
  package = "REnviMet",
  mustWork = TRUE
)
getSpacingX(buildingsEDX)
```

`getSpacingY` *Get the spacings along the Y axis*

Description

Returns the vector of spacings along the Y axis.

Usage

```
getSpacingY(EDXFile)
```

Arguments

`EDXFile`	The EDX file from which the data are extracted.

Details

`getSpacingY` returns the vector of spacings along the Y axis.

Value

Vector(numeric).

Examples

```
### Example 1: get the values of spacing along the y axis from atmosphere files
atmosphereEDX <- system.file(
  "extdata",
  "atmosphere/atmosphere.EDX",
  package = "REnviMet",
  mustWork = TRUE
)
getSpacingY(atmosphereEDX)

### Example 2: get the values of spacing along the y axis from buildings files
buildingsEDX <- system.file(
  "extdata",
  "buildings/buildings.EDX",
  package = "REnviMet",
  mustWork = TRUE
)
getSpacingY(buildingsEDX)
```

`getSpacingZ` *Get the spacings along the Z axis*

Description

Returns the vector of spacings along the Z axis.

Usage

```
getSpacingZ(EDXFile)
```

Arguments

`EDXFile`	The EDX file from which the data are extracted.

Details

`getSpacingZ` returns the vector of spacings along the Z axis.

Value

Vector(numeric).

Examples

```
### Example 1: get the values of spacing along the z axis from atmosphere files
atmosphereEDX <- system.file(
  "extdata",
  "atmosphere/atmosphere.EDX",
  package = "REnviMet",
  mustWork = TRUE
)
getSpacingZ(atmosphereEDX)

### Example 2: get the values of spacing along the z axis from buildings files
buildingsEDX <- system.file(
  "extdata",
  "buildings/buildings.EDX",
  package = "REnviMet",
  mustWork = TRUE
)
getSpacingZ(buildingsEDX)
```

`getUniqueSpacingX` *Get the unique values of spacings along the X axis*

Description

Returns the vector of the unique values of spacings along the X axis.

Usage

```
getUniqueSpacingX(EDXFile)
```

Arguments

`EDXFile`	The EDX file from which the data are extracted.

Details

`getUniqueSpacingX` returns the vector of the unique values of spacings along the X axis.

Value

Vector(numeric).

Examples

```
### Example 1: get the unique values of spacing along the x axis from atmosphere files
atmosphereEDX <- system.file(
  "extdata",
  "atmosphere/atmosphere.EDX",
  package = "REnviMet",
  mustWork = TRUE
)
getUniqueSpacingX(atmosphereEDX)

### Example 2: get the unique values of spacing along the x axis from buildings files
buildingsEDX <- system.file(
  "extdata",
  "buildings/buildings.EDX",
  package = "REnviMet",
  mustWork = TRUE
)
getUniqueSpacingX(buildingsEDX)
```

`getUniqueSpacingY` *Get the unique values of spacings along the Y axis*

Description

Returns the vector of the unique values of spacings along the Y axis.

Usage

```
getUniqueSpacingY(EDXFile)
```

Arguments

`EDXFile`	The EDX file from which the data are extracted.

Details

`getUniqueSpacingY` returns the vector of the unique values of spacings along the Y axis.

Value

Vector(numeric).

Examples

```
### Example 1: get the unique values of spacing along the y axis from atmosphere files
atmosphereEDX <- system.file(
  "extdata",
  "atmosphere/atmosphere.EDX",
  package = "REnviMet",
  mustWork = TRUE
)
getUniqueSpacingY(atmosphereEDX)

### Example 2: get the unique values of spacing along the y axis from buildings files
buildingsEDX <- system.file(
  "extdata",
  "buildings/buildings.EDX",
  package = "REnviMet",
  mustWork = TRUE
)
getUniqueSpacingY(buildingsEDX)
```

`getUniqueSpacingZ` *Get the unique values of spacings along the Z axis*

Description

Returns the vector of the unique values of spacings along the Z axis.

Usage

```
getUniqueSpacingZ(EDXFile)
```

Arguments

`EDXFile`	The EDX file from which the data are extracted.

Details

`getUniqueSpacingZ` returns the vector of the unique values of spacings along the Z axis.

Value

Vector(numeric).

Examples

```
### Example 1: get the unique values of spacing along the z axis from atmosphere files
atmosphereEDX <- system.file(
  "extdata",
  "atmosphere/atmosphere.EDX",
  package = "REnviMet",
  mustWork = TRUE
)
getUniqueSpacingZ(atmosphereEDX)

### Example 2: get the unique values of spacing along the z axis from buildings files
buildingsEDX <- system.file(
  "extdata",
  "buildings/buildings.EDX",
  package = "REnviMet",
  mustWork = TRUE
)
getUniqueSpacingZ(buildingsEDX)
```

`getVariablesNames` *Get the variables' names of an EDX file*

Description

Returns the variable names of an EDX file.

Usage

```
getVariablesNames(EDXFile)
```

Arguments

`EDXFile`	The EDX file from which the data are extracted.

Details

`getVariablesNames` returns the variable names of an EDX file. The special characters are replaced with alphanumeric characters or underscores.

Value

Vector(characters).

Examples

```
### Example 1: get the variable names of the variables in atmosphere files
atmosphereEDX <- system.file(
  "extdata",
  "atmosphere/atmosphere.EDX",
  package = "REnviMet",
  mustWork = TRUE
)
getVariablesNames(atmosphereEDX)

### Example 2: get the variable names of the variables in buildings files
buildingsEDX <- system.file(
  "extdata",
  "buildings/buildings.EDX",
  package = "REnviMet",
  mustWork = TRUE
)
getVariablesNames(buildingsEDX)
```

`getVariablesUnits` *Get the variables' units of an EDX file*

Description

Returns the variable units of an EDX file.

Usage

```
getVariablesUnits(EDXFile)
```

Arguments

`EDXFile`	The EDX file from which the data are extracted.

Details

`getVariablesUnits` returns the variable units of an EDX file. The special characters are replaced with alphanumeric characters or underscores. By default, the units are displayed between brackets.

Value

Vector(characters).

Examples

```
### Example 1: get the variable units of the variables in atmosphere files.
atmosphereEDX <- system.file(
  "extdata",
  "atmosphere/atmosphere.EDX",
  package = "REnviMet",
  mustWork = TRUE
)
getVariablesUnits(atmosphereEDX)

### Example 2: get the variable units of the variables in buildings files
buildingsEDX <- system.file(
  "extdata",
  "buildings/buildings.EDX",
  package = "REnviMet",
  mustWork = TRUE
)
getVariablesUnits(buildingsEDX)
```

`readEDTFile` *Read EDT file contents*

Description

Renders the EDT file contents as a matrix.

`readEDTFile` returns the EDT file contents as a matrix.

Usage

```
readEDTFile(file, minimized = TRUE)
```

Arguments

`file`	The file path of the EDT file, with or without its extension.
`minimized`	A boolean to indicate if rows with empty data have to be deleted.

Value

A matrix containing the contents of an EDT file.

Examples

```
### Example 1: read data of atmosphere files
atmosphereEDT <- system.file(
  "extdata",
  "atmosphere/atmosphere.EDT",
  package = "REnviMet",
  mustWork = TRUE
)
atmosphere <- readEDTFile(atmosphereEDT)
atmosphere

### Example 2: read data of buildings files
buildingsEDT <- system.file(
  "extdata",
  "buildings/buildings.EDT",
  package = "REnviMet",
  mustWork = TRUE
)
buildings <- readEDTFile(buildingsEDT)
buildings

### Example 3: read data of buildings files, keeping rows with no data
buildingsEDT <- system.file(
  "extdata",
  "buildings/buildings.EDT",
  package = "REnviMet",
  mustWork = TRUE
)
buildings <- readEDTFile(buildingsEDT, minimized = FALSE)
buildings
```

Index

E

COMPARISON OF THE DIFFERENT PHOTOVOLTAIC GENERATION MODELS

As seen in section 3.3.1.1 on page 52, the electrical response of a solar cell to illumination is non-linear. The subsection 3.3.2.1 on page 58 highlights the method of resolution for the single-diode model. The following section aims to evaluate the accuracy of the single- and double-diode models with a confrontation between experimental data and numerical results.

E.1 COMPARISON OF THE PERFORMANCES OF THE DIODE-BASE MODELS

E.1.1 *Characteristics of the Photovoltaic Panel*

Two different PV panels are considered for the comparison between manufacturer data and the PV generation models. Those PV panels are the single-crystalline Siemens SM55 and the poly-crystalline BP 3235T. Their characteristics are given in the tables table E.1 on page XLII and table E.2 on page XLIII.

Two factors influence the electrical response of the PV panels : the temperature and the irradiance. Indeed, the higher the irradiance, the higher the generated PV power. A higher irradiance leads to an increase of temperature. Nonetheless, the higher the temperature of a solar cell, the lower the power. Thus, irradiance can have a positive direct impact on the PV power generation as well as a negative indirect impact. Moreover, the influence of these two factors is non-linear. The importance of the calculation of the electrical response appears then to be a crucial issue in the evaluation of the PV power potential.

Table E.1.: Parameters of the Solar Module SM55

Electrical Parameters			
Maximum Power Rating	P_{max}	[W]	55
Minimum Power Rating	P_{min}	[W]	50
Rated Current	I_{mp}	[A]	3.15
Rated Voltage	V_{mp}	[V]	17.4
Short Circuit Current	I_{SC}	[A]	3.45
Open Circuit Voltage	V_{OC}	[V]	21.7
Thermal Parameters			
Nominal Operating Cell Temperature	NOCT	[°C]	45
Change of I_{SC} with Temperature	α	$[\mathrm{mA} \cdot {}^{\circ}\mathrm{C}^{-1}]$	+1.2 $(0.04\,\% \cdot \mathrm{K}^{-1})$
Change of V_{OC} with Temperature	β	$[\mathrm{V} \cdot {}^{\circ}\mathrm{C}^{-1}]$	-0.077 $(-0.34\,\% \cdot \mathrm{K}^{-1})$
Physical Parameters			
Number of Series Cells			36
Length		[mm]	1293
Width		[mm]	329

Table E.2.: Parameters of the Solar Module BP3235T

Electrical Parameters			
Maximum Power Rating	P_{max}	[W]	235
Current at P_{max}	I_{mp}	[A]	7.89
Voltage at P_{max}	V_{mp}	[V]	29.8
Short circuit current	I_{SC}	[A]	8.48
Open circuit voltage	V_{OC}	[V]	37.2
Thermal Parameters			
Nominal Operating Cell Temperature	NOCT	[°C]	47 ± 2
Temperature Coefficient of I_{SC}	α	$[\% \cdot K^{-1}]$	0.105
Temperature Coefficient of V_{OC}	β	$[\% \cdot °C^{-1}]$	-0.360
Temperature Coefficient of P_{max}	γ	$[\% \cdot °C^{-1}]$	-0.45
Physical Parameters			
Number of series cells			60
Length		[mm]	1667
Width		[mm]	1000

E.1.2 *Temperature Dependance of the Photovoltaic Panel Characteristics*

The surface temperature of a PV cell has an influence on its efficiency and so on the solar potential. As can be seen in the table E.2 on page XLIII, an increase of the temperature leads to a decrease in the output power of a solar module. Thus, the higher the temperature, the lower the output power. This evolution can be seen in figure E.1b on page XLVII. Nevertheless, the relationship between the evolution of the temperature and the output power is not linear. So, it is important to have a model able to take into consideration the evolution of the solar cell temperature.

Besides having an influence on the efficiency of a solar cell, the temperature has an impact on the accuracy of the PV power generation model as well. Indeed, as shown in figure E.1 on page XLVII, the predicted output power are closer to the measured one for lower temperature. This figure also shows that the accuracy of the double-diode model is much higher than that of the single-diode model. This is especially true for the higher temperatures.

In terms of accuracy, the root mean squared error (RMSE) and the mean absolute percentage error (MAPE) are considered as indicators. Their definitions are given in equation (5.8) on page 141 and equation (5.9) on page 141, respectively.

Measurements are needed to evaluate the RMSE and the MAPE. Those measurements are from (Chaibi et al., 2019).

The table E.3 on page XLV gives the values of the RMSE for the single- and double-diode models. Its reading is double. Indeed, on the one hand it shows that the RMSE tends to slowly increase with the temperature for both of the models, from 0.322 to 0.632 for the single-diode model and from 0.053 9 to 0.069 8 with a temperature from 20 °C to 60 °C. On the other hand, it shows that the double-diode model is much more accurate than the single-diode model, which has a RMSE five to six times lower. This higher accuracy is confirmed by the MAPE. Indeed, the MAPE of the double-diode model remains strictly lower than 10 %, whatever the temperature while that of the single-diode model keeps strictly greater than 25 %.

Table E.3.: Comparison of the Root Mean Squared Error under Varying Temperatures

Temperature (°C)	Single-diode Model	Double-diode Model
20	0.322	0.053 9
30	0.333	0.048 3
40	0.338	0.051 3
50	0.342	0.061 1
60	0.362	0.069 8

Table E.4.: Comparison of the Mean Absolute Percentage Error under Varying Temperatures

Temperature (°C)	Single-diode Model	Double-diode Model
20	30.0 %	6.94 %
30	26.7 %	4.10 %
40	28.3 %	5.36 %
50	31.7 %	7.04 %
60	32.3 %	8.09 %

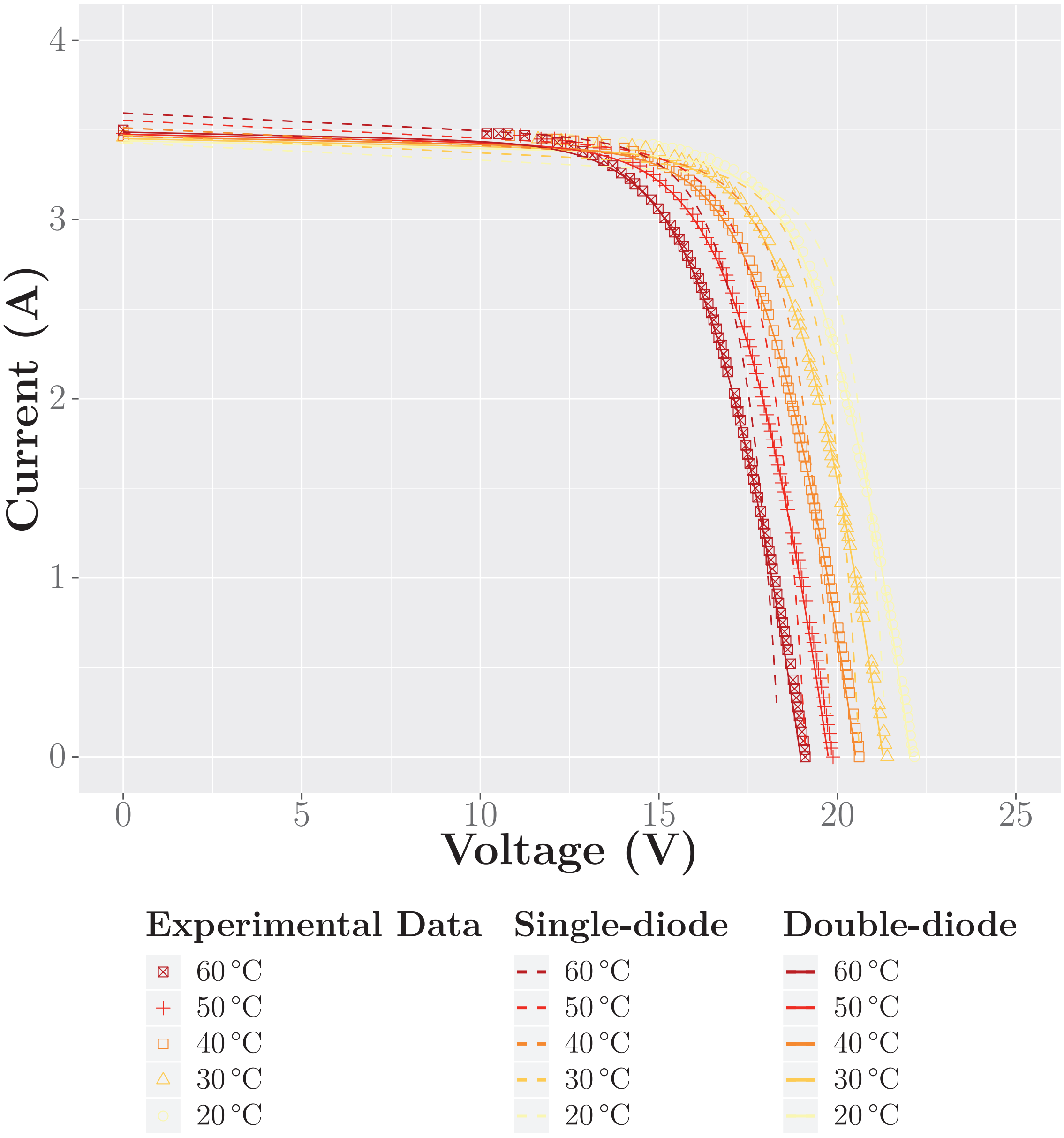

(a) Current-voltage Characteristics

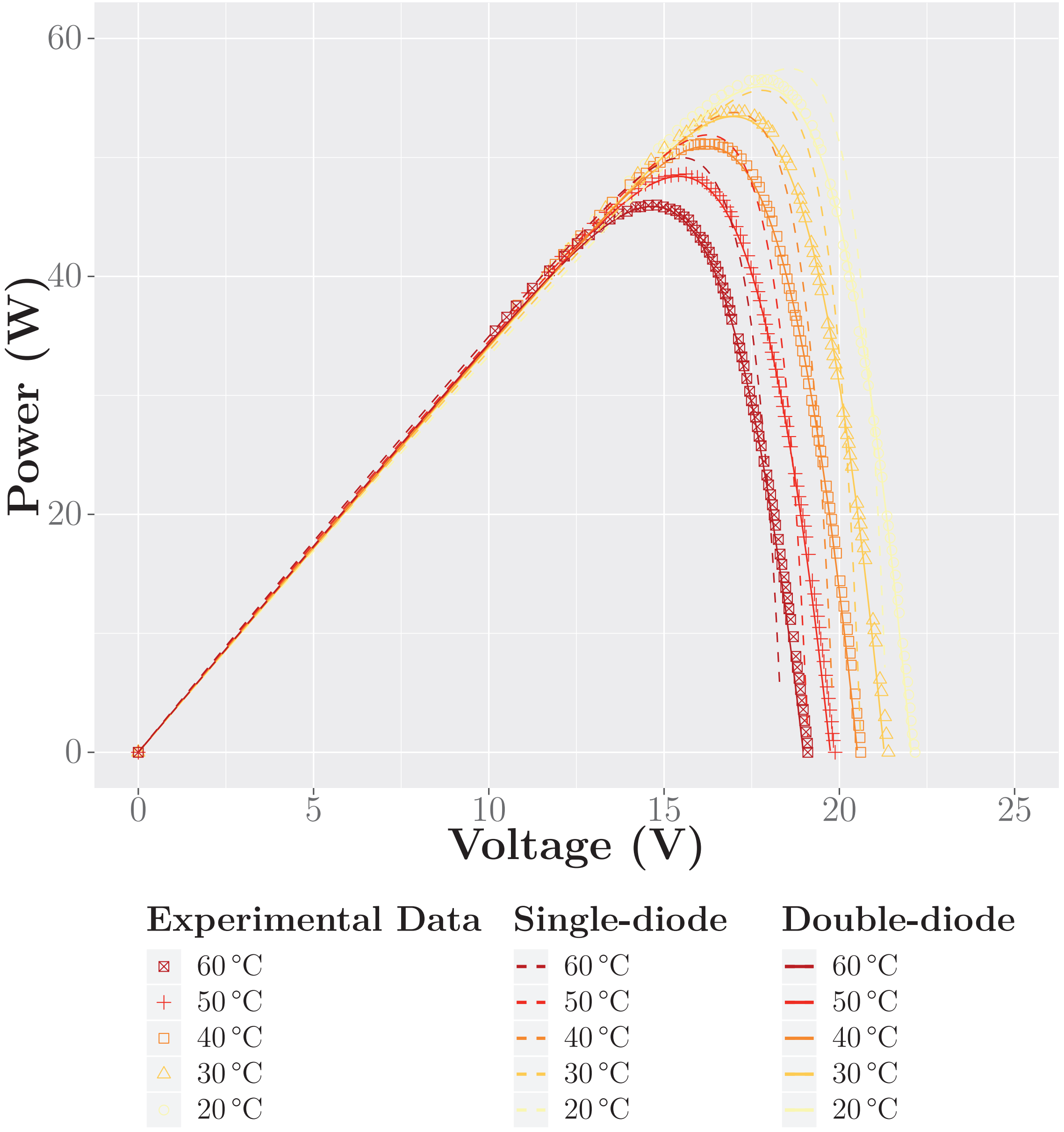

(b) Power-voltage Characteristics

Figure E.1.: Comparison of the Single- and Double-diode Models Versus Experimental Data under Varying Temperatures and an Irradiation Level of $1\,000\,\mathrm{W \cdot m^{-2}}$ (Measurements from (Chaibi et al., 2019))

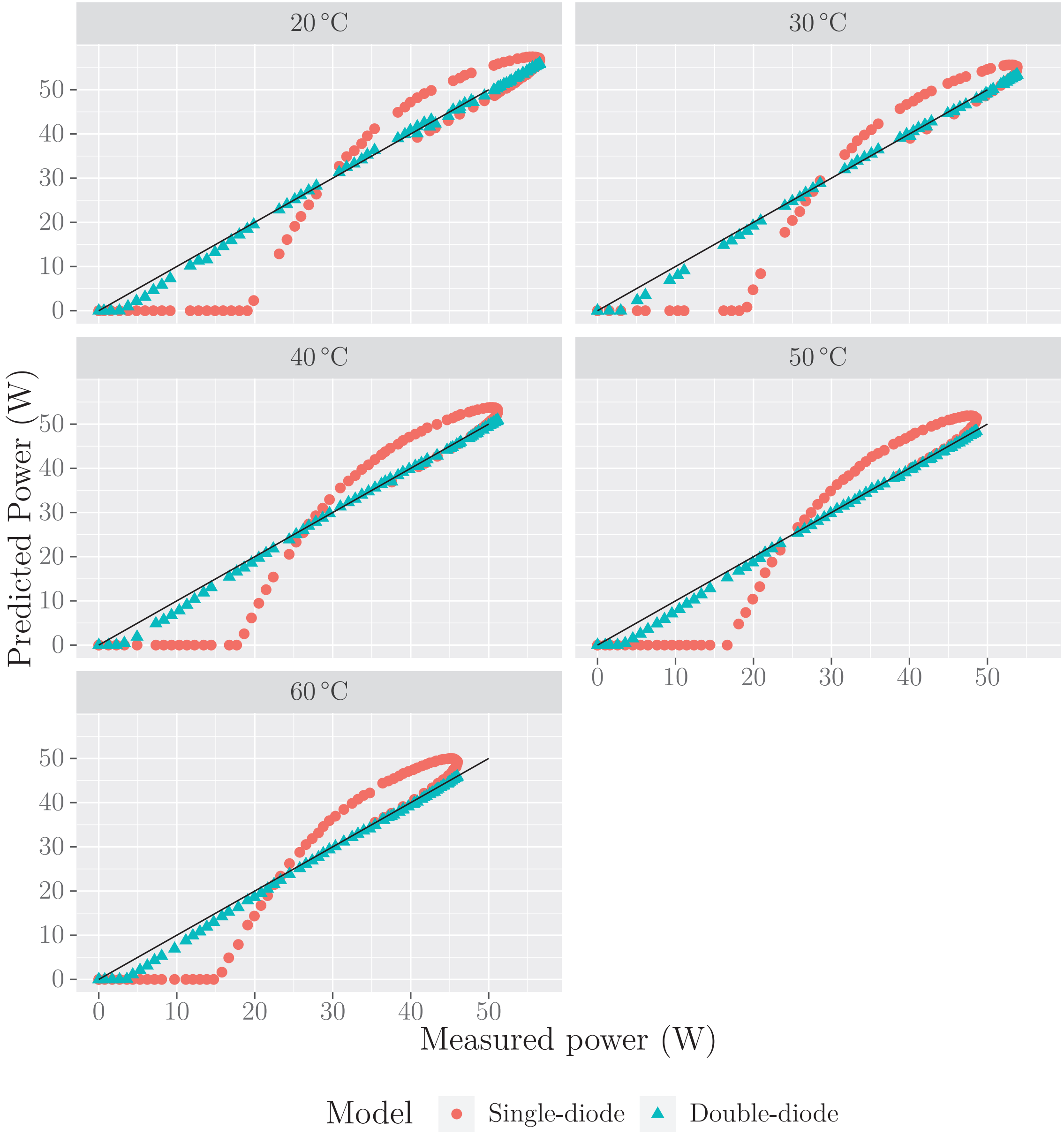

Figure E.2.: Correspondence of the Single- and Double-diode Models with Measurements for Temperature from 20 °C to 60 °C (Measurements from (Chaibi et al., 2019))

E.1.3 *Irradiance Dependance of the Photovoltaic Panel Characteristics*

The irradiance is the second factor of influence regarding the PV power generation of a solar cell. Indeed, the higher the irradiance, the higher the output power of a solar cell as can be seen in figure E.3b on page LII. As the relationship between the evolution of the temperature and the output power, the one between the latter and the irradiance level is not linear. The evolution of the irradiance is then to be taken into consideration in the PV power generation model.

Unlike the temperature, the higher the irradiance, the less accurate the predicted generated PV power. Indeed, as shown in figure E.3b on page LII, the higher the irradiance, the closer the match between the measured and the predicted values. In terms of RMSE, the table E.5 on page L shows that, once again, the double-diode model is much more accurate than the single-diode model with a RMSE strictly lower than 0.1 for the double-diode model while that of the single-diode model is more than ten times higher.

In terms of MAPE, the double-diode model appears as the most accurate, relatively to the single-diode model, but as a precise and reliable model as well. Indeed, while the MAPE for the single-diode model is around 15 % for irradiance levels from $600\,\mathrm{W} \cdot \mathrm{m}^{-2}$ to $1\,000\,\mathrm{W} \cdot \mathrm{m}^{-2}$ (which correspond to irradiance levels that usually occur during the afternoon for sunny days), the one of the double-diode model is lower than 10 %. The difference, in terms of accuracy between the two models is even more visible in the case of lower radiations. Indeed, while the MAPE of the double-diode model remains low, the one of the single-diode model sharply rises to almost 70 %.

Table E.5.: Comparison of the Root Mean Squared Error under Varying Irradiation Levels

Irradiation Level ($\mathrm{W \cdot m^{-2}}$)	Single-diode Model	Double-diode Model
200	0.420	0.013 7
400	0.259	0.045 6
600	0.172	0.082 0
800	0.167	0.097 6
1 000	0.247	0.069 9

Table E.6.: Comparison of the Mean Absolute Percentage Error under Varying Irradiation Levels

Irradiation Level ($\mathrm{W \cdot m^{-2}}$)	Single-diode Model	Double-diode Model
200	68.5 %	2.04 %
400	29.3 %	6.68 %
600	16.9 %	8.03 %
800	14.4 %	8.70 %
1 000	17.8 %	6.11 %

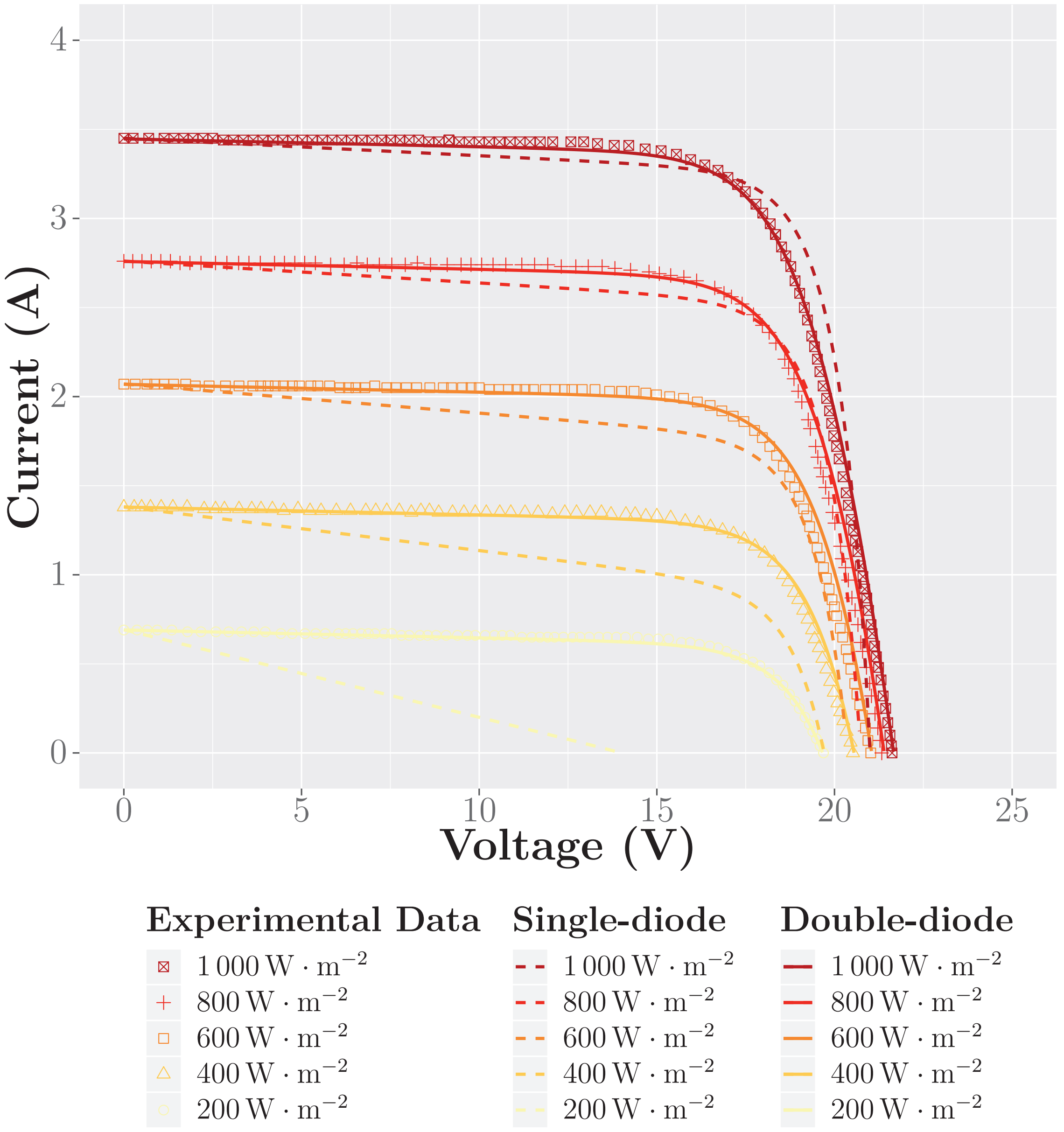

(a) Current-voltage Characteristics

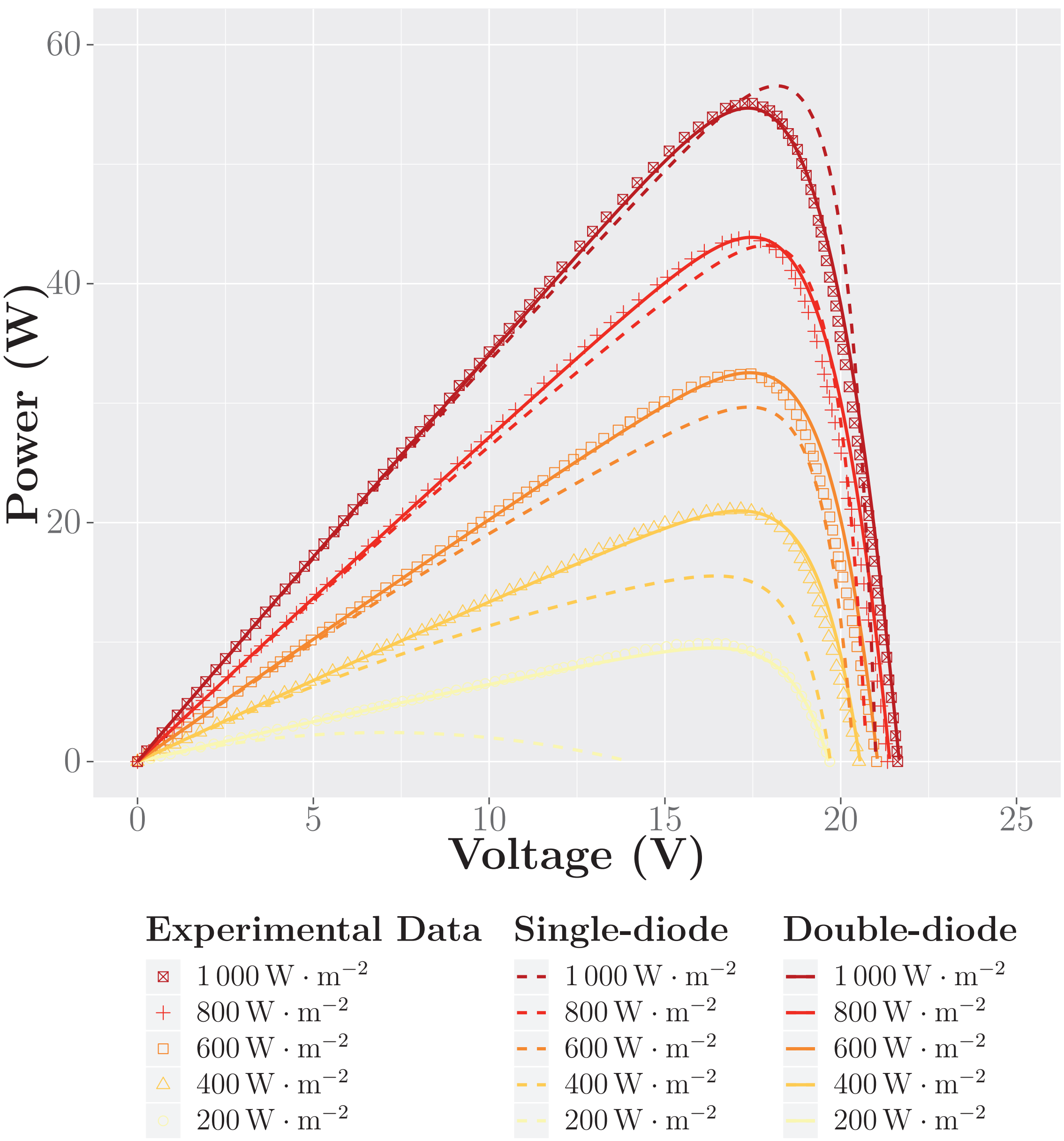

(b) Power-voltage Characteristics

Figure E.3.: Comparison of the Single- and Double-diode Models Versus Experimental Data Under Varying Irradiation Levels and a Temperature of 25 °C

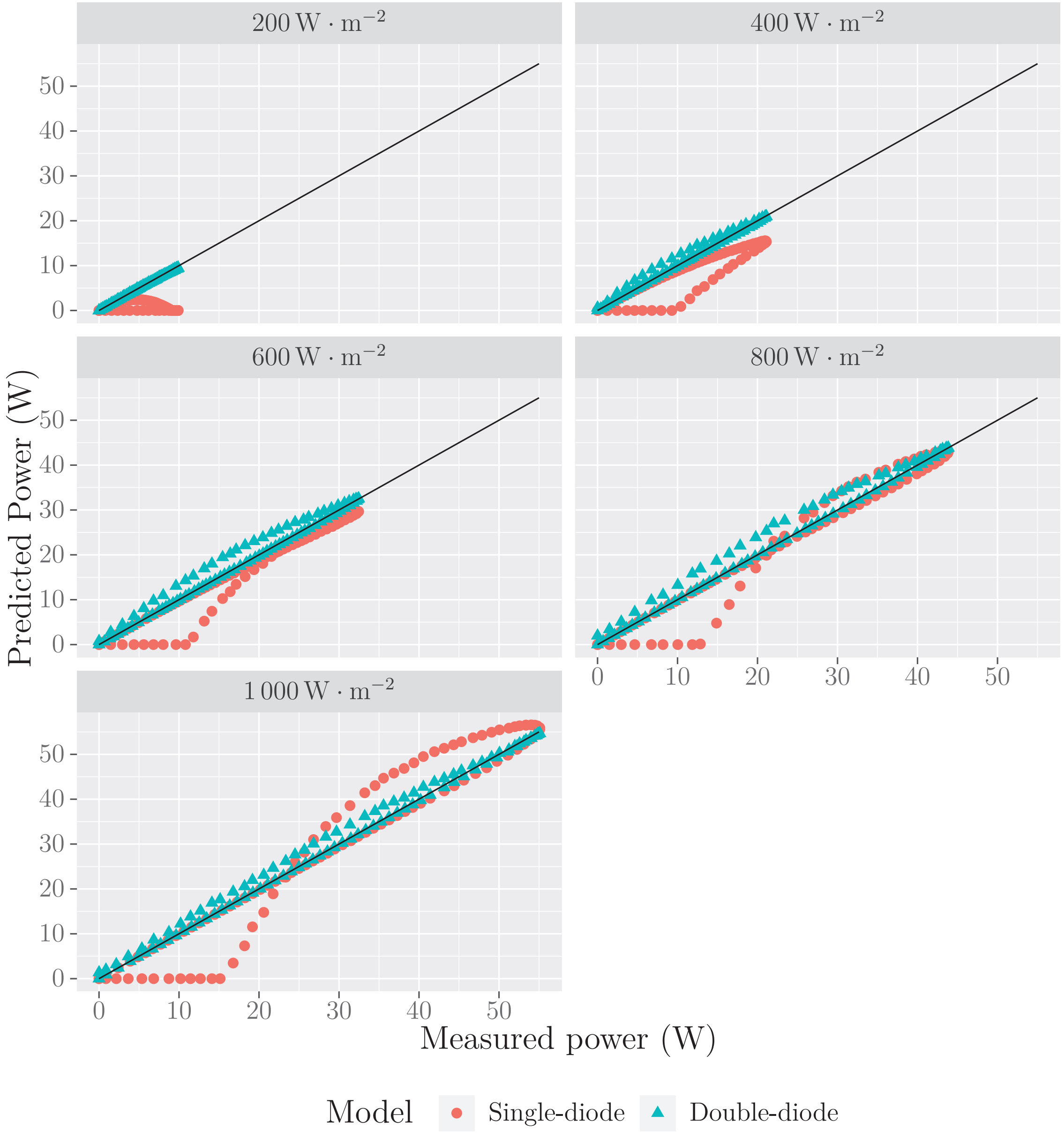

Figure E.4.: Correspondence of the Single- and Double-diode Models with Measurements for Irradiance from 200 W · m^{-2} to 1 000 W · m^{-2} (Measurements from (Chaibi et al., 2019))

REFERENCES RELATED TO THE POSITIONING OF THE DIODE-BASED MODELS

Chaibi, Y., Malvoni, M., Allouhi, A., & Mohamed, S. (2019). Data on the I–V characteristics related to the SM55 monocrystalline PV module at various solar irradiance and temperatures. *Data in Brief*, *26*, 104527. https://doi.org/https://doi.org/10.1016/j.dib.2019.104527 (Cited on pages XLIV, XLVII, XLVIII, LIII)